MAGNETIC RESONANCE LINE-SHAPE AND RELAXATION TIME STUDIES OF ROTATIONAL DIFFUSION IN LIQUIDS

by

P.S.PHILLIPS

B.Sc. The University of Sussex, 1974

M.Sc. The University of British Columbia, 1978

A THESIS SUBMITTED IN PARTIAL FULFILMENT OF

THE REQUIREMENTS FOR THE DEGREE OF

DOCTOR OF PHILOSOPHY

in

THE FACULTY OF GRADUATE STUDIES

DEPT. OF CHEMISTRY

We accept this thesis as conforming

to the required standard

THE UNIVERSITY OF BRITISH COLUMBIA

JUNE 1985

In presenting this thesis in partial fulfilment of the requirements for an advanced degree at the The University of British Columbia, I agree that the Library shall make it freely available for reference and study. I further agree that permission for extensive copying of this thesis for scholarly purposes may be granted by the Head of my Department or by his or her representatives. It is understood that copying or publication of this thesis for financial gain shall not be allowed without my written permission.

DEPT. OF CHEMISTRY

The University of British Columbia
2036 Main Mall,
Vancouver, Canada
V6T 1Y6

Date: JUNE 20th 1985

Abstract

A new numerical analysis method, dispersion *vs.* absorption plots (DISPA), has been developed for ESR. This method may be used for semi-quantitative line-shape studies and is useful both as a diagnostic and analytical tool. In addition it provides a method of automatic phasing for magnetic resonance spectra. Numerous examples of its applications, both simulated and experimental are presented, with emphasis on spin-probe studies. The digital acquisition and processing methods used for these studies are also briefly discussed.

ESR and NMR relaxation time studies of the bis(dialkyl-N-carbodithioate) metal(II) class of spin-probes have been performed. The T_1's of ^{13}C and ^{2}H enriched nickel complex were measured by NMR. The line-widths of ^{63}Cu complex were measured by ESR and analysed by Redfield theory. The two sets of results were combined to give the principal elements of the rotational diffusion tensor for the pyrollidine derivative in toluene. This is the first time that ESR and NMR studies have been combined to measure a diffusion tensor. A general strategy for this approach is presented.

ESR data from previous work has been re-analysed in the light of the new results. The analysis shows that the commonly used assumption of isotropic diffusion is extremely misleading.

Table of Contents

PART 3.

ELECTRON SPIN RESONANCE STUDIES

PART 4.

NMR STUDIES

PART 5.

COMMENTS ON THE COMBINED NMR-ESR STUDIES

PART 6.

NOTES ON THE DIGITAL ACQUISITION OF ESR SPECTRA

APPENDICES

LIST OF TABLES

LIST OF FIGURES

Acknowledgements

I wish to sincerely thank Dr. F.G. Herring for his help, guidance and patience throughout my research.

I would also like to thank Dr.K.A.Mitchell and Dr.R.F.Snider for useful comments on the thesis, Dr.A.Storr for the eight year loan of his molecular models and Kam Sukul, Mike Hatton and other members of the electronic shop for their never ending maintainence of the equipment.

I also wish to acknowledge the Chemistry Department of the University of British Columbia for providing financial support, despite an unfavourable economic climate, during the course of this work.

"Onwards always Onwards,

In Silence and in Gloom..."[1]

---

[1] "Fungus the Bogeyman", Raymond Briggs, Hamish Hamilton, London (1977)

PART 1.

DISPERSION VS. ABSORPTION PLOTS: DISPA

1. INTRODUCTION

Any line in a spectrum may be characterised by its amplitude, position and shape. The amplitude is usually a function of the concentration of the species associated with the line. The position gives structural information. The shape is usually assumed to be Lorentzian and the width of the line is then used to complete the characterisation. The width of the line can give information about the species' dynamics.

In recent years there has been great interest in extracting motional information from ESR line-widths. It is very important, for these studies, to be sure that the line is in fact Lorentzian, or the line-width will not accurately reflect the relaxation time and hence the motion of the species. A quick and easy method for assessing deviations from the Lorentzian line-shape would be of great value to such studies. To this end we have developed a method of analysing the line-shape of ESR spectra. The method is based on Cole-Cole plots *(1)* and not only detects deviations from Lorentzian behaviour, but also identifies the cause of the deviation. It is thus useful as both a diagnostic and analytical tool.

A plot of an absorption signal *vs.* its corresponding dispersion signal will produce an approximately circular graph. Such a plot is known (here) as a DISPA plot. If the absorption signal is Lorentzian then the DISPA plot is a circle. If the signal is distorted by, for instance, a

second line, then a distorted ellipse is produced. The graph's deviation from a circle is characteristic (often uniquely so) of the distorting mechanism. DISPA plots thus provide a method of quantitating the shape of a line and for detecting unresolved features. However, it should be emphasised that the utility of DISPA lies not only with the information obtained, but also with the ease with which it is obtained. A DISPA plot requires no special experiment and only takes a few minutes at most. Simulations, for example, can take days.

1.1 A BRIEF HISTORY

Dispersion *vs.* absorption plots have been long used in dielectric studies (as Cole-Cole plots) to analyse relaxation mechanisms *(1)*. There have been brief allusions to DISPA plots in magnetic resonance literature *(2)(3)(4)*, but its full potential as a tool in line-shape analysis was not realised until developed for NMR by Marshall *(5)(6)(7)(8)*. Its application to ESR was initially hampered by the difficulties of producing ESR dispersion spectra. This problem was circumvented by using the Kramers-Kronig relations *(9)* to generate dispersion spectra from absorption spectra. However, this method proved impractical until a more efficient algorithm utilising the fast Fourier transform (FFT) was introduced *(10)*. It rapidly became apparent that data processing for ESR spectra was considerably different (and more difficult) than it was for

NMR spectra and the development of DISPA for these two techniques diverged. Marshall continued to refine DISPA for NMR *(11)(12)(13)* and Herring and Phillips *(10)(14)* developed the method for use with ESR. Only the latter research will be discussed here.[2]

---

[2] Much of this work is applicable to NMR and some overlap with Marshall's work is inevitable.

2. THE BASIC THEORY OF DISPA

A line is characterised by its width, height, area, position and shape. A theoretical treatment of DISPA plots should take all of these variables into acccount. Unfortunately, general analytical expressions for most of the cases do not exist so the basic theory is restricted to simple distributions of Lorentzian lines. More complex cases have to be dealt with empirically.

2.1 THE DISPA CIRCLE

In magnetic resonance the absorption ($A(\omega)$) and dispersion ($D(\omega)$) signals for a single Lorentzian line are given by *(15)*

$$A(\omega) = \frac{M_0 \gamma B_1 T_2}{1+T_2^2(\omega-\omega_0)^2+\gamma^2 B_1^2 T_1 T_2}$$

$$D(\omega) = \frac{M_0 \gamma B_1 T_2^2(\omega-\omega_0)^2}{1+T_2^2(\omega-\omega_0)^2+\gamma^2 B_1^2 T_1 T_2} \qquad (2.1)$$

The experimentally observed signals, v for absorption, u for dispersion, are[3]

---

[3] Strictly speaking, for ESR, the signals are the differentials of these functions. The absorption signal is always integrated before use so this is of little immediate consequence.

$$v = \frac{Ab}{1+(bp)^2+S}$$

$$u = \frac{Apb^2}{1+(bp)^2+S} \qquad (2.2)$$

where A is the amplitude of v at resonance ($\sim M_0\gamma B_1$), b = T_2, p = $(\omega-\omega_0)$ and S is the saturation term ($\gamma^2 B_1^2 T_1 T_2$). If we note that v=bp$u$ we can eliminate the parameter p from Eqn.2.2 and after rearranging we get (if there is no saturation, *i.e.*, S<<1)

$$u^2 + v^2 = bAv$$

$$\text{or} \quad u^2 + (v-\tfrac{1}{2}bA)^2 = (\tfrac{1}{2}bA)^2 \qquad (2.3)$$

if we let $\frac{1}{2}$bA=R then we get

$$u^2 + (v-R)^2 = R^2 \qquad (2.4)$$

This is a circle of radius R displaced along the v axis by R (Fig.2.1). R is proportional to the spectrum line-width and amplitude.

A plot of u *vs.* v superimposed on a reference circle (a circle of radius equal to the maximum of v, R, in this case and displaced along the v axis by R) is called a DISPA plot (in the Cole-Cole format). Such a plot is only a circle for

a pure Lorentzian line. Generally a distorted ellipse is observed (see Fig.2.1). The distortion is characteristic for the mechanism causing deviations from Lorentzian behaviour.

Note from Eqn.2.4 that the frequency dependence (the p term) has been eliminated so that DISPA plots are independent of line position. Also, if the spectrum is scaled to a fixed amplitude before plotting, the line-width and amplitude dependence of DISPA plots are removed.

In magnetic resonance the spectral lines can often be considered as composites of many Lorentzian lines distributed in amplitude, frequency or width (and combinations thereof). The various cases are discussed below.

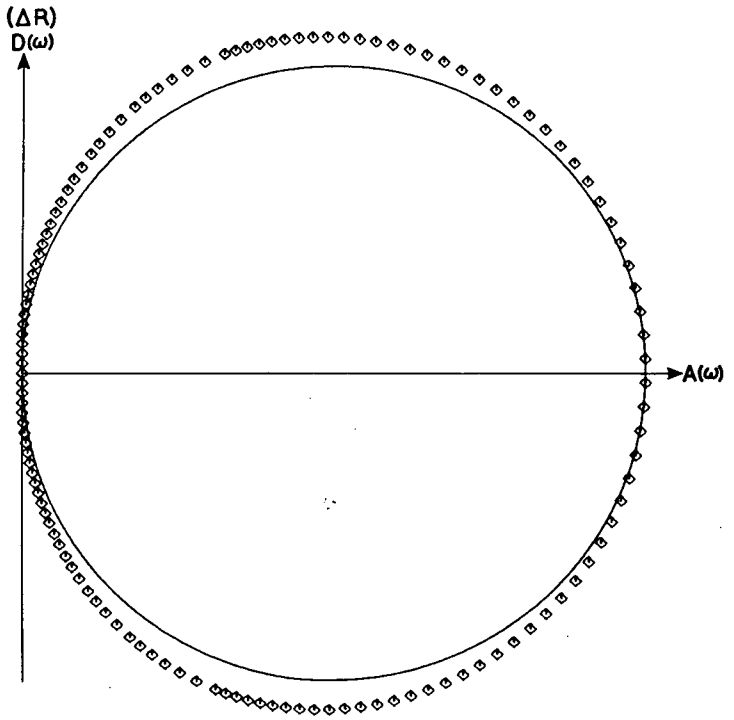

Figure 2.1. Typical Cole-Cole format DISPA plot for a single line. The solid line is the reference circle. The diamonds are the data.

2.2 LORENTZIAN LINES DISTRIBUTED IN AMPLITUDE

The amplitude, A, in Eqn.2.2 is simply a height scaling factor. So providing that the lines have the same width and position adding Lorentzian lines together just produces a DISPA circle of larger radius. As the spectra are always scaled to a constant height for DISPA studies this effect is not observed. The corollary to this is that anything that changes only the spectrum amplitude (small power and modulation changes, amplifier gain *etc.*) does not affect the DISPA plot for that line. This is true even if the line is non-Lorentzian. Another point is that, for a single Lorentzian line, a change in line-width only affects the amplitude and so is not observed in DISPA plots. These rather trivial results lead to the important conclusion that, for a single Lorentzian line, homogeneous broadening mechanisms do not affect the DISPA plot. The most commonly encountered homogeneous broadening mechanisms are; lifetime broadening due to exchange or motion, dipolar broadening and microwave saturation.

2.3 THE EFFECT OF SATURATION ON LORENTZIAN LINES

If we eliminate p from our equations as before, but retain the saturation term S we get

$$v^2(1+S) + u^2 = Abv \qquad (2.5)$$

if we let $q=\sqrt{(1+S)}$ then we obtain

$$u^2 + (vq-bA/q)^2 = (\tfrac{1}{2}bA/q)^2 \qquad (2.6)$$

As pointed out by Abragam *(4)* and shown numerically by Marshall *(11)*, this is an ellipse whose major axis is parallel to the u axis The length of which depends on the microwave power. The position and width of the ellipse are also a function of microwave power, but this effect disappears because the absorption spectra are scaled to a constant amplitude, *vide supra*.

The absorption line in the presence of saturation is still Lorentzian, only its width and amplitude change. Similarly for the dispersion line. The elliptical behaviour arises because the amplitude dependence on microwave power of a saturated dispersion line is different from that of a saturated absorption line *(16)*. However, the dispersion line is generated by a Hilbert transform[a] of the absorption line. The computer program just has a Lorentzian data set of a given width and height and generates the corresponding (in width and height) dispersion line. The saturation term does not appear explicitly so the elliptical behaviour disappears from the DISPA plot.

---

[a] The Hilbert transform is only valid for linear, *i.e.*, unsaturated, systems. *(17)*

2.4 DISTRIBUTION IN LINEWIDTHS OF LORENTZIAN LINES

If we assume the line is composed of several Lorentzian lines of the same resonant frequency, but different relaxation times then we have to substitute $Ab=\sum_i A_i b_i$ into Eqn.2.3,[5] hence we get i circles

$$\left[\left[\sum_i u_i\right]^2 + \left[\sum_i \left(v_i - \tfrac{1}{2}A_i b_i\right)\right]^2 = \left[\sum_i \tfrac{1}{2}A_i b_i\right]^2\right] \qquad (2.7)$$

where

$$u_i = \frac{\underline{A}_i \underline{b}_i}{1+(bp_i)^2+S} \qquad etc. \qquad (2.8)$$

Eqn.2.7 represents a set of circles each of radius $b_i/2$ and displaced by $b_i/2$, which, when summed, will form a distorted oblate ellipse (Fig.2.2).

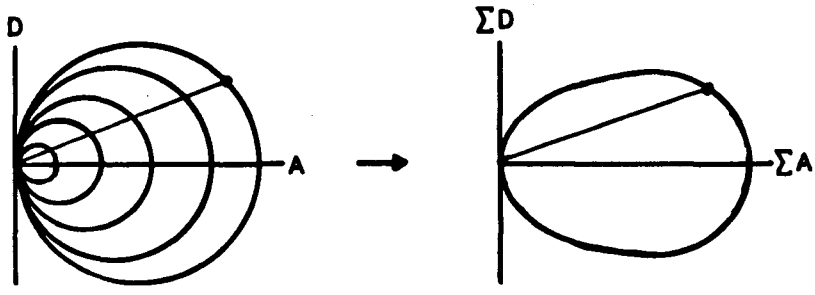

Figure 2.2. DISPA for superimposed Lorentzian Lines.

---

[5] A and b are linked by the area of the line, which in turn is proportional to the concentration of the species. However, it is sometimes convenient to regard these parameters as independent variables.

The radius of the i'th circle depends on both the line-width and concentration of species i so it is not possible to make useful quantitative statements about the distortion except maybe for the case of i=2. The distribution for i>1 is very common in dielectric studies. Its characterisation has been discussed by Cole & Davidson *(18)*.

2.5 DISTRIBUTION IN RESONANT FREQUENCY OF LORENTZIAN LINES

In this case we substitute $p=\sum_i p_i$ into Eqn.2.3, where

$$p_i = \omega_{0i} - \omega = \omega_0 - \omega + \Delta_i$$

so that Δ_i represents the shift of the i'th line from the center of the spectrum, ω_0. Eqn.2.3 is in an inconvenient form for this substitution, but can be recast into a convenient form using polar coordinates. A circle in polar coordinates is given by $r=2R\cos\theta=Ab\cos\theta$. See Fig.2.3 for a definition of terms.

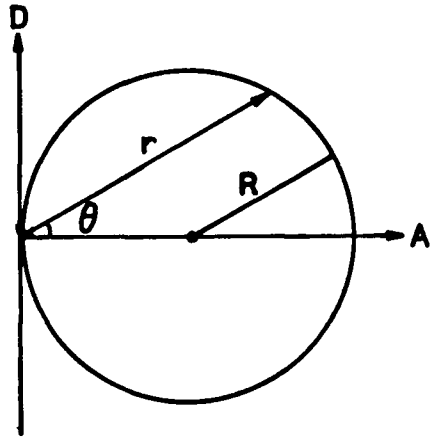

Figure 2.3. DISPA circle in polar coordinates.

The angle, θ, is given by

$$\theta = \arctan\{D(\omega)/A(\omega)\} = \arctan\{bp\} \qquad (2.9)$$

So for a distribution of resonant frequency we get

$$\Sigma_i r_i = A\cos\{\arctan\Sigma_i[b(p+\Delta_i)]\} \qquad (2.10)$$

Note that this equation represents <u>one</u> circle. The position of any given point on the circle, for a given frequency, p, depends on Δ_i. The composite figure in this case is difficult to visualise, but it will be a distorted prolate ellipse (Fig.2.4).

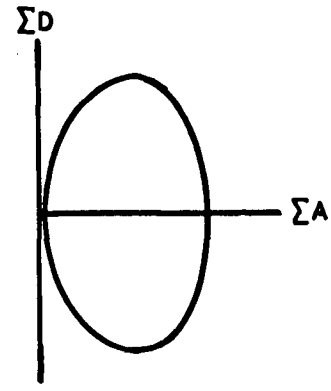

Figure 2.4. DISPA for overlapping Lorentzian lines.

2.6 DISTRIBUTION IN RESONANT FREQUENCY AND AMPLITUDE

This is an important distribution as it includes the case of unresolved hyperfine structure. The DISPA plot is simply given by

$$\Sigma_i r_i = b\Sigma_i A_i \cos\{\arctan\Sigma_i[(b_i p+\Delta_i)]\} \qquad (2.11)$$

The exact shape of the DISPA plot will depend on Δ_i and how the amplitudes are distributed, but it will be, as above, a distorted prolate ellipse. If Δ_i is constant and A_i follow the binomial distribution, then ν represents a line with unresolved hyperfine coupling (approximately the Voigt line-shape). In the limit of $\Delta \rightarrow 0$ Eqn.2.11 gives the result for a Gaussian line (A_i distributed normally) or a

Voigt line *(19)* (A_i distributed as a convolution of a Lorentzian and a Gaussian).

2.7 MODULATION BROADENING

The absorption and dispersion signals modified to allow for modulation are *(10)(20)*

$$v = \sum_{k=0} \frac{AbF(k)}{1+b^2(p+k\omega_m)^2}$$

$$u = \sum_{k=0} \frac{Ab^2F(k)(p+k\omega_m)}{1+b^2(p+k\omega_m)^2 m}$$

where $$F(k) = J_k^2\{\gamma B_m/\omega_m\}\frac{2k\omega_m}{\gamma B_m} \qquad (2.12)$$

J is a Bessel function of the first kind, ω_m is the modulation frequency, B_m is the modulation amplitude and γ is the electron gyromagnetic ratio. If we combine A and F(k) (to give A_k) and note the similarity of $k\omega_m$ and Δ_i in Eqn.2.11 we get

$$\sum_i r_i = \sum_k A_k b_k \cos\{\arctan[\sum_k b_k(p+k\omega_k)]\} \qquad (2.13)$$

which is the same as Eqn.2.11, a superposition of Lorentzian lines distributed in frequency (the harmonics of ω_m) and amplitude (a function of the modulation amplitude and frequency). The shape of the DISPA plot is different from

that caused by unresolved hyperfine coupling as generally $\omega_m << \Delta_i$ (at 100kHz, $\omega_m \simeq 30$mG) and A_i is distributed according the Bessel functions as opposed to a Pascal triangle. Although in practice the differences are often obscured by noise.

2.8 THE EFFECT OF DISPERSION

For a poorly phased spectrometer the observed signal $O(\omega)$ and its quadrature $Q(\omega)$ are given by *(21)*

$$\begin{aligned} O(\omega) &= A(\omega)\cos(\theta)+D(\omega)\sin(\theta) \\ Q(\omega) &= D(\omega)\cos(\theta)-A(\omega)\sin(\theta) \end{aligned} \qquad (2.14)$$

where $A(\omega)$ and $D(\omega)$ are the absorption and dispersion signals respectively. The angle θ is called the 'phase angle' or 'phase'. From Cartesian geometry for the rotation of coordinates, the locus of $(O(\omega),Q(\omega))$ (the DISPA plot) is just the locus of $(A(\omega),D(\omega))$ rotated by θ. If $A(\omega)$ is Lorentzian then dispersion leakage simply gives a rotated circle (Fig.2.5). For other functional forms of $A(\omega)$, the effect is the same, the DISPA plots are just rotated by θ. This is the only mechanism that causes asymmetric DISPA plots for spectra with symmetric absorption lines (free from baseline and filter artefacts). A more detailed discussion of the effect of spectrometer phase can be found in *(22)* and

Sect.5.2.

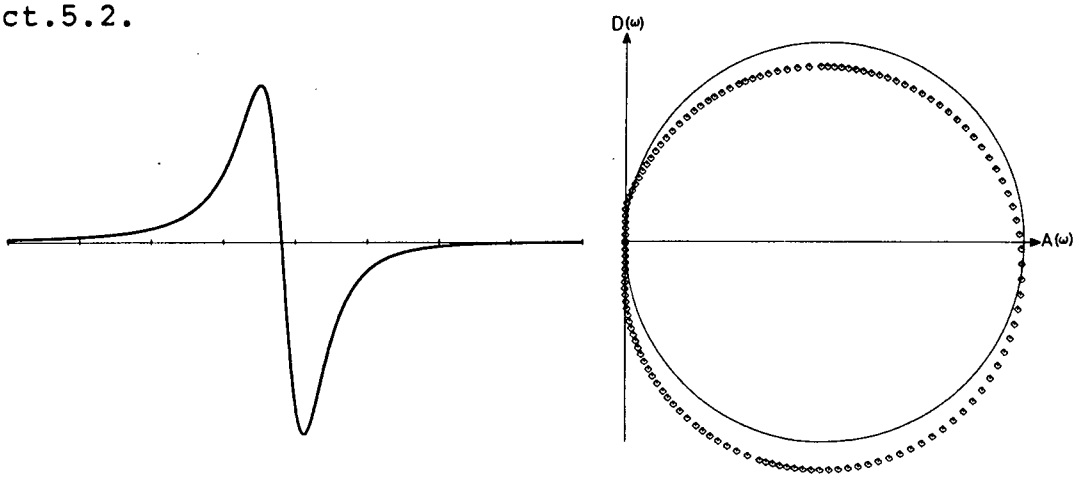

Figure 2.5. DISPA plot for a poorly phased line. θ=10°.Corresponding spectrum on the left.

2.9 THE DYSONIAN LINE

The Dysonian line-shape arises from paramagnetic centers in a conductor *(23)*. The exact form of the line-shape depends on the system; conductor thickness, diffusion rate of the center *etc.*, but the spectrum is, in all cases, similar to (and in some cases actually is) an admixture of absorption and dispersion signals. A simulated spectrum is shown in Fig.2.6. The DISPA plot is similar to Fig.2.5, except that the circle is rotated ≃45°.

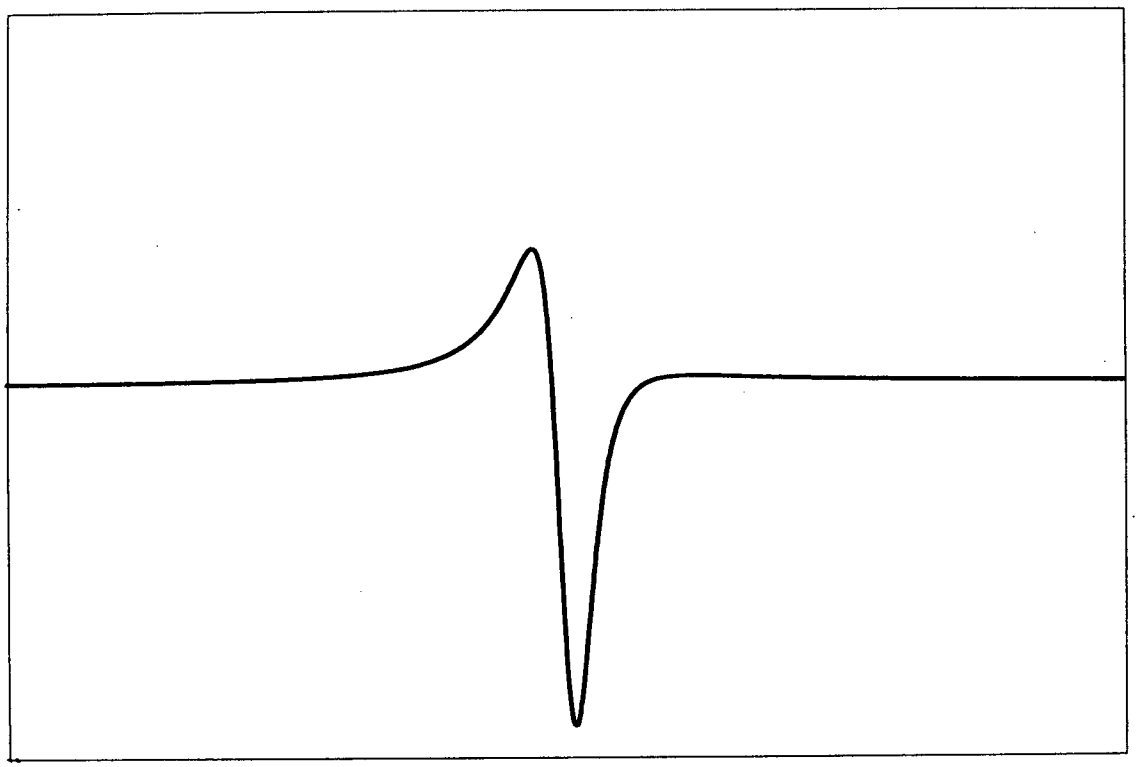

Figure 2.6. The Dysonian Line-shape.

3. THE HILBERT TRANSFORM AND DATA PRESENTATION

3.1 GENERATING THE DISPERSION SPECTRUM

ESR dispersion spectra are very difficult to produce directly. Also it is not currently possible to produce the absorption and dispersion spectra simultaneously, which presents very serious scaling problems. The dispersion spectrum can, however, be obtained *via* Kramers-Kronig relations *(9)*.

$$A(\omega') = +\pi^{-1} P\int_{-\infty}^{\infty} D(\omega)\frac{d\omega}{\omega-\omega'},$$

$$D(\omega') = -\pi^{-1} P\int_{-\infty}^{\infty} A(\omega)\frac{d\omega}{\omega-\omega'}, \qquad (3.1)$$

The P denotes use of the Cauchy principle value. This is more usually known as a Hilbert transform and is completely general for all spectroscopy except non-linear systems.[6] Eqn.3.1 can be solved numerically as it stands. However, the computation is very slow and the pole (at $\omega_0=\omega$) can cause problems. The transform can be done very efficiently once it is recognised as a convolution integral *(24)* so that

---

[6] A Hilbert transform can be done with any spectroscopic data set. However, the quadrature spectrum so obtained may not be the true quadrature signal (see Sect.2.3 on saturation). This generally does not affect DISPA's use as a diagnostic tool, but care should be taken when making comparisons with NMR data, where the true quadrature signal is always available.

$$F^{-1}\{\int_{\infty}^{\infty} D(\omega)\frac{d\omega}{\omega-\omega'}\} = F^{-1}\{D(\omega)\}F^{-1}\{\omega^{-1}\} \qquad (3.2)$$

where F^{-1} is the reverse Fourier transform.[7] [8]

but $F^{-1}\{\omega^{-1}\} = i.\pi.\mathrm{sgn}(\omega)$

so $F^{-1}\{D(\omega)\} = i.\pi F^{-1}\{A(\omega)\}.\mathrm{sgn}(\omega)$

The problem is thus readily soluble by using the fast-Fourier-transform (FFT) algorithm *(25)(26)*. A few words of caution are needed as the FFT algorithm is not exactly equivalent to the analytic transform. First, the ESR spectrum is collected as a function of time in units proportional to Gauss. It is nevertheless a spectrum in the frequency domain. This means that, if one wishes to maintain an analogy with FT-NMR, one has to use the inverse transform to generate the ESR equivalent of the free induction decay (FID); multiply by the sgn function; then do a forward transform to recover the dispersion spectrum. Secondly the discontinuity of the sgn function should lie at the origin of the data set. For a data set generated by an FFT the ordinate is not defined (its an array index), the origin, as

---

[7] The sgn function is defined as -1 for x<0 and +1 for x>0, *i.e.*, it simply a sign change centered at the origin.

[8] The transform from the time domain to the frequency domain is called the forward transform and is defined as

$$S(\omega) = F\{G(t)\} = \int G(t)e^{-i\omega t}dt$$

The reverse transform (frequency to time) is defined as

$$G(t) = F^{-1}\{S(\omega)\} = \tfrac{1}{2}\pi^{-1}\int S(t)e^{+i\omega t}dt$$

such lies at the N/2th data point (for N data pts.). If N is even, then strictly speaking the N/2 point will be undefined after multiplication by the sgn function as it lies on a discontinuity. In practice it can be multiplied by ±1 as convenient. (This is equivalent to setting the pole of Eqn.3.4 equal to one of the adjacent points). Finally the FFT algorithm uses independent real and imaginary parts. The absorption spectrum is usually regarded as the imaginary part so should be loaded to the imaginary part of the data array for the transform. The resultant transform will also be imaginary. This will be then multiplied by the sgn function and the product forward transformed to give the dispersion spectrum which will be in the real part of the array. The choice of which part of the spectrum is real and imaginary is a matter of convention so one can take liberties as to the direction of the transform and which part of the array is used to store the data. However, it is important to keep track of where the data are at each stage of the transform. This is especially true if the absorption spectrum's maximum does not lie at the origin (N/2) as the time domain spectrum (FID) will contain both real and imaginary components (and both parts have to be multiplied by the sgn function). This can create problems with minicomputers as they often only permit real data to be used for the forward transform. Furthermore, the data must consist of 2^n (where n is integral) equally spaced data points. Also the absorption spectrum is required, not the

derivative, as is produced in ESR. The latter two problems are discussed in the next section.

3.2 PRE-PROCESSING OF THE SPECTRUM FOR THE FFT

The derivative spectrum can be readily integrated using Simpsons Rule or the trapezoidal rule., but care must be taken to avoid low data densities *(27)*. Baseline offset and drift present problems. Baseline correction methods are discussed in Sect.21.10. The effects of poor baseline correction on DISPA plots are outlined in Sect.4.3.

Unlike NMR, ESR data are not usually equally spaced. Algorithms for Fourier transforming unequally spaced data are available, but are much slower to run, *e.g.(28)*. It is more convenient to interpolate the data to obtain an equally spaced data set. This is discussed in Sect.21.7.

A data set of 2^n data points is easily produced by adding extra data points; padding. The padding should be done symmetrically (so that any artefacts are symmetric) in such a manner that there are no discontinuities in the spectrum or at the ends of the spectrum. (The ends of the data set should be at zero). The effects of padding are discussed in Sect.4.8.

The optimum method seems to be to pad the data by interpolation to 1024 pts; reduce the data set back to 512 points by box-carring; symmetrically pad this data set to 1024 points using a linear ramp; do the Hilbert transform, then recover only the part of the dispersion spectrum

corresponding to the 512 point absorption spectrum. A flow chart for the basic procedure is given in Fig.3.1. (This is for the LSI-11 computer, for a larger computer it would be better to double the number of points *i.e.*, do a 2048 point transform).

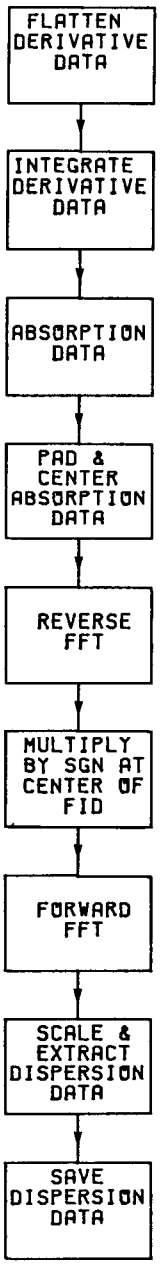

Figure 3.1. Flow-chart for generating the dispersion data from equally spaced derivative data.

3.3 THE DIFFERENCE PLOT

The Cole-Cole format for DISPA plots is quite striking (Fig.2.1), but is unsatisfactory for many purposes as the observed distortion is only a few *per-cent* of the reference circle's radius. A plot of the difference between the reference circle and the experimental plot as ordinate would be more useful.[9] The radial difference, ΔR, (difference between the reference circle's radius and the distance of an experimental point from the center of the reference circle) is the most convenient ordinate use. Other schemes, such as using the vertical differences or the difference in polar angle for experimental dispersion points and the corresponding points on the reference circle, are very difficult to implement on a computer and offer no advantages over the radial difference plot. There is a wide choice of abscissa. Marshall has investigated a number of these, but restricted his choice to functions of spectrum frequency. This is inconvenient in ESR as the frequency is both instrument and sample dependent. Three other schemes have been developed, using as abscissa; the absorption signal, $A(\omega)$, the array index of the absorption signal, I, and the polar angle, θ, of the experimental data. However, before discussing these it is necessary to define some conventions.

---

[9]At low data densities this is not a very useful format as the data points become too spread out. This is not a problem with ESR, but sometimes occurs in NMR.

The reference circle is defined as a circle whose radius is equal to that of the maximum height of the absorption and displaced along the abscissa by the radius of the reference circle (R). It should be noted that the absorption amplitude is fixed by scaling. For this work the absorption signal was always scaled to 25000, corresponding to a DISPA reference circle of radius 10cm. Any displacement outside of the reference is considered to be a positive radial difference and displacements within the circle negative. The radial difference, ΔR, is usually expressed as a per-centage of the reference circle's radius, R_0, *i.e.*, $\Delta R=(R_{obs.}-R_0)100/R_0$. The spectrum has to be phased such that the double integral is positive. The spectrum is assumed to be swept from left to right (*i.e.*, the left of the spectrum is taken to correspond to low field). It is convenient if the center of the spectrum corresponds to the center of the data set. This can be readily achieved by padding and makes comparisons of various data sets easier.[10] A diagrammatic definition of the difference plot is given in Fig.3.2

---

[10] If DISPA is used for asymmetric spectra another definition of the center should be found. The point corresponding to g_{iso} as found by Hydes *(29)* algorithm is probably a good choice.

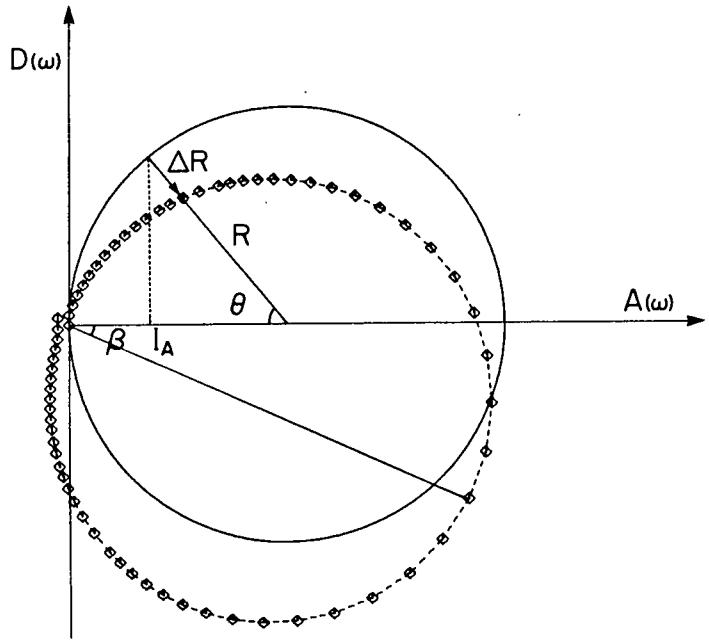

Figure 3.2. Diagrammatic definition of a difference plot.

It is convenient to define two more parameters, the lobe height ($=\Delta R_{max.}$), and the lobe separation, $\Delta S=(S_l-S_r)/R_0$, where S_l is the position of the left lobe and S_r is the position of the right lobe.[11] Another useful parameter is the lobe asymmetry Δ_d, defined as; $\Delta_d = \Delta_l-\Delta_r$; where Δ_l is ΔR_{max} for the left lobe and Δ_r is that for the right lobe. A diagrammatic definition for these parameters can be found in Fig.3.3.

---

[11] The lobe splitting was found to have a weak dependence on the spectrum parameters and was not very useful as a diagnostic parameter. A normal splitting was taken to mean $\Delta S\approx 0.5$; a wide splitting >0.7; a narrow splitting <0.3.

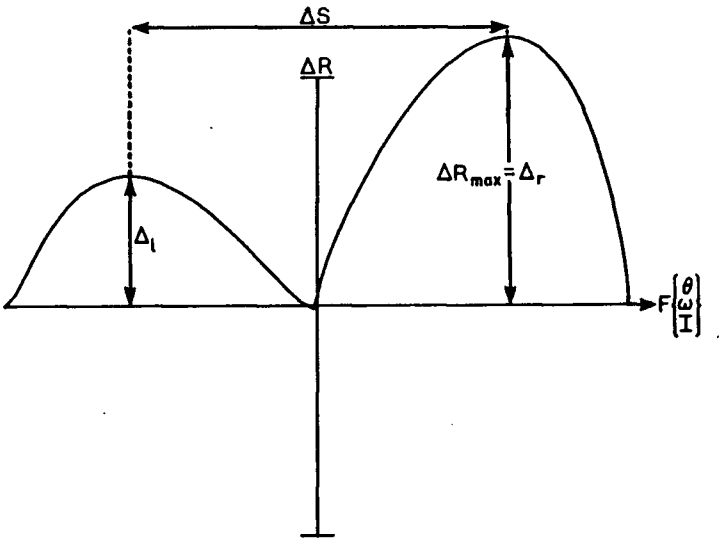

Figure 3.3. Diagrammatic definition of the lobe parameters for a typical difference plot.

Subsequent references to the term DISPA plot will be taken to mean the difference type DISPA plot rather than the Cole-Cole type plot. Unless otherwise stated all examples are for a line with unresolved hyperfine coupling; 12 protons coupling to 3G line with a coupling constant of 1.0G.

3.3.1 THE INDEX DIFFERENCE PLOT

The abscissa is simply a function of the index of the absorption data array scaled to a suitable value (if necessary). The abscissa, F(x), is calculated as follows.

$$F(x) = f(I_{max}-I).k \qquad I < I_{max}$$

$$F(x) = f(I-I_{max}).k \qquad I > I_{max} \qquad (3.3)$$

where I_{max} is the index at which maximum absorption occurs; k is some scaling factor; f(I) is a function of the index of the data array. Plots for F(I) where 'f' is one (linear), 'f' is $\sqrt{}$ (square-root), 'f' is logarithmic (ln) and 'f' is Lorentzian (Lz), are shown in Fig.3.4-Fig.3.5

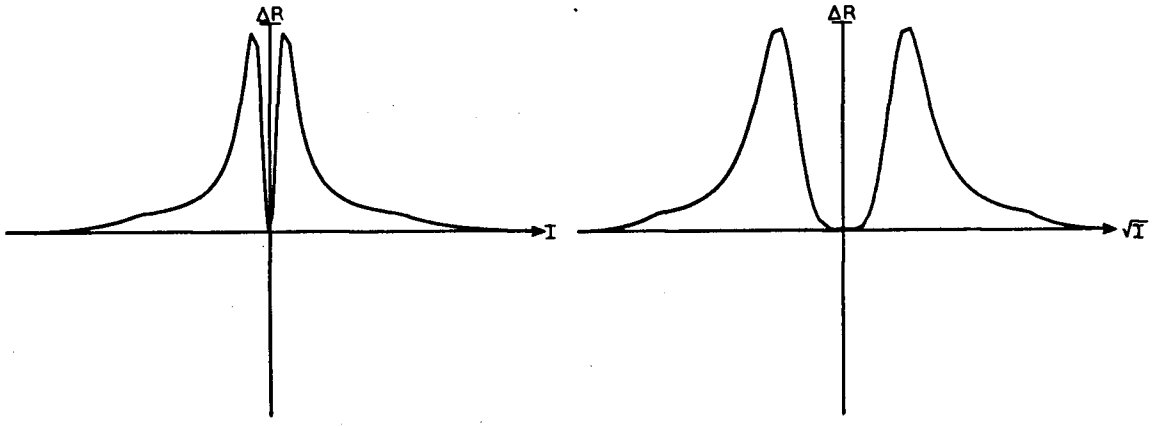

Figure 3.4. Linear and square root indexed difference plots.

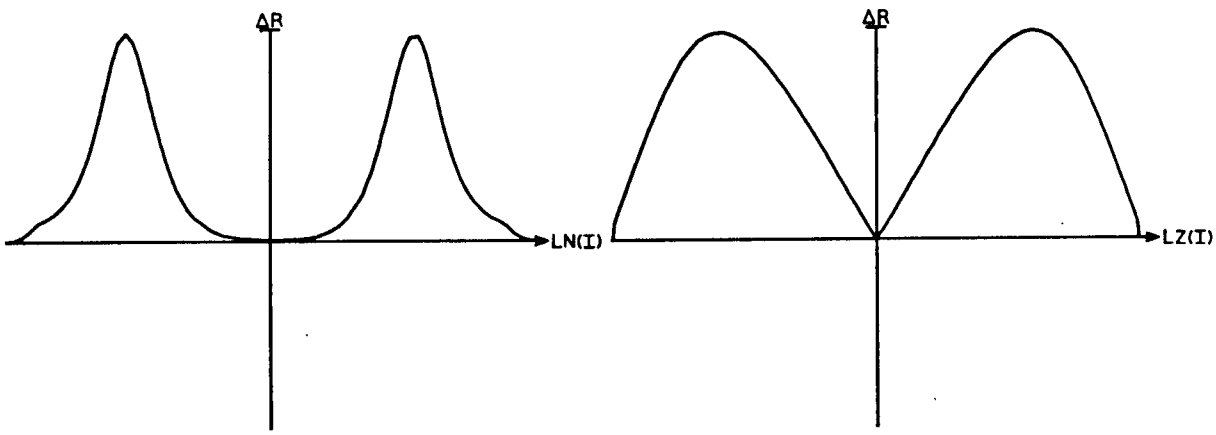

Figure 3.5. Logarithmic, LN, and Lorentzian, LZ, indexed difference plots.

The linear plot has the unfortunate effect of expanding the baseline region and compressing the region of interest. This is of no consequence for numerical computations, but makes it difficult to use for manual interpretations. The log plot is useful for general diagnostic work. The Lorentzian plot is very good for diagnostic work, but the choice of the width of the Lorentzian is arbitrary. The square root plot is useful for picking out satellites and other peaks in the shoulders of the main peak. The main advantage of index plots is that the ordinate is independent of the experimental data so that the plotting routine is stable with pathological data sets. The main disadvantage is that the lobe separation of index plots is line-width dependent. (Fig.3.6)

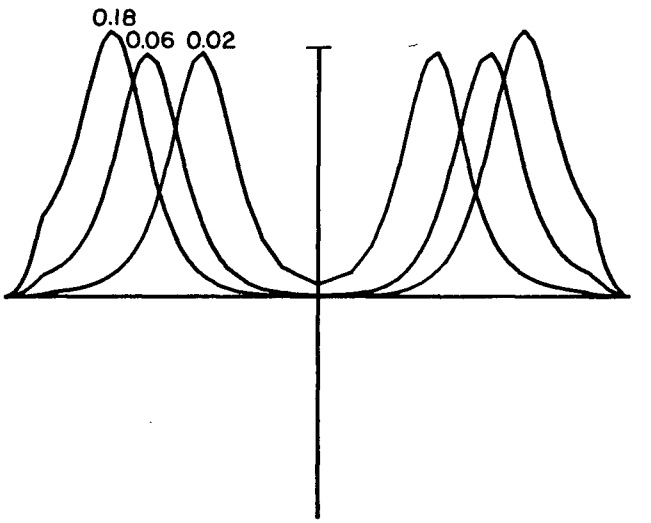

Figure 3.6. Logarithmic indexed plot as a function line-width/sweep-width.

The glitch in the tails of the plots is a truncation artefact.

3.3.2 THE POLAR DIFFERENCE PLOT

As DISPA plots are circular, polar coordinates are the most natural way of expressing them. The polar angle, θ, is given in Fig.3.2. A typical plot is shown in Fig.3.7.

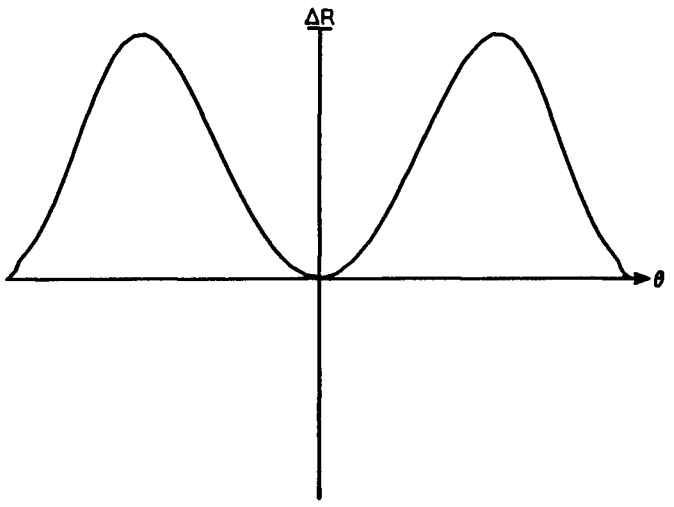

Figure 3.7. Polar difference plot.

This plot distributes the data in a satisfactory manner (baseline data compressed with respect to the main peak) and has the advantage that the difference plot retains any symmetry (about the vertical axis) that the Cole-Cole plot has. Its main disadvantage is instability, it is not always possible to unambiguously assign the quadrant that θ (Fig.3.2) lies in. The resultant plot may jump around. This is especially noticable with poorly phased spectra.

3.3.3 THE ABSORPTION DIFFERENCE PLOT

Using a sigmoid type function as the abscissa will also distribute the data as required. A natural choice would be the hyperbolic tangent because, besides being sigmoid, it is the integral of a Lorentzian, *i.e.*, the double integral of the original data set may be a useful abscissa. However, baseline artefacts could cause

considerable instability in such a plot. A more suitable (approximately sigmoidal) function can be constructed from the absorption data using Eqn.3.3, with $A(\omega)$, used instead of 'f'. This gives more stable plots than the polar difference plot, but the symmetry is lost. The example for unresolved hyperfine coupling is given in Fig.3.8. Unfortunately the absorption plots loop-the-loop if partially resolved features are present. This is very entertaining, but can seriously hamper numerical analysis of the plots. The principal advantage of these plots is that they are easily compared with the Cole-Cole type plots as both are plotted as a function of $A(\omega)$.

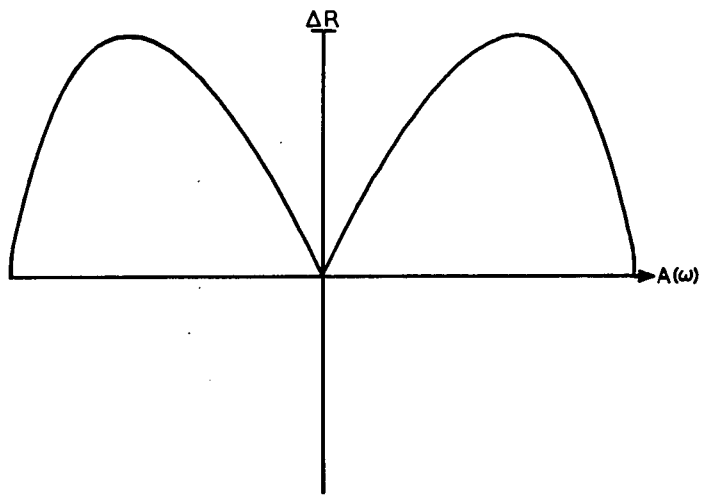

Figure 3.8. The absorption difference plot.

An absorption difference plot along with its corresponding Cole-Cole plot is shown in Fig.3.9. (The scale of the abscissa for the difference plot is halved with respect to the Cole-Cole plot). The ordinate is the

dispersion signal for the Cole-Cole type plot and the per-cent radial difference for the difference plot. This format of DISPA plot is preferred by some workers, but it will not be used here.

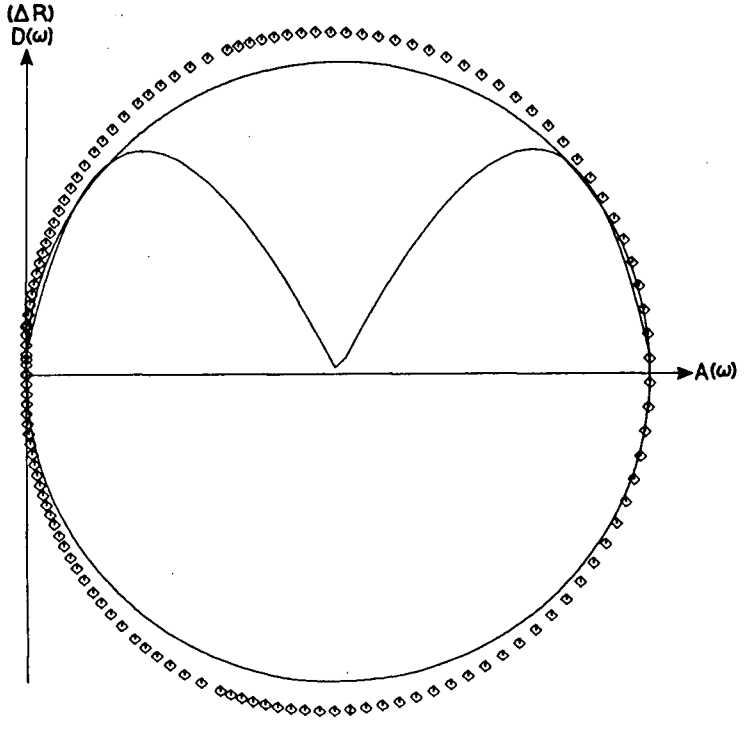

Figure 3.9. Typical Cole-Cole and difference DISPA plot.

Generally the absorption type of plot was used for diagnostic work (unless otherwise stated all difference plots in this work are absorption difference plots) and the linear indexed plot was used for numerical work. Polar plots (when stable) were useful where aesthetic plots were required.

3.4 THE GAUSSIAN DIFFERENCE PLOT

The Gaussian line-shape and its close relative, the Voigt line-shape, are very common in ESR spectroscopy. The shape of the difference plot for a Gaussian line is independent of its line-width (except for truncation effects, Sect.4.8). This led Marshall to propose a renormalisation procedure whereby a Gaussian line would give a circular Cole-Cole plot (linear difference plot) so that the DISPA plot would now reflect deviations from Gaussian behaviour. This would be very useful, but an efficient, reliable and consistent algorithm remains to be developed.[12] The problems that arise are as follows: a) The Gaussian dispersion spectrum is not an analytic function and is not amenable to rapid numerical evaluation. This makes the generation of a reference circle difficult. b) A look-up table for the dispersion line, with interpolation, was used by Marshall *(12)*, but this is very unstable in the presence of noise. c) The shape of the difference plot is independent of line-width, but the positions of the points on the locus of the difference plot are not, *c.f.* Eqn.1.10. Simply subtracting a reference difference plot is thus not possible. d) Using a look-up table for a reference difference plot is also possible, but a large table ($\simeq 10^5$ points) is required, beyond the capacity of our current computer. These problems need further investigation, but will not be pursued here.

---

[12] Marshall has demonstrated the utility of the technique *(12)*, but his algorithm involves a Gaussian reference line of arbitrary width.

4. INSTRUMENTAL DIAGNOSTICS AND APPLICATIONS

Instrumental artefacts should be removed before any kind of line-shape analysis is undertaken. This is especially true for DISPA, which is very sensitive to line distortions. However, this sensitivity may be used to identify and thus help remove instrumental distortion. In particular it can be used for the automatic phasing of spectra.

In ESR spectroscopy distortion may arise from a number of sources; saturation, overmodulation, amplifier and bridge misphasing, over-filtering, high frequency noise and low frequency noise (baseline drift and offset). These problems are discussed in turn in the following sections.

As before all examples are for a single line with unresolved hyperfine coupling unless otherwise stated.

4.1 TIME CONSTANT

The influence of the phase-sensitive-detection (PSD) amplifiers time constant on line-shape is well documented *(30)*. However, the size of this distortion is often under-estimated.[13] An example is shown in Fig.4.1. This effect is easily avoided by setting the time-constant to 1/100th the time it takes to scan (peak-to-peak) the sharpest line in the spectrum. Nevertheless it is worth

---

[13] A vertically mounted chart recorder has an asymmetric time constant due to gravity. This may operate in the opposite sense of the phase-sensitive-detection amplifiers time constant and the two factors partially cancel. This is not apparent until digital data are used.

checking a standard spectrum with DISPA to ensure that the phase-sensitive-detection amplifier filter is as marked.

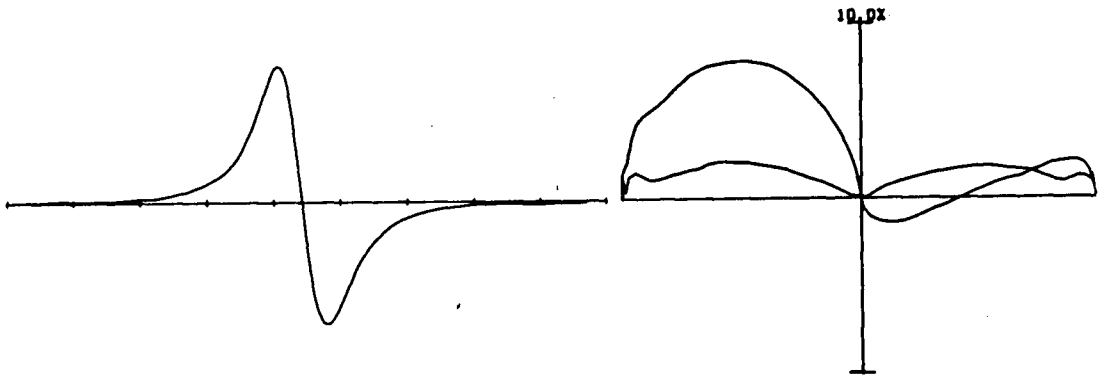

Figure 4.1. Effect of a large PSD filter on a DISPA plot. Spectrum on the left. 3.2G line-width, sweep-rate 5G/min. The low amplitude symmetric lobes are for a 0.125s filter. The other lobes are for a 4.0s filter.

4.2 NOISE

Reducing the phase-sensitive-detection amplifier filter increases the noise level. The sensitivity of DISPA to noise is thus an important factor. The integration of the derivative improves the (apparent) SNR substantially. No problems have been encountered with noise, but it can be very difficult to flatten the baseline for a noisy spectrum. An example (unresolved hyperfine coupling as before) is shown in Fig.4.2.

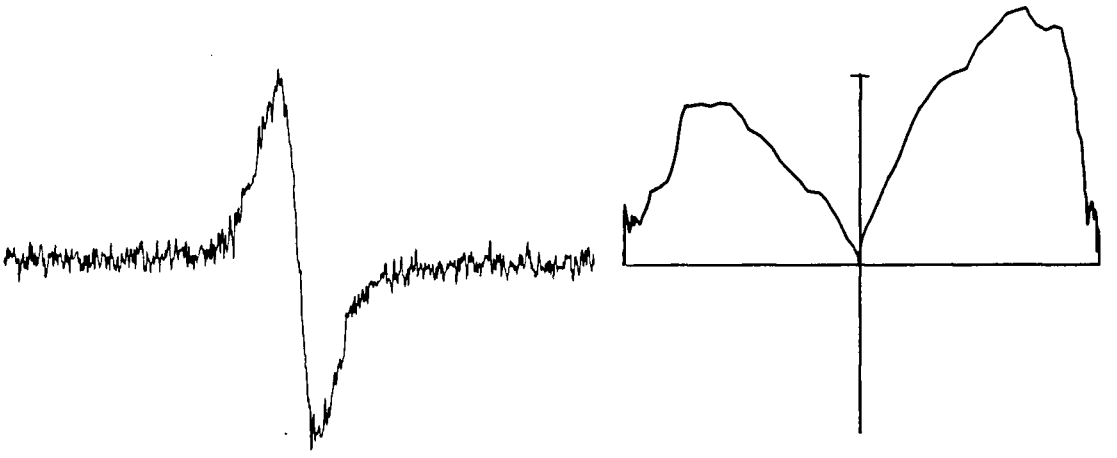

Figure 4.2. Effect of noise on a DISPA plot. The SNR (peak-peak signal/peak-peak baseline noise) is 10:1.

4.3 BASELINE ARTEFACTS

DISPA is very sensitive to baseline distortion and this must be removed before doing any DISPA analyses (Sect.21.10). An example of its effects are shown in Fig.4.3. Note that this example is for a small drift/offset that is not visible in the original derivative spectrum.

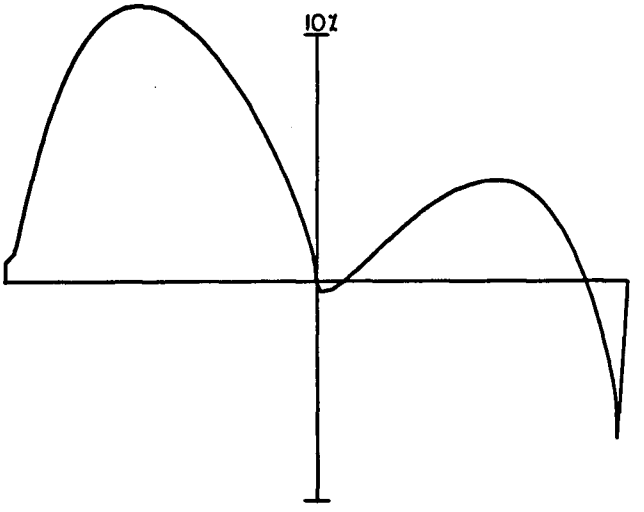

Figure 4.3. DISPA plot showing the effect of baseline artefacts. The distortion is for a DC offset of +0.1% of the peak-peak height. A drift of +0.2% at the right side causes the same distortion.

4.4 AMPLIFIER PHASING

An ESR spectrometer has a number of amplifiers that have to be phased correctly. Only the phase-sensitive-detection amplifier has front panel control though. This control only affects the line amplitudes and does not affect the DISPA plots (Sect.2.2) *(10)*.[14] The automatic frequency control amplifier should be correctly phased or baseline artefacts will arise. The modulation amplifier output should also be correctly phased or asymmetric lines will result. These problems are readily cured, but may not be observed until DISPA analyses are attempted.

---

[14]For phase changes of ≈90°, or multiples thereof, some effects are observed, but generally one has to deliberately mis-set the phase-sensitive-detection amplifier phase to see such effects

4.5 MICROWAVE-BRIDGE PHASING

Reflection mode cavities are arranged such that the dispersion component is eliminated by the automatic frequency control amplifier. However, spurious reflections in the wave guides can give rise to dispersion leakage. Also some bridge designs do not have an automatic frequency control or have to be phased for each experiment *e.g.(31)*. The effect of dispersion leakage (poor phasing) is shown in Fig.4.4 The lobe asymmetry (Sect.3.3) is a linear function of the phase angle and can be used for automatically phasing the spectrum. (*(22)*, Sect.5.2)

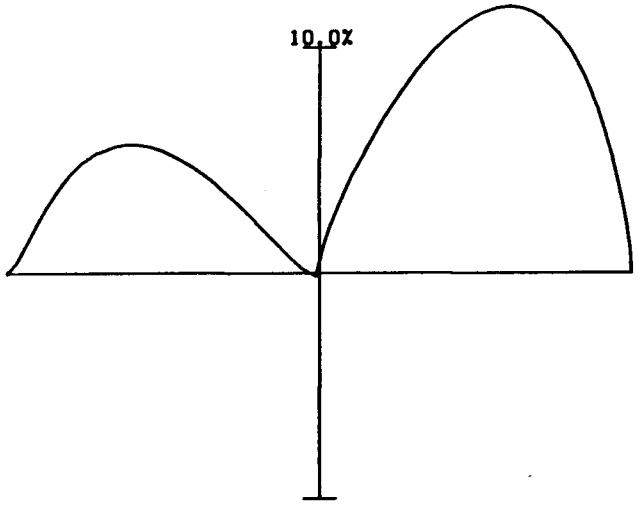

Figure 4.4. DISPA plot for a mis-phased microwave bridge. A pure Lorentzian line with $\theta = 2°$.

4.6 SATURATION

Saturation does not affect a pure Lorentzian line (Sect.2.3). However, it does affect the DISPA plots of composite lines. The distortion of the DISPA plot for

composite lines is a function of the ratio of the line-widths to each other or their separation. (see Sect.6.5). Saturation broadens lines so this will change the DISPA plot depending on the saturation characteristics of the individual lines. Generally the DISPA distortion will decrease.

4.7 MODULATION

Modulation has been discussed previously *(10)*. The difference plot for overmodulation is shown in Fig.4.5. Note that it is similar to, but distinguishable from the distortion caused by unresolved hyperfine coupling as it changes with modulation amplitude. One can in fact crudely calibrate the modulation amplitude using DISPA *(32)* and this is useful for quick checks of the modulation amplitude, which changes whenever the cavity is changed.

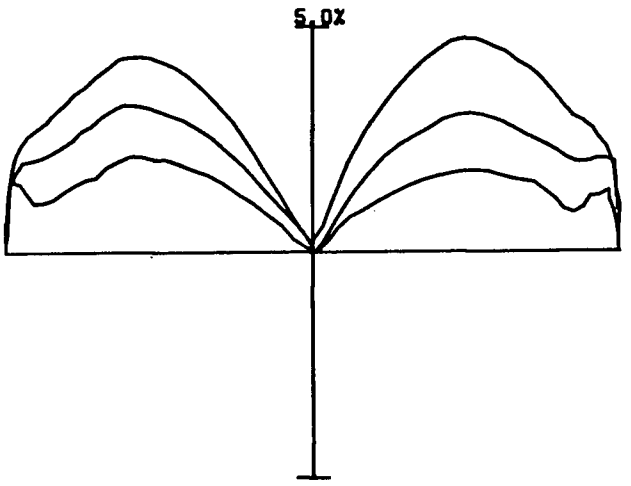

Figure 4.5. DISPA plot for an overmodulated line. High-field line of CuPydtc in chloroform. Natural line-width is 3.21G. Modulation levels are 0.50G, 1.67G and 2.63G respectively.

4.8 LINE TRUNCATION AND PADDING

Lorentzian and Dysonian lines have very long tails. If the sweep width is too narrow these lines are truncated and artefacts appear in the DISPA plots. (The bounds of the integral, Eqn.3.1, should be infinite). Using a sweep width of at least 10x the peak-peak width of the line will avoid this problem. In practice 5x is usually adequate as most real lines have Gaussian tails (*i.e.*, decay rapidly after five line-widths). Unfortunately this problem is unavoidable with simulated spectra, large sweep widths give unmanageably large data sets or too small data densities. Padding the spectrum helps reduce the problem, but artefacts still occur. The effects of truncation (on a 'ramp' padded spectrum) are shown in Fig.4.6

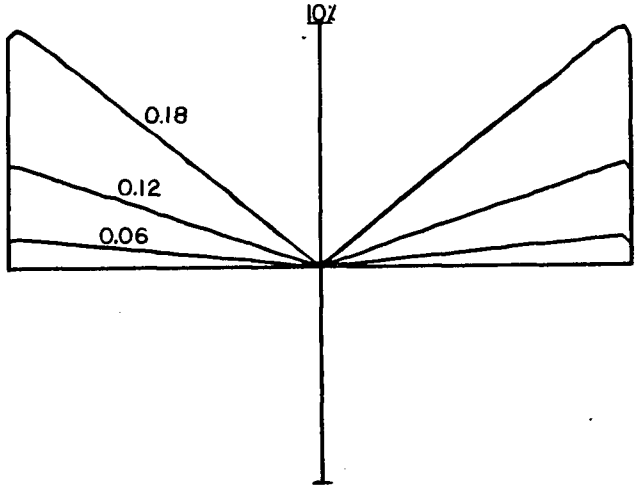

Figure 4.6. DISPA plot for a truncated Lorentzian line for various values of line-width/sweep-width.

The v-lobes are additive so that the most obvious effect is

that the tails and end points of the difference plot are raised. (Fig.4.7) This does not interfere with the qualitative interpretation of the plots.

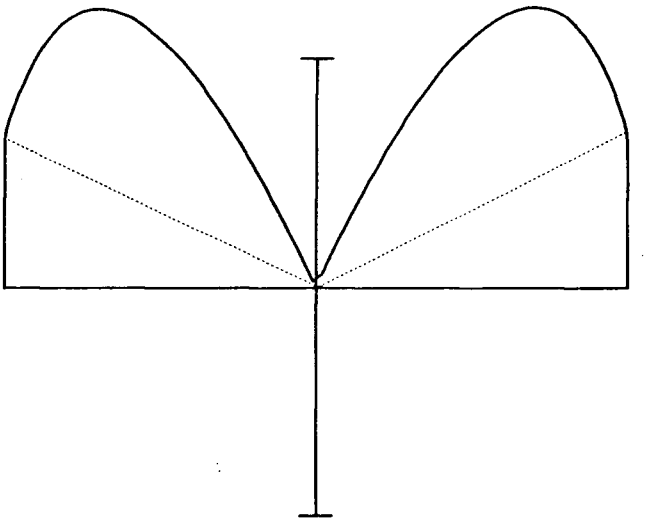

Figure 4.7. DISPA plot for a truncated line with unresolved hyperfine coupling. The dotted line indicates the superimposed v-lobes caused by truncation.

If the baseline goes to zero (it's usually forced to zero by interactive baseline flattening) then all reasonable padding schemes are equivalent to padding with zeroes. If it does not go to zero then extra artefacts, which depend on the padding scheme used, are introduced. The effects of interpolative padding, zero padding (padding with zeroes), tail padding (padding the left and right sides of the spectrum with the first and last data points respectively) and ramp padding (padding with a function that decays linearly to zero from the ends of the spectrum), on a spectrum with a small DC offset are shown in Fig.4.8.

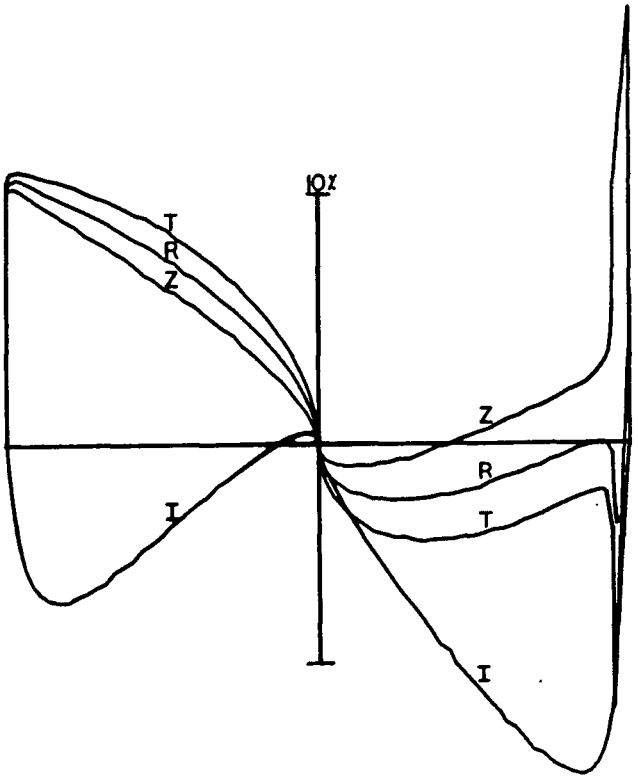

Figure 4.8. Effect of various padding schemes on the DISPA plot. Lorentzian line with a DC offset of 0.1% of the derivative amplitude. I is the interpolative padding. R is ramp padding. Z is zero padding. T is tail padding.

There is little to choose between interpolative padding and ramp padding, except that the v-lobes from ramp padding are more easily recognised as an artefact than the w-lobes that occur with interpolative padding.

5. THE AUTOMATIC PHASING OF SPECTRA

Dispersion leakage is characterised by rotation of the Cole-Cole DISPA plot (Sect.2.1) which gives rise to an asymmetric difference plot. This suggests the possibility of a method of automatic phase correction of magnetic resonance spectra. Discussion here, will be restricted to the ESR case. A more general discussion (by the author) can be found in *(22)*. Applications to NMR are dealt with in *(33)* and this method is now in commercial use.

5.1 BASIC THEORY OF PHASE CORRECTION

Consider a signal, $S(\omega)$, and its Hilbert transform, $Q(\omega)$, *i.e.*,[15]

$$H\{S(\omega)\} = Q(\omega)$$

where

$$S(\omega) = A(\omega)\cos(\theta)+D(\omega)\sin(\theta)$$
$$Q(\omega) = D(\omega)\cos(\theta)-A(\omega)\sin(\theta) \qquad (5.1)$$

and $A(\omega)$ and $D(\omega)$ are the absorption and dispersion signal respectively. They also form a Hilbert transform pair.

---

[15]For further discussion see *(34)(35)*. Also note that $H\{H\{S(\omega)\}\} = -S(\omega)$. H, here, denotes the Hilbert transform; not to be confused with the Hamiltonian, which is not used in this part of the thesis.

$$H\{A(\omega)\} = Q(\omega) \tag{5.2}$$

Now consider a phase correction ϕ to $S(\omega)$ to give $S'(\omega)$. Also drop the (ω) for convenience. Hence

$$\begin{aligned} S' &= S\cos(\phi)-Q\sin(\phi) \\ Q' &= Q\cos(\phi)+S\sin(\phi) \end{aligned} \tag{5.3}$$

substituting back we get

$$S' = A\cos\theta\cos\phi + D\sin\theta\sin\phi - D\cos\theta\sin\phi + A\sin\theta\sin\phi \tag{5.4}$$

which reduces to

$$S' = A\cos(\theta-\phi)+D\sin(\theta-\phi) \tag{5.5}$$

and similarly for O' (which may also be obtained from the Hilbert transform of S'). This may be repeated so that after the i'th correction we get for S'

$$S(\omega) = A\cos(\theta-\sum_i\phi_i)-D\sin(\theta-\sum_i\phi_i) \qquad (5.6)$$

This forms the basis of phase correction. If we could characterise θ directly then only one phase correction is required, ϕ is set to θ in Eqn.1.5. However, if we cannot do that, we can incrementally change ϕ until the desired correction is achieved. In this case we need some criterion to establish when $\Sigma\phi_i=\theta$.[16] DISPA plots are a candidate in either case.

5.2 USE OF DISPA PLOTS FOR PHASE CORRECTION

To characterise θ explicitly, requires that a known relation exists between the phase angle, θ, and some parameter of the difference plot. For the iterative method, the functional form of the relation need not be known, but it should be monotonic with a unique zero for it, or its first differential, at θ=0.

From difference plots of single Lorentzian lines, superimposed Lorentzian lines and unresolved hyperfine coupling (Fig.5.1) it can be descried that the lobe asymmetry, Δ_d=d, is linearly related to θ (Fig.5.2) for $\theta<30°$.

---

[16] This is the basis of manual phase correction. The criterion used is that of baseline symmetry about the peak being phased.

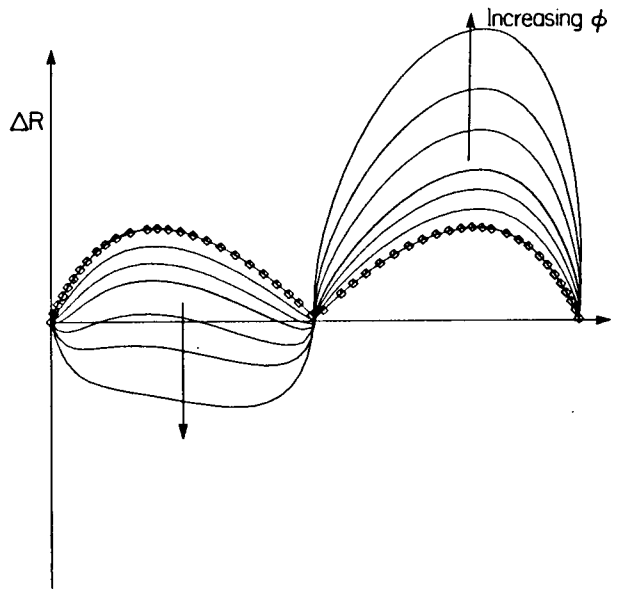

Figure 5.1. Radial difference plots for various phase angles; 0, 1, 2, 3, 5, 7 and 10 degrees.

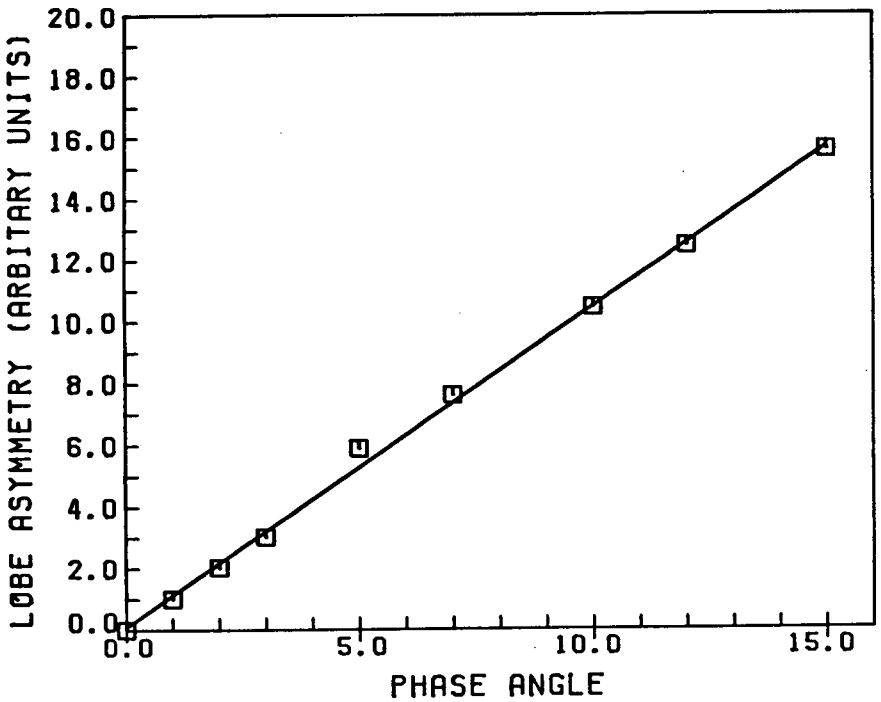

Figure 5.2. Difference plot lobe asymmetry as a function of phase angle for various spectra.

This suggests using an iterative correction with the

increments, ϕ, controlled by the relation $\phi_{i+1}=k\sum_{l}^{i}d_{i}$, where k is the proportionality constant between θ and d for $\theta<30°$. The basic flow chart is shown in Fig.5.3. For further details see *(22)*. For further examples of phase correction procedures see *(36)(37)(35)(33)(38)*.

The whole procedure predicates on the spectrum being centro-symmetric, which it usually is for ESR solution spectra. It is important to note that the spectrum only needs a center of symmetry, the technique works for unresolved lines (see Fig.5.7).[17] The spectrum should be centered as there is a small dependence of the observed phase angle on the line-position (Fig.5.4). The center of the spectrum is located from the smoothed power spectrum and shifted as necessary.

---

[17] If the center of symmetry has +ve curvature (*e.g.* a doublet), rather than -ve curvature (*e.g.* a triplet), then the algorithm has to be modified. The spectrum has to be smoothed to remove the valleys, then the value of θ established with that spectrum. The value so obtained is then used to correct the original spectrum.

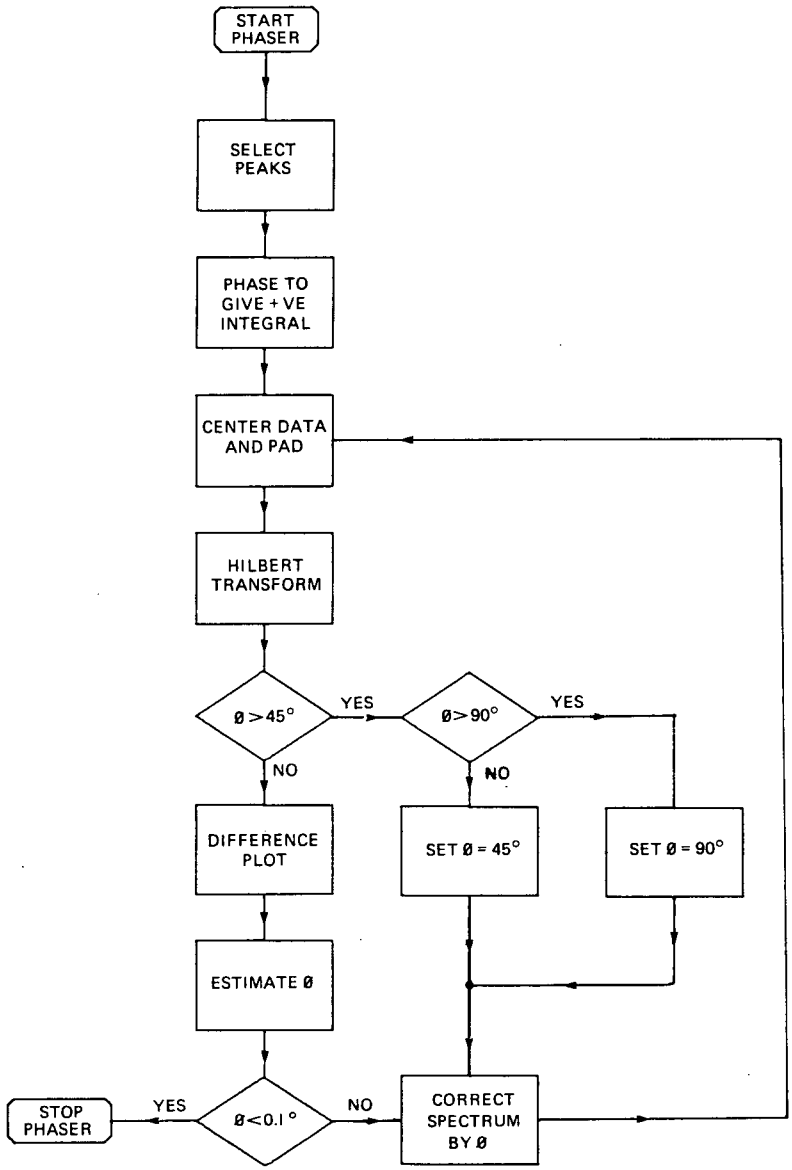

Figure 5.3. Flow chart for the automatic phase correction of spectra.

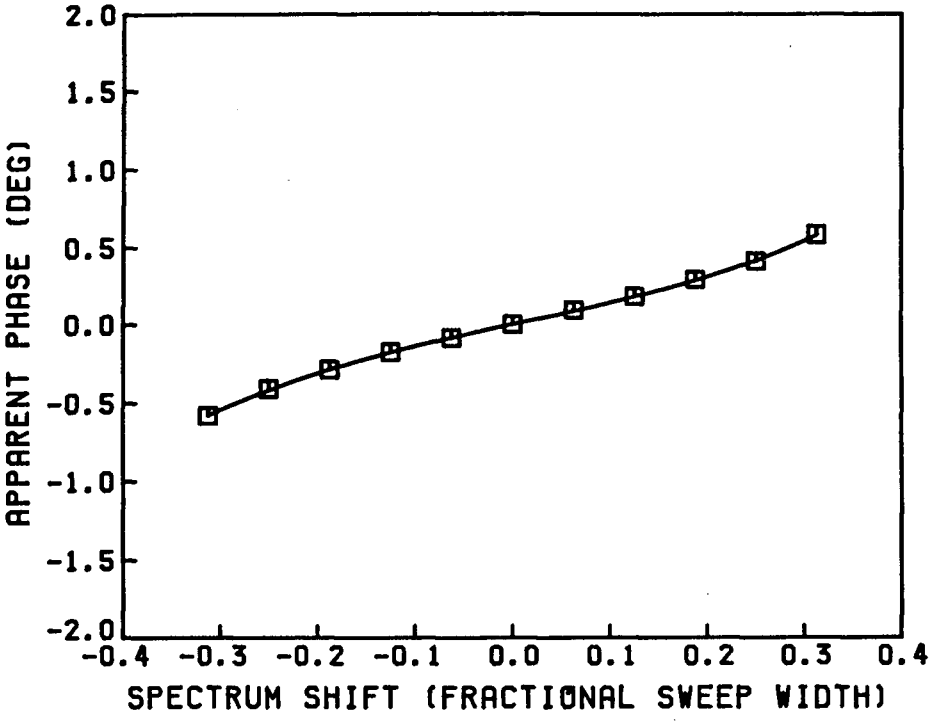

Figure 5.4. Phase error as a function of line-position.

Examples for the phase correction of a single line and a multiplet are shown in Fig.5.5-Fig.5.7

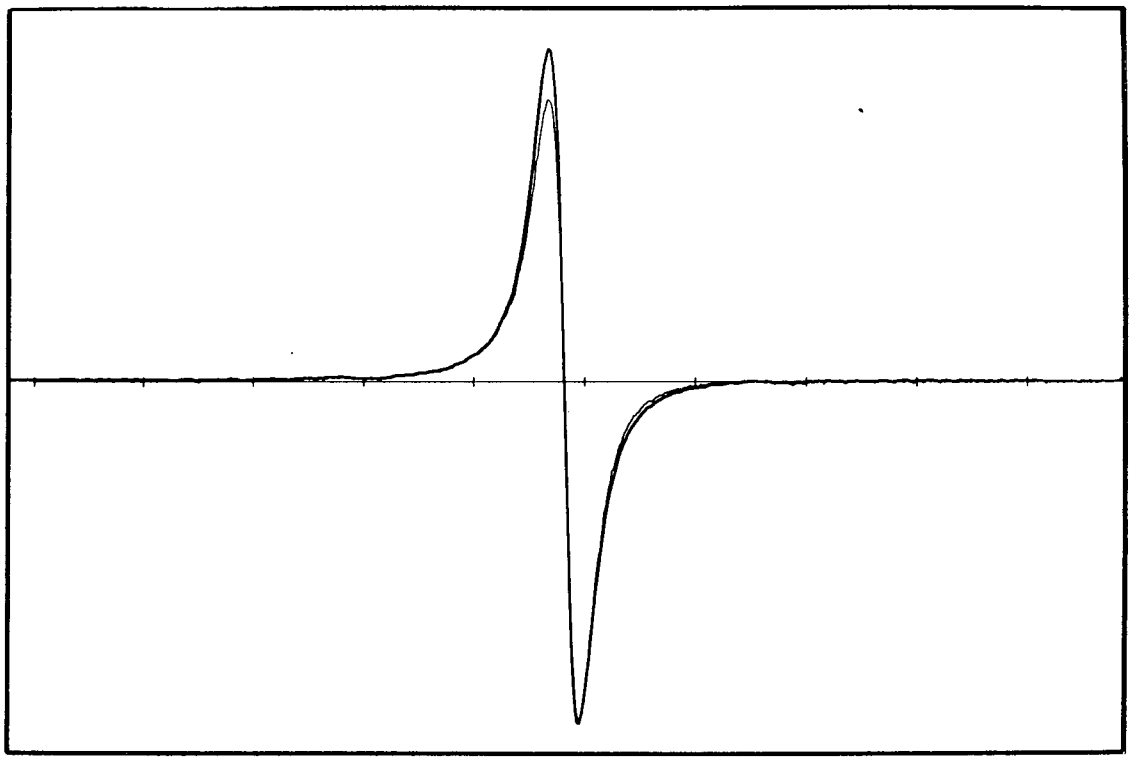

Figure 5.5. The center line for Fremies salt before (light line) and after (heavy line) automatic phase correction. ($\phi \simeq -8°$).

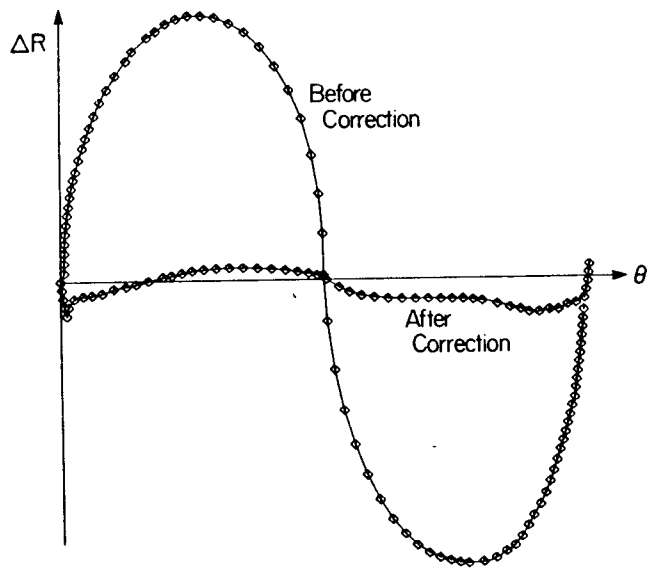

Figure 5.6. The radial difference plot corresponding to the diagram above.

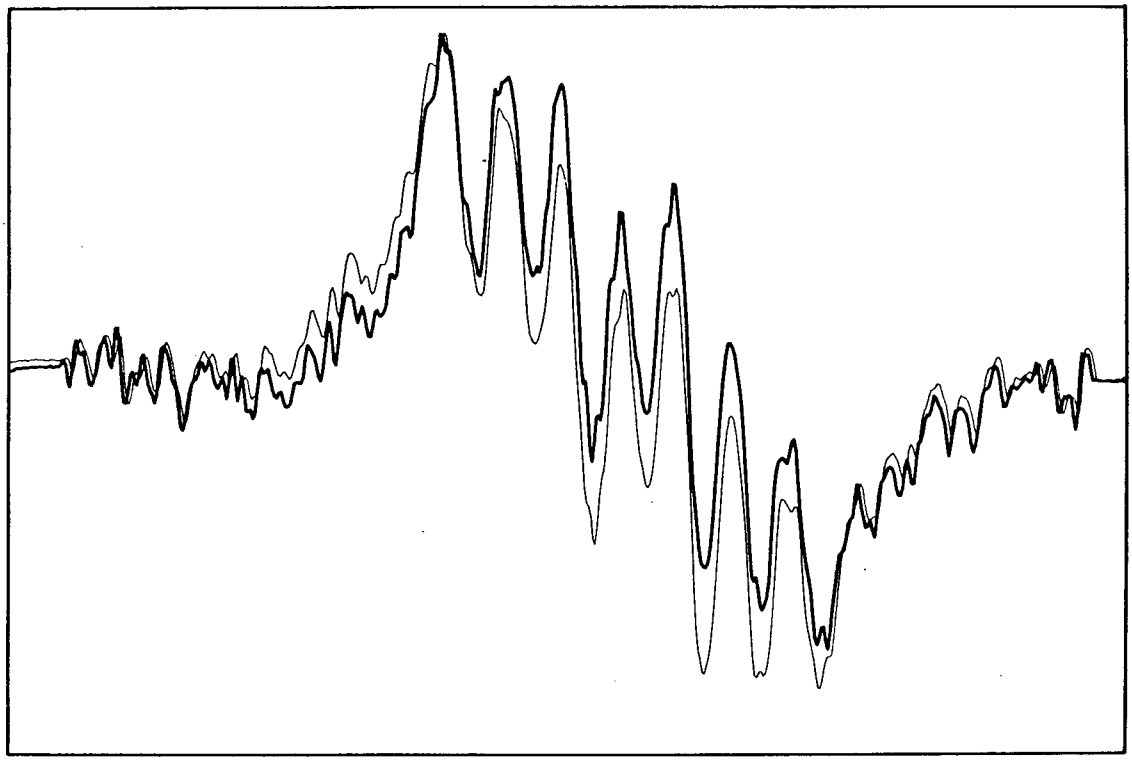

Figure 5.7. An unidentified radical before (light line) and after (heavy line) automatic phase correction. $\phi \simeq 20°$. In this case the dispersion leakage was not apparent until a simulation was attempted.

6. APPLICATIONS TO LINE SHAPE ANALYSIS IN LIQUIDS

DISPA is applicable to any spectroscopic line-shape from any kind of sample. The range of possible line-shapes is thus endless. Here we will restrict the discussion to spectra composed of two Gaussian or Lorentzian lines. Such line-shapes are commonly encountered in magnetic resonance spectra of solutions. Furthermore, the discussion will be restricted to cases where a single (unresolved) line is observed. Partially, or fully resolved spectra can usually be analysed by inspection. Also the corresponding DISPA plots are usually complex and difficult to analyse.

The main objective is to demonstrate the utility of DISPA plots for analysing ESR spectra. The results are equally applicable to NMR or any other technique though. However, it should be noted that resolved derivative spectra do not necessarily give resolved absorption spectra (Fig.6.1)(or even noticeably distorted spectra, especially if noise is present) so the results are slightly restricted with respect to NMR spectra, which gives the absorption spectrum.

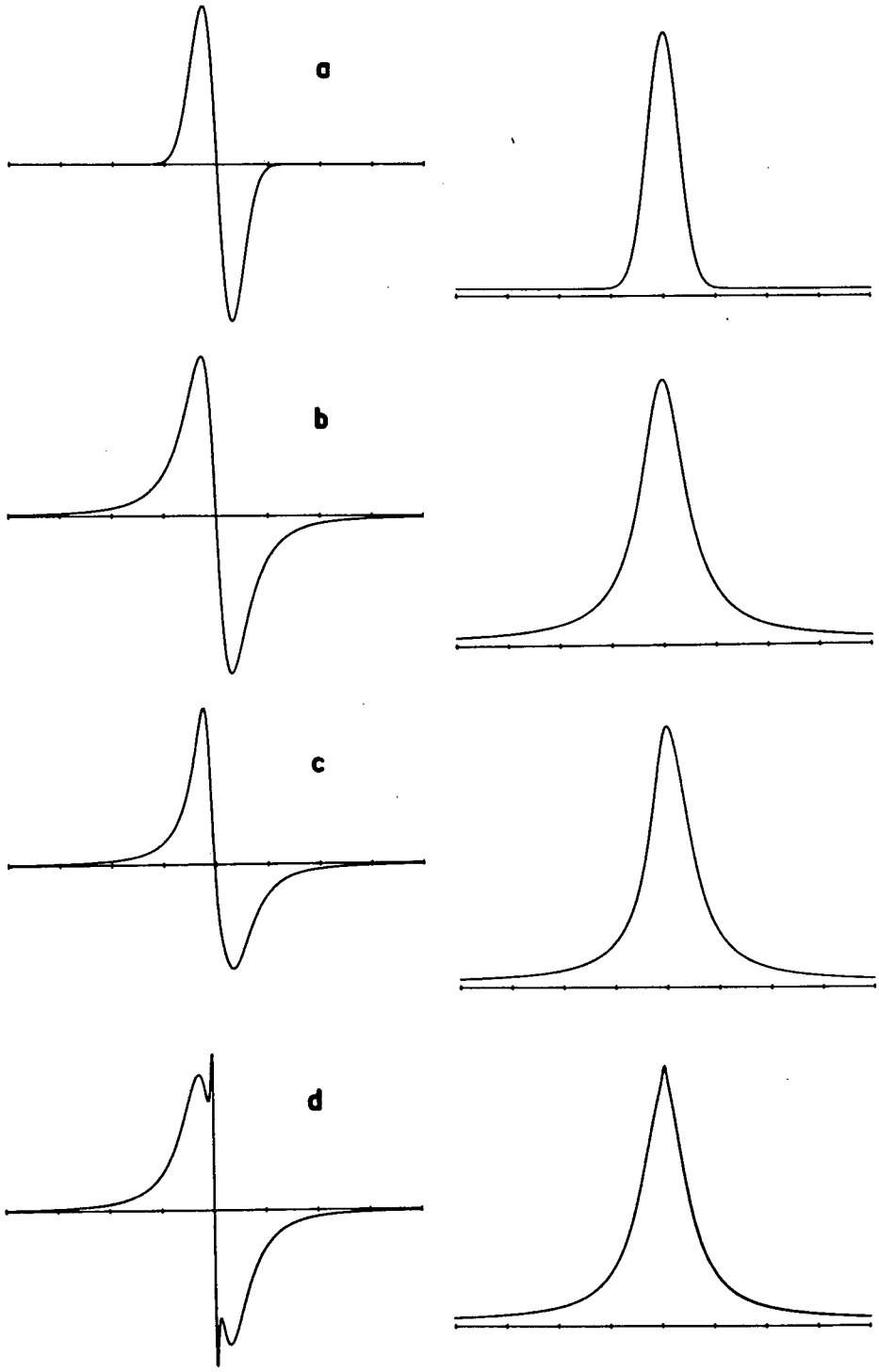

Figure 6.1. The influence of integration on resolution. a) Pure Gaussian line. b) Pure Lorentzian line. c) Two Lorentzian lines of different widths and positions. d) Two Lorentzian lines of different widths.

6.1 CLASSIFICATION OF LOBES

The amplitudes and separation of the lobes of a DISPA plot are rarely adequate criteria to completely characterise the plot. It is thus desirable to classify the overall shapes of the lobes somehow. DISPA plots were simulated for pairs of lines for a wide range of combinations of amplitude, separation, widths and line-shape. It was found that the DISPA plots generally retain their mammiform character and fall into one of the two sequences shown in Fig.6.2. The G sequence is characteristic of Gaussian lines, the L-W sequence is characteristic of Lorentzian lines. If the spectral lines are asymmetric then the DISPA plots will be asymmetric, one lobe will fall in one part of the sequence and the other in another part of the sequence. The sequences shown are approximate. For instance, the sequence G(2)-G(3)-G has been observed (Fig.6.10-Fig.6.11), but not the sequence G(2)-G(3)-G(4). Plots may of course be at intermediate points of the sequence. Furthermore, the plots may be modified by instrumental artefacts (Fig.6.3); for instance, truncation adds in v-lobes; poor phasing adds in antisymmetric lobes to give asymmetric lobes. The curvature of the lobes can vary substantially, but usually only with asymmetric plots.

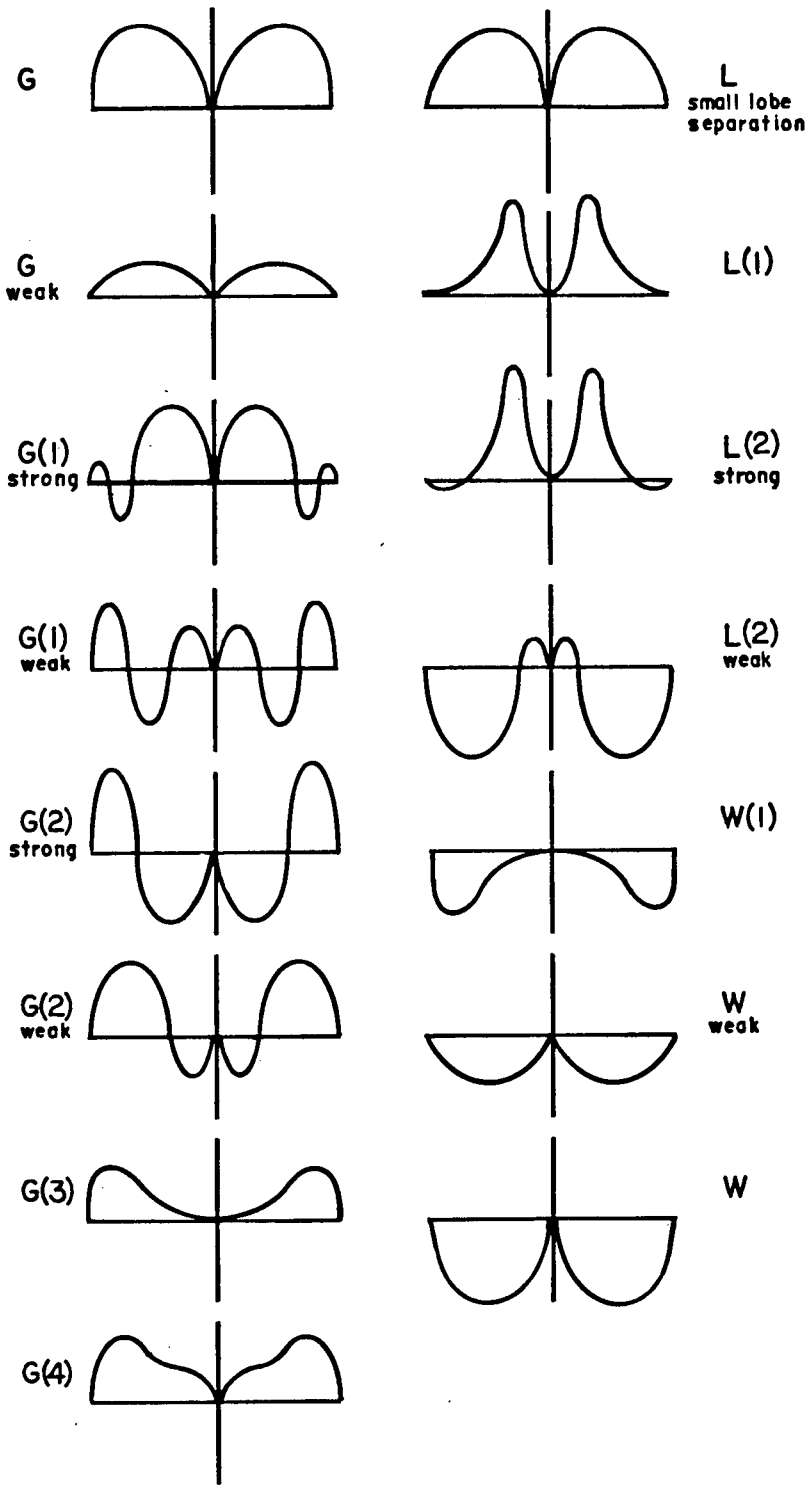

Figure 6.2. Classification of difference plots.

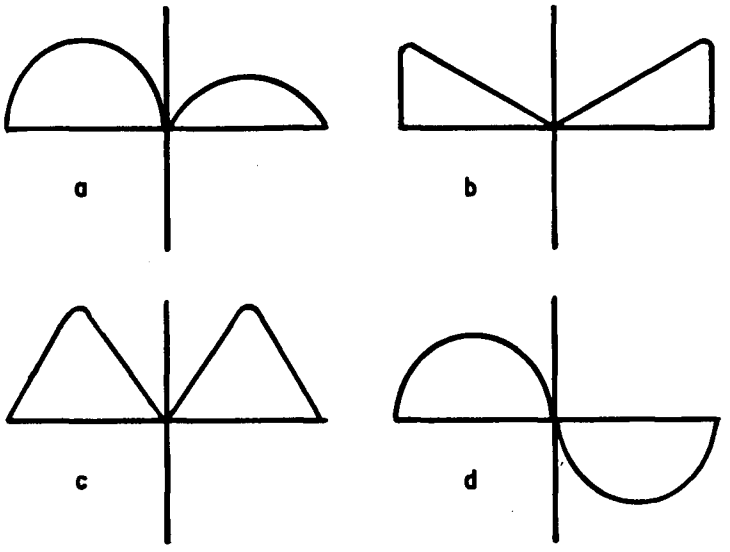

Figure 6.3. Miscellaneous classification of difference plots. a)asymmetric lobes, b) v-lobes, c) sharp G-lobes, d) antisymmetric lobes.

6.2 NOTES ON THE SIMULATIONS AND PLOTS

The difference plots are shown along with their corresponding derivative spectra. The correspondence is not one-to-one; the diagrams illustrate the trends only. The plots were selected from many simulations as being representative of a particular combination of lines.

All difference plots pass through the origin so for asymmetric plots the left and right lobes are classified separately. It is important to note that the left and right lobes undergo mirror reflection about the ordinate if the direction of field scan is reversed or the order of the pairs of the lines is reversed.

All numeric information is given as a ratio with respect to a reference line. The reference line is considered to have a constant amplitude, width and position. The second line, added to the reference line, is variable, its width and height are divided by the corresponding values for the reference line to obtain the line-width and line-height ratios respectively. The position of the variable line is defined in terms of the line-width of the reference line. A negative shift means the variable line is to the left of the reference line. A positive shift places the line to the right of the reference. Hence a shift of -1.5 from a 3.0G reference line means that the variable line is 4.5G to the left of the reference. As mentioned earlier, changing the sign of the shift just causes the lobes to reflect through the ordinate.

All shifts and ratios are restricted such that the observed line is unresolved and only slightly distorted. The simulations do not include phasing or baseline artefacts, which influence the symmetry of the lobes. Also note that although the absorption lines as plotted may appear to be readily distinguishable, in practice the differences are often obscured by noise.

6.3 DETECTING TWO SUPERIMPOSED LORENTZIAN LINES

This case might be expected to occur when a system contains a spin label in two sites, one site, bound and therefore giving broad lines, the other site unbound and thus giving

sharp lines. If we think in terms of circle plots, Eqn.1.3, it is immediately obvious that varying the ratio of the heights of the line is indistinguishable from varying the ratios of the widths of the lines; the radius of the circle is proportional to amplitude/line-width.

The DISPA plots are of the W-type, the amplitude of which varies with the line-width and amplitude ratios. (Fig.6.4-Fig.6.6). As expected line-height variations are indistinguishable from line-width variations.

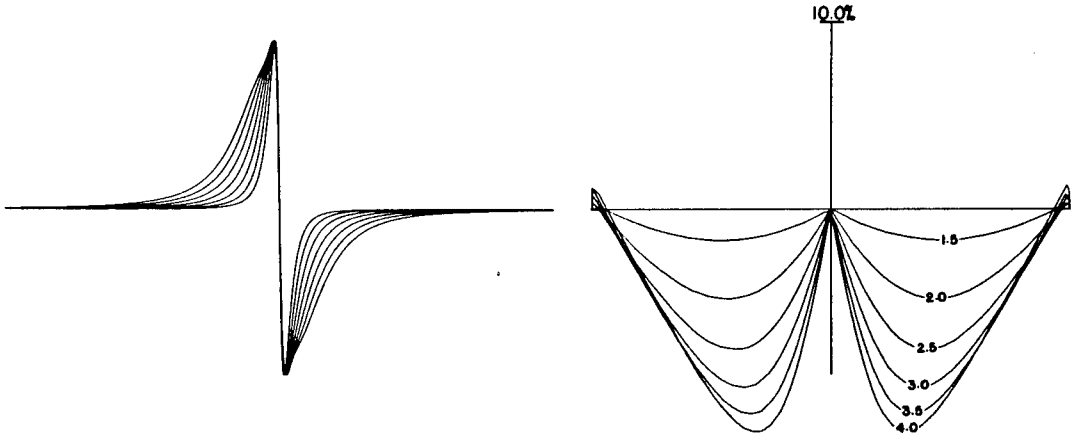

Figure 6.4. DISPA plots for superimposed Lorentzian lines and their corresponding derivative spectra, for various line-width ratios, but the same amplitude. Ratios for the spectra are 1.0, 1.5, 2.0, 2.5, 3.0, 3.5, 4.0.

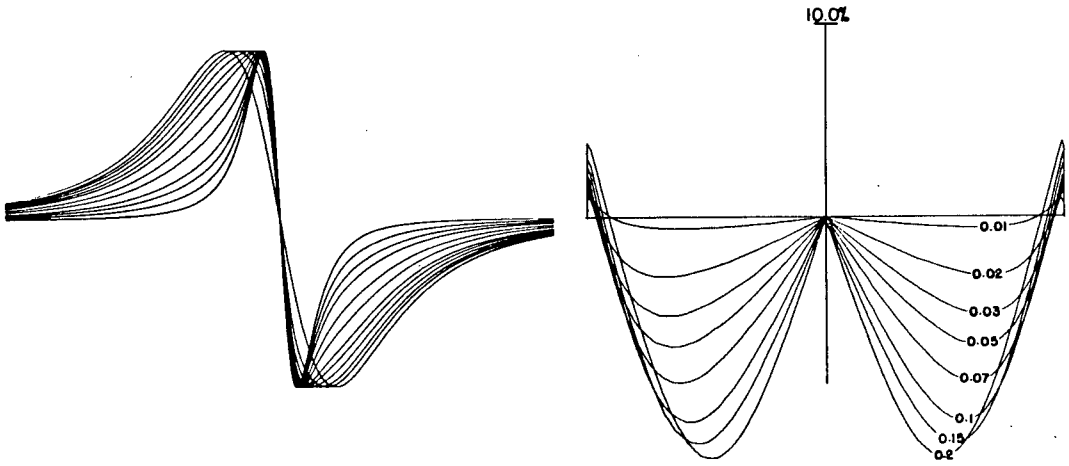

Figure 6.5. DISPA plots for superimposed Lorentzian lines and their corresponding derivative spectra, for various line-height ratios. Line-width ratio is 3.33. The sequences just reverses (slowly) for ratios > 0.2. Ratios for the spectra are 0.0, 0.1, 0.2, 0.3, 0.5, 0.7, 1.0, 1.2, 1.5, 2.0, 3.0, ∞.

6.4 DETECTING TWO SUPERIMPOSED GAUSSIAN LINES

This case may occur for liquids (or solids) containing two different organic radicals with unresolved hyperfine coupling. Superimposing a second Gaussian just redistributes the amplitude term, A_i, in Eqn.1.11. The lobe behaviour is thus expected to be (and is) mainly G-type. Several examples are given in Fig.6.6-Fig.6.11.

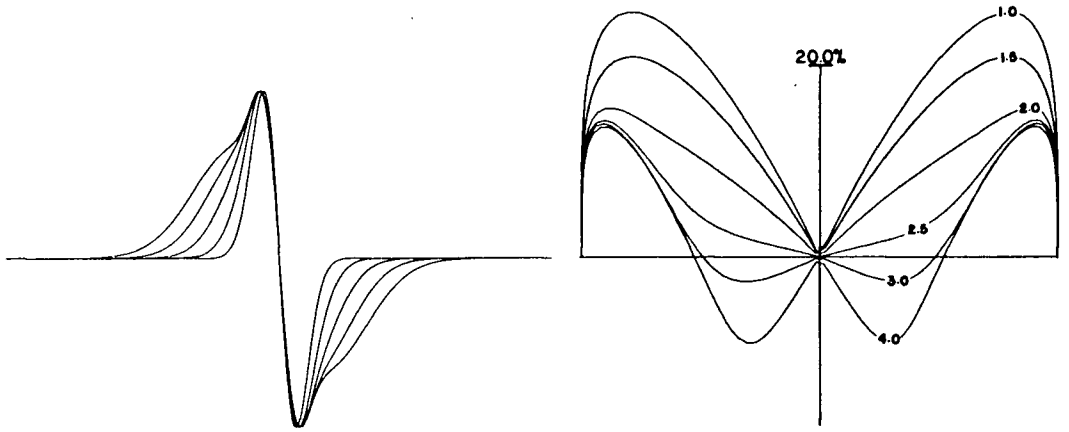

Figure 6.6. DISPA plot for superimposed Gaussian lines for various line-width ratios. Lines are the same height. Ratios for the spectra are; 0.0, 1.5, 2.0, 2.5, 3.0.

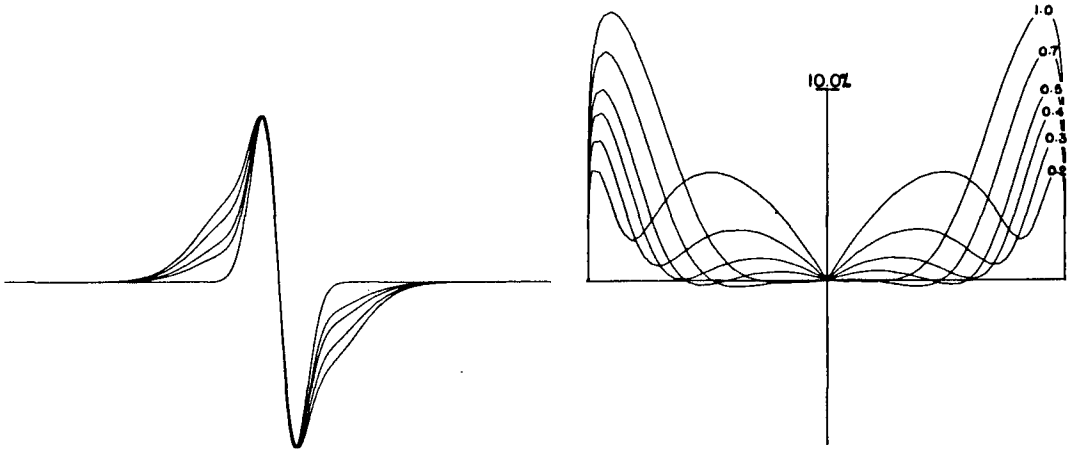

Figure 6.7. DISPA plot for superimposed Gaussian lines for various line-height ratios. Line-width ratio is 2.7. Ratios for spectra are; 0.0, 0.2, 0.5, 0.7, 1.0.

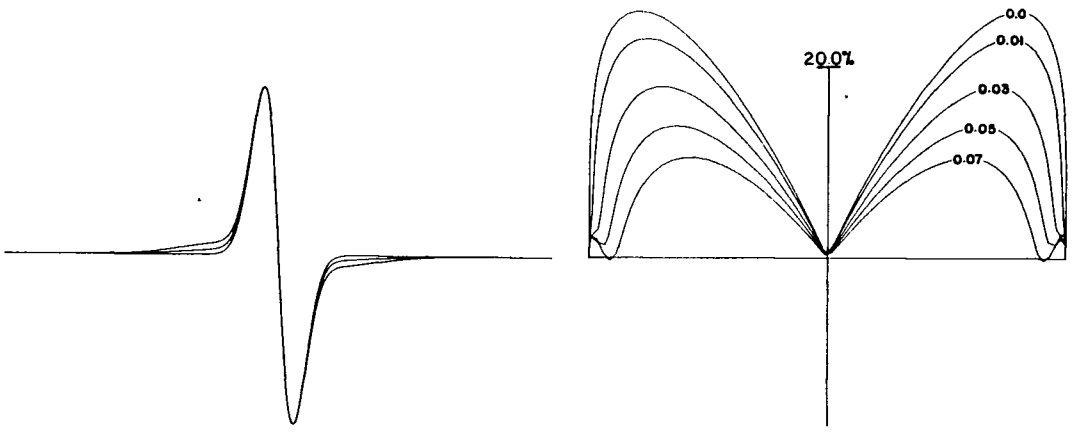

Figure 6.8. DISPA plot for superimposed Gaussian lines for various line-height ratios. Line-width ratio is 3.3. Ratios for spectra are; 0.0, 0.03, 0.07.

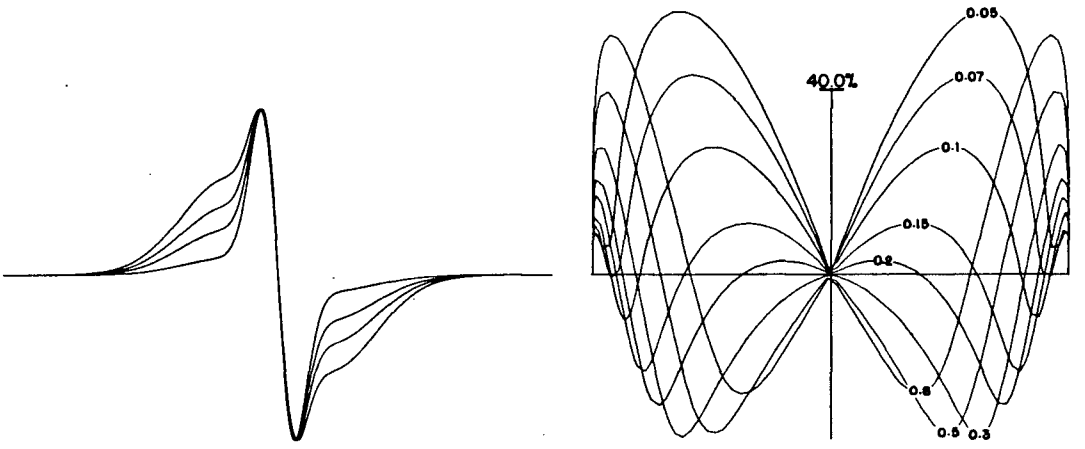

Figure 6.9. DISPA plot for superimposed Gaussian lines for various line-height ratios. Line-width ratio is 3.3. Ratios for spectra are; 0.1, 0.3, 0.5,0.8.

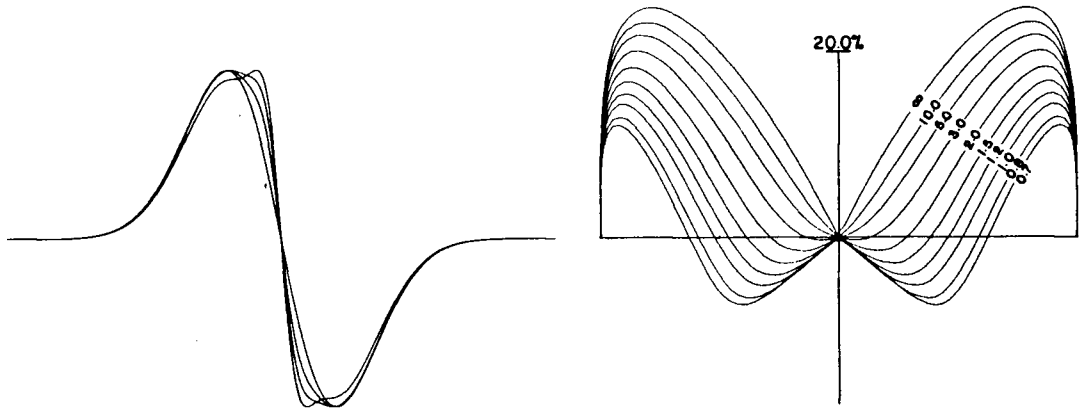

Figure 6.10. DISPA plot for superimposed Gaussian lines for various line-height ratios. Line-width ratio is 3.3. Ratios for spectra are; 1.0, 2.0, 3.0, ∞.

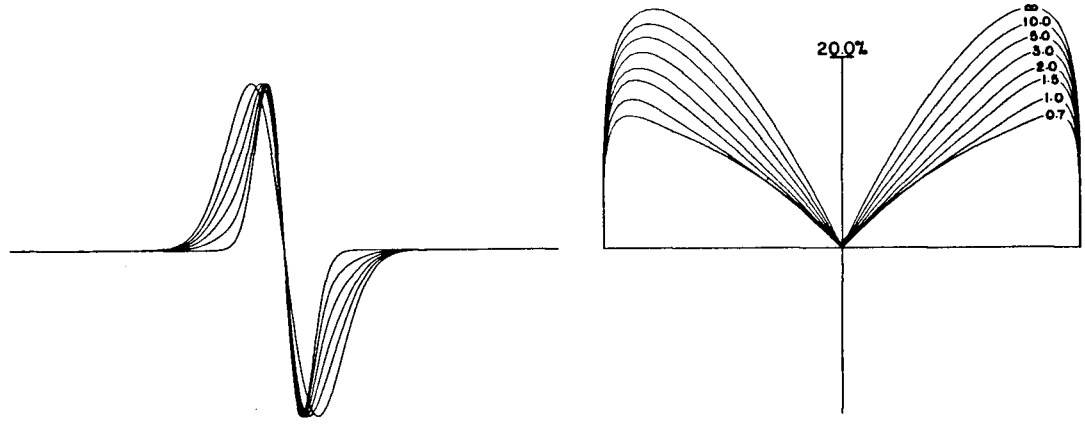

Figure 6.11. DISPA plot for superimposed Gaussian lines for various line-height ratios. Line-width ratio is 2.0. Ratios for spectra are; 0.0, 0.2, 0.5, 1.0, 2.0, ∞.

6.5 DETECTING TWO OVERLAPPING LORENTZIAN LINES

Radicals occupying two different sites (*vide supra*) may have different g-shifts. A case of special interest is that of chemical exchange, where, for instance, the exchange of a ligand causes a g-shift.

The simplest case is for two lines of equal amplitude and height being split apart. L-type lobes are obtained (Fig.6.12). The combinations for different linewidths, amplitudes and splittings are endless, but a pattern does emerge. If the lines are of the same width, but different amplitude an asymmetric L-type plot is obtained (Fig.6.13 and Fig.6.14). As the separation of the line increases the asymmetry increases. The smaller of the two lobes eventually forms a G(2)-type lobe. The larger lobe remains G-type.

If the lines are of different widths as well, W-L lobe types dominate. The plots are an asymmetric W-type (Fig.6.15). The asymmetry of the lobes increases as the lines split apart, with the smaller lobe becomeing an L(2)-type for large splittings.

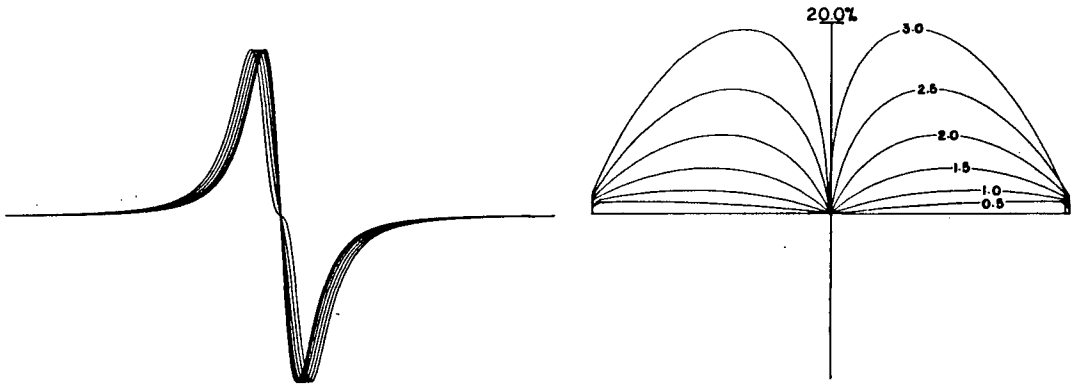

Figure 6.12. DISPA plot for overlapping Lorentzian lines for various splittings. Lines are the same height and width. Splittings for the spectrum are; 0.0, 1.0, 1.5, 2.0, 2.5, 3.0.

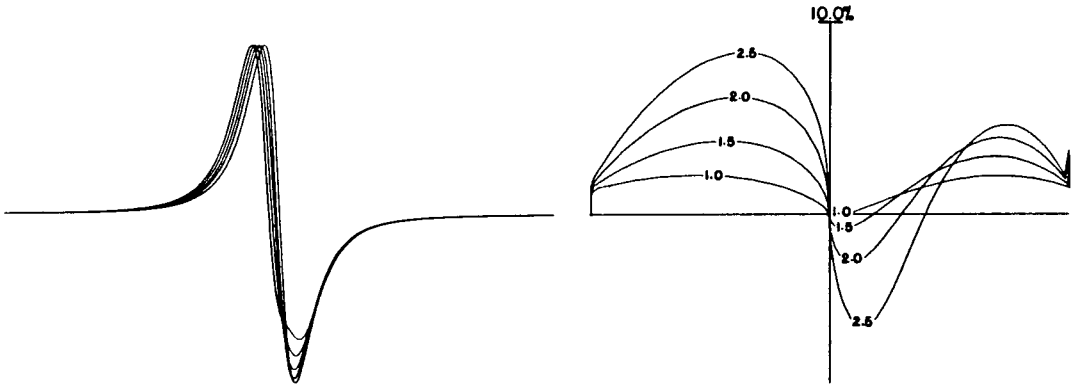

Figure 6.13. DISPA plot for overlapping Lorentzian lines for various splittings. Lines are the same width. Height ratio is 0.33. Splittings for the spectrum are; 0.0, 1.0, 1.5, 2.0, 2.5.

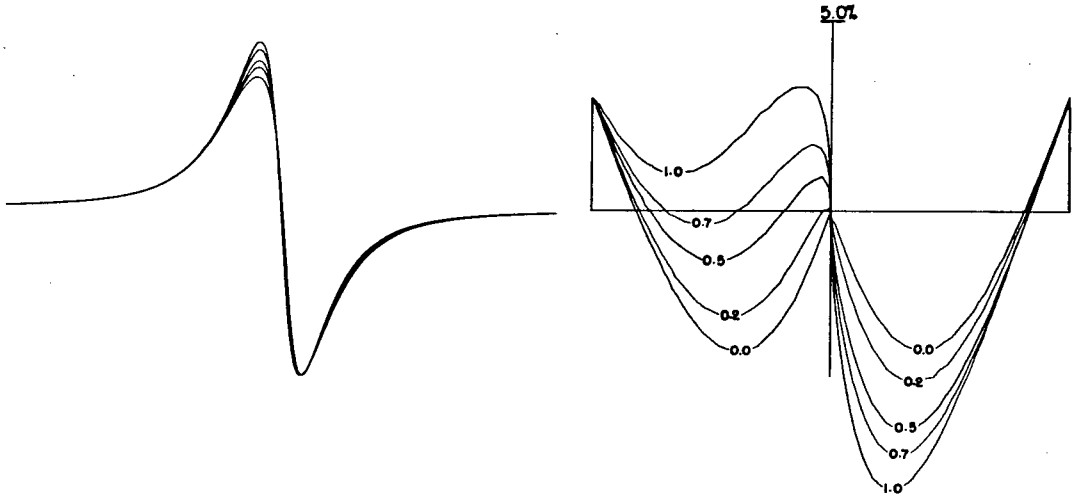

Figure 6.14. DISPA plot for overlapping Lorentzian lines for various splittings. Width ratio is 2.0. The heights are the same. Splittings for the spectrum are; 0.0, 0.2, 0.5, 0.7, 1.0. Note the similarity to next figure.

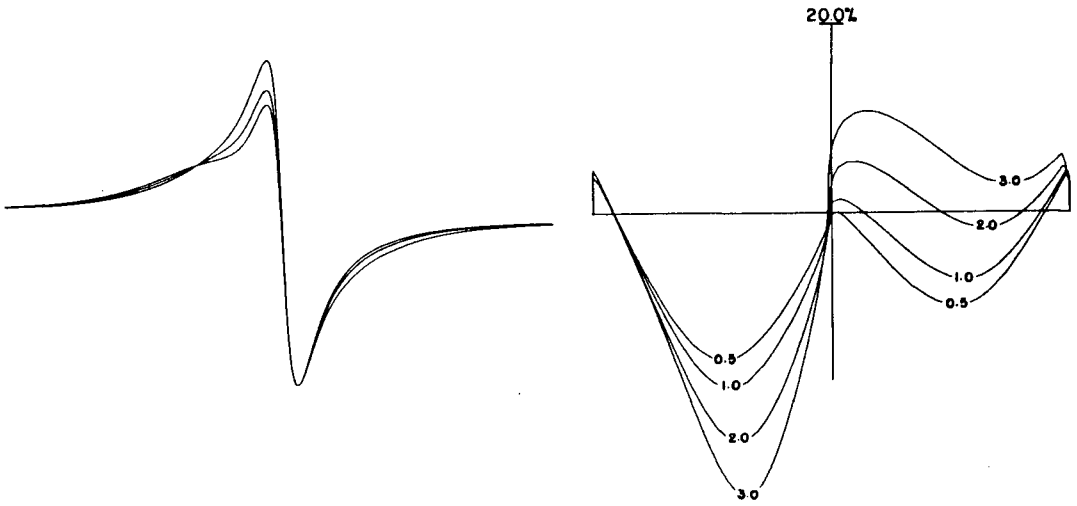

Figure 6.15. DISPA plot for overlapping Lorentzian lines for various splittings. Width ratio is 3.33. Height ratio is 0.33. Splittings for the spectrum are; 0.0, 0.5, 2.0, 3.0. The shifts are negative.

The raised tails in each case are due to a v-type contribution from truncation. (Sect.4.8).

6.6 DETECTING TWO OVERLAPPING GAUSSIAN LINES

This case is of interest because organo-sulfur radicals, which occur in coal, are g-shifted with-respect-to 'ordinary' radicals, which also occur is coal. The ESR spectra of coal are thus expected to be two overlapped Gaussian lines.

Two Gaussian lines of the same width and height just redistribute the amplitudes of the circles in Eqn.1.11, with more intensity appearing in the wings of the DISPA plot as the lines split apart. This gives rise to G-type behaviour (Fig.6.16).

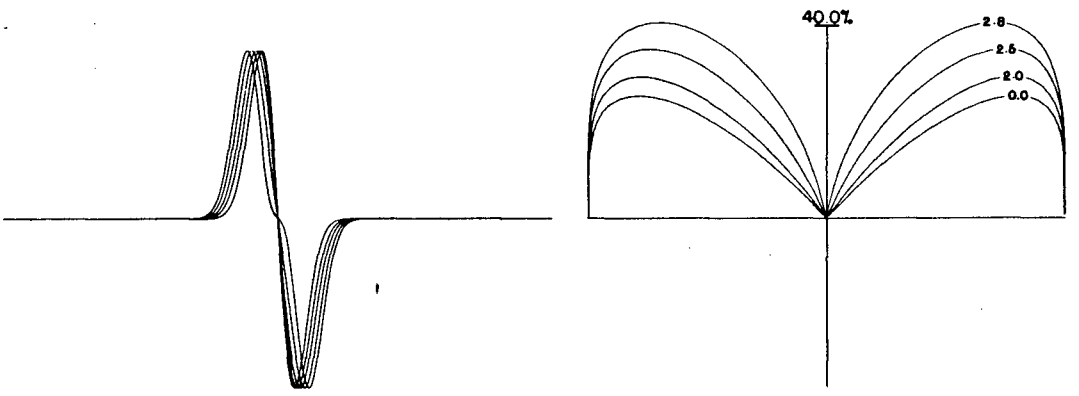

Figure 6.16. DISPA plot for overlapping Gaussian lines for various splittings. Lines are the same height and width. Splittings for the spectar are; 0.0, 1.5, 2.0, 2.5, 3.0.

If the lines are not the same amplitude or height then asymmetric G lobes occur. (Fig.6.17).

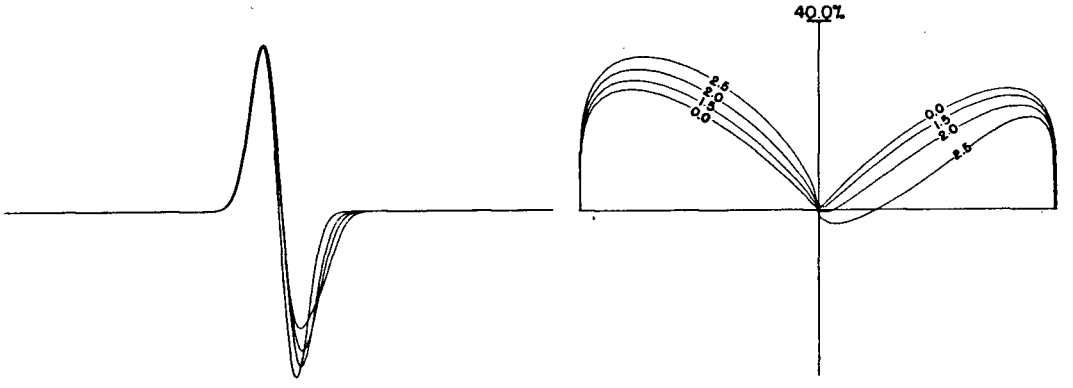

Figure 6.17. DISPA plot for overlapping Gaussian lines for various splittings. Lines are the same width. Height ratio is 0.333. Splittings for the spectra are; 0.0, 1.5, 2.0, 2.5.

It should be noted that the amplitude ratios chosen here are not arbitrary. Smaller ratios give smaller, but similar effects. Larger ratios give derivative spectra that

are partially resolved and thus were not used.

6.7 DETECTING COMBINATIONS OF LORENTZIAN AND GAUSSIAN LINES

This case may seem rather contrived, but can be used to account for the shape of DISPA plots from coal. The lobe behaviour is superficially similar to the cases for overlapping Gaussian lines, but on the whole the plots are unique to mixed Lorentzian and Gaussian lines. (Fig.6.18-Fig.6.21)

The following figures are representative of a range of many possible combinations of lines.

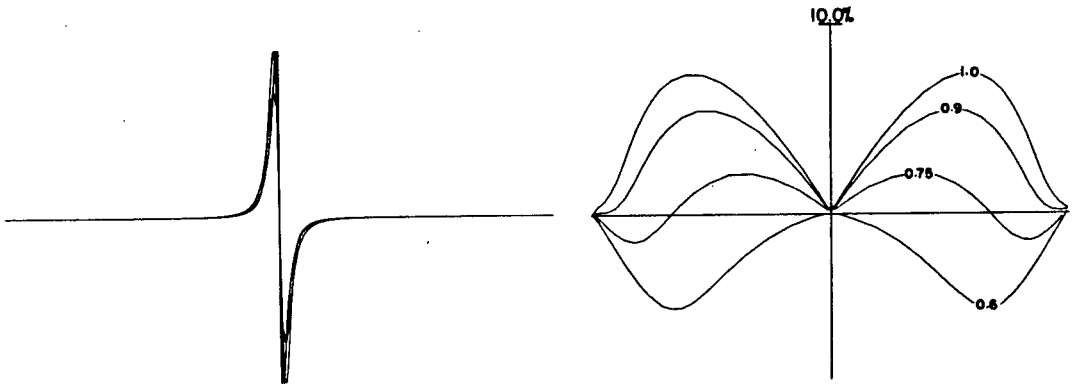

Figure 6.18. DISPA plot for a mixture of a Lorentzian and Gaussian lines for various width ratios. Amplitudes are the same. Splittings for the spectra are; 0.2, 0.5, 1.0. (The Lorentzian is the reference line).

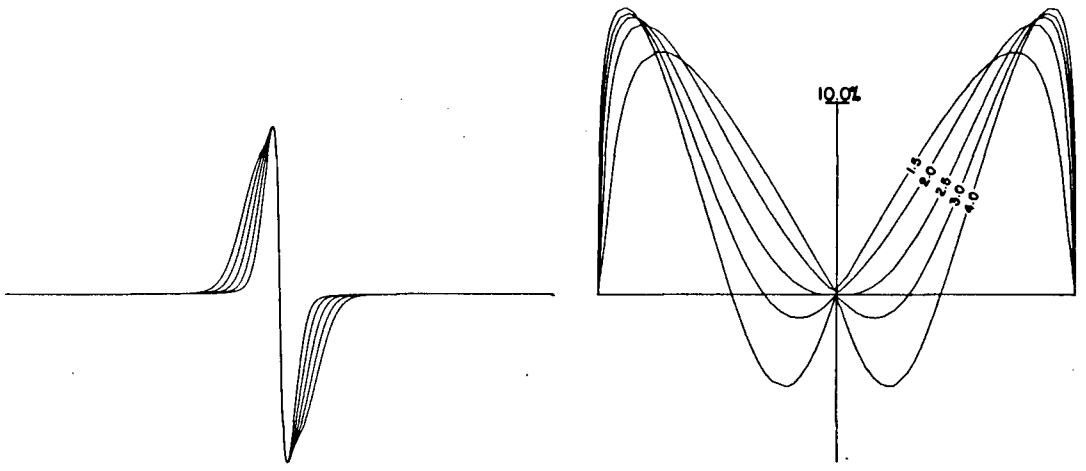

Figure 6.19. DISPA plot for a mixture of a Lorentzian and Gaussian lines for various width ratios. Amplitudes are the same. Ratios for the spectra are; 0.2, 0.5, 1.0. (The Lorentzian is the reference line).

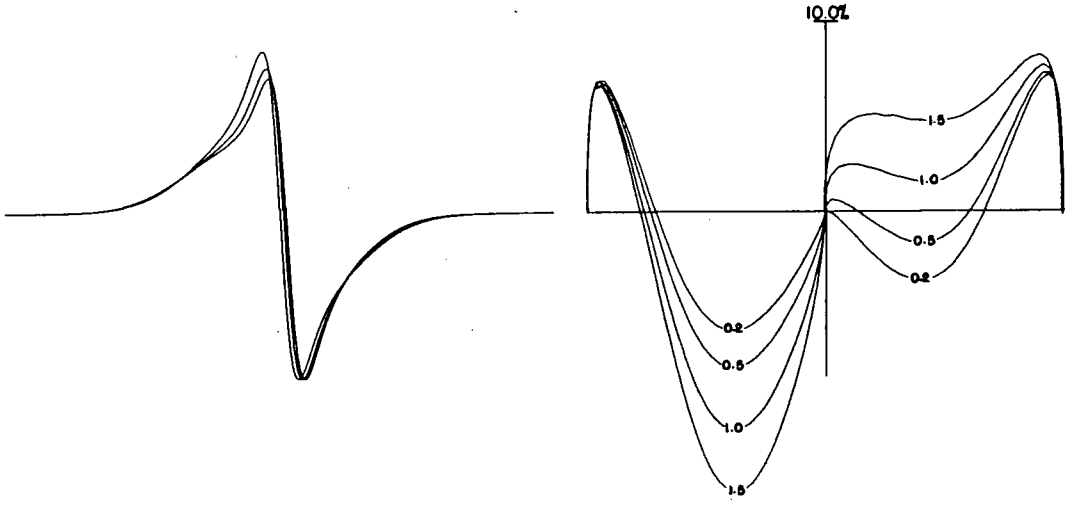

Figure 6.20. DISPA plot for a mixture of a Lorentzian and Gaussian lines for various width ratios. Amplitudes are the same. Ratios for the spectra are; 2.0, 2.5, 3.0, 3.5, 4.0. (The Lorentzian is the reference line).

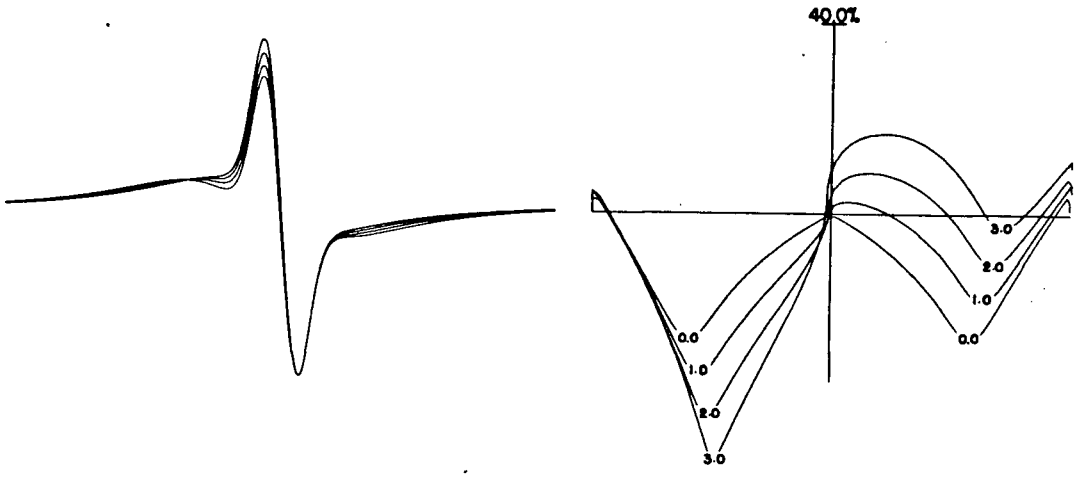

Figure 6.21. DISPA plot for a mixture of a Lorentzian and Gaussian lines for various splittings. Amplitudes ratio is 0.2. Width ratio is 4.0. Splittings (negative here) for the spectra are; 0.0 1.0, 2.0, 3.0. (The Gaussian is the reference line).

6.8 DETECTING AND MEASURING UNRESOLVED HYPERFINE COUPLINGS

Unresolved hyperfine coupling is very common in ESR, notably in the nitroxide type spin labels. The DISPA equation for this type of system (Eqn.1.11) seems quite unmanageable. However, the number and spin of the nuclei responsible for the unresolved hyperfine coupling is often known or can be easily guessed so that 'i' in Eqn.6.11 is defined. The amplitudes, A_i, follow the binomial distribution so the only unknown is Δ, the hyperfine splitting constant. If there is only one type of spin a calibration chart is easily constructed from the difference plots.

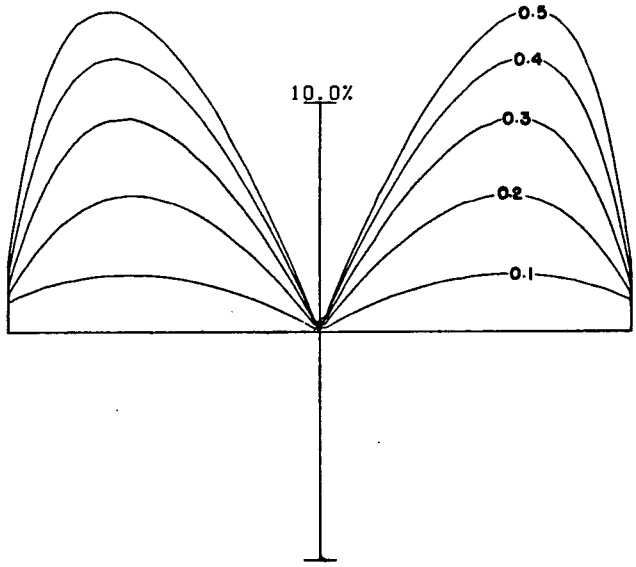

Figure 6.22. DISPA plot for unresolved hyperfine coupling for various reduced coupling constants (coupling constant/natural line-width). Hyperfine splitting is for 12 equivalent protons.

The height of the lobes are related to Δ (Fig.6.22). A calibration plot for 2 –> 12 spin half nuclei is shown in Fig.6.23. The apparent reduced coupling constant is the coupling constant expressed as a fraction of the observed line-width.

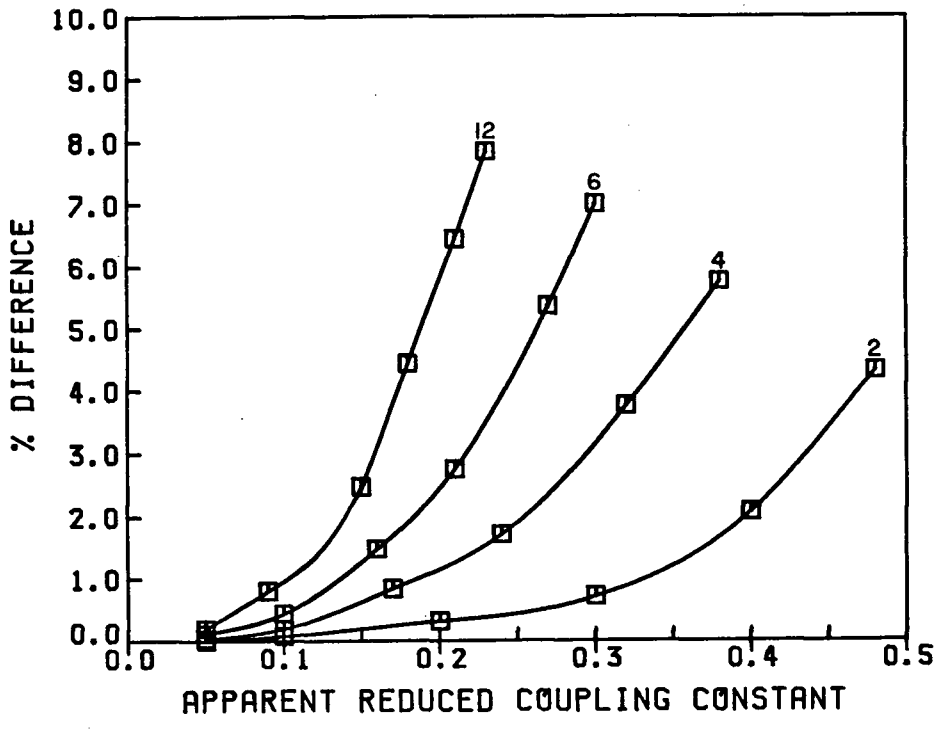

Figure 6.23. Calibration chart for unresolved hyperfine coupling. The numbers refer to the no. of spin 1/2 nuclei coupled to the electron.

6.9 APPLICATIONS TO LINE-SHAPE ANALYSIS OF SOLIDS

In solids where Gaussian or Lorentzian lines occur the analysis discussed in the sections above is applicable. However, symmetric (or near symmetric), single line, powder patterns can arise, that are not Gaussian or Lorentzian in nature. For instance, a radical with a small orthorhombic g-tensor may give rise to a symmetric line with small shoulders. This could be mistaken for superimposed Gaussian lines. Also, asymmetric difference plots may arise from slightly anisotropic g-tensors (or g-tensors averaged by

motion *(39)*) rather than from two overlapping lines. Powder pattern simulations are needed to clarify this. The Gaussian difference plot (Sect.3.4) would probably be very useful in this case.

The examples given in the next section been interpreted in terms of the analysis for solution spectra. As such these results should be regarded as a demonstration of the potential utility of the technique as applied to solids and not as a definitive interpretation of the spectrum. A detailed analysis of DISPA plots for solids will be worth pursuing, because coal and wood, two solids of great commercial value, both give single line ESR spectra.

7. EXPERIMENTAL EXAMPLES

7.1 TEMPERATURE DEPENDENCE OF UNRESOLVED HYPERFINE

If the unresolved hyperfine coupling is temperature dependent then the residual line-width (Sect.14.5) is also temperature dependent and this hampers spin relaxation studies. The unresolved hyperfine coupling contribution to nitroxide type spin-probes is quite large (Fig.7.1, *(40)*). Proving that the unresolved hyperfine coupling is temperature independent is very difficult, the effects are masked by motional line-broadening. One method of solving this problem is to fix the correlation time of the probe and then study the DISPA plots as a function of temperature. In practice, this is achieved by examining the probe in a series of non-polar solvents at temperatures chosen such that the viscosity/temperature (η/T) remains constant. This of course assumes that the rotational correlation time depends only on η/T and that the effect of the solvent on rotational anisotropy can be neglected.

DISPA plots of TEMPONE[18] were obtained in pentane, heptane, decane and dodecane for η/T values of 0.001 and 0.002 cP K^{-1},[19] over a temperature range of -20°C to +70°C for the $m_i(0)$ line (for which motional effects are the smallest). Within experimental error no temperature dependence of the DISPA plot (Table 7.1) and hence of the

---

[18] TEMPONE = 4-oxo-2,2,6,6,-tetramethylpiperidine-1-oxyl
TEMPO = 2,2,6,6,tetramethylpiperidine-1-oxyl.
[19] cP=centi-Poise.

unresolved hyperfine coupling, was observed.

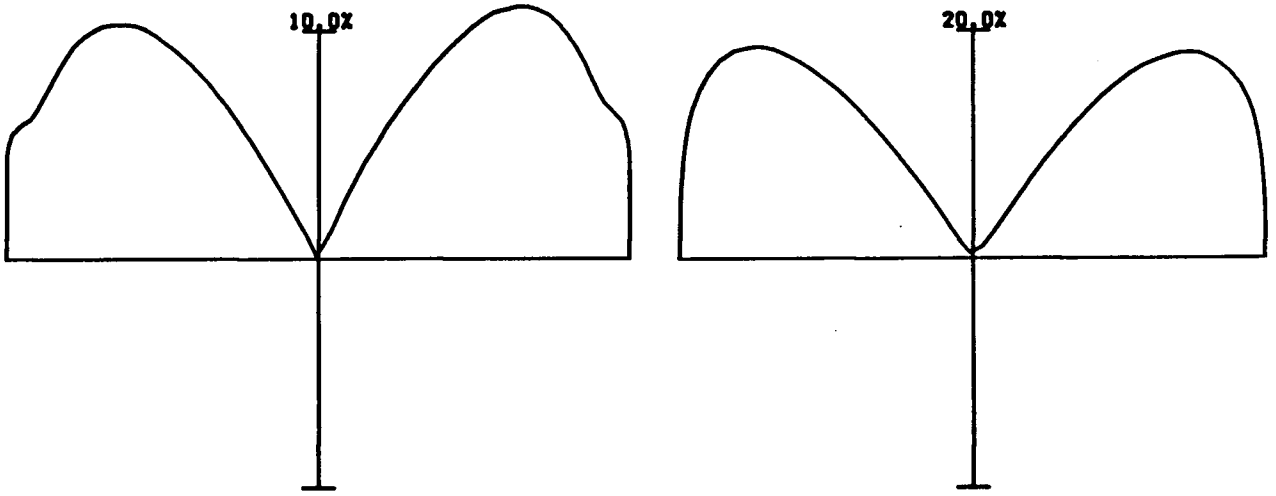

Figure 7.1. Difference plots for TEMPO and TEMPONE, showing the large unresolved hyperfine coupling contribution to the line-widths. TEMPO is on the left.

η/T	Solvent	Temp °C	Line-width	%R
0.001	Hexane	24.4	1.46	11.2
	Heptane	46.7	1.44	10.8
0.002	Hexane	-23.3	1.38	14.5
	Heptane	-3.0	1.37	15.3
	Decane	47.8	1.38	15.6
	Dodecane	72.7	1.40	15.6

Table 7.1. Temperature dependence of the unresolved hyperfine coupling for TEMPONE

7.2 MIXTURES OF SPIN PROBES

Establishing the degree of binding of a spin-label to the host molecule is important if meaningful motional studies are to be done. As the bound and unbound labels will not differ much in g-shift this can be very difficult to measure. DISPA is ideally suited for analysing such a case. To simulate this, TEMPO (line-width ≃ 3.0G to represent a bound spin-probe) was mixed with TEMPONE (line-width ≃1.5G to represent the unbound probe) in a 1:3 concentration ratio.[20] The DISPA plot is quite different from that of the individual probes (Fig.7.2) as might be expected from Sect.6.4. Semi-quantitative results can be obtained if a calibration chart for the system can be prepared (the widths of the unbound and the pure bound probe are required).

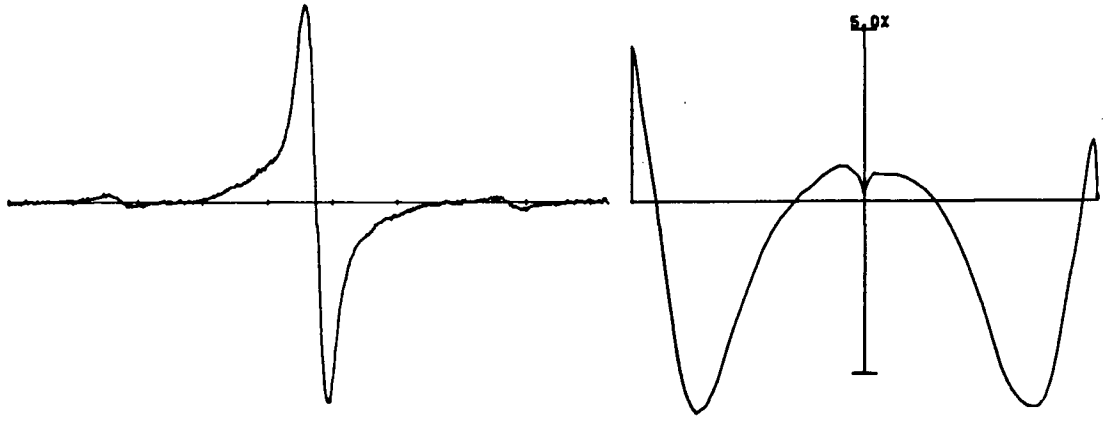

Figure 7.2. The DISPA plot for two superimposed spin labels.

An application of this to a real case[21] is shown in Fig.7.3.

---

[20] This was one of a series of samples prepared by L.F.Yip in an attempt to quantify the method.
[21] Taken from work performed by E.Lam in this laboratory *(41)*.

Here a spin label is partitioned between a cell membrane ('bound probe') and the surrounding fluid (free probe). The spectrum shows some distortion, but its clear from the DISPA exactly what is causing it; a mixture of free and bound probes accompanied by a slight g-shift with-respect-to each other.

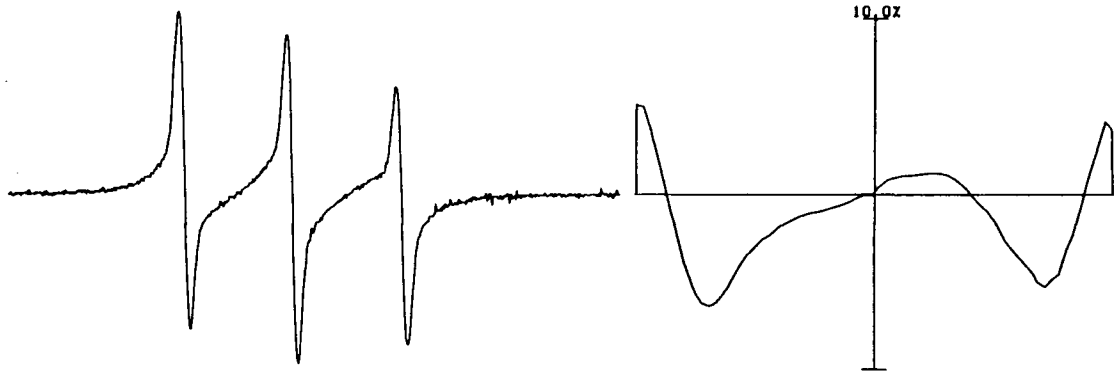

Figure 7.3. The DISPA plot for an amphipathic spin-probe incorporated into red blood cells in the presence of crystals of mono sodium urate mono-hydrate. The difference plot is for the center line.

7.3 UNRESOLVED HYPERFINE COUPLING CONSTANTS

It is useful to determine what proportion of the residual line-width of the copper dithiocarbamate class of spin-probes is due to unresolved hyperfine coupling. The dimethyl derivative is a simple case to study as it has twelve equivalent protons. The difference plots for this probe are shown in Fig.7.4. The unresolved hyperfine coupling contribution can be measured from these plots. From Fig.6.23 and Fig.7.4, we get a reduced coupling constant of

0.13, which corresponds to an unresolved hyperfine coupling constant of 0.6G for an observed line-width of 4.6G with coupling to 12 protons. This agrees reasonably well with values from simulations (0.3G *(42)*) and by comparison with the per-deuterated compound (0.4G *via* Bales formulas *(43)*). The slightly high value can be attributed to the satellites and line truncation. It nevertheless provides a good starting point for simulations.

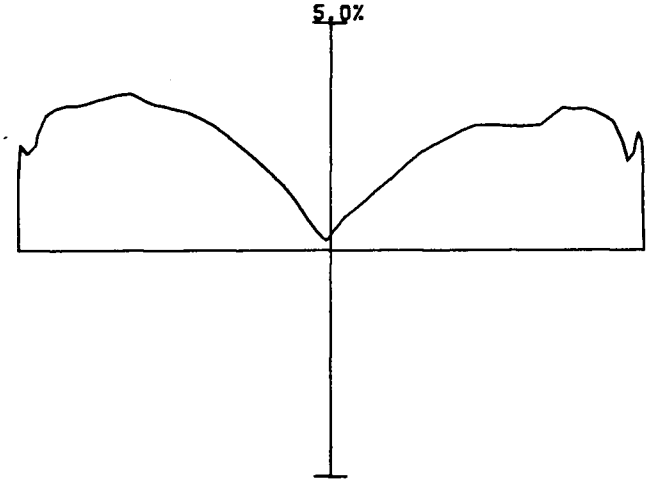

Figure 7.4. The DISPA plot for $^{65}CuMe_2dtc$ in toluene. The high-field line.

7.4 USING DISPA PLOTS TO DETECT SATELLITES

The abscissa of a difference plot is usually chosen to compress the baseline and expand the resonance region of a spectrum. However, the converse case can be useful if we wish to detect satellites in the wings. Fig.7.5 shows the square-root plot for per-deuterated CuPydtc in d-chloroform. The central peaks are due to unresolved hyperfine coupling

from the deuterons, residual hydrogen and ^{13}C satellites. The two outer peaks are due to the ^{33}S satellites (four lines), which are in the wings of the spectrum *(44)(45)*.

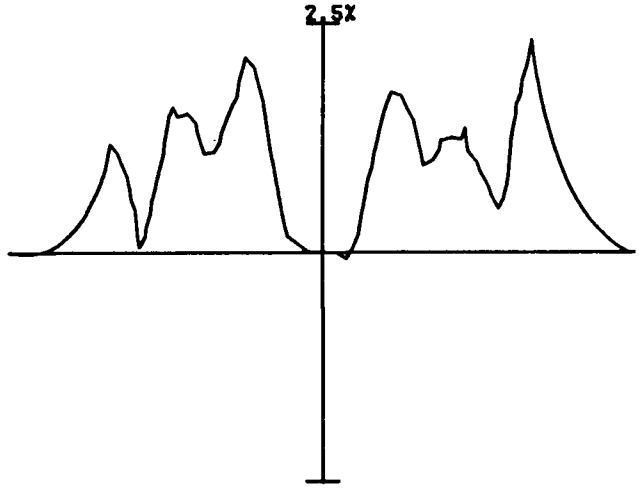

Figure 7.5. A Square-root difference plot showing satellites.

7.5 THE DETECTION OF CHEMICAL EXCHANGE. SOLVATION EFFECTS

Pyridine exchanges with dithiocarbamates *(46)* on the ESR time-scale and consequently broadens the lines. For a 50:50 mixture of pyridine and toluene the broadening, in this case, is about 2 Gauss (from 5G), but otherwise the line is unchanged. The DISPA plot is shown in Fig.7.6. The plot is very different from that obtained in the absence of pyridine (Fig.7.4 and corresponds to the DISPA of two overlapped Lorentzian lines of similar width and intensity (Fig.6.13)), showing that the broadening is due in part to the pyridine changing the magnetic parameters of the *dtc* and not just by

changing its motion.

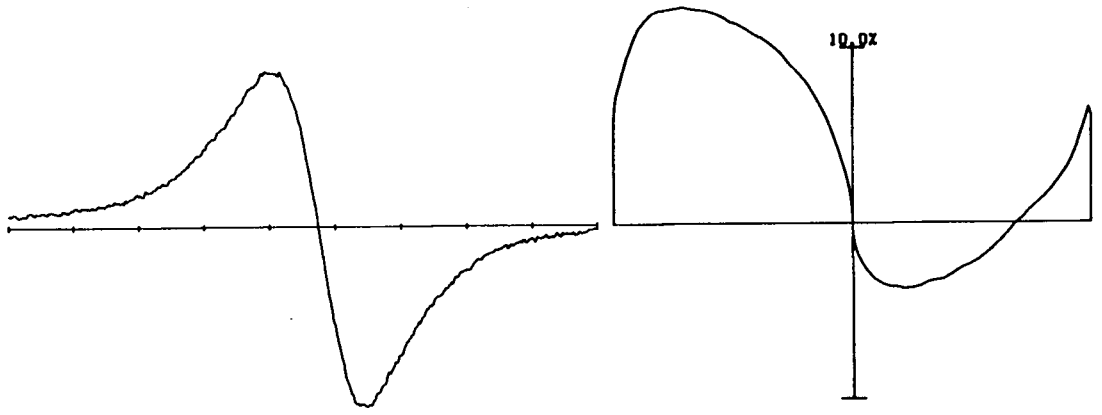

Figure 7.6. DISPA plot showing Chemical Exchange. The high-field line of ^{65}CuPydtc in 50:50 toluene/pyridine.

7.6 THE SPECTRUM OF GREY PITCH

Grey pitch is a standard sample for ESR *(47)*. It is not of any great interest other than for that purpose, but it does have a single line ESR spectrum. The DISPA plot (Fig.7.7) shows that the line may be considered as a superposition of two (or more) Gaussian or Lorentzian lines of different widths and heights (see Fig.6.5, Fig.6.9 and Fig.6.18) and thus the sample contains two (or more) radicals or radical sites. However, this effect may be due to a single radical with a small orthorhombic g-tensor.

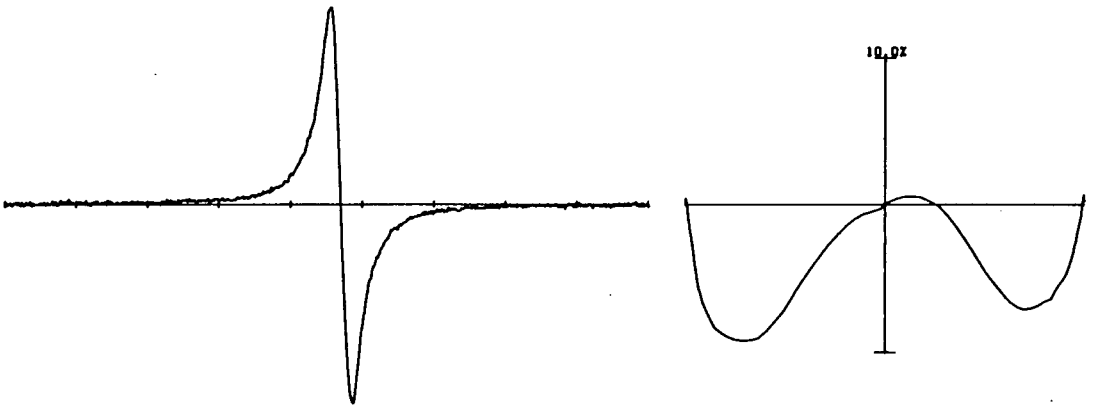

Figure 7.7. The DISPA plot for grey-pitch.

7.7 GRAPHITE SPECTRA

Graphite is a two-dimensional conductor and should give a Dysonian line-shape (Fig.2.6). The shoulder observed in Fig.7.8 is not typical of the Dysonian line, its origin is unknown, but its amplitude varies with the degree and type of intercalation. *(48)*.[22] The DISPA plot is not very useful and casts no light on the problem, but it may be regarded as a control for coal, *vide infra*, which may contain graphitic like domains *(49)*.

An interesting possibility for Dysonian lines of the type shown in Fig.2.6 is to use the auto-phase algorithm (Sect.5) to remove the dispersion component of the line and then to characterise the remaining line by its width, position and phase correction.

---

[22] This sample was obtained from Dr.F.Aubke and is extremely pure.

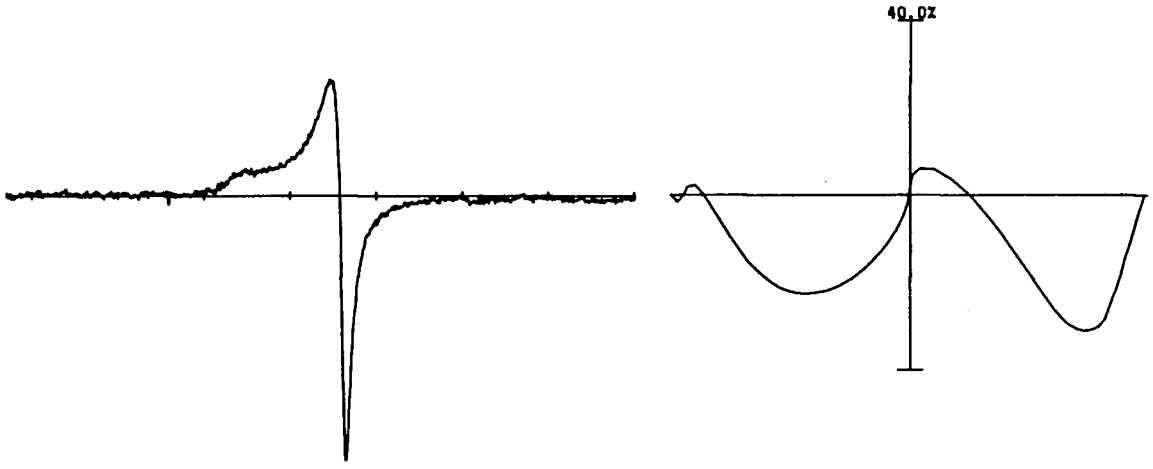

Figure 7.8. DISPA plot for SP1 graphite.

7.8 COAL SPECTRA

Coal[23] gives a single line spectrum. Various examples are shown overleaf. The plots may be interpreted as a Lorentzian and Gaussian line with various degrees of overlap. One line probably corresponds to a carbon based radical and the other a sulphur based radical. The plots were blind ranked in terms of increasing line separation (lobe asymmetry). Note that the spectra are almost indistinguishable. From Table 7.2 its clear that the ranking correlates well with the sulphur content, an important measure given Canada's current concern with acid rain. A more detailed study is obviously warranted.

---

[23] The samples were obtained from Dr.Tao of the Coal Institute UBC. The spectra taken by Dr.N.R.Jagannathan.

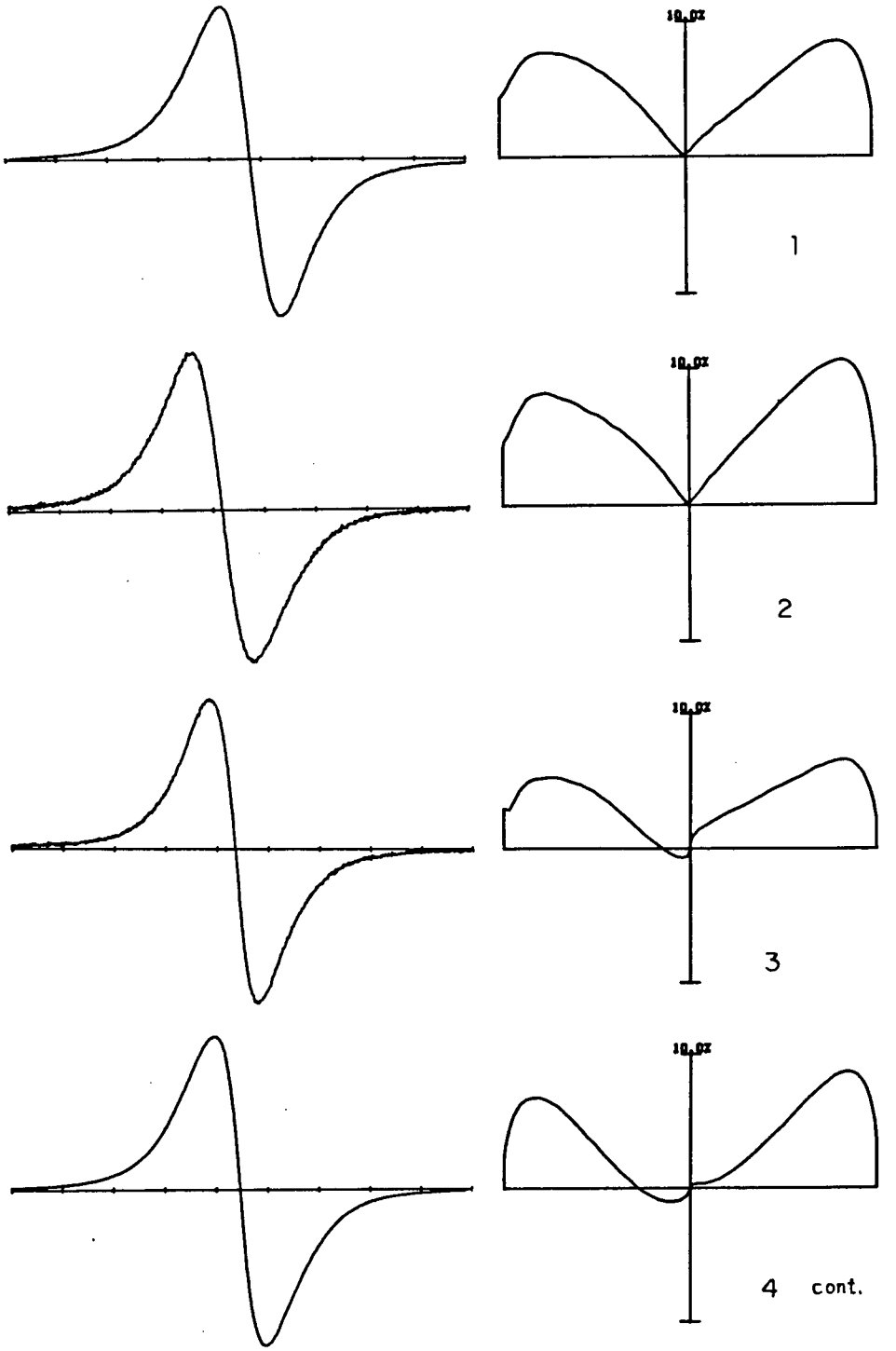

Figure 7.9. DISPA plots for various coal samples. (cont. overleaf).

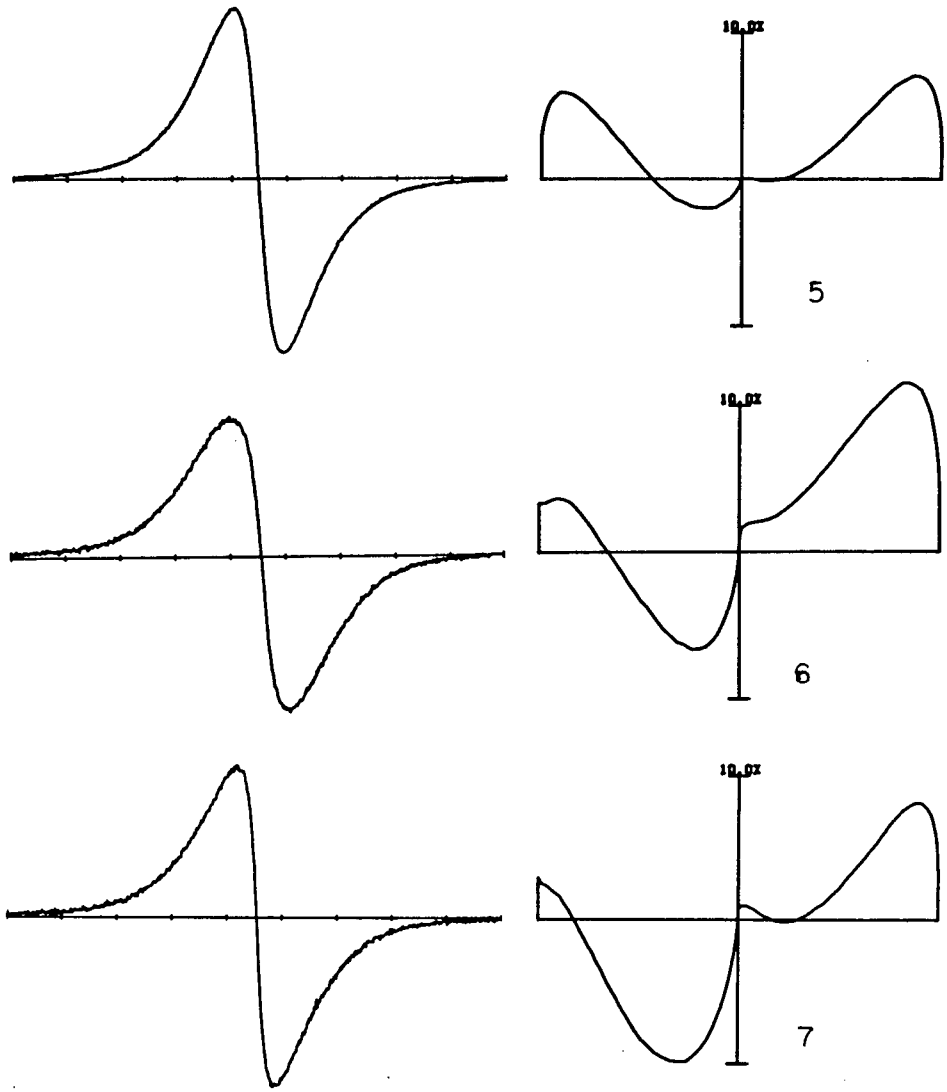

Figure 7.10. DISPA plots for various coal samples. (cont. from previous page).

SAMPLE NO.	COMMENTS
1	Coronach. Saskatchewan lignite. <0.5% pyrite may contain organic sulphur.
2	Forestburg. SW Alberta. Sub-bitumeous coal <0.5% pyrite.
3	Onakawana. N.Ontario. May contain organic sulphur. More organic sulphur than above samples.
4	Fording Adit 23. S.E. B.C. bitumeous coal. More pyrite than above samples, but less organic sulphur.
5	Sukunka. Alberta bitumeous coal. More pyrite, but less sulphur than above samples.
6	Devco. Nova Scotia coal. High sulphur bitumeous coal. 2-3% sulphur.
7	Minto. High pyrite coal. 7% sulphur.

Table 7.2. Identification of and notes on the coal samples.

7.9 WOOD SPECTRA

The spectra and DISPA plots for decayed Aspen wood at various stages of photo-irradiation are shown in Fig.7.11-Fig.7.13.[24] Natural decayed wood gives a DISPA spectrum (Fig.7.11) consistent with two radicals of similar width, but slightly different amplitudes and g-values. After irradiation the proportion of one of the radicals increases (Fig.7.12). The radical concentration then slowly decays over a number of days, back to near the original concentration (Fig.7.13). One may postulate that one radical

---

[24] These samples were obtained from Lai Hong of the UBC Forestry department.

is a chemical decay product and the other of photolytic origin. As with the coal samples, the original spectra reveal very little, but the DISPA plots are quite different.

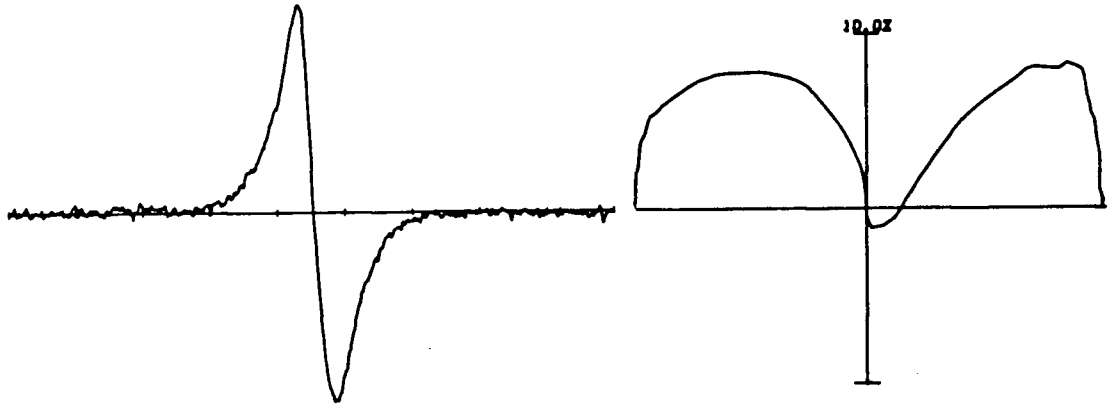

Figure 7.11. DISPA plot for natural decayed wood.

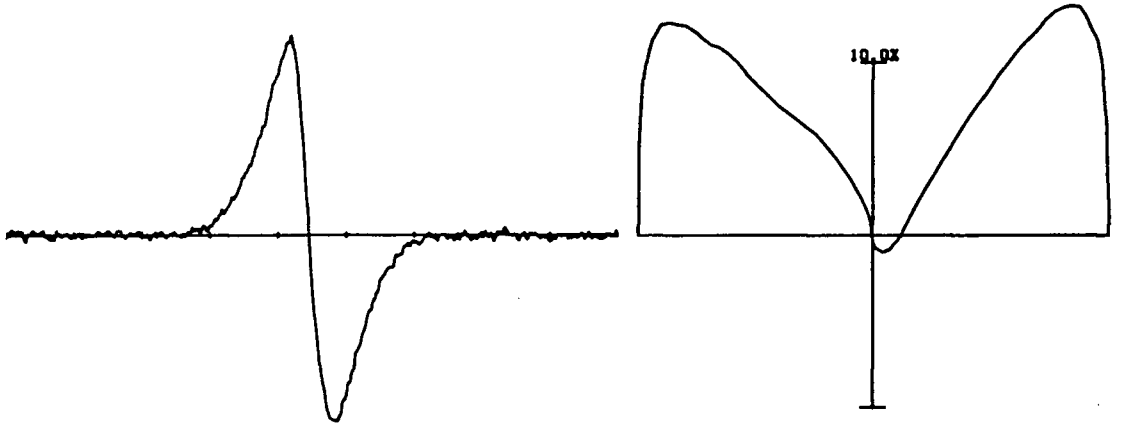

Figure 7.12. DISPA plot for decayed wood after irradiation.

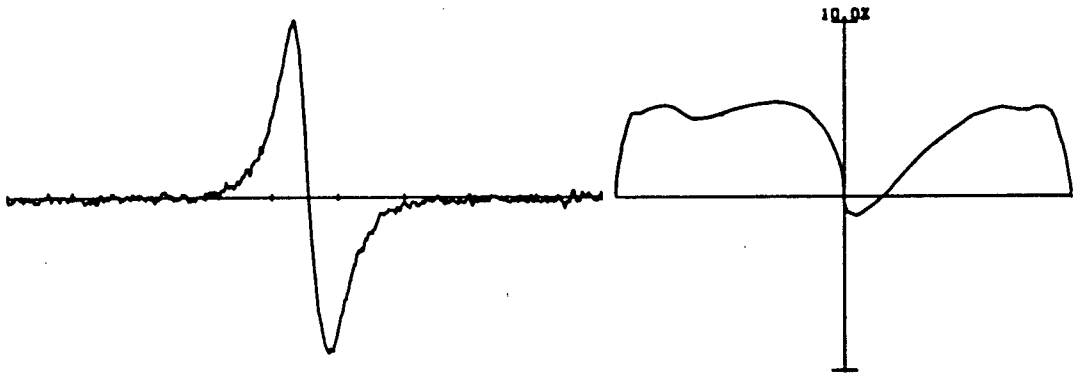

Figure 7.13. DISPA plot for decayed wood after irradiation and relaxation.

7.10 NITROXIDES IN THE SLOW-MOTIONAL REGIME AND POWDER SPECTRA

Both the spectra and the difference plots are complex (Fig.7.14-Fig.7.15). In this case an indexed plot is more useful as the absorption plot is unstable. However, neither type of difference plot is readily interpretable and have only been included for completeness and to demonstrate one of the limitations the DISPA technique. Variable temperature experments may yield useful results, but this approach has not been investigated.

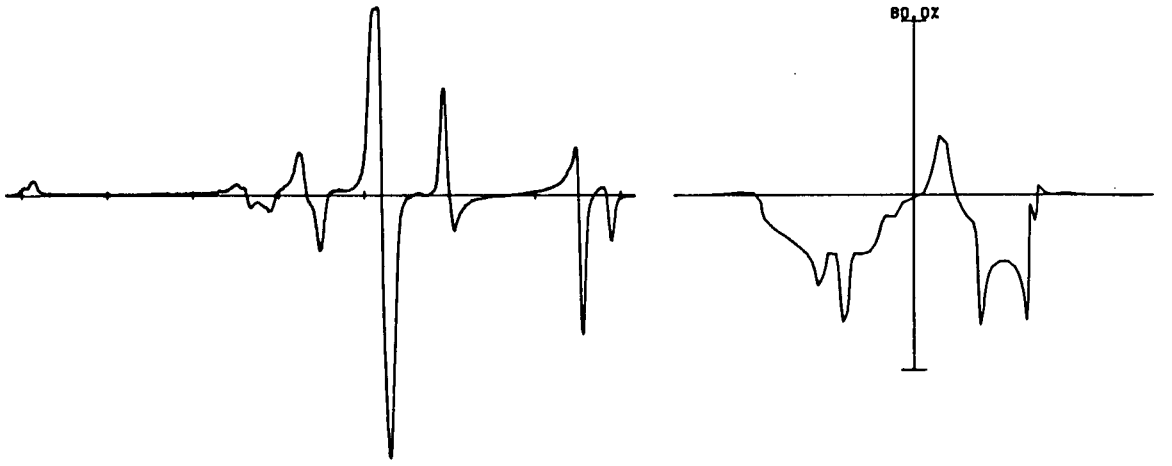

Figure 7.14. DISPA plot for a powder spectrum. The spectrum of CuPydtc doped into the corresponding nickel salt. Log-index plot.

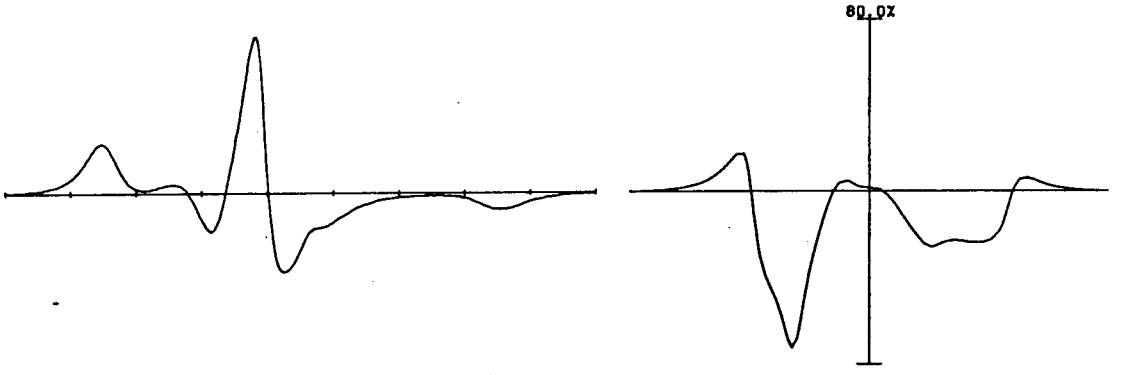

Figure 7.15. DISPA plot for a nitroxide in a membrane. Log-index plot.

8. CONCLUSIONS

8.1 SUMMARY OF RESULTS

LOBE DESCRIPTION	DIAGNOSIS
Lobes of different amplitude, but otherwise symmetric	Mis-phased spectrometer or close overlap of similar lines
Similar to above, but right tail drops	Phase-sensitive-detection amplifier time constant too large
Tails of lobes raised	Line truncation
Twin positive going lobes	Unresolved hyperfine coupling, overmodulation or any distribution in line-position
Twin negative going lobes	Superimposed lines. *e.g.* a distribution of correlation times for a one species
Asymmetric lobes	See rules of thumb

Table 8.1. Summary of results for simple DISPA plots.

8.2 RULES-OF-THUMB

These rules of thumb essentially summarise the results of Sect.6.

a) W-lobe behaviour is characteristic of a superposition of lines of equal resonant frequency, but different widths.

b) G-lobe behaviour is characteristic of a symmetric superposition of lines of different frequencies, with the line amplitude decaying as the distance of the line from the center of symmetry increases.

c) Combining a) and b) and retaining a center of symmetry results in a mixture of G-lobe and W-lobe behavior. Multilobe difference plots may result.

d) Asymmetric lobes from liquid spectra are (in the abscence of instrumental artefacts) characteristic of two or more lines of different width or amplitude at different resonant frequencies.

e) Solid state spectra can give simple DISPA plots, but care should be used when using the generalisations above.

8.3 CONCLUSIONS

DISPA is an experimentally and conceptually simple numerical analysis method that enables us, for the first time, to get a general, but concrete grasp of spectral line-shapes; a useful addition to line-width and line-position information. Probably the most outstanding feature of DISPA plots are their sensitivity to deviations from Lorentzian behaviour. Spectra that are almost indistinguishable, give very different DISPA plots and because we have developed a sound basis for DISPA, these plots are, in most cases, quantitatively (*e.g.* unresolved hyperfine coupling) or qualitatively (*e.g.* coal samples) interpretable. Of more immediate relevance, DISPA can be exploited in spin-probe

studies to assess spectrometer performance and also to investigate the ESR spectra of paramagnetic species to determine their suitablity for such studies.

Although much of the information from DISPA can be obtained by other methods (*e.g.* simulations) these methods are usually extremely laborious and often give non-unique solutions. DISPA needs no special equipment (other than a computer) or experiments and can give a definitive solution.

PART 2.

RELAXATION STUDIES BY MAGNETIC RESONANCE

9. INTRODUCTION TO THE MOTIONAL STUDIES

9.1 INTRODUCTION

In recent years it is has become apparent, especially in biochemistry, that molecular structure is not only intimately related to function, but is probably as important as the 'chemistry'. Unfortunately, there is a paucity of techniques for determining molecular geometry in solution. One possible approach, developed in the last few years, is to relate molecular reorientation to molecular structure. The problems, however, are quite formidable. Firstly one has to relate the experimentally accessible parameters to the correlation function for the motion. This then has to be related to the molecular motion, which finally has to be related to molecular geometry. Each one of these steps alone constitute major and challenging areas of research.

Molecular reorientation (often loosly referred to as rotation) in solution is generally studied by measuring the response of the solution to a radiation field. For such measurements to reflect the reorientation of the molecule in the solution, the interaction between the field with the molecule must depend on the orientation of the molecule in that field, *i.e.*, the interaction and the radiation field must be anisotropic.

Generally the response of a system at a frequency ω, $J(\omega)$, to a perturbing field, $\underset{\sim}{T}$ is given by *(50)*

$$J(\omega) = F\{G(t)\} \tag{9.1}$$

where F{x} denotes the Fourier transform and G(t), the correlation function, is given by

$$G(t) = \langle [\underset{\sim}{T}(0).\underset{\sim}{F}(0)].[\underset{\sim}{T}(t).\underset{\sim}{F}(t)] \rangle \tag{9.2}$$

where $\underset{\sim}{F}$ is a molecular tensor property that interacts with the field. The <> denotes an ensemble average. It is convenient to transform the two tensors into the same reference frame. This is most conveniently done in a spherical basis so for example transforming to the molecular frame we get

$$\underset{\sim}{F}_k^{mol}(t) = \sum_m F_m^{l\,ab} D_{mk}^{j}[a\beta\gamma(t)] \tag{9.3}$$

where D is the Wigner rotation matrix and $(a\beta\gamma)$ are the Euler angles relating the laboratory (field) frame to the molecular frame, 'm' and 'k' are the tensor element indices and j is the rank of the tensor (1 for a scalar, 2 for a vector and 3 for a tensor).[25] Tensor products are quite simple in a spherical basis, hence

---

[25]Scalars are rotationally invariant and are of no interest here.

$$[\underset{\sim}{T}.\underset{\sim}{F}] = {}_{k,m}\Sigma_{m}(-1)^{k} T^{mol}_{-k} F^{l\,ab}_{m} D^{j}_{mk}[a\beta\gamma(t)] \qquad (9.4)$$

Note that the time dependence is carried entirely by the Wigner rotation matrix. Hence we find for G(t)

$$G(t) \simeq \langle D^{j}_{mk}(0)_{a} . D^{j}_{mk}(t)_{b} \rangle \qquad (9.5)$$

Eqn.9.4 & Eqn.9.5 hold the key to experimental design for molecular rotation studies. The subscripts 'a' and 'b' in Eqn.9.5 denotes different molecules; the evaluation of Eqn.9.5 not only depends on the orientation of a given molecule, but also on the orientation of its neighbours. When a=b, always, G(t) is called a single particle correlation function (intermolecular interactions do not influence the rotation or the molecules interaction with the field). When a≠b, generally, then it is called a multi-particle correlation function (neighbouring molecules interact). Multi-particle correlation functions are extremely difficult to interpret and there is no satisfactory way of relating them to single particle correlation functions, which are more manageable. For instance, if we perform dielectric studies, where $\underset{\sim}{F}$ is the dipole moment of the molecule, we obtain multi-particle correlation functions because of the contributions from induced dipoles. On the other hand if we do infra-red (IR) studies, where

$\underset{\sim}{F}$ is the time derivative of the dipole moment, we obtain single particle correlation functions. Although the dipoles are coupled, fluctuations in them are not, or only weakly so.

The dipole moment is a vector property, hence only two spectral densities, $J^{1,0}$ and $J^{1,\pm 1}$ are observable. Light scattering or Raman studies, which involve the polarisibility, a tensor, gives five spectral densities, $J^{1,0}$, $J^{1,\pm 1}$, $J^{2,0}$, $J^{2,\pm 1}$, $J^{2,\pm 2}$. Obviously the more data the better.

Magnetic resonance, the subject of this part of the thesis, is an obvious choice for motional studies. However, it differs in a number of ways from the methods mentioned above. There are several choices for the interaction tensor (quadrupole, chemical shift anisotropy *etc.*; these are discussed in detail in the next section). Furthermore, the technique is quite sensitive, the optical methods are restricted to pure solvents or concentrated solutions. NMR and ESR may be used with dilute solutions (*i.e.*, 10% solute or less) and the the dynamics of solutes not just neat solvents can be studied. Unfortunately magnetic resonance is a single frequency technique. Unlike the other techniques where the whole correlation function is available (its the Fourier transform of the $J(\omega)$, the line-shape), magnetic resonance can only give spectral densities for two frequencies, the spectrometer frequency and zero frequency. Also the sensitivity of magnetic resonance arises from its

selectively (ESR only detects paramagnetic species). This can make it difficult to obtain enough independent information to measure the diffusion tensor. In the past it has been necessary to combine NMR with optical studies, *e.g.(51)*, or to perform multi-nuclear NMR studies, *e.g.(52)*, to obtain enough information. Here, for the first time, we combine NMR studies with ESR studies to measure a diffusion tensor.

A flow chart of the general strategy for a multi-technique approach is shown in Fig.9.1. This work will be restricted to the fast motional case (Redfield theory) and the Debye diffusion model. The results will be examined using simple hydrodynamic models.

For an overveiw of strategies in molecular dynamics see *(53)(54)(55)* (optical methods), *(56)(57)*, (theoretical studies) and *(58)(59)* (multi-technique approach).

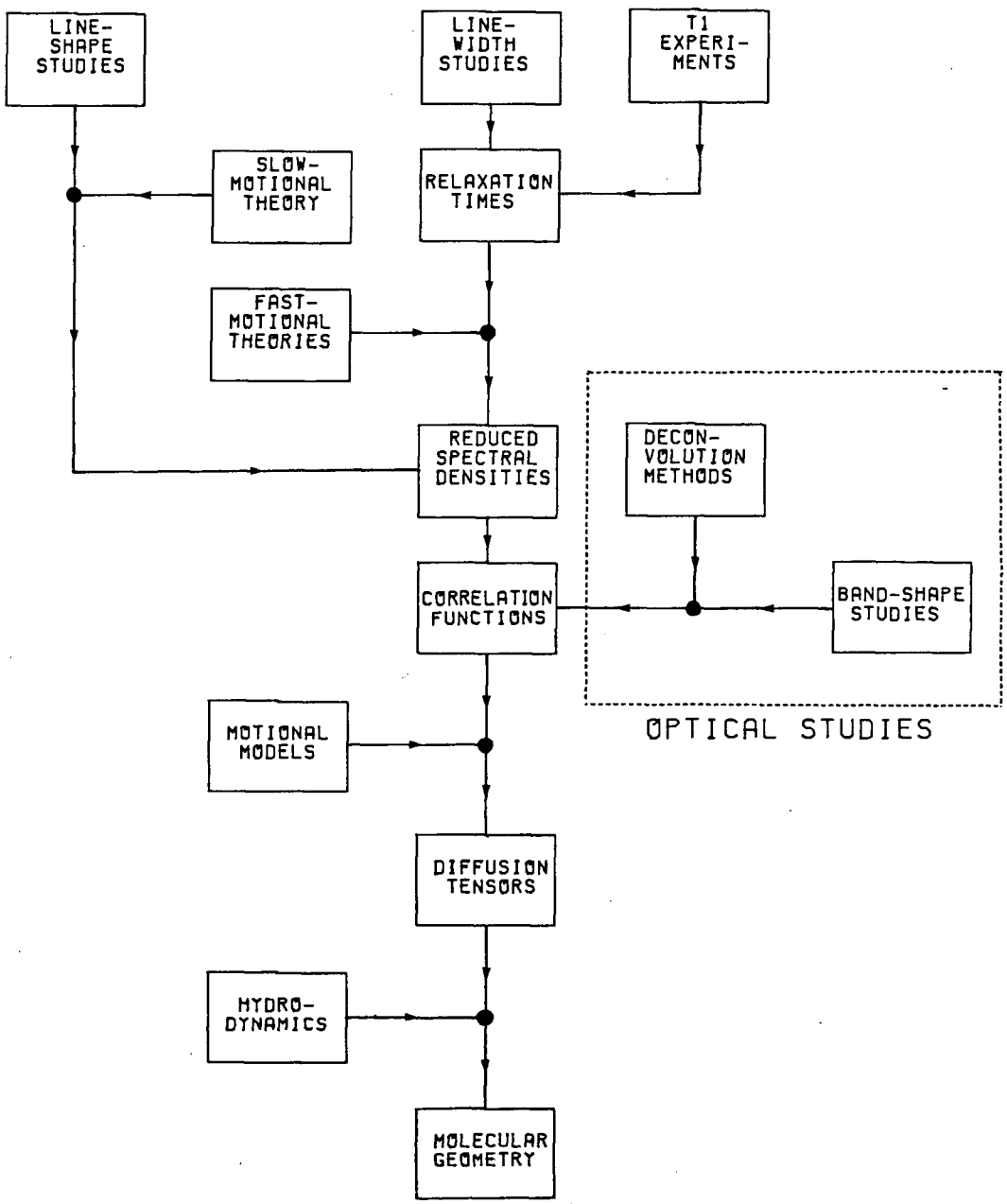

Figure 9.1. The general strategy for obtaining geometric information from motional studies by magnetic resonance.

9.2 CHOICE OF SPIN PROBE

The objective of this thesis is to exploit the flexible chemistry of the dithiocarbamate class of spin-probe and to combine NMR and ESR studies and measure the diffusion tensor for the probes in solution. The original choice of probe is historical, but it is appropriate to discuss the advantages of this probe over other classes of spin probe.

Firstly, it should be pointed out that the purpose of the exercise is to study the motion of the spin-probe in solution. This is entirely different from studying the motion of the solvent, or from the concept of spin-labelling, whereby a spin-probe is attached to a macromolecule and the motion of the macromolecule is deduced from the spectra of the spin-label. In the latter case perturbation is important (distortion of the local structure or the local motion by the spin-probe itself); the probe must be small and the results interpreted carefully as artefacts can occur. In our case perturbation is irrelevant as long as one interprets the data in terms of the nature of the probe and its interaction with the solvent and does not try to generalise the conclusions to the overall structure and motion of the solvent.

The nitroxide type spin-probes are relatively small and fairly stable. Their small size minimises perturbation problems and they have been extensively used for biological spin-probe and spin-labelling studies. However, for 'pure'

motional studies they have a number of problems: They have a large unresolved hyperfine coupling contribution to the line-width (which may be overcome by deuteration, but this is generally very tedious to do); they do not have simple geometries, by virtue of the protecting groups; the line-widths have a relatively large spin rotation contribution, this can make extraction of the correlation times unreliable; the hyperfine anisotropy is small so that the m_I dependence of the line-width is small (see Eqn.20.2), this also decreases the reliability of the determined correlation times; they have a three line spectrum so that the diffusion tensor cannot be determined (at least four lines are needed, three to get the tensor and one for the spin-rotation term); and finally there are no readily available diamagnetic analogs, thus NMR studies cannot be used to provide more information.

Many of the problems associated with the nitroxide spin-probes can be overcome by the use of metal complexes. This approach was pioneered by Kivelson *et al* who used copper acetyl-acetonate complexes *(60)(61)(62)(63)*. Unfortunately these complexes have very large g anisotropies so analysis is complicated by the spin-rotation term, as with nitroxides, and also by line overlap. Also the chemistry of these complexes is inflexible, *e.g.* it is difficult to change their geometry in a systematic manner. However, these compounds are part of a large class of ML_4 complexes, where L = O *(64)*, N *(65)(66)*, S *(67)(68)(69)(70)*,

Se *(71)* and various combinations thereof *(72)(73)*. Oxygen based ligands give complexes with large g-anisotropies *(74)*, P, N and Se based ligands all give (undesirable) hyperfine splittings. MS_4 type compounds have neither of these problems and all have similar spin Hamiltonian parameters. (*i.e.*, axially symmetric tensors with $A_0 \simeq 80G$ and $g_0 \simeq 2.04$). Of this class of compounds, the dithiocarbamates are the easiest to prepare in a wide range of substitutions, isotopic and otherwise. They are also well characterised *(44)(69)(70)(75)(76)(77)(78)(79)(80)(81)* and generally very stable. ESR motional studies with these complexes was pioneered by Herring *et al.* *(82)(83)(84)*.[26] Preparation is *via* secondary amines (see Sect.11) which are readily available with various isotopic substitutions. The ligands also form complexes with a wide range of metals so that multinuclear NMR of the diamagnetic complexes is possible with these compounds. Dithiocarbamates have been used to study biological systems *(86)*. Also, attempts have been made to synthesise water soluble derivatives for biological studies *(74)*.

---

[26] Gibson *(85)* was the first to do motional studies of a dithiocarbamate, but he used mixed copper isotopes for his investigation. His work is of historical interest only.

9.3 CHOICE OF PROBE SUBSTITUENTS

The general formula for a metal (II) dithiocarbamate is

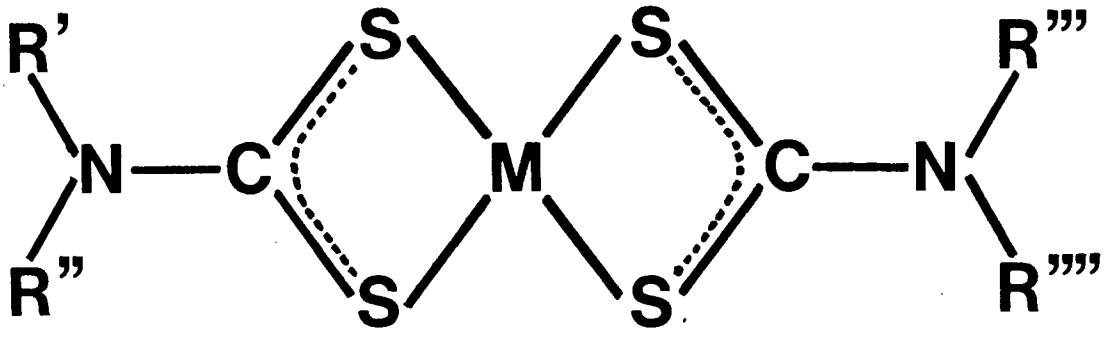

Figure 9.2. Typical metal dithiocarbamate.

R', R'', R''', R'''' are not necessarily, but usually are, the same. The R', R'' and R''', R'''' pairs may constitute a cyclic group. (Abbreviations for the R substituents and general nomenclature are given in appendix 22.1). These substituents may be readily changed to give a wide range of molecular geometries.

The requirements for the choice of R are; the compound must be reasonably soluble (for the NMR studies), the complex should be rigid with a well defined geometry (to eliminate relaxation contributions from internal motion and to simplify the use of hydrodynamic models), the complex should be stable[27] and for deuterium NMR studies, the alkyl moiety has to be substituted such that at least two C-D bonds lie out of the MS_4 plane and these bonds should not be

---

[27] The pyrrole derivative has a very desirable geometry, however it is unstable *(87)*. Generally though dithiocarbamates complexes are extremely stable and are extensively used in analytical chemistry *(79)*.

related by symmetry (see Sect.20.6).

In general, small or rigid substituents give derivatives that have low solubilities (see Table 11.2). The methyl derivative is good for ESR studies *(82)* (it is readily deuterated and has a simple geometry), but is too insoluble for NMR studies. The pyrollidine derivative was somewhat better for NMR studies, but ^{13}C work requires a compromise and the relatively soluble ethyl derivative was used. This derivative has a poorly defined structure (in solution, as do the most of the other derivatives in Table 11.2), but molecular models indicate that the motion of the ethyl groups is probably very small due to steric hindrance. Also it is known from previous ESR studies *(88)(84)* that the ethyl and pyrollidine derivatives behave similarly.

9.4 CHOICE OF CENTRAL METAL

As we wish to maintain simple geometries to assist the analysis of the data, the central metal should be chosen such the complex is square planar. This restricts our choice to divalent metals. For ESR, the complex must be paramagnetic, for NMR, diamagnetic. Clearly two different metals are needed, but the resulting complexes must be isostructural.

9.4.1 CENTRAL METAL FOR ESR EXPERIMENTS

The central metal should have a nuclear spin > 1 (to solve for three diffusion constants and a spin

rotation term requires that we must have at least four observable lines). The two most suitable candidates are copper and vanadium. Unfortunately the vanadium complexes oxidise readily to V=O type complexes *(74)*, which are not very soluble. Also the geometric simplicity is destroyed. The copper complexes are very stable and well characterised. Copper has two isotopes, ^{63}Cu and ^{65}Cu. The ^{63}Cu was used for historical reasons.

9.4.2 CENTRAL METAL FOR NMR EXPERIMENTS

A metal with a zero nuclear spin is useful, but not necessary. Obvious candidates are Ni, Zn and Pd. The zinc complexes are distorted tetrahedral and are thus not isostructural with the copper complexes *(89)* and were not used. Palladium is interesting because it has a non-zero spin and can be studied directly by NMR. Unfortunately its gyromagnetic ratio is too small to exploit with the available spectrometers ($\omega_0 \simeq 10$MHz at 4.7T). The nickel complexes are isomorphous with the copper complexes, have zero spin and thus were used. However, they are much less soluble than the corresponding copper complexes (as are the palladium complexes) and this somewhat limits the usefulness of these complexes for NMR studies.

10. GENERAL THEORY

Motional relaxation theory for magnetic resonance is dominated by three theories; Redfield theory *(90)(91)(92)*, Kubo-Tomita theory as developed by Kivelson *(93)*, and the stochastic Liouville theory as exploited by Freed *(39)*. Kubo-Tomita theory has a relatively easy physical interpretation, but its popularity has waned due to the unwarranted controversy surrounding its ability to handle degenerate transitions *(94)*. Stochastic Liouville theory is probably the definitive relaxation theory and can handle the slow-motion case. However, it is based on a slowly converging series, for which it is difficult to assign physical meaning. Also the computer time required for these calculations is not justified for the simple relaxation cases. Redfield theory is based on a rapidly converging series (for short correlation times) with a simple physical interpretation[28] and is well suited for describing NMR relaxation. It can be readily adapted for ESR studies if first order wavefunctions are used where necessary, but cannot be used in the slow-motional regime.

The principal problem with all relaxation theories is the evaluation of the correlation function for molecular motion. Several approaches have been made to this problem *(50)(96)*, but all these theories converge to the Debye diffusion case in the fast motional limit. Also the theory of anisotropic motion has only been developed for the Debye

---

[28] An expansion to, and physical interpretation of, higher order terms is given by Sillescu and Kivelson *(95)*

diffusion. For that reason only Debye diffusion and its extensions will be discussed in this work. Reviews of the other approaches are given by Steele *(96)* and McClung *(50)*.

10.1 INTRODUCTION TO REDFIELD THEORY

Redfield relaxation theory for nuclear magnetic resonance is dealt with in a number of texts *(91)(97)*. Redfield theory for ESR can be found in papers by Freed and Fraenkel *(90)* and Freed *(98)*.

Generally magnetic field inhomogeneity makes very little contribution to the linewidths of ESR spectra and hence it is possible to accurately measure T_2's from the spectral linewidths. This however, is not so for NMR, where field inhomogeneity is the principal source of line broadening. In this case T_1's are measured. The development of Redfield theory for T_1's and T_2's is the same and a brief outline is given below. However ESR and NMR differ sufficiently in detail to merit separate discussions. (Sect.12 and Sect.16).

An element of the relaxation matrix (R) for a state, $|a\rangle$, is given by *(91)*[29]

---

[29] Freed *(98)* drops the factor of 2 in this equation. It arises from the definition used for the spectral densities, where a factor of a half is often introduced.

$$-R^{(r)}_{aa'\beta\beta'} =$$

$$\left[2J_{aa\beta'\beta'}(\omega_{\beta'\beta'}) - J_{a'a\beta\beta'}(\omega_{\beta\beta'}) - J_{a'a\beta'\beta}(\omega_{\beta'\beta}) - J_{aa'\beta\beta'}(\omega_{\beta\beta'}) - J_{aa\beta\beta}(\omega_{\beta\beta})\right]^{(r)} \quad (10.1)$$

where the primes denote the corresponding upper spin states, β represents any other spin state in the system (its choice will depend on the relaxation rate required) and γ represents all other spin states in the system (*e.g.* from hyperfine splittings) and takes into account the fact that the relaxation pathways are not necessarily the reverse of the excitation pathway (the leading term). The spectral densities for each transition frequency, ω, are given as follows. (Some authors introduce a factor of 1/2 here as it simplifies the spectral densities in the case of isotropic diffusion):

$$J_{aa'\beta\beta'} = \mathbf{F}\{G_{aa'\beta\beta'}\} \quad (10.2)$$

where $\mathbf{F}\{X\}$ denotes the Fourier transform.

$$\mathbf{F}\{G(t)\} = \int_{-\infty}^{\infty} G(t)e^{-i\omega t}dt \quad (10.3)$$

The correlation function G(t) is

$$G_{\alpha\alpha',\beta\beta'} = \langle \hat{H}_1(t)_{\alpha\alpha'}, \hat{H}_1^*(t+\tau)_{\beta\beta'} \rangle \qquad (10.4)$$

where H_1 is the perturbing Hamiltonian. The angle brackets denote an ensemble average. Dropping $\alpha\alpha'$ and $\beta\beta'$ for convenience, the time dependent perturbation is given by,

$$\hat{H}_1(t) = \sum_{\lambda} \hat{H}_1^{(\lambda)}(t) + \epsilon(t) \qquad (10.5)$$

The λ is used to label the different type of interaction Hamiltonian; hyperfine coupling, spin-rotation, quadrupole coupling *etc.* The parameter $\epsilon(t)$ is the r.f. field used for detection. In pulsed NMR this is zero during observation. In ESR this term may be dropped as it oscillates on a time scale much faster than T_2 and therefore does not contribute to the relaxation *(82)*.

The Hamiltonian terms are themselves combinations of spin operators (**A**) and magnetic interaction tensors ($\underset{\sim}{\mathbf{F}}$) so

$$\hat{H}_1^{(\lambda)}(t) = \sum_{i,j} \mathbf{A}_{ij}^{(\lambda)} \mathbf{F}_{ij}^{(\lambda)}(t) \qquad (10.6)$$

It is more convenient to define the tensors in a spherical basis *(90)(99)(100)(101)* so that

$$\sum_{i,j} \mathbf{A}_{ij}\mathbf{F}_{ij}(t) = \sum_{m} (-1)^{m}\mathbf{A}^{(l,m)}\mathbf{F}^{(l,-m)}(t) \qquad (10.7)$$

where l is the rank of the tensor and m=$-l$ -> $+l$

Here we have defined the spin operators in the laboratory frame and the magnetic tensors in the molecular frame.[30] The latter thus carries the time dependence for molecular rotation. The magnetic interaction tensor is transformed into the laboratory frame with the assumption that the molecular and magnetic interaction tensors are coincident. This is readily done with Wigner rotation matrices *(99)(103)(104)*.

$$\mathbf{F}^{(l,m)}_{\text{lab.}}(t) = \sum_{q} \mathbf{D}^{(l)*}_{mq}(\alpha\beta\gamma)\mathbf{F}^{(l,-q)}_{\text{molec.}}(t) \qquad (10.8)$$

where α,β,γ are the Euler angles relating the molecular frame component q with the laboratory frame component m. The Euler angles carry the time dependence of the rotation. For magnetic resonance we only have scalar and tensor (l=0 and 2 respectively) interactions. As scalar interactions are

---

[30] The choice of transforming the operators in to the molecular frame or transforming the magnetic interaction tensors in to the laboratory (observers) frame is arbitrary. As the eigenvalues of quantum mechanical operators are by definition observables, it is philosophically more satisfactory to leave the operators in the laboratory frame. Also there is a choice in the definition of Eqn.10.7 *(102)*, the main consequence of this is whether the $(-1)^m$ term in Eqn.10.7 is a coefficient of **A** or **F**.

rotationally invariant they do not contribute to the relaxation. So, dropping the l (implicitly setting it to 2), we get from (Eqn.10.4-Eqn.10.8)

$$G_{aa',\beta\beta'}(t)=\sum_{\nu\mu}\sum_{mm'q'}A^{(m)}_{\nu}{}_{aa'}A^{(-m')*}_{\mu}{}_{\beta\beta'}<D^{*}_{mq}(t)D_{m'q'}(t+\tau)>F^{(-q)}_{\nu}F^{(q')}_{\mu} \quad (10.9)$$

where ν and μ denote the different type of interactions (previously defined as λ) and

$$A^{(m)}_{\mu}{}_{aa'} = <a|A^{(m)}_{\mu}|a'>. \quad (10.10)$$

Spherical tensors obey the following symmetry relations

$$A^{(l,m)*} = (-1)^{m}A^{(l,-m)} \quad (10.11)$$

also $<a|A|a'>^{*} = <a'|A^{*}|a>$ as A is Hermitian hence

$$A^{(m)*}_{\nu}{}_{aa'} = (-1)^{m}A^{(-m)}_{\nu}{}_{a'a} \quad (10.12)$$

and similarly for F and the $\beta\beta'$ terms so Eqn.10.9 becomes

$$G_{aa',\beta\beta'}(t) = \sum_{mq} A^{(m)}_{\nu\,aa'} A^{(-m)}_{\mu\,\beta',\beta} \langle D^{*}_{mq}(t) D_{mq}(t+\tau)\rangle F^{(q)}_{\nu} F^{(-q)}_{\mu} \quad (10.13)$$

the m' and q' terms disappear because of the orthogonality relations of the Wigner rotation matrices *(99)(104)*. Note that the $\beta\beta'$ subscript reverses because of Eqn.10.12

It is convenient to define a reduced correlation function, g_{mq}

$$g_{mq} = \langle D^{*}_{mq}(t) D_{mq}(t+\tau)\rangle \quad (10.14)$$

and also a reduced spectral density (as this is the only time dependent term), j_{mq}

$$j_{mq}(\omega) = \mathbf{F}\{g_{mq}(t)\} \quad (10.15)$$

where $\mathbf{F}\{x\}$ is the Fourier transform as defined before (Eqn.1.8).

Finally we get

$$J_{aa',\beta\beta'}(\omega) = \sum_{\nu,\mu} \sum_{m,q} A^{(m)}_{\nu\,aa'} A^{(-m)}_{\mu\,\beta',\beta} j_{mq}(\omega) F^{(-q)}_{\nu} F^{(q)}_{\mu} \quad (10.16)$$

and hence from Eqn.10.1, $R_{aa',\beta\beta'}$.

Explicit expressions for the magnetic interaction tensors (**F**) and the spin operators (**A**) are given in *(90)(105)* and appendix 22.6. Expansion of Eqn.10.16 for the ESR case is discussed further in Sect.12.3.

The evaluation of the correlation function (Eqn.10.14) remains one of the most challenging aspects of molecular dynamics. The basic goal of molecular dynamics studies by magnetic resonance is to deduce $g(\omega)$ from $j(\omega)$, which, in principle can be obtained for relaxation time measurements.

10.2 ON SPECTRAL DENSITIES

Reduced spectral densities are extremely useful quantities to measure as they are independent of the motional model used. This greatly facilitates comparisons between results from different experimental methods. Unfortunately there are often more spectral densities than independent variables. Also it is usual to assign some physical meaning to the results and so a diffusion model is assumed and correlation times calculated instead. This generally hampers comparisons of different studies and techniques.

Reviews of the various rotational diffusion models can be found in *(50)(96)*. Useful discussions can also be found in *(106)*. Three facts emerge from these reviews; the Debye diffusion model and its extensions are the most successful model; in the limit of fast motion or isotropic motion all models reduce to the Debye model; and currently only the Debye model is developed for the case of anisotropic motion.

For these reasons the Debye model is the most widely used rotational diffusion theory.

The Debye model is, briefly, as follows. The molecule is considered to undergo a random small step angular rotation (rotational Brownian motion) about three independent axes (usually, but not necessarily the molecular axes). The rates of rotation are characterised by three diffusion constants R_x, R_y and R_z, the principal elements of the rotational diffusion tensor, $\underset{\sim}{R}$. This diffusion tensor is considered to be independent (*i.e.*, not coupled to) the translational diffusion tensor. The problem is to relate these diffusion constants to the reduced spectral densities, $j(\omega)$. For isotropic Debye diffusion (the most commonly used model for NMR), $j(\omega)$ is given by

$$j(\omega) = \frac{\tau_c}{1+(\omega\tau_c)^2} \qquad (10.17)$$

where τ_c is known as the correlation time and $\tau_c = 1/6R$, where R is the isotropic diffusion constant. In this case $j(\omega)$ is referred to as the Debye spectral density, not to be confused with the spectral density, $J(\omega)$.

For anisotropic motion we get for $j(\omega)$ *(98)(107)*

$$j_{ij}(\omega) = {}_{i,k}\Sigma \frac{C_{lk}\tau_{lk}}{1+(\omega\tau_{lk})^2} = \lambda_{ij}(\omega) \qquad (10.18)$$

where C_{lk} are a combination of the rotational diffusion constants and the τ's are the eigenvalues for the asymmetric rotor which are combinations of the rotational diffusion constants. Explicit expansion of the reduced spectral densities[31] will be given in the appropriate section.

Generally we calculate the λ terms directly or by a least squares fit of the relaxation times. The reduced spectral densities can be then inverted using Newton-Raphson methods to give the diffusion tensor.

10.3 CHOICE OF THE AXIS SYSTEM

An essential part of Redfield theory and Debye diffusion theory is tensors. As the tensors are not necessarily diagonal in the same frame it is convenient to introduce a reference frame or axis system; a frame in which at least one of the tensors is diagonal.

Assignment of the axis system is confused by the choice of a number of reference frames. In our case there are five

---

[31] There is some confusion of nomenclature in the literature as 'spectral density' is often synonymous with 'Debye spectral density'. Here 'spectral density' will refer to $J(\omega)$ as defined by Eqn.10.2, $j(\omega)$ is the 'reduced spectral density' as defined by Eqn.10.15. The term 'Debye spectral density' will refer to the reduced spectral density for the case of isotropic diffusion. For anisotropic Debye diffusion the reduced spectral density will be denoted by λ (following Freeds notation).

possible choices; the laboratory frame, the molecular frame, the magnetic frame, the diffusion frame and the inertial frame. We are not interested in inertial models so the inertial frame is not used.[32] The laboratory frame would give a time dependent diffusion tensor so this is not used. We are trying to measure the diffusion tensor, thus this is not a good choice for a reference frame. However, we do assume the diffusion frame is coincident with the molecular frame. There are several magnetic frames ($\underset{\sim}{g}$, $\underset{\sim}{A}$, quadrupole and chemical shift tensors). In our system the **g** and **A** tensors are coincident with each other and with the molecular frame. As the choice of molecular frame is somewhat arbitrary (because of the high degree of symmetry) it is convenient to define the axes of the molecular frame using the g and A tensors (which by convention are defined such that $|A_{zz}|>|A_{xx}|>|A_{yy}|$ in a right-handed coordinate system). The axis system is thus

---

[32] The inertial frame is of relevance to the spin-rotation contribution to relaxation. However this contribution is determined empirically and it is difficult to extract inertial information from it. Also the inertia tensor is axially symmetric ($I_y=I_z\neq I_x$. So that choice of axes in this frame would be essentially arbitrary.

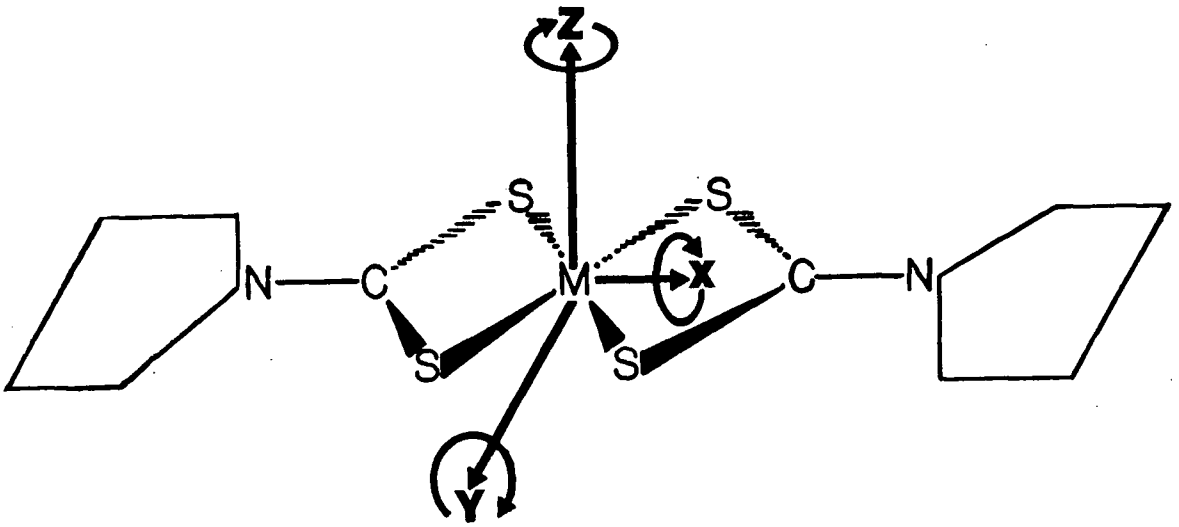

Figure 10.1. Axis system for tensors. Note that this figure is drawn in the left-handed coordinate system for convenience. Y is -Y in the right-handed coordinate system.

i.e., the x axis is parallel to the C-N bond, the y axis is in the MS_4 plane and perpendicular to the C-N bond and the z axis is perpendicular to the MS_4 plane. This frame will be used to define the Euler angles for all other tensors, notably the chemical shift tensor and the quadrupole tensor.

A simplistic interpretation of rotational diffusion of the dithiocarbamates would give a diffusion tensor coincident to the reference frame, but with $R_{xx}>R_{yy}\simeq R_{zz}$. R_{xx} *etc.* are the principal elements of the diffusion tensor $\underset{\sim}{R}$,[33] where R_{xx} is the rotational diffusion constant for rotation about the x axis *etc.* This is important to note as

---

[33] **R**, rather than **D**, is used here. **D** being reserved for the translational diffusion tensor. Some texts use **D** to denote both translation and rotational diffusion tensors. Futhermore this **R** should not be confused with the relaxation matrix, which is usually subscripted.

some theoretical derivations assume *a priori* that the molecular and diffusion frames are coincident (*i.e.*, $R_{zz}>R_{xx}>R_{yy}$) and do not allow such promiscuous assignment of the reference frame.

10.4 HYDRODYNAMIC MODELS FOR ROTATIONAL DIFFUSION

According to the hydrodynamic model the rotational diffusion constant about a given axis 'i' is given by *(106)*

$$R_i^{-1} = \frac{L_i \eta}{kT} \tag{10.19}$$

where L_i is the torque about the 'i'th axis and is given by

$$L_i = \lambda_i f(V) \tag{10.20}$$

where λ_i is the friction coefficient and f(V) is a function of molecular geometry. For a sphere, f(V) is proportional to its volume, for an ellipsoid (or other shapes) the relationship is more complex. The important point though is to note that the diffusion tensor is directly related to the molecular geometry.

The torques are calculated by solving the Stokes-Navier equation for the appropriate geometry and boundary conditions. To date only ellipsoids have been considered, but solutions for more complex shapes are, in principle,

possible. Solutions for two types of boundary conditions have also been investigated; the 'slip' boundary condition and the 'stick' boundary condition. In the latter case the tangential velocity of the solvent molecules at the solvent-solute interface is assumed to be zero, *i.e.*, there is a solvation cage stuck to the solute (on the time scale of the rotation). This problem was solved in a classic paper by Perrin *(108)* and later repeated by Favro *(109)*. The 'slip' boundary condition just assumes that the solvent doesn't penetrate the solute, the frictional damping is due to the volume of solvent swept aside during rotation. This boundary condition requires a numerical solution and this was done by Hu and Zwanzig *(110)* and also Youngren and Acrivos *(111)*.

The stick model is fairly successful with ionic species and for translational diffusion.[34] Tables of friction coefficients for ellipsoids are given in *(110)(111)(106)*. Note that the tables differ slightly because of the way the molecular volume has been defined *(106)*. It is interesting to note that for extreme geometries (disks and needles) the slip and stick models give identical friction coefficients. Also rough spheres with slip boundary conditions give stick like results *(114)*.

---

[34] Ionic species have well defined solvation shells so the stick boundary conditions are reasonable*(112)*. The slip and stick solutions for translational diffusion differ only by a factor of two *(113)*; swept volume is the only important parameter in this case.

A discussion of other motional models is given in *(50)(96)*. These other models are more elegant in that they make realistic assumptions about the the solvent (hydrodynamic models assume the solvent is continuous at the molecular level). However, they are for spheres only and cannot be extended to other geometries. As such they are of little use.

11. GENERAL EXPERIMENTAL

The experimental methods can be divided into two types, acquisitive and preparative.

Data acquisition in ESR and NMR differ considerably and are discussed separately in the appropriate sections (Sect.12 and Sect.16).

Preparation of the spin-probes (transition metal dithiocarbamate complexes) and their solutions is almost identical for ESR and NMR and it is convenient to discuss it in one (this) chapter. Each spin-probe is isotopically substituted as appropriate. For the deuterium relaxation studies perdeuterated amines were used in the preparations. For the ^{13}C studies ^{13}C enriched carbon disulphide was used. For ESR studies ^{63}Cu was used as the central metal.

11.1 PREPARATION OF SODIUM DITHIOCARBAMATES AND CARBODITHIOATES

All compounds were prepared by the standard procedure of mixing stoichiometric quantities of carbon disulphide, sodium hydroxide and the appropriate secondary amine *(69)(115)*.

$$CS_2 + KOH + R_2NH \rightarrow R_2NCS_2^- + K^+ + H_2O$$

The dithiocarbamate derivative is formed preferentially to the xanthate. Details are given below.

The secondary amine (0.1mmol) was dissolved in alcoholic sodium hydroxide (100ml of 0.1M). Carbon disulphide (0.1M) in ethanol (≃50ml) was then added dropwise over a period of 30 min. to the stirred mixture. (*n.b.* the order of addition is critical as both KOH and the amine react with CS_2 irreversibly to form a xanthate and the amino double salt *(115)* respectively).

The resultant mixture was purified by recrystallisation from hot ethanol or by precipitation from a cold saturated solution with ether. (The potassium salts were more soluble than the corresponding sodium salts and hence were more difficult to purify in high yields). Yields were reasonably high (≃70%) in all cases. The final products were stored under nitrogen in the dark at ≃-20°C to minimise decomposition.

All per-deuterated salts were checked for residual hydrogen by NMR (none was detected). Purity of the salts was checked *via* analysis of the copper or nickel salts (see below Table 11.1 below) as these compounds are the desired end product.

The following potassium dithiocarbamates were made. (Others are described in previous work *(88)*). Listing is by parent amine.

dimethylamine*

^{15}N dimethylamine

d_3-dimethylamine

diethylamine*

pyrollidine*

d_9-pyrollidine

All compounds were prepared with and without ^{13}C substitution at the CS_2 group. The compounds are annotated with an asterisk are commercially available, but were prepared for use for microanalysis.

All starting materials are commercially available (Aldrich and Merck, Sharpe and Dohme).

11.2 TRANSITION METAL DITHIOCARBAMATES

These are simply prepared by mixing aqueous solutions of the appropriate transition metal salts and the potassium dithiocarbamate. Further details are given in Sect.13. The copper salts were prepared for all the non-isotopically[35] substituted dithiocarbamate ligands and submitted for microanalysis. (see Table 11.1)

---

[35]Deuterium analysis is not routinely available. ^{15}N and ^{13}C are not resolvable using microanalysis so their use for analysis is an expensive waste.

COMPOUND	C	H	N
CuPydtc	33.98(33.78)	4.44(4.45)	7.87(7.88)
$CuEt_2dtc$	33.17(33.36)	5.60(5.60)	7.80(7.79)
d_9-NiPydtc	32.36(32.70)	-	7.47(7.63)
NiPydtc	34.20(34.20)	4.59(4.59)	8.03(7.98)

Table 11.1. Microanalyses for Dithiocarbamates. ( ) denotes calculated value. Other numbers are the analysis. The analyses were performed by P.Borda of the UBC Chem. Dept.

11.3 PREPARATION OF SOLUTIONS

Toluene was used in previous studies *(116)*, but the nickel derivatives are not soluble enough in this solvent to permit NMR relaxation studies. Other solvents were investigated (see Table 11.2) and chloroform was found to be the best compromise. Accurate viscosity data are available for chloroform *(117)*. Previous studies *(43)(42)(88)* indicate that the relatively low boiling point (70 °C) is not too restrictive.

Unfortunately chloroform reacts with metal dithiocarbamates in the presence of water *(118)* and it is essential that the solvent is dry.

All samples were sealed under vacuum after freeze-pump-thaw cycles to remove dissolved oxygen. Thermal degradation products (from sealing the tubes) initiate decomposition of the pyrollidine dithiocarbamate solutions

and great care has to be taken when sealing the samples.

Chloroform possibly weakly coordinates to the copper explaining the greater solubility of the copper complexes. Alternatively there maybe an intermolecular Ni-S coordination in the solid leading to increased lattice energy and lower solubility, but crystallographic evidence suggests otherwise *(119)*. Bulky alkyl groups interfere with the crystal packing (the dioctyl derivative is a thick oil at room temp.) thus increasing the solubility.

SOLVENT	COMPLEX	SOLUBILITY mg/ml
Dichloromethane	NiPydtc	0.9
Dichloroethane	"	0.4
Trichloroethane	"	1.1
Carbon Tetrachloride	"	<0.1
Trichloroethylene	"	<0.1
Nitrobenzene	"	high, but complexes
Nitromethane	"	<0.1
Acetone	"	≃0.1
Toluene	"	≃0.2
Benzene	"	≃0.2
Tetrahydrofuran	"	≃0.2
Ethanol	"	≃0.1
Methanol	"	≃0.1
Cyclohexane	"	≃0.2
Pentane	"	≃0
Chloroform	"	1.5
"	$NiEt_2dtc$	≃37
"	NiHxmdtc	≃30
"	NiMpdtc	<0.1
"	$NiMe_2dtc$	≃2
"	$CuEt_2dtc$	≃50
"	$CuMe_2dtc$	≃20
"	CuPydtc	≃40
"	$CuOc_2dtc$	∞
"	$PdEt_2dtc$	≃30

Table 11.2. Solubilities of metal *dtc*'s.

PART 3.

ELECTRON SPIN RESONANCE STUDIES

12. ESR THEORY

There are a number of approaches to ESR relaxation theory; Kubo-Tomita theory *(93)*; stochastic Liouville theory *(39)*; Redfield theory *(90)(91)(92)*.[36] Stochastic Liouville theory is the most rigorous approach and can be extended into the slow motional regime (see appendix 22.9). Kubo-Tomita theory has the advantage of being fairly straight-forward with an easy physical interpretation for most of the terms. Redfield theory also has a simple physical interpretation, but has been developed mainly in the context of NMR (*i.e.*, with zero order wave-functions). Here we develop Redfield theory for the ESR case with first order wavefunctions, which surprisingly has not been discussed before.

The Brownian rotational diffusion model and the spin-rotation contribution to relaxation are also discussed briefly.

12.1 THE ISOTROPIC ESR SPECTRUM

The spin Hamiltonian, $\hat{\mathbf{H}}$, for an unpaired electron interacting with a single nucleus is *(121)*

$$\hat{\mathbf{H}} = \beta \underline{\mathbf{B}} . \underset{\sim}{\mathbf{g}} . \hat{\underline{\mathbf{S}}} - \beta_n . \underline{\mathbf{B}} . \underset{\sim}{\mathbf{g}}_n . \hat{\underline{\mathbf{I}}} + \hat{\underline{\mathbf{S}}} . \underset{\sim}{\mathbf{A}} . \hat{\underline{\mathbf{I}}} \qquad (12.1)$$

where $\underline{\mathbf{B}}$ is a static magnetic field, $\underset{\sim}{\mathbf{g}}$ is the g tensor, $\underset{\sim}{\mathbf{g}}_n$ is

---

[36] For a useful, but dated reveiw see *(120)*.

the chemical shift tensor, $\underset{\sim}{A}$ is the hyperfine coupling tensor, β is the Bohr magneton, β_n is the nuclear magneton and $\hat{\underline{I}}$ and $\hat{\underline{S}}$ are the electron and nuclear spin vector operators respectively.

If we define $\underline{B}$ to be along the z axis, *i.e.*, $\underline{B}=B_z\underline{k}$, then for isotropic motion tensors in Eqn.12.1 average out so it reduces to *(121)*

$$\hat{H} = g_o\beta B_z\hat{S}_z - g_n\beta_n B_z\hat{I}_z + A_o\hat{I}_z\hat{S}_z + \frac{A_o}{2}\left[\hat{S}_+\hat{I}_- + \hat{S}_-\hat{I}_+\right] \qquad (12.2)$$

where g_o, g_n and A_o are the traces of the corresponding tensors. The remaining terms have their usual meanings *(122)*. The nuclear Zeeman term is small compared with the other terms (Sect.14.3) and can be neglected.

The final term of Eqn.12.2 is also small, but non-negligible and is conveniently treated by perturbation theory. *i.e.*, $\hat{H} = \hat{H}_o + \hat{H}'$

where $$\hat{H}' = \frac{A_o}{2}\left[\hat{S}_+\hat{I}_- + \hat{S}_-\hat{I}_+\right]$$

and $$\hat{H}_o = g_o\beta B_z\hat{S}_z + A_o\hat{I}_z\hat{S}_z \qquad (12.3)$$

The second order energies are given by *(123)*

$$E_m = E_m^0 + \langle n|\hat{H}'|n\rangle + \sum_{n\neq m} \frac{\langle n|\hat{H}'|m\rangle\langle m|\hat{H}'|n\rangle}{E_n - E_m} \qquad (12.4)$$

$$E_{m_i m_s} = g_0\beta B_0 m_s + A_0 m_i m_s + \frac{A_0^2}{4g_0\beta B_0}\left[\frac{I(I+1)-m_i}{g_0\beta B_0 m_s} + \frac{(m_i \pm 1)}{A_0 m_i m_s}\right] \qquad (12.5)$$

where the sign in the second order term is the same as the sign of m_s and $|n\rangle$ and $|m\rangle$ are arbitrary basis elements of the system; $|m_s, m_i\rangle$. m_s is the electron spin quantum number projected onto the z axis and m_i is the corresponding projection for the nuclear spin quantum number.

The transition frequency, ω_0, between $|m\rangle$ and $|n\rangle$ (to second order) is readily obtained from Eqn.12.5. (The selection rules are $\Delta m_s = 1$ and $\Delta m_i = 0$).

$$\omega_{mn} = \frac{\Delta E}{h}mn = g_0\beta B_0 + A_0 m_i + \frac{A_0^2}{2g_0\beta B_0}\left[I(I+1) - m_i^2\right] \qquad (12.6)$$

where I is the nuclear spin quantum number.

For ^{63}Cu (and ^{65}Cu) I=3/2 and A_0 is negative thus we will see four lines with the $m_i = -3/2$ at low field. Each line will be shifted from its zero order position by $\simeq$1G at 9GHz. A typical spectrum is shown in Fig.12.1. (The spectrum parameters are given in the appendix 22.4). The variation of line-height (width) is due to molecular motion and is

discussed in the next section.

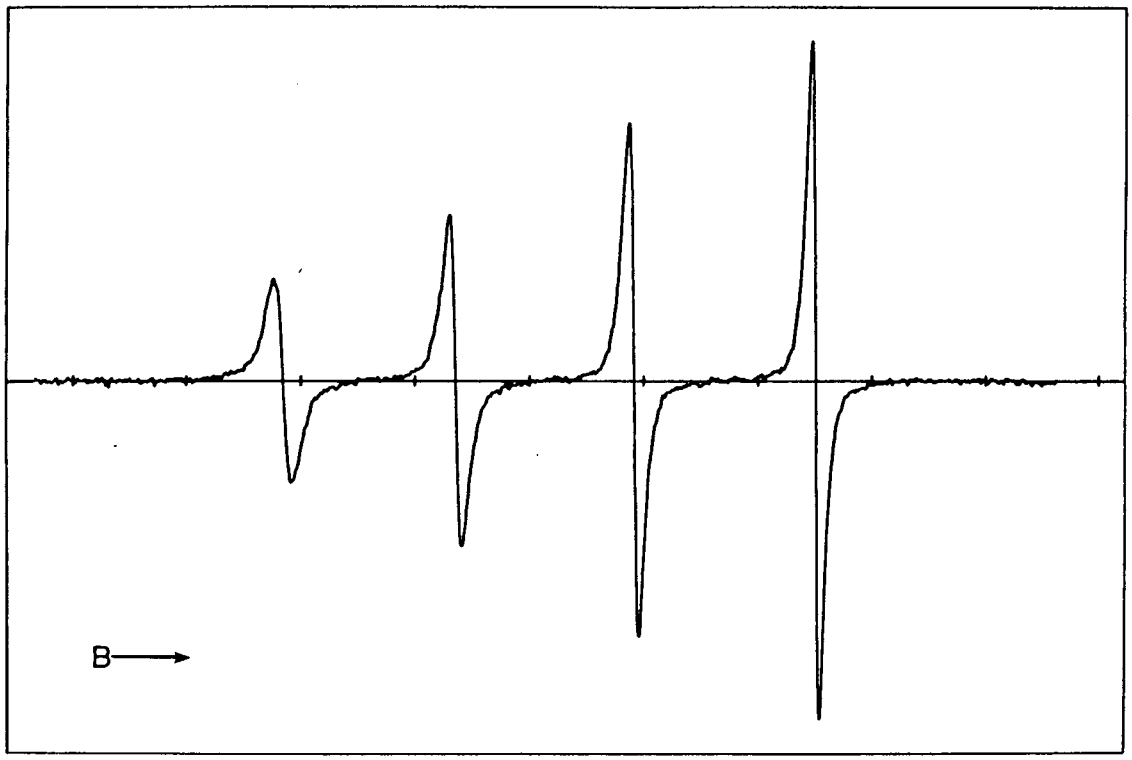

Figure 12.1. Typical metal dithiocarbamate spectrum. Calibration interval is 50G.

The first order wavefunctions are also readily obtained by perturbation theory.

$$|a_m\rangle = |m\rangle + \sum_{n \neq m} \frac{\langle n|\hat{H}'|m\rangle}{E_n - E_m}|n\rangle \qquad (12.7)$$

If we use $|a\rangle$ to denote the low energy first order wavefunction and $|a'\rangle$ the high energy wavefunction, then it is easy to show that

$$|a\rangle = |-\tfrac{1}{2}, m_i\rangle + p_m|+\tfrac{1}{2}, m_i - 1\rangle$$

$$|a'\rangle = |+\tfrac{1}{2}, m_i\rangle + q_m|-\tfrac{1}{2}, m_i + 1\rangle \qquad (12.8)$$

For convenience, the basis states, Eqn.12.8, will be denoted $|-m\rangle$ and $|+m\rangle$ respectively. Hence

$$|a\rangle = |-m\rangle + p_m|+m-1\rangle$$

$$|a'\rangle = |+m\rangle + q_m|-m+1\rangle \qquad (12.9)$$

where

$$p_m = \frac{-A_o}{2g\beta B_o}\Big[\, I(I+1) - m_i(m_i+1)\Big]^{\frac{1}{2}}$$

$$q_m = \frac{+A_o}{2g\beta B_o}\Big[\, I(I+1) - m_i(m_i-1)\Big]^{\frac{1}{2}} \qquad (12.10)$$

12.2 THE ESR PROBLEM: DEVELOPMENT OF THE REDFIELD EQUATION

Development of the Redfield theory for ESR differs from that for NMR in four major ways; a)T_2's are required, b)first order wavefunctions (*vide supra*) have to be used, c)the spectral densities cannot be simplified (Sect.14.2),

d)the first order corrections to the line-position are large so that $B_z \neq B_0$. These factors make the expansion of the Redfield equation extremely tedious (albeit straight-forward). Only the salient features will be presented here. The development follows that suggested by Park *(42)*. The results were cross-checked with the aid of a symbolic algebra reduction program *(124)*.

We make the phenomenological identification that the relaxation within a spin state is T_2 *(125) i.e.*,

$$-(1/T_2)_{m_i} = (R_{aa'\,aa'})^{(r)}_{m_i} \tag{12.11}$$

$$= \Big[2J_{aaa'\,a'}(\omega_{a'\,a}) - \sum_{\gamma} J_{a'_\gamma aaa'_\gamma}(\omega_{aa'_\gamma}) - \sum_{\gamma} J_{a'_\gamma aa'_\gamma a}(\omega_{a'_\gamma a}) - \sum_{\gamma} J_{aa'_\gamma aa'_\gamma}(\omega_{aa'_\gamma}) - \sum_{\gamma} J_{aa_\gamma aa_\gamma}(\omega_{aa_\gamma})\Big]^{(r)}_{m_i} \tag{12.12}$$

where γ labels the sum over the hyperfine states, m_i labels the line being measured and the superscript 'r' denotes the real part of the relaxation rate. (The imaginary part gives the (small[37]) frequency shifts *(97)(126)*). The spectral densities, $J(\omega)$, are expanded as given by Nordio *(99) i.e.*,

---

[37]These are of the order of the static second order correction to the line-positions and were not included in the analysis.

$$J_{aa',aa'} = \sum_{\nu,\mu} \sum_{m,q} \mathbf{A}^{(m)}_{\nu\,aa'} \mathbf{A}^{(-m)}_{\mu\,a',a} j_{mq}(\omega) \mathbf{F}^{(-q)}_{\nu} \mathbf{F}^{(q)}_{\mu} \qquad (12.13)$$

where **A**, **F** are given in appendix 22.6 and the reduced spectral density, $j(\omega)$, is given by Eqn.10.15. The transition frequencies are discussed below.

12.2.1 THE TRANSITION FREQUENCIES

The transition frequencies for the spectral densities are assigned by Fig.12.2 and shown in Table 12.1 The transition frequency depends on how the operators, **A**, couple the first order part of the wavefunctions. The second order part of the wavefunctions modify the transition probabilities at those frequencies. The terms of the relaxation equation are often categorised according to the transition frequency associated with the term *(90)*. Secular terms are those associated with the S_z and I_z operators, *i.e.*, zero frequency. The pseudo-secular terms are those attached to the nuclear transitions, ω_a, resulting from the $I_\pm$ and $S_zI_\pm$ operators. The non-secular terms, $\omega=\omega_0\pm\omega_a$, result from the $S_\pm I_\pm$ operators.

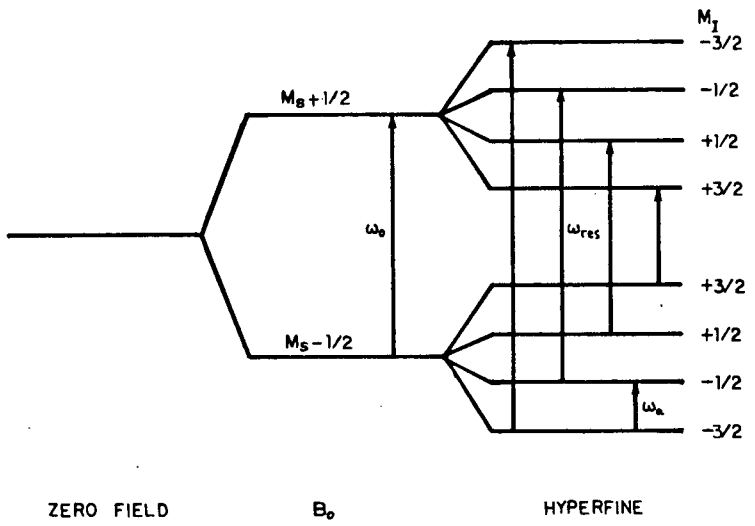

Figure 12.2. Transition diagram. Note that this diagram corresponds to a frequency-swept experiment. In the (usual) field-swept experiment a low energy transition corresponds to a higher resonance field.

Note that the signs of the m_i components can only be assigned to the spectrum if we know the sign of A_0. For *dtc*'s it is negative *(127)*.

STATE OPERATOR	*aa* and *a'a'* transitions	*aa'* and *a'a* transitions
$(A_a^{\pm 2})^2$	†	$\omega_{res} + \omega_a$
$(A_a^{\pm 1})^2$	ω_a	ω_{res}
$(A_a^0)^2$	0	$\omega_{res} - \omega_a$
$(A_g^0)^2$	0	†
$(A_g^{\pm 1})^2$	†	ω_{res}
$A_a^{\pm 1} A_g^{+1}$	†	ω_{res}
$A_a^0 A_g^0$	0	$\omega_{res} - \omega_a$

Table 12.1. Spectral density Frequencies. † denotes that the operators do not connect these states to first order. $\omega_a = A_0/2$; $\omega_{res} = \omega_0 + 2m_i \omega_a$

12.3 THE FINAL EQUATION

The interactions of interest here are the hyperfine coupling tensor (denoted F_a) and the g-tensor (denoted F_g) (The spin-rotation term also contributes, but is determined empirically, Sect.12.5). As both these tensors are axially symmetric (Sect.14.1) $q=0$ always, hence Eqn.12.12 and Eqn.12.13 become (for T_2)

$$R_{aa',aa'} =$$

$$\sum_m j_{\delta\delta}(\omega)\Big[F^0_a F^0_a A^{(m)}_{a_{aa'}} A^{(-m)}_{a_{a',a}} + F^0_g F^0_g A^{(m)}_{g_{aa'}} A^{(-m)}_{g_{a',a}}$$

$$+F^0_a F^0_g (A^{(m)}_{a_{aa'}} A^{(-m)}_{g_{a',a}} + A^{(m)}_{g_{aa'}} A^{(-m)}_{a_{a',a}})\Big] \qquad (12.14)$$

where $$A^{(m)}_{\mu_{aa'}} = \langle a|A^{(m)}_{\mu}|a'\rangle \quad etc. \qquad (12.15)$$

The wavefunctions are selected according to the subscripts of the spectral densities in Eqn.12.12. Care must be taken to keep track of the running variable λ. It should also be noted that the *a*'s are the first order wavefunctions (Eqn.12.9) in this case.

The operators and magnetic interaction tensor elements are given by *(90)* and are reproduced in appendix 22.6 for convenience. Note that B_z is one element of a vector operator ($B_x = B_y = 0$) and is not equal to the static field, B_0, because of the first order frequency shift.

The contribution of the individual matrix elements to each J is given in Table 12.2. The elements individual terms for Eqn.12.14 are given by the row denoted $A^{(m)}_a A^{(-m)}_g$, or as appropriate, and the column $J_{aa',aa'}$, *etc.*, again as required. (The subscript reversal arises from the Hermitian property, Eqn.10.12). The abbreviations are

$v = Cx^2$

$z = -Cy^2$

m = Nuclear spin quantum no. for line at B_z

B_z = Line-position in magnetic field units

$x^2 = [K-m(m+1)]$

$y^2 = [K-m(m-1)]$

$K = I(I+1)$

$C = \frac{A_0}{2g_0\beta B_z}$

$j_{oo}(a) = j(\omega_a)$

$j_{oo}(\omega \pm a) = j(\omega_{res} \pm \omega_a)$

For example, consider the evaluation of the contribution of operator elements ±2 for the hyperfine coupling contribution to the $J_{a'aa'a}$ term in Eqn.12.14 *i.e.*,

$$A^{(+2)}_{\nu_{aa'}} A^{(-2)}_{\mu_{a'a}} j_{oo} F_a^{(0)} F_a^{(0)} \qquad (12.16)$$

The spin Hamiltonian parameter, F_a^0, is known from experiment. The operator elements are non-secular, $\frac{1}{2}\hat{S}_{\pm}\hat{I}_{\pm}$, so that $\omega = \omega_{res} + \omega_a$. Hence the matrix element for the operator alone is

$$\frac{1}{4}\sum_{\gamma} \langle a'|\hat{S}_+\hat{I}_+|a_\gamma\rangle\langle a_\gamma|\hat{S}_-\hat{I}_-|a'\rangle \qquad (12.17)$$

The wave function is reversed for the second part because it's Hermitian. Note especially that the running variable, γ must also be reversed. The wave functions, a, are given by Eqn.12.9. The electron operators are evaluated first because they eliminate the most terms so we get

$$\frac{1}{4}\sum_{\gamma}(\langle +m|+q_m\langle -m+1|)|\hat{I}_+|m_\gamma\rangle\langle -m_\gamma|+p_m(\langle +m-1|\hat{I}_-|-m\rangle) \qquad (12.18)$$

where m is the m_i value for the line of interest and m_γ is the running variable. Evaluating the nuclear operators Eqn.12.18 reduces to

$$\frac{1}{4}\sum_{\gamma}(\delta_{m,m_\gamma+1}x_{m_\gamma})(\delta_{m_\gamma,m-1}y_m) \qquad (12.19)$$

This equation is only non-zero when m_γ=m-1, thus (as is with all the terms) only one of the running quantum numbers is retained. If we note that $x_{m-1}=y_m$ then the term reduces to y_m^2, *i.e.*, Eqn.12.17 is

$$\frac{1}{4}j_{oo}(\omega_{res}+\omega_a)(F_a^{(0)})^2y_m^2 \qquad (12.20)$$

The reduced spectral density is given by $\frac{1}{5}\lambda_{oo}$, where λ_{oo} is an eigenvalue of the asymmetric rotor (see Sect.12.4.). This process has to be repeated with each operator element for every term in Eqn.12.14 for each of the spectral densities, J, in Eqn.12.12. For simplicity only the evaluated operator terms are given in the table overleaf.

	$2J_{aaa'a'}$	$-J_{aaaa}$	$-J_{a'a'a'a'}$	$-J_{aa'aa'}$	$-J_{a'aa'a}$
$A_a^{+2}A_a^{-2}$	0	0	0	0	$(\frac{Y}{2})^2$
$A_a^{-2}A_a^{+2}$	0	0	0	$(\frac{X}{2})^2$	0
$A_a^{+1}A_a^{-1}$	0	$-\frac{1}{4}(m-1)v+\frac{1}{4}(\frac{Y}{2})^2$	$\frac{1}{4}mv+\frac{1}{4}(\frac{Y}{2})^2$	0	$\frac{1}{4}m^2+\frac{1}{4}m(v-z)$
$A_a^{-1}A_a^{+1}$	0	$-\frac{1}{4}mz+\frac{1}{4}(\frac{X}{2})^2$	$\frac{1}{4}(m+1)z+\frac{1}{4}(\frac{X}{2})^2$	$\frac{1}{4}m^2+\frac{1}{4}m(v-z)$	0
$A_a^0A_a^0$	$\frac{1}{3}m^2+\frac{1}{3}m(v-z)$	$\frac{1}{6}m^2+\frac{1}{3}mv$	$\frac{1}{6}m^2-\frac{1}{3}mz$	$\frac{1}{6}(\frac{Y}{2})^2+\frac{1}{6}v$	$\frac{1}{6}(\frac{Y}{2})^2+\frac{1}{6}z$
$A_g^0A_g^0$	$\frac{1}{3}B_z^2$	$\frac{1}{6}B_z^2$	$\frac{1}{6}B_z^2$	0	0
$A_g^{+1}A_g^{-1}$	0	0	0	0	$\frac{1}{4}B_z^2$
$A_g^{-1}A_g^{+1}$	0	0	0	$\frac{1}{4}B_z^2$	0
$A_a^0A_g^0$	$\frac{1}{3}(m+v)B_z$	$\frac{1}{6}(m+v)B_z$	$\frac{1}{6}(m-z)B_z$	0	0
$A_g^0A_a^0$	$\frac{1}{3}(m-z)B_z$	$\frac{1}{6}(m+v)B_z$	$\frac{1}{6}(m-z)B_z$	0	0
$A_a^{+1}A_g^{-1}$	0	$-\frac{1}{8}vB_z$	$\frac{1}{8}vB_z$	0	$\frac{1}{4}mB_z+\frac{1}{8}(v-z)B_z$
$A_a^{-1}A_g^{+1}$	0	$-\frac{1}{8}zB_z$	$\frac{1}{8}zB_z$	$\frac{1}{4}mB_z+\frac{1}{8}(v-z)B_z$	0
$A_g^{+1}A_a^{-1}$	0	$-\frac{1}{8}vB_z$	$\frac{1}{8}vB_z$	0	$\frac{1}{4}mB_z+\frac{1}{8}(v-z)B_z$
$A_g^{-1}A_a^{+1}$	0	$-\frac{1}{8}zB_z$	$\frac{1}{8}zB_z$	$\frac{1}{4}mB_z+\frac{1}{8}(v-z)B_z$	0

Table 12.2. The Matrix Elements for Redfield Theory. The elements include the $(-1)^m$ term and also negated so that T_2 is +ve (Eqn.12.11).

The final expression, obtained from Table 12.1 and Table 12.2 is

$$T_2^{-1} = 1/12\Big[j(0)\{8(Am^2+2A_g m+G) + 8C(K-m^2)(A[m+1]+2A_g)\} + j(a)\{3A(K-m^2+2Cm)\} + j(\omega-a)\{A(K-m^2+6Cm)\} + j(\omega)\{6(Am^2+2A_g m+G) + 12C(K-m^2)(Am+A_g) + j(\omega+a)\{6A(K-m^2)\}\Big] + X \qquad (12.21)$$

Approximating $\omega_{res} \pm \omega_a \Rightarrow \omega_0$ and $\omega_a \Rightarrow 0$ (see Sect.14.2.) we get

$$T_2^{-1} = 1/2\Big[j(0)\{A(3K+5m^2)+8(2A_g m+G) + 8C(K-m^2)(A[m+1]+2A_g)+6CAm\} + j(\omega)\{A(7K-m^2)+6(2A_g m+G) + 12C(K-m^2)(Am+A_g)+4CAm\}\Big] + X \qquad (12.22)$$

where X is the residual line-width (see Sect.14.5.)

$$A = (F_a^0)^2 \qquad G = B_z^2(F_g^0)^2 \qquad A_g = B_z F_a^0 F_g^0$$

and

$$F_a^0 = \tfrac{1}{2}(A_{xx} - A_{yy}) \qquad F_g^0 = \tfrac{1}{2}(g_{xx} - g_{yy})$$

Eqn.12.22 can be readily rearranged into a cubic in m_i to recover the results given by other workers *(128)(129)(130)(131)(99)* by letting $B_z = B_0$. (The coefficient 'C' identifies the second order contributions. The first order equation is derived by setting this to zero. See appendix 22.5 for comments on comparing the second order terms with other theories).

The data can be readily inverted to obtain the two spectral densities and a residual linewidth. The latter can be attributed in part to experimental artefacts (dipolar broadening from the solvent, unresolved hyperfine coupling *etc.* see Sect.14.5.1), but is mainly due to the spin rotation contribution (see Sect.12.5).

The spectral densities can be further inverted (in principle) to obtain the elements of the diffusion tensor $\underset{\sim}{R}$. The relationship between the spectral densities and $\underset{\sim}{R}$ depend on the diffusion model used. We will concentrate on the Debye diffusion model, because of its simple relationship to molecular geometry as well as the other reasons outlined in Sect.10.4.

12.4 THE DEBYE DIFFUSION MODEL FOR AN ASYMMETRIC ROTOR

The eigenvalues for rotational diffusion of an asymmetric rotor are given by Freed *(98)* and Favro *(109)*. In our case only one eigenvalue (one reduced spectral density, $=1/5\lambda_{00}$, in Freeds notation) is measurable because of the near axial symmetry of the magnetic interaction tensor. Using Freeds

equations and an algebraic manipulation program *(124)* we can obtain the following relation for anisotropic diffusion

$$\lambda_{oo} = \frac{12R_a(R_s+3R_z) + 3\omega^2(R_s-R_z)}{\omega^4 + 8(2R_s^2-3R_a)\omega^2 + 144R_a^2} \qquad (12.23)$$

where $$R_s = R_x + R_y + R_z$$

$$R_a = R_xR_y + R_xR_z + R_zR_y$$

The x,y,z axes are assigned as discussed in Sect.10.3. We only have two reduced spectral densities, j(0) and j(ω), so it is not possible to invert the data for all three diffusion constants. Moreover, Eqn.12.23 is symmetric with-respect-to the interchange of R_x and R_y so, except for the case of axial diffusion, we need two extra pieces of information to invert the data (this is discussed further in Sect.15.4). This data may be obtained from NMR and that is essentially the objective of the thesis.

12.5 SPIN ROTATIONAL RELAXATION

As a molecule rotates the electrons generate a magnetic moment. The motion of the electrons is not rigidly coupled to the motion of the molecular frame, they lag slighty, so this moment can couple with the nuclear spins (the NMR case)

or, the unpaired electron spin (the ESR case) *(132)(133)(134)*. This is known as spin-rotational coupling. The magnitude of the coupling is related to the electronic structure (and is characterised by the spin-rotation tensor) and the angular momentum of the molecule (the larger the momentum the larger the lag and hence a larger coupling). If the coupling is modulated then relaxation can occur. Modulation of the angular momentum occurs during collision and can be characterised (for the case of isotropic diffusion) by a correlation time τ_j. Modulation of the spin-rotation tensor itself, by collision, is usually considered to be negligible *(135)* (*i.e.*, $\tau_c >> \tau_j$). The angular momentum and hence its correlation time, τ_j, is clearly related to the strength of the intermolecular torques and the moments of inertia of the molecule. Valuable information is thus available from τ_j. Unfortunately the spin-rotation tensor is usually unknown and has to be calculated from the g-tensor. The accuracy of such calculations is open to question. Also the inertia tensor is generally anisotropic so the angular momentum is characterised by more than one correlation time. These times cannot be obtained from one relaxation time. More importantly, the relationship between τ_c and τ_j is unclear, especially in the case of anisotropic motion so although the spin-rotation contribution to relaxation can be readily measured (Sect.14.5) it is not possible to extract any motional information from it. One important point though is

that τ_j is proportional to temperature(T) *(136)*, whereas τ_c is proportional to 1/T. This accounts for the quadratic behaviour of the spectrum line-widths as a function of temperature.

13. ESR EXPERIMENTAL

Preparation and purification of the copper dithiocarbamate spin-probes is straight-forward.

Precise and accurate acquisition and analysis of spectra is less easy, but is considerably enhanced by the use of digital techniques. (This has been discussed in earlier work *(88)* and also in Part.6). DISPA (dispersion *vs.* absorption plots, Part.1) was also found to be a great aid in optimising spectrum acquisition and analysis.

13.1 PREPARATION OF ^{63}COPPER(II) CHLORIDE

Isotopically enriched (99.99% AERE Harwell) ^{63}Cu metal was dissolved in concentrated nitric acid and the solution evaporated. The residue was repeatedly crystallised from concentrated hydrochloric acid to form ^{63}copper(II) chloride.

The chloride was used in preference to the nitrate as it is less deliquescent. It is also thermally stable so that excess acid can be readily removed by heating.

13.2 PREPARATION OF COPPER(II) DITHIOCARBAMATE COMPLEXES

A slight excess of the appropriate sodium dithiocarbamate salt in aqueous solution was added to the isotopically enriched copper chloride (≃20mg, 0.15mMol) in solution. The brown copper complex precipitate was extracted from the aqueous phase by shaking with chloroform. In some cases it was necessary to add ethanol to break up the

water/chloroform emulsions that form in the presence of the complex.

After separation, the chloroform solution was washed several times with water and then filtered. The solution was allowed to evaporate and the residue dried at 80°C. The complex was recrystallised by dissolving in a minimum amount of boiling chloroform and rápidly cooled in an ice bath to form blue-black crystals.

13.3 PREPARATION OF COPPER-FREE NICKEL COMPLEXES FOR ESR MATRIX EXPERIMENTS

In matrix experiments the ^{63}copper complex is doped into its nickel analog at a level of 0.1% w/w. Consequently the host nickel complex must contain <0.005% (50ppm) of mixed isotope copper impurity. However, (for unknown reasons) all the nickel salts tried gave nickel complexes containing ≃0.1% copper. To circumvent this problem the nickel salts had to be treated as follows: An excess of the aqueous nickel salt was added to a solution of the appropriate sodium dithiocarbamate salt, the solution filtered and the residue discarded. The filtrate is now copper free (<0.001% by ESR). The pure nickel complex was then prepared by adding aqueous sodium dithiocarbamate to the filtrate, filtering and recrystallising the residue to give green-black crystals. These nickel salts were also used for the NMR relaxation studies.

13.4 POLYCRYSTALLINE ESR SPECTRA

The polycrystalline spectra of the copper complexes were recorded in toluene glasses. The $\underset{\sim}{g}$ and $\underset{\sim}{A}$ parameters were obtained by simulation procedures due to Tait *(137)*. Studies in chloroform glasses were not successful due to the formation of triplet states, probably dimers *(138)*.

13.5 PREPARATION OF THE SOLUTIONS FOR ESR

Spectrograde or d_1-chloroform was dried over Type 4A molecular sieves and then further purified just prior to use by passage through an alumina column. A 10ml solution of 0.2 to 0.7mM of the complex was prepared. Approx 0.5ml of the solution transferred to a 'flamed out' ESR tube and degassed by several freeze-pump-thaw cycles to a pressure of $<10^{-5}$ Torr on a greaseless vacuum line and then sealed off. It should be noted that molecular sieves remove the stabilising agent (ethanol) from chloroform which then rapidly oxidises to phosgene, chlorine and hydrogen chloride. These impurities are removed by the alumina.

All solution manipulations were done in a glove bag under an atmosphere of dry nitrogen. The samples were stored at $\simeq$-20°C in the dark to prevent decomposition *(118)*.

13.6 ESR SAMPLE TUBES

The sample tubes were constructed from special thin walled pyrex tubing (5mm OD,4mm ID) to maximise the sample volume. Each tube was filled to a depth of 3-4 cm (this minimises

temperature gradients due to convection; see Sect.14.6). and sealed off at 4-5 cm (this prevents the solvent from distilling out of the cavity area). Care was taken to leave a gap of ≃1cm between the top of the solvent and the seal to allow for liquid expansion.

13.7 RECORDING ESR SPECTRA

All spectra were recorded on a home-built X-band homodyne ESR spectrometer *(139)* (Fig.13.1) which consisted of: a 12in magnet and MkII Fieldial control; an HP716B klystron power supply and sweep unit; a home-built AFC; 100 kHz modulation unit; an Ithaco Dynatrack 391A phase-lock amplifier. The microwave bridge was a reflective homodyne design using a TE-102 cavity, three port circulator, Schottky detector diode and a microwave bucking arm. Microwave power was measured with an HP431C power meter and the frequency was measured with an HP5246L frequency counter fitted with a 5256A plug-in module. The cavity was fitted with a dewar system and the temperature controlled by a Varian E257 control unit. The magnetic field was calibrated with a Varian E500 proton magnetometer. The spectrometer was interfaced to a microprocesser controlled digital acquisition system *(140)*. (see Sect.6). The spectra, along with calibration data, were recorded on a Kennedy 9800 tape unit *via* the F8 microprocesser. The same recording conditions were maintained for all samples. These are summarised in Table 13.1.

The whole spectrometer was periodically tested with standard samples to check for sensitivity, amplifier phase, magnet stability, modulation amplitude and dispersion leakage. Extensive use of the DISPA technique was made for this purpose *(10)(14)* & Part.1.

One complete spectrum was always recorded at room temperature to check for paramagnetic impurities.

CONTROL	SETTINGS/COMMENTS
Microwave Freq.	≃9.04GHz
Microwave Power	1-5mW, for chloroform solvent. Cudtc's saturate at ≃200mW *(42)*
Modulation	<0.8G. Narrowest observed line is 3.0G.
Scan Time & Sweep Width	5 mins for 25G, 50G or 100G scans as appropriate. Each line was recorded separately.
Time Constant	125mS or 400mS (≃1/100 of the time to sweep the line.
Temperature	15SCFH N_2 flow rate with $CO_2/(CH_3)_2CO$ coolant *(88)*.
Sampling rate	2.5Hz or ≃750 pts. per line.

Table 13.1. Spectrum Recording Conditions.

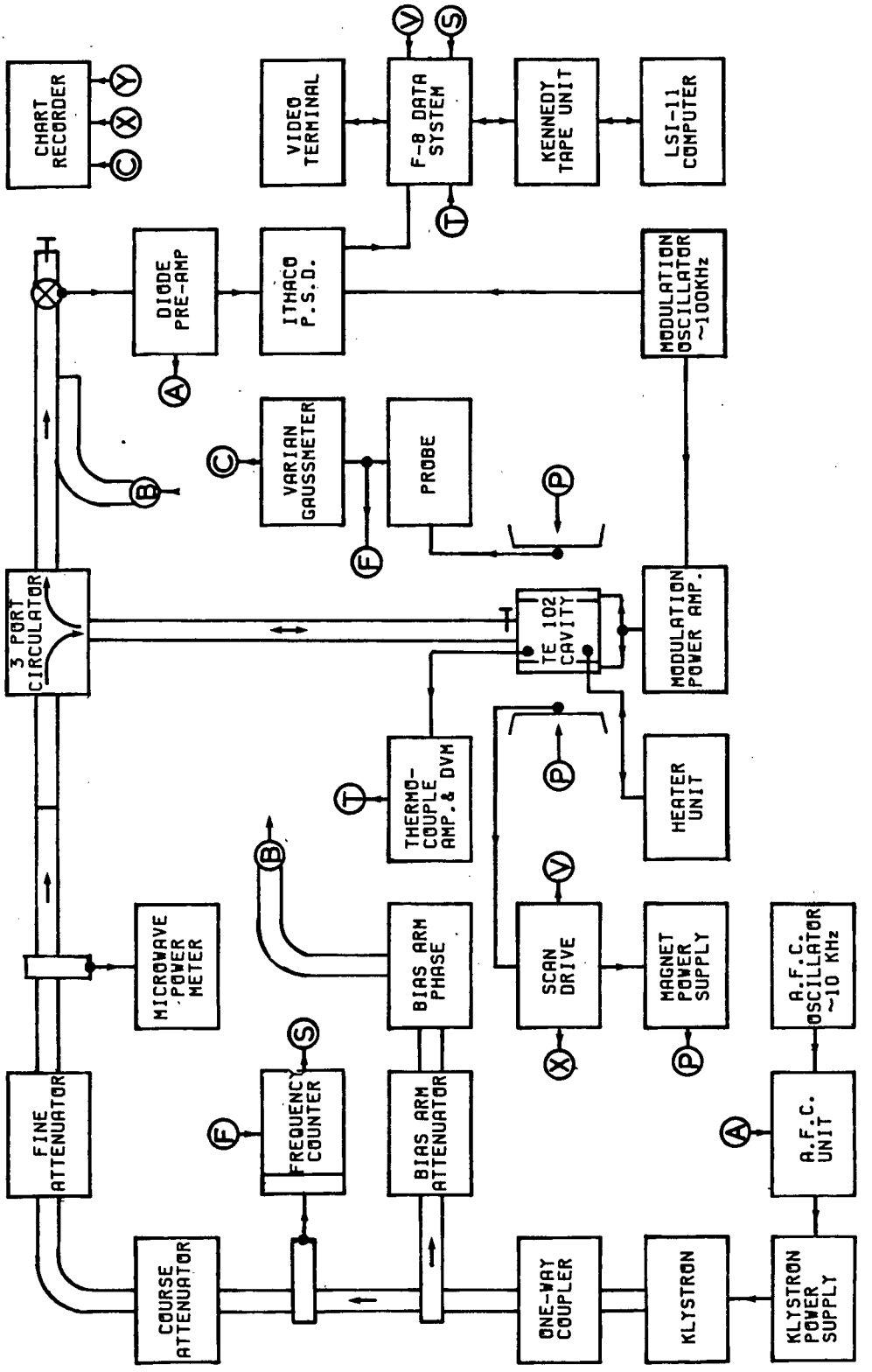

Figure 13.1. The Spectrometer.

13.8 TEMPERATURE MEASUREMENT IN ESR EXPERIMENTS

The temperature was measured with a copper/constantan thermocouple inserted into the top of the cavity near to the sample. Care was taken not to decouple the cavity. The thermocouple EMF was amplified 1000x by a low drift D.C. amplifier which was connected to the digital acquisition unit. The microprocesser recorded the temperature for 100mS (which was averaged later to eliminate noise) at the start and end of each recorded spectrum.

13.9 FIELD CALIBRATION OF ESR SPECTRA

Each spectrum was calibrated absolutely using the Varian tracking Gaussmeter. The calibration procedure was as follows. The magnetometer was tapped to provide r.f. (the proton precession frequency $\simeq$ 14MHz) for the HP frequency counter. The counter was sampled automatically every 50 data points of the spectrum, concurrently with the corresponding Fieldial voltage and stored by the microprocesser. This information was then copied as a table (magnetometer frequency *vs.* Fieldial voltage) to the magnetic tape unit at the end of each spectrum. All required calibration data was then recovered from the table using a least-squares-fit. Two parameters were obtained from the fit, the slope (Gauss/volt) and the intercept (the absolute field at the left edge of the spectrum).

13.10 COLLECTION AND ANALYSIS OF ESR SPECTRA

The spectra were analysed as follows. Each line of the spectrum was recorded and calibrated individually. The gain, scan width and time constant were adjusted to suit each peak using the criteria given in previous work *(88)*.

Each line with its associated calibration table, temperature and other data were recorded on magnetic tape as 16 bit X-Y data point pairs. The magnetic tape was read at the computing center and transferred to a line file and processed there. Alternatively the data were transferred to the DEC LSI-11 minicomputer located in the ESR laboratory.

The spectra were analysed as follows *(88)*. The peak tops were located automatically (Amdahl program) or interactively (DEC LSI-11 programs) and fitted to a cubic. This was solved to locate the exact extremum. The crossovers were also approximately located and then found exactly by locally fitting to a straight line and finding its intersection with the baseline. The results can then be converted to Gauss by means of the calibration table and written to a file as line-width and line-positions, along with the corresponding temperature and microwave frequency. The reduced spectral densities, $j(0)$, $j(\omega)$ and the residual line-width were extracted from Eqn.12.22 using a least-square-fit *(141)* in the line-widths (see appendix 22.7 for a brief discussion of units). Inversion of $j(0)$ and $j(\omega)$ to get the diffusion tensor is discussed in Sect.15 and Sect.20.

14. ESR ERROR DISCUSSION

The errors arise from four principal sources; approximations inherent in the theory; instrumental artefacts; experimental artefacts; computational artefacts. Many of the experimental and instrumental artefacts can be assessed with the aid of DISPA and subsequently minimised or eliminated. Computational artefacts can be eliminated by careful program design. Theoretical approximations were investigated carefully as they affect the program design, the accuracy of the results and generally simplify the data analysis.

14.1 THE AXIAL SYMMETRY APPROXIMATION FOR THE SPIN HAMILTONIAN

This approximation eliminates all 0 and ±1 tensor elements considerably simplifying Eqn.12.13. However, this is at the expense of some information. Rotations that interchange the 'zz' and 'xx' tensor components are indistinguishable from rotations that interchange the 'zz' and 'yy' components.

The magnetic parameters for CuPyDtc (these values vary very little for the alkyl substituted copper dithiocarbamate complexes) are

$$A_{xx} = -119\text{MHz} \qquad g_{xx} = 2.022$$
$$A_{yy} = -106\text{MHz} \qquad g_{yy} = 2.018$$
$$A_{zz} = -474\text{MHz} \qquad g_{zz} = 2.088$$

That is, approximately, but not exactly axially symmetric.

The magnetic interaction tensors (in a spherical basis) are given by *((90)(101)* and in appendix 22.6).

$$F_a^{\pm 2} = \tfrac{1}{2}(A_{xx} - A_{yy}) \qquad F_g^{\pm 2} = \tfrac{1}{2}(g_{xx} - g_{yy})$$

$$F_a^0 = \sqrt{\tfrac{2}{3}}\left[A_{zz} - \tfrac{1}{2}(A_{xx}+A_{yy})\right] \qquad F_g^0 = \sqrt{\tfrac{2}{3}}\left[g_{zz} - \tfrac{1}{2}(g_{xx}+g_{yy})\right]$$

(the ±1 elements are zero because the tensors are symmetric).

In the relaxation equation (Eqn.12.22) the terms are cross multiplied or squared. Substituting the parameters given above we find that

$$(F_a^{\pm 2})^2 \simeq 40\text{MHz}^2 \qquad (F_a^0)^2 \simeq 86000\text{MHz}^2$$

$$F_a^{\pm 2} F_g^{\pm 2} \simeq -0.01\text{MHz} \qquad F_a^0 F_a^0 \simeq -70.0\text{MHz}$$

$$(F_g^{\pm 2})^2 \simeq 4\text{x}10^{-6} \qquad (F_g^0)^2 \simeq 6\text{x}10^{-2}$$

The axial symmetry approximation amounts to dropping the $F^{\pm 2}$ term and retaining the F^0 terms in Eqn.12.13. Using the data above, this will introduce an error of ≃0.05% for each F term so the total error for this approximation will be ≃0.2%, within experimental error.

14.2 ON APPROXIMATING SPECTRAL DENSITIES

The spectral densities are of the form

$$j(\omega) = \frac{\tau_c}{1+(\omega\tau_c)^2} \qquad (14.1)$$

where ω is: ω_{res}, the transition frequency for a given spectral line, or ω_a, the hyperfine coupling frequency ($\frac{1}{2}A_o$), or a mixed term, $\omega_{res} \pm \omega_a$, or zero. In our case

$\omega_{res} \simeq 56.9$ Grad s^{-1} and τ_c is 10-200pS. In NMR $(\omega\tau_c)^2 << 1$ (see Sect.18.1). and this term can be dropped. However, for ESR this is not the case (see Fig.14.1) and approximations of this kind need more careful examination. This is readily investigated by substituting the appropriate approximations into Eqn.12.22. It should be noted that some of the following approximations are necessary if the data are to be inverted *via* the spectral densities.

14.2.1 THE $(\omega_0\tau_c)^2 << 1$ APPROXIMATION

The frequency ω_{res} is approximately the Larmor frequency for the electron, ω_0. From Fig.14.1 its clear that setting $\omega_{res} \rightarrow 0$ is not a good approximation. The $\omega_0\tau_c$ terms must be explicitly included in all the calculations.

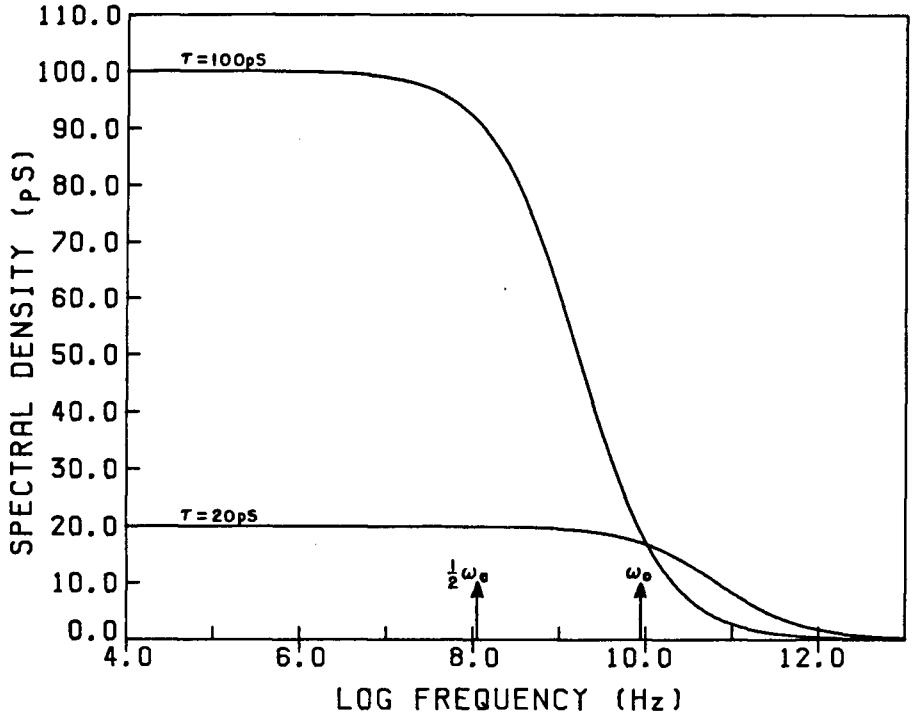

Figure 14.1. Spectral densities *vs.* frequency.

14.2.2 THE $(\omega_a\tau_c)^2<<1$ APPROXIMATION

For τ_c<120pS this approximation does not introduce any significant error (<0.5%, see Fig.14.2 *i.e.*, $j(\omega_a)$ and j(0) are experimentally indistinguishable).

14.2.3 THE $\omega_a<<\omega_0$ APPROXIMATION

This would allow us to set $\omega_{res}\pm\omega_a => \omega_0$ and $\omega_{res} => \omega_0$. Both of these approximations introduce negligible error (<0.5%, see Fig.14.2). This is very useful as the the relaxation time depends on only two spectral densities, j(0) and $j(\omega)$. However, this does not imply that $B_z(=B_{res})=B_0$.

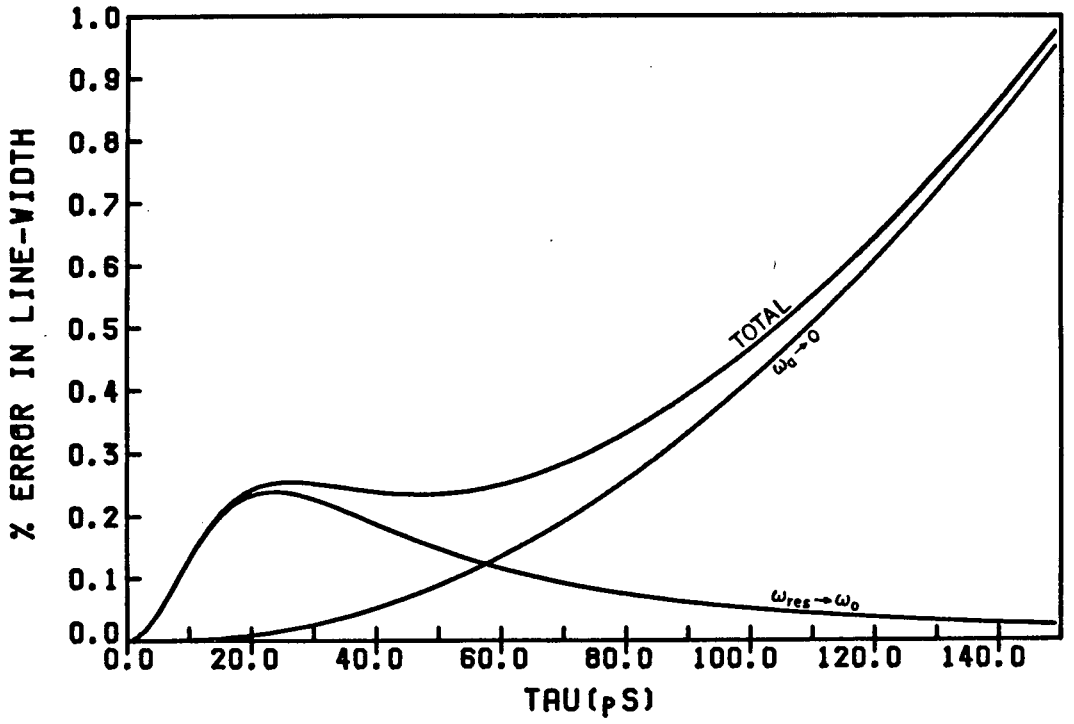

Figure 14.2. Line-width Errors for the Spectral Density Approximations. The plot is for the m_i=-3/2 line.Errors for the other lines are less than half of this.

14.3 CONTRIBUTIONS FROM THE NUCLEAR ZEEMAN TERM

The nuclear Zeeman term (Eqn.12.2.) makes small contributions to the transition frequencies and hence to the spectral densities. For an X-band ESR spectrometer (*i.e.*, at a field of 0.32T) the Larmor frequency of ^{63}Cu and ^{65}Cu is about 4MHz. This is small compared to the electron resonant frequency (≃9GHz). It is not quite negligible with respect to the hyperfine coupling frequency (220MHz). However, the hyperfine coupling frequency contributes <1% (Sect.14.5.5)

to the spectral densities. Hence the nuclear Zeeman contribution can be neglected.

14.4 THE FIRST AND SECOND ORDER CONTRIBUTION

The second order contribution to the relaxation times (the 'C' terms in Eqn.12.22) is easily calculated from this equation. For typical reduced spectral densities of $j(0) \simeq 10pS$ and $j(\omega) \simeq 5pS$, this contribution is <0.5%. However, first order correction shifts the linewidths by 5% and one care has to taken to use the line-positions, B_z, not B_0, in Eqn.12.22.

14.5 THE RESIDUAL LINEWIDTH

A number of factors influence the observed linewidth, other than those discussed in Sect.12. The linewidth after subtracting the theoretical linewidth (from Eqn.12.22) is known as the residual linewidth and is determined empirically. The principal contribution is the spin-rotation term (Sect.12.5.). However, there are several other (small) contributions. These are discussed below.

14.5.1 DIPOLAR BROADENING

This arises from electron-nuclear spin interactions between the solvent protons and the copper complex. It can be minimised by the use of deuterated solvents. Comparison of perdeuterated CuMedtc in $CDCl_3$ and $CHCl_3$ shows that this contribution is 0.04G in a linewidth of

3.6G. (*i.e.*, 1% at maximum).[38]

14.5.2 PARAMAGNETIC BROADENING

This arises from (unpaired) electron-electron interactions. The copper complexes thus show broadening at high concentrations ($>10^{-3}$M), but this contribution is negligible at the usual working concentration ($\simeq 10^{-4}$M). Another source of unpaired electrons is dissolved oxygen. This must be removed by freeze-thaw-pump cycles of the solution on a vacuum line.

14.5.3 SOLVENT COORDINATION

Solvent coordination will modulate the linewidths *e.g.(46)*. The influence of water (wet solvents) is unknown (except see *(118)*), although it is unlikely to coordinate with the complexes. The solvents were nevertheless thoroughly dried before use.

14.5.4 INTERNAL MOTION

The C-N bond has significant double bond character *(142)* and there is no evidence of rotation about the bond on the NMR time scale *(125)*. The ring of the pyrollidine is slightly puckered and may contribute to the relaxation *via* the unresolved hyperfine coupling contribution. However, the unresolved hyperfine coupling

---

[38] The effect is even smaller for the pyrollidine derivative, <0.1%, see Sect.14.5.5.

contribution (*vide infra*) and the contribution from fluctuations in the conformation (appendix 22.8) have both been shown to be negligible.

14.5.5 UNRESOLVED HYPERFINE

The protons couple to the unpaired electron on the copper giving rise to broadening from the unresolved hyperfine coupling. DISPA studies *(14)*, simulations *(42)* and studies with ordinary and per-deuterated ^{63}CuMedtc show the coupling constant to be ≃0.5G, broadening the narrowest line by 10% (0.3G on 3G).[39] This effect can be minimised by the use of perdeuterated compounds or by use of correction procedures *(143)*. However, the effects on τ_c are small (Table 14.1) and do not affect the observed trends.

---

[39] For the pyrollidine derivatives the effect is even less, 0.04G in a 3.6G line, about the same as dipolar broadening from the solvent.

TEMP°C	τ_c(D)pS	τ_c(H)pS	τ_c(corr)pS
-50	105±2	104±2	108±4
-30	55±1	52±2	55±2
-20	41±2	40±1	41±1
0	26±0.5	24±0.5	25±0.5
20	17±1	16±1	17±1.0
30	15±0.5	14±0.5	14±0.5
45	13±0.5	11±0.5	11±0.5

Table 14.1. Effect of hyperfine on correlation times. Data is from *(88)*. (D) denotes the correlation time for the per-deutero derivative. (H) denotes the normal derivative. (corr) denotes that line-widths corrected by Bales method were used.

14.5.6 MAGNETIC FIELD INHOMOGENEITY

Typically <5mG across the ESR sample. (manufacturers spec.) This is small with respect to the line-width of *dtc*'s (>3G) and can be ignored.

14.5.7 SPECTROMETER PHASING

Line-heights are very sensitive to any misphasing (dispersion leakage) of the spectrometer and this interferes badly with line-height analysis methods used in the past *(131)*. The line-widths (but not the line-shapes) are not sensitive to phase misadjustments (Table 14.2) and this is not a problem if the analysis uses the line-widths directly as is done here.

Phase Angle	Observed* Line-width	Line-width from Heights
0	1.000	1.000
1	1.006	1.005
2	1.006	1.010
5	1.006	1.029
10	1.013	1.060
15	1.014	1.101
20	1.022	1.151

Table 14.2. Effect of Phase on Observed Line-widths. *-There is an error of ≃±5mG associated with this measurement.

14.5.8 TIME CONSTANT AND MODULATION

The effect of the time constant and modulation amplitude on ESR spectra is well documented *(30)*. Line broadening of the narrowest line by the time constant is negligible (<0.1%). Broadening from the modulation is <1% (≃ 30mG with 0.8G modulation) in the worst case and is typically much less.

14.6 TEMPERATURE INHOMOGENEITY

A temperature gradient across the sample will affect the observed linewidth and cause inaccurate thermocouple readings. This has been previously investigated *(88)*. The temperature gradient was <0.5°C with an overall stability/accuracy of 0.05°C. A 1°C shift in temperature will change the line-width by 3% of the line-width in the worst case (m_I=3/2 line at ≃-50°C), but would be typically

≃0.5% of the line-width.

14.7 FITTING ARTEFACTS AND NOISE

The influence of noise on peak fitting is discussed extensively in the literature *e.g. (144)*. Under the experimental conditions used here (an SNR of 50:1 with 50 points for a fit) we expect a noise related error of <1.0% *(145)*.

Fitting artefacts arise because the data (within in a window about the peak) are fitted to a cubic. If the fitting window is too small noise becomes a problem, if it is too large the cubic no longer adequately approximates the peak shape. This is not a problem for interactive peak fitting (unless the noise level is very high) as the operator controls the window width and position. With the automated routines the line-width is unknown to the program and choice of the correct window is difficult, especially if the line-widths vary within a spectrum or set of spectra. This problem was investigated in previous work *(88)*. Typically errors in the line positions are ±20mG (<1% of the sweep-width) and ±0.5% in the line-width for both methods.

14.8 FIELD CALIBRATION AND CAVITY SHIFT

The Varian Gaussmeter is (incorrectly) calibrated with the free proton precession frequency instead of that of a proton in solution. (*i.e.*, the meter is not corrected for the diamagnetic shift). Typically the meter reads ≃0.1G high.

The correct value can be recovered by multiplying the meter reading by 234.868/234.874. However, we tap the probe to obtain the proton precession frequency directly so this problem is not relevant.

The gate times[40] for the tracking Gaussmeter and the frequency counter are ≃0.1s, this leads to an error in the field calibration of <(sweep-rate)*(gate-time), or <15mG for a 5min., 25G scan. This will average out to a systematic calibration error of ≃ -5mG for a low-to-high field sweep. However, this only affects the absolute line-positions, not line-widths or splittings hence the error is negligible.

The Gaussmeter probe is outside the ESR cavity so a field shift with respect to the center of the cavity is expected. This was checked with Fremys salt. The center line of a $1x10^{-4}$M solution of Fremys salt in a 0.05M solution of potassium carbonate was measured 7X. The mean field position corrected for microwave frequency shifts was 3238.355±0.003G (the gating error in this case should be <1mG). Using g_0=2.00545 and A_0=13.0910 *(130)*, the line-position, to second order, should be 3238.450, *i.e.*, a cavity shift of 0.095G should be added to the Gaussmeter readings. The cavity shift fortuitously cancels the error of the Gaussmeter to within 0.01G.

---

[40] To obtain an accuracy of 1:10^6 (≃3mG) one must count the frequency for at least 10^6 cycles, *i.e.*,≃ 0.1s for 13MHz, the Larmor frequency of a proton in a 3000G field

15. ESR RESULTS AND DISCUSSION

15.1 ESR RESULTS

Line-width data for ^{63}Cu d_5-Pydtc in d-chloroform were obtained over a temperature range of -50°C to +70°C. The results are shown in Fig.15.1. The data are in appendix 22.10.

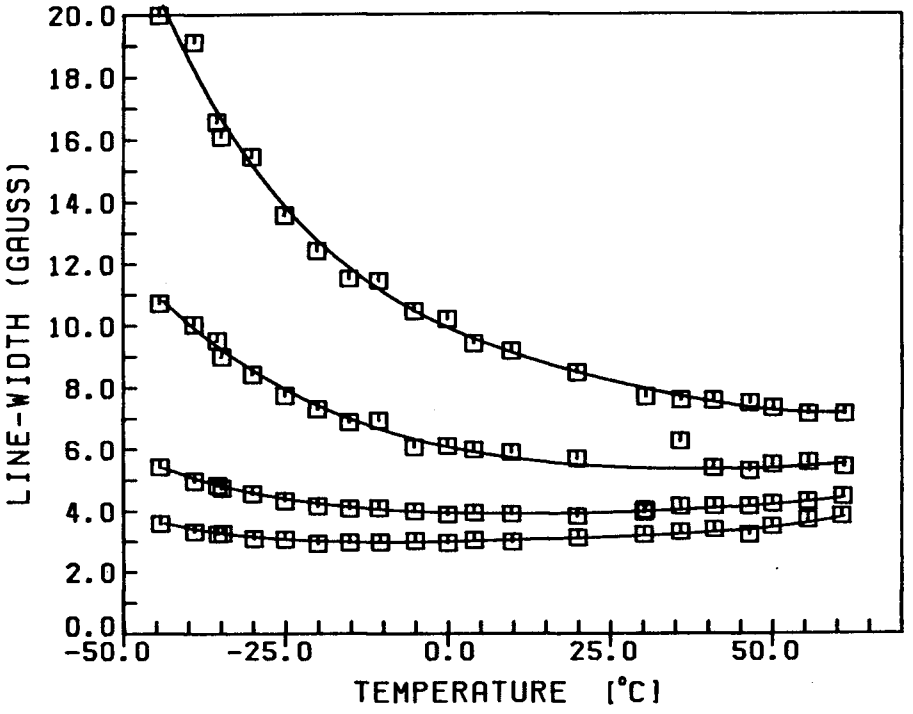

Figure 15.1. Pyrollidine *dtc* line-width data.

Line-widths for 310, 323 and 333K were obtained by interpolation and substituted into Eqn.12.22. The reduced spectral densities, j(0), j(ω) and the residual line-width factor were obtained *via* a least squares fit *(141)*. The results are shown in Table 15.1.

Temp(K)	j(0)	$j(\omega)$	Residual
310	0.0115	0.00448	0.0176
323	0.0102	0.00381	0.0205
333	0.00825	0.00428	0.0373

Table 15.1. Spectral densities for CuPydtc in chloroform. Fitting errors on the parameters are all <1%.

By combining these results with the ^{13}C or ^{2}H data, we can, in principle, for a Debye diffusion model, obtain the diffusion tensor. This is discussed in Part.5.

15.2 APPROXIMATE METHODS FOR DATA ANALYSIS

In view of the large body of ESR data available from previous studies it is useful to examine Eqn.12.23 (λ_{oo}) in detail to gain some insight into the diffusion tensor, without resorting to NMR studies to do so. There are two approaches to this, simulations or approximations. Three approximations are of interest here: The isotropic assumption, $R_x=R_y=R_z=R$, which is useful for obtaining order of magnitude values. The axial approximation with $R_y=R_z=R_p$ and the fast anisotropic approximation, with $R_x>>R_y,R_z$. The latter two approximations are expected to be valid on geometric grounds and both give unique values for R_x.

15.2.1 SIMULATIONS

One can simulate data to produce tables of spectral densities for various values of the diffusion tensors, but this approach is not useful unless the approximate values are already known. However, we can get order of magnitude figures for the tensor elements (*vide infra*). Also we know that the diffusion tensor elements are all positive. Furthermore we also have good reasons to suppose that $R_x > R_y, R_z$ so one can limit the size of the tables.

By automatically matching experimental data (to say within 5%) with simulated values one can obtain a set of values for the possible diffusion elements. A unique solution is not possible, but the data obtained for our system is consistent with motion approximately axially symmetric ($R_x \simeq R_z$) and $R_x > R_y, R_z$.

15.2.2 THE ISOTROPIC ASSUMPTION

Eqn.12.23 reduces in this case to

$$\lambda_{00}(\omega) = {}_{\omega^2} \frac{6}{+ 36R^2} \qquad (15.1)$$

The interesting feature of this approximation is that two estimates of the isotropic correlation time are obtained; one from j(0), R(0), and the other from j(ω), R(ω). These two values are only equal if the motion is

isotropic. The ratio, $R(0)/R(\omega)$, thus gives a measure of the anisotropy of the motion. This may be a useful criterion to apply to nitroxide type spin-probes, but it will not be pursued here.

15.2.3 THE FAST MOTIONAL APPROXIMATION

On geometric grounds we expect R_x to be larger than R_y, or R_z. The approximation $R_x >> R_y, R_z$ thus may be useful. In this case Eqn.12.23 reduces to

$$\lambda_{00}(0) = \frac{1}{12}(R_y + R_z)$$

$$\lambda_{00}(\omega) = \frac{3R_x[4R_x(R_y+R_z) + \omega^2]}{\omega^4 + (4R_x\omega)^2 + [12R_x(R_x+R_y)]^2} \qquad (15.2)$$

Simulations show that R_x and (R_y+R_z) are underestimated if the ESR data are inverted using this approximation. The errors in R_x are $(R_y+R_z)/R_x$% and those for (R_x+R_y) about twice as much.[41] These errors are ≃20% for our case, but this approximation does provide useful starting values for the diffusion tensor for the non-linear inversion methods.

15.2.4 THE AXIAL APPROXIMATION

Eqn.12.23 reduces to

---

[41]These results are for 9GHz, the errors change with frequency, but not in a systematic manner.

$$\lambda_{oo}(0) = \frac{5R_p+R_x}{12R_p(2R_x+R_p)}$$

$$\lambda_{oo}(\omega) = \frac{12R_p(2R_x+R_p)(5R_p+R_x+3\omega^2(R_p+R_x)}{\omega^4 + 8(5R_p^2+2R_pR_x+2R_x^2)\omega^2 + [12R_p(2R_x+R_p)]^2} \quad (15.3)$$

for this approximation. Again R_x and $(R_y+R_z)=R_p$ are underestimated, but it works well for a wider range of values than the previous approximation. The errors are typically

$$<5\% \text{ error for } R_x \text{ if } |(R_y-R_z)/R_x|<0.3$$

$$\text{and the \% error for } R_p \simeq 10(R_y-R_z)^2/R_p$$

Providing the motion is approximately axial we can get a reasonable estimate for R_x. This is discussed further in Sect.15.4. Note that this method requires a non-linear inversion and so is not useful for obtaining starting values.

15.3 USING THE APPROXIMATIONS

The results of applying the above approximations to the data in Table 15.1 are shown below.

Temp	R(0)	R(ω)	R_x	R_p	R_x	R_y+R_z
310	14.5	37.1	63.8	4.8	48.9	7.3
323	16.3	43.7	90.1	5.1	67.1	8.2
333	20.2	38.9	82.5	4.3	54.4	10.1

Table 15.2. ESR data inverted with approximations.

The data for the axial approximation shows good agreement with the known values for the complete tensor at the high temperature (Sect.20.3). If we can remain confident that $R_y \simeq R_z$ for a wide temperature range, the axial approximation is a useful method for inverting ESR data, *vide infra*. The fast R_x approximation is useful because it provides reasonable starting values for the axial approximation. The isotropic values give order-of-magnitude values as expected.

15.4 INVERSION OF DATA WITH THE AXIAL APPROXIMATION

Data obtained from this approximation is rather scattered and is only useful for examining trends.

The results of the various approximations for Pydtc in toluene is shown in Table 15.3

Temp	R(0)	R(ω)	R_x	R_y+R_z	R_x	$2R_p$
-29.7	4.2	35.1	37.6	2.1	38.7	2.3
-19.3	5.1	66.7	93.3	2.5	96.7	2.7
-8.8	7.0	41.2	51.2	3.5	55.5	4.0
-0.2	8.1	46.0	61.8	4.1	68.1	4.6
9.0	9.6	51.7	77.4	4.8	87.8	5.4
19.5	11.6	51.4	81.8	5.8	97.2	6.8
28.8	13.9	46.0	71.0	6.7	89.7	8.4
39.4	16.0	47.0	77.2	8.0	102.0	9.6
49.1	17.7	47.2	79.7	8.9	110.0	10.8
51.4	20.0	42.7	65.8	10.0	96.0	12.8

Table 15.3. Axial approximation used with CuPydtc in toluene.

Both R_x and R_p increase with temperature as expected and have respective activation energies of 7±2kJ/mol and 13±0.5kJ/mol. This is an extremely interesting result as it implies the motion is not only not viscosity dependent (*i.e.*, is not hydrodynamic, the activation energy would be ≃9.5kJ/mol if it were), but also the damping mechanism is different for the two motions.

Table 15.4 and Table 15.5 show the results for CuMeOddtc (a 17 carbon-chain derivative) in two solvents, toluene and cyclohexane.[42] The data are rather poor, but R_x is approximately constant in both cases. R_x≃50 for the probe in cyclohexane and R_x≃200, four times faster, in toluene. This implies that the long hydrocarbon tail of the probe is coiled up in the cyclohexane, but not in toluene. As these solvents have the same dielectric constant this effect must reflect the local structure of the solvent, although what

---

[42]The latter data were taken from a study done by M.Yu. in this laboratory.*(146)*

that is, is unclear.

Temp	η/T	τ_c	R_x	R_y+R_z	R_x	R_p
24.3	3.05	97.3	23.6	1.7	24.8	1.0
31.2	2.66	86.1	61.6	1.9	62.6	1.0
32.8	2.57	83.6	53.6	2.1	55.2	1.2
37.1	2.37	77.5	31.2	2.2	32.8	1.3
52.1	1.81	60.3	27.1	2.9	30.0	1.9
62.6	1.52	52.1	126.0	3.0	132.0	1.6
73.3	1.29	47.2	53.9	3.6	58.6	2.1

Table 15.4. Axial approximation used with CuMeOddtc in cyclohexane. τ_c is taken form previous work. η/T is cP/Kx10^3.

Temp	η/T	τ_c	R_x	R_y+R_z	R_x	R_p
10.0	2.32	107.3	59	1.6	60	0.8
46.9	1.33	52.2	232	3.1	244	1.6
51.3	1.25	48.2	205	3.3	218	1.7
56.5	1.17	43.6	153	3.6	164	1.9
78.0	0.91	29.8	198	4.9	224	2.6
88.9	0.81	27.9	131	5.6	153	3.1
98.3	0.74	23.1	94	6.4	115	3.7

Table 15.5. Axial approximation used with CuMeOddtc in toluene.

For comparable values of η/T, τ_c is similar in both cases so that the isotropic approximation completely obscures the behaviour of R_x. However, Some caution has to be exercised when using this approximation because $j(\omega)<<j(0)$ and as such is subject to large errors. It might be better to invert the data directly for R_x and R_p rather than *via* the reduced spectral densities. Also this approximation predicates on the motion being approximately axial over the entire temperature range not just at high temperatures. Perhaps more importantly, the results in Table

15.4 and Table 15.5 show that R_p is $\simeq$1GHz; the slow-motional regime (see appendix 22.9). Its not clear what the effect of this is.

15.5 DIRECT INVERSION USING THE ISOTROPIC ASSUMPTION

If we assume that the motion is isotropic then the spectral densities assume a simple form; Eqn.15.1. In such a case we can invert the data directly rather than *via* the spectral densities. This was done in earlier work by Park *et al (82)* and in fact most motional data (ESR, NMR and light scattering) are obtained *via* this approximation. The question thus arises, as to the relationship between λ_{oo} and τ_c as calculated by Park if the motion is anisotropic. The calculation is complicated by second order terms, but to first order it is easy to see from Eqn.15.1 that

$$j(\omega)/j(0) = (1+\omega^2\tau_c^2)^{-1}$$

hence

$$\tau_c = \omega^{-1}[j(0)/j(\omega)-1]^{\frac{1}{2}} \qquad (15.4)$$

Comparison of the values of τ_c calculated from Parks method is fairly straight-forward, but given the complexity of the theoretical expressions for $j(0)$ and $j(\omega)$, (Eqn.12.23), relating τ_c to the diffusion tensor is difficult. We can obtain a functional form for τ_c from simulations though.

Temp	τ_cPark	τ_c(Eqn.15.4)
-30	83	83
-19	61	61
-9	39	48
0	38	40
9	37	33
20	33	27
29	27	22
39	25	19
49	23	17
56	19	15

Table 15.6. Comparison of τ_c's. Parks method *vs.* this work. Data is from Table.15.3 and previous work.

It is interesting to note that the τ_c calculated from Eqn.15.4 do not deviate from linearity at high temperatures as much as Parks results do.

15.6 INTERPRETING DATA FROM ISOTROPIC INVERSIONS

The most popular model for interpreting τ_c *vs.* η/T plots is given by *(147)*

$$\tau_c = \frac{V\eta}{kT} + \tau_0 \qquad (15.5)$$

where V is a hydrodynamic term (Sect.20.4.), usually the molecular volume, T is the temperature and k is the Boltzmann constant and τ_0 is a 'free-rotor' correlation time *(148)*. This is a source of some controversy as the model is unsatisfactory for a number of reasons (other than those that can be levelled against the hydrodynamic model in

general). For a purely hydrodynamic model the intercept is zero, in a number of studies a finite intercept has been observed. It has been proposed that this can be accounted for by adding a 'free-rotor' correlation time. However, correlation times cannot be added, only the corresponding rates. The correct expression is $\tau_{obs}=\tau_h\tau_0[\tau_h(1-p_0)+p_0\tau_0]$, where τ_h is the hydrodynamic correlation time, p_0 is the fractional population of freely rotating molecules and τ_0 their correlation time. Secondly the observed intercept is negative in a number of cases *(88)(149)(150)*. This is probably due to non-linearity of the plots. Finally the model implicitly assumes isotropic motion and there is no reason to believe that such plots are meaningful if the motion is anisotropic.

Given that the intercepts and non-linearity are real, then the question is, "can we account for these effects by including anisotropic motion in the model ?"

Assuming that the diffusion process has an Arrhenius temperature dependence, then we have

$$R_{obs} = R_xA_1e^{-E_1/RT} + R_yA_2e^{-E_2/RT} + R_zA_3e^{-E_3/RT} \qquad (15.6)$$

For the hydrodynamic model the 'activation energies', E_1, E_2 and E_3 should be all equal to the activation energy for viscous flow, E_η*(88)*. The collision frequencies, A_1, A_2 and A_3 will be related to the friction coefficients for the

molecule (Sect.20.4). For convenience we will use a semi-empirical model. The activation energies and the collision frequencies were chosen such that $R_x=10R_y=20R_z$, τ_{obs}=20pS at 310K and the simulated activation energy for τ_{obs} was 13.6kJ/mol. (Obtained from previous work). The observed correlation time was calculated using Eqn.15.4 and Eqn.15.6. The results are shown in Fig.15.2. Some results from earlier work are also shown in Fig.15.3. Results for isotropic motion were also calculated for comparison.

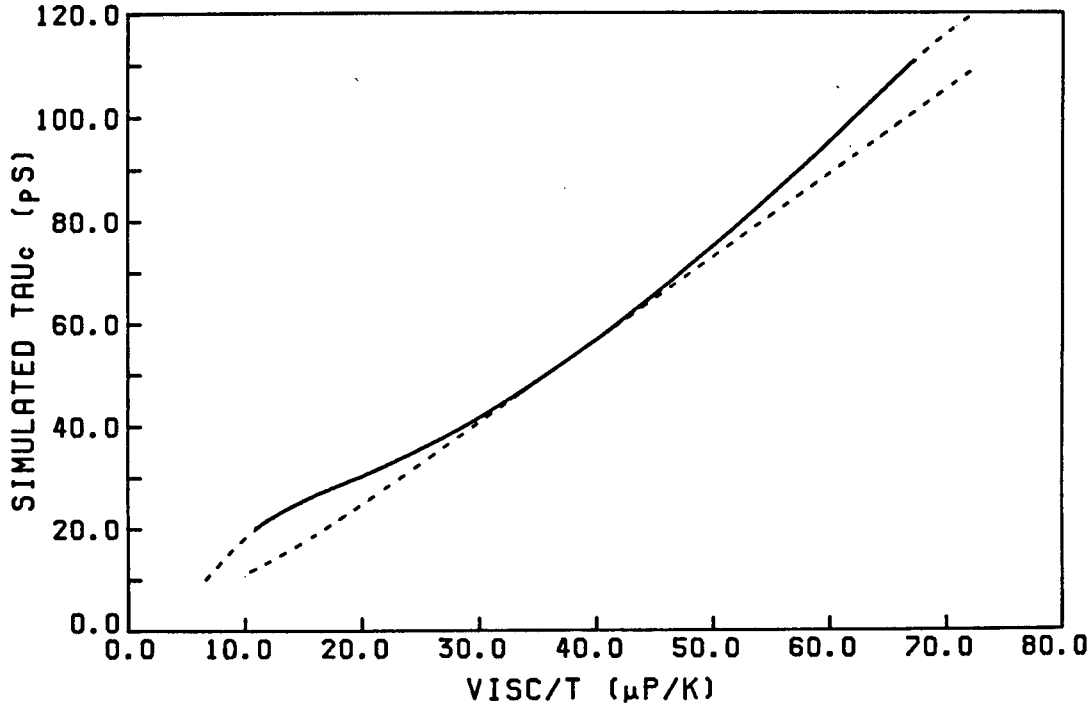

Figure 15.2. The effect of anisotropy on η/T plots. The dashed line is for isotropic motion. The dotted extensions show the functional form of the plot in experimentally inaccessible regions.

The graphs show a break in the slope at about 30μP/K. Above this point the graphs are almost identical, below this point the match is poor, but both show a finite intercept.

This implies that τ_0 may be a measure of motional anisotropy, not an alternative relaxation mechanism.

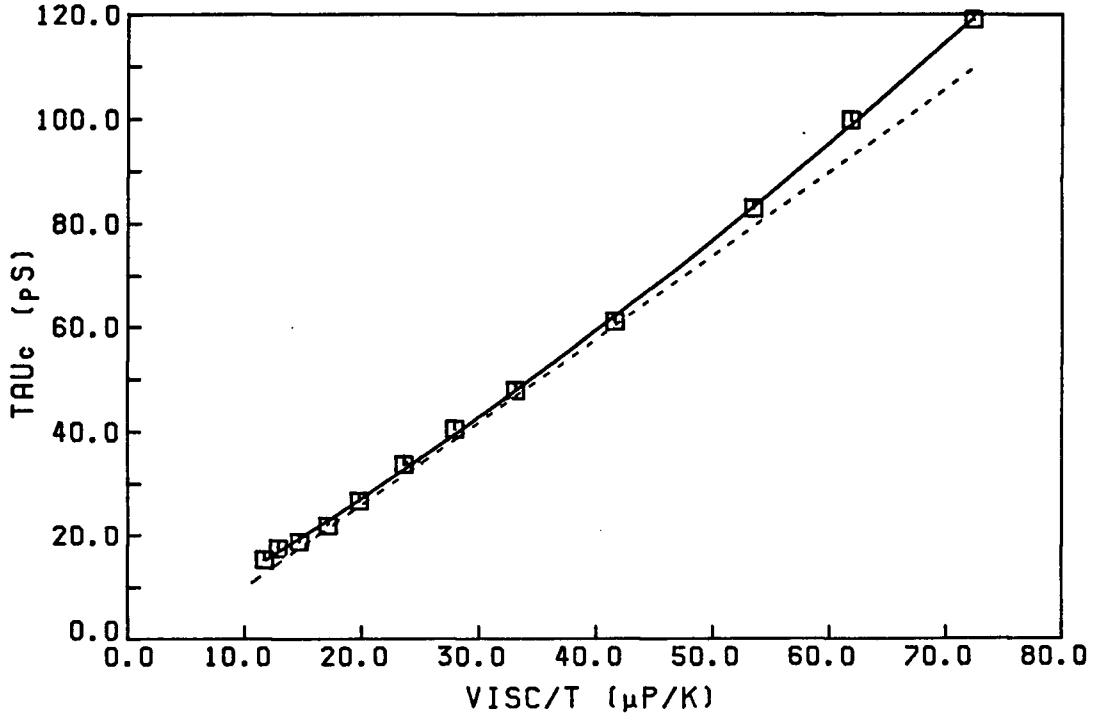

Figure 15.3. A η/T plot from previous work. This plot is typical of all previous results. All show the same form except at low η/T values where the curve up is often smaller. The dotted line is the same as in the previous figure.

The deviation for η/T<30μP/K however does indicate that an additional diffusion mechanism maybe important at high temperatures. Table 15.7 shows that in this temperature regime the spin-rotation term accounts for 80% of the line-width of the narrowest line and 50% of the broadest line and overall 50% of the relaxation. The least-squares-fit may not be very reliable under these conditions and produce a systematic artefact that is responsible for the observed curvature. (*c.f.* Table 15.6).

It should be noted that Eqn.15.6 is not a proposed model for fitting the experimental data, it is merely to demonstrate that, if the motion is anisotropic then we can partially account for the non-linearity of the τ_c *vs.* η/T plots and wholly account for the presence of the finite intercept. That is, τ_0 is an artefact of the isotropic approximation. This example clearly demonstrates the dangers of assuming an isotropic model when doing motional studies.

Temp(°C)	Zero Freq.	Larmor Freq.	Residual
-30	2.2	0.5	0.7
	13.6	1.5	0.7
+10	1.0	0.3	1.9
	6.0	1.0	1.9
+60	0.5	0.4	3.4
	2.9	1.2	3.4

Table 15.7. Relative relaxation contributions at various temperatures, in Gauss, for CuPydtc in toluene. The first row of each entry is for the narrowest line, the second row is for the broadest line

15.7 CONCLUSIONS

We have demonstrated that by assuming isotropic motion that not only is information lost, but also that artefacts are introduced. The free-rotor term postulated by Pecora *(147)* probably[43] arises from the non-linearity introduced into

---

[43]The NMR equations are similar, but more complex than for the ESR case and it is difficult to demonstrate for the general case that artefacts arise. Each case has to be considered separately.

τ_c *vs.* η/T plots by assuming isotropic motion, when it is in fact anisotropic. The isotropic assumption also obscures the fact that the activation coefficients for the diffusion constants may be different, which casts serious doubts on the validity of the hydrodynamic model. Also other effects, such as the proposed chain coiling for the MeOd derivative and the entry of some of the tensor elements in to the slow-motional regime are obscured.

The data are conveniently inverted *via* the spectral densities. The inversion process is linear and independent of the motional model used. However, diffusion constants obtained *via* approximations and the spectral densities tend to be 'noisy'. Its not clear whether the method is inherently unreliable because $j(\omega)<<j(0)$, or whether the precision of the more direct methods used by Park is an illusion; R_{iso} will be $\sqrt{3}$ more precise than the anisotropic values because of averaging. The 'noisy' data probably gives a better reflection of the accuracy (reliability) of the results though.

The assumption of isotropic diffusion does not produce trends that reflect the trends for the individual tensor elements, in fact it produces very misleading results. Despite its simplicity the isotropic model should be abandoned and τ_c's replaced by spectral densities. Although the use of spectral densities is not without problems they are less misleading and probably reflect our lack of understanding of the problems better.

PART 4.

NMR STUDIES

16. NMR THEORY

NMR relaxation theory is well developed and is discussed in a number of texts *(91)(92)*. There are many mechanisms that contribute to the relaxation times of a nucleus. The most efficient mechanism is quadrupolar relaxation and for nuclei with I>1/2 this is the dominant mechanism and indeed the only mechanism that need be considered. For this reason there have been numerous relaxation studies using quadrupolar nuclei *e.g. (102)(151)(149)(152)(153)*. For I=1/2 nuclei there are several competing relaxation mechanisms; proton dipolar coupling is usually the principal one. However for *dtc's* the 'thio' carbon is remote from the protons and the other mechanisms are more important. The one of most interest is relaxation due to the chemical shift anisotropy (CSA). This mechanism and quadrupolar relaxation are discussed below. The other mechanisms make small contributions and are discussed briefly in the error section (Sect.18).

16.1 CHEMICAL SHIFT ANISOTROPY (CSA)

The CSA contribution to the ^{13}C relaxation time for a planar rotor is given by *(102)*

$$T_1^{-1} = (3/10)\omega_0^2\delta_x^2 f(\Omega,D) \qquad (16.1)$$

where

$$f(\Omega,D) = (3/4R_r)^{-1}\left[a\cos^2\theta + b\sin^2\theta - c\sin^2\theta\cos^2\theta\right] \qquad (16.2)$$

and

$$a = (1/3)[4R_x+(\eta-1)^2R_y+(\eta+1)^2R_z]$$

$$b = (1/3)[4R_y+(\eta-1)^2R_x+(\eta+1)^2R_z]$$

$$c = (1/9)(\eta-3)^2\left(\frac{R}{R_z}x\frac{-R}{+R_s}y\right) \qquad (16.3)$$

where $\eta=(\delta_y-\delta_z)/\delta_x$, θ is the angle of δ_x, the traceless x component of of the CSA tensor, from an arbitrarily chosen x axis, (but z must be perpendicular to the plane of the rotor and is defined by Fig.10.1), R_x, R_y and R_z are the principal elements of the diffusion tensor. For a *dtc*, ϕ=0 as the ^{13}C CSA tensor is co-linear with the molecular frame. Eqn.16.1 thus reduces to

$$J(\omega) = (4R_r)^{-1}[4R_x+(\eta-1)^2R_y+(\eta+1)^2R_z] \qquad (16.4)$$

Note the similarity of this equation with Eqn.12.23 for $\eta\&\omega=0$. In principle we can combine the ^{13}C data with the ESR data (if $\eta\neq0$), or the deuterium data (or both) to obtain the diffusion tensor.

16.1.1 ISOLATING THE CSA TERM

For isotropic diffusion the CSA ^{13}C relaxation time is given by

$$T_1^{-1} = (9/10)\omega_0^2\delta_x^2(1+\eta^2/3)\tau_c \qquad (16.5)$$

In our case $\eta=2.12$ and $\delta_x=76.9$ppm. Using a value of 20pS for τ we get a relaxation time of 38s. Note that this relaxation time is field dependent so we can separate the CSA term from all the other relaxation mechanisms by multifield NMR experiments. Most notably we can separate out the spin rotation (SR) contribution which is usually similar in size and in fact directly related to *(154)* the CSA term.

To separate the terms we define

$$T_{csa}^{-1} = a\omega^2$$
$$T_{res.}^{-1} = b$$
$$T_{obs.}^{-1} = a\omega^2+b$$

so for experiments with the CXP200 and WH400 we get

$$(T_{obs.}^{-1})_{200}-(T_{obs.}^{-1})_{400} = a(200^2-400^2)$$

Thus we can determine 'a' and T_{csa}^{-1}. Unfortunately $T_{csa}^{-1} \simeq T_{res.}^{-1}$ and the error in 'a' is thus large, which compounds the experimental errors in $T_{obs.}^{-1}$.

16.2 QUADRUPOLAR RELAXATION

The relaxation time of an I=1 nucleus in a planar asymmetric rotor is given by (for η=0) *(102)*

$$1/T_1 = 3/8\chi^2 J(0) \qquad (16.6)$$

where χ, the quadrupolar splitting constant is $e^2qQ/\hbar$ (Q is the quadrupole moment and q the electric field gradient) and $J(0)=f(\Omega,D)$ which is defined by Eqn.16.2,

but where $a = R_z + R_s$

$$b = (R_z+R_s)\cos^2\phi + (R_y+R_s)\sin^2\phi - \frac{(R_x-R_y)^2}{R_z+R_s}\cos^2\phi\sin^2\phi$$

$$c = \frac{(R_z-R_x)^2}{R_y+R_s}\cos^2\phi + \frac{(R_z-R_y)^2}{R_x+R_s}\sin^2\phi - \frac{(R_x-R_y)^2}{R_z+R_s}\cos^2\phi\sin^2\phi \quad (16.7)$$

where θ is now the polar angle (C-D) bond angle with respect to the z-axis and ϕ is the planar angle (angle with respect to the x axis). The choice of axis is arbitrary, we will use the axis system previously described. Note that this function is symmetric with respect to R_x and R_y if the planar angles are symmetry related. (*e.g.* for two nuclei 'a' and 'b', $\phi_a \neq \phi_b + n\pi/2$, where n is integral)

For the pyrollidine derivative there are two magnetically distinct types of deuterium. We thus need a third piece of information to invert the data to get the rotational diffusion tensor. The ^{14}N relaxation time is an obvious, but impractical choice (*vide infra*). Relaxation times from ESR or ^{13}C spectra are other possibilities.

There are two quadrupolar nuclei of interest in our compounds, D and ^{14}N. The ^{14}N case is very similar to that of pyridine *(151)*. If we assume isotropic motion as before we get that

$$T_1^{-1} = 24\chi^2\tau_c \qquad (16.8)$$

for ^{14}N, $\chi \simeq 5MHz$ and (from ESR) $\tau_c \simeq 20pS$. Hence T_1 will be <0.1mS. Hence, T_2 will be $\simeq$0.1mS, implying a half-height line-width of $\simeq$3kHz. This fact coupled with the low resonant frequency (11MHz at 4.7T) and low sensitivity of the nucleus means that ^{14}N T_1 for our system measurement are not feasible with the available spectrometers.

Deuterium measurements however, are possible. This nucleus is 10x more sensitive than ^{14}N and $\chi \simeq 100kHz$ so that the T_1's are approximately 1sec.

16.3 SPIN ROTATIONAL RELAXATION

The T_1 for spin rotational relaxation is given by Speiss *(107)* as

$$T_1^{-1} = \tfrac{2}{3}\frac{kT}{\hbar^2} \sum_{i,j} \theta_j c_{ij}^2 \tau_j \qquad (16.9)$$

where θ is the inertia tensor, c_{ij} is the spin rotation tensor in the inertial frame, τ_j is the angular momentum correlation time.

As with ESR the spin-rotation tensor may be calculated from the chemical shift tensor data.[44] The spin-rotation

---

[44] This has been done successfully for fluorine in a number highly symmetric metal fluorides *(155)(156)*. The applicability of this method to ^{13}C in asymmetric transition metal complexes is open to question.

contribution can often be extracted from experimental data by measuring T_1 over a wide temperature range. The spin-rotation term dominates at high temperature as it varies with temperature, T, whereas all other relaxation mechanisms vary as 1/T. However, even if spin-rotation data of reasonable accuracy is obtained its interpretation is, as with the ESR case (Sect.12.5), not currently possible.

16.4 CHOICE OF T_1 EXPERIMENT

A number of methods for measuring T_1'S have been proposed *(157)(158)(159)(160)(161)(162)(163)* and analysed with respect to precision and efficiency *(164)(165)(157)(166)(158)(167)(168)(169)(170)(171)(172)(173)(174)*. A good introduction to the various methods is given in *(175)*. The two most reliable methods are inversion recovery (IR) and saturation recovery (SR). The former method is generally regarded as the faster (for a given precision) of the two methods, although there is some confusion in the early literature about this. The latter method is relatively insensitive to instrument settings and thus probaly more accurate.

16.4.1 THE INVERSION RECOVERY EXPERIMENT

There has been a lot of discussion of the relative efficacy of IR *vs.* SR techniques *(157)(158)(167)(176)(174)* Basically the IR method is considered more efficient because a) it has twice the dynamic range of

the SR technique (the data are spread from $-m_\infty$ to $+m_\infty$[45] as opposed to 0 to m_∞ for SR). b) The m_∞ value is, in principle, recoverable at time zero. One doesn't have to wait for $5T_1$'s to get the value. In practice these advantages are rather small. Reliable results for m_∞ could not be obtained at time zero. The 90° and 180° pulses have to be set independently (because the pulse shape is not perfect) to within 1° *(172)*.[46] and maintained there (*i.e.*, the transmitter must be stable for the duration on the experiment). Also each pulse sequence must contain a $5T_1$ (minimum) delay *(168)(169)(170)* so one has to establish an approximate T_1 to set this delay correctly. All these factors lead to long set-up times (≃5hrs in the case of the CXP200), which can abrogate the dynamic range advantage that the IR experiment has over the SR experiment, which is easier to set up.

16.4.2 THE SATURATION RECOVERY EXPERIMENT

This method eliminates the need for the $5T_1$ wait between pulses, but one has to collect four times as much data as with the IR experiment to achieve the same precision. Also the m_∞ value cannot be obtained at time zero, getting this value can account one third of the data collection time. However, this method is quite

---

[45] The equilibrium magnetisation.
[46] There are multiple pulse sequences that minimise this problem *(177)(178)(179)*, but they increase set-up time further

insensitive to the pulse length setting and hence to the r.f. inhomogeneity and the offset *(180)*. The pulse length and offset should be set reasonably close to the correct value to maximise sensitivity, but do not have to be exact. This considerably reduces the set-up time. Because the SR method is insensitive to instrument artefacts it should be more accurate than the IR method for a given precision. Unfortunately, this method only gives correct results for samples where $T_2^* << T_1$.

16.4.3 INVERSION RECOVERY VS. SATURATION RECOVERY

The final conclusion is that if the instrument is perfect and properly set-up, then IR is the more efficient method to use. In practice the ease of set-up and insensitivity to artefacts of the SR method overides the theoretical efficiency advantage of the IR method for samples with long T_1's. Hence the IR method was used to measure the deuterium T_1's and the SR method was used for the ^{13}C relaxation measurements.

17. NMR EXPERIMENTAL

17.1 PREPARATION OF THE SOLUTIONS FOR NMR

The samples were prepared as with the ESR samples (Sect.13), except that the saturated solution of the appropriate isotopically substituted nickel complex was used. The nickel salts were prepared from copper free nickel chloride (Sect.3.3), but otherwise they were prepared in the same manner as the copper complexes.

17.2 NMR SAMPLE TUBES

Samples for use on the WH400 were sealed in 5mm NMR tubes using standard methods. Samples for the CXP200 were sealed in short lengths (3.5-4.0cm) of 7mm o.d. glass tubing. Only a small 'bubble' was left, to minimise r.f. inhomogeneity. (However, the 'bubble' must be large enough to accomodate thermal expansion of the solvent).

Solutions of the pyrollidine derivative were prepared as needed rather than stored because of problems with decomposition of the samples (Sect.3.5).

17.3 POWDER SPECTRA

The ^{13}C chemical shift anisotropy was measured from ^{13}C powder spectra using standard cross polarisation techniques *(181)*. The pulse sequence used is shown below.

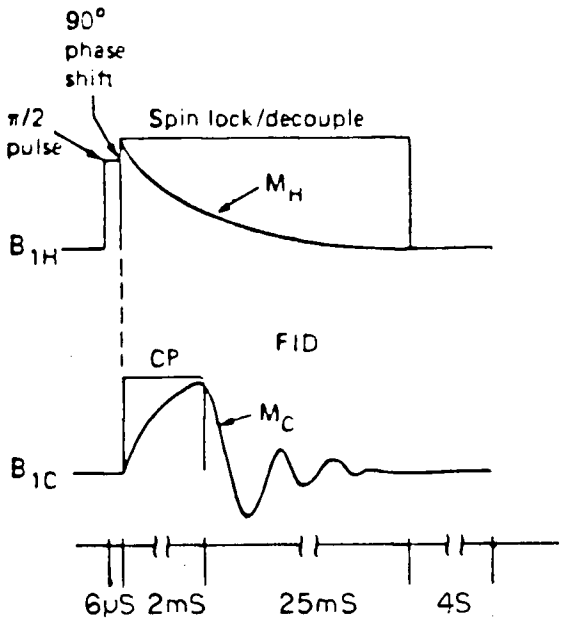

Figure 17.1. Schematic of the pulse sequence used to obtain the powder spectrum.

17.4 T_1 MEASUREMENTS

Deuterium spectra were initially recorded at 30.7MHz using a phase alternating inversion recovery (IR) experiment.

$$[(+X)_{180}\text{-}\tau\text{-}(+X)_{90}\text{-}5T_1,(+X)_{180}\text{-}\tau\text{-}(-X)_{90}\text{-}5T_1$$
$$-(-X)_{180}\text{-}\tau\text{-}(+X)_{90}\text{-}5T_1,(-X)_{180}\text{-}\tau\text{-}(-X)_{90}\text{-}5T_1]$$

Typically 2000 scans were used. Later experiments were performed on the WH400 using the Bruker IR experiment. A typical set of results is shown in Fig.17.2.

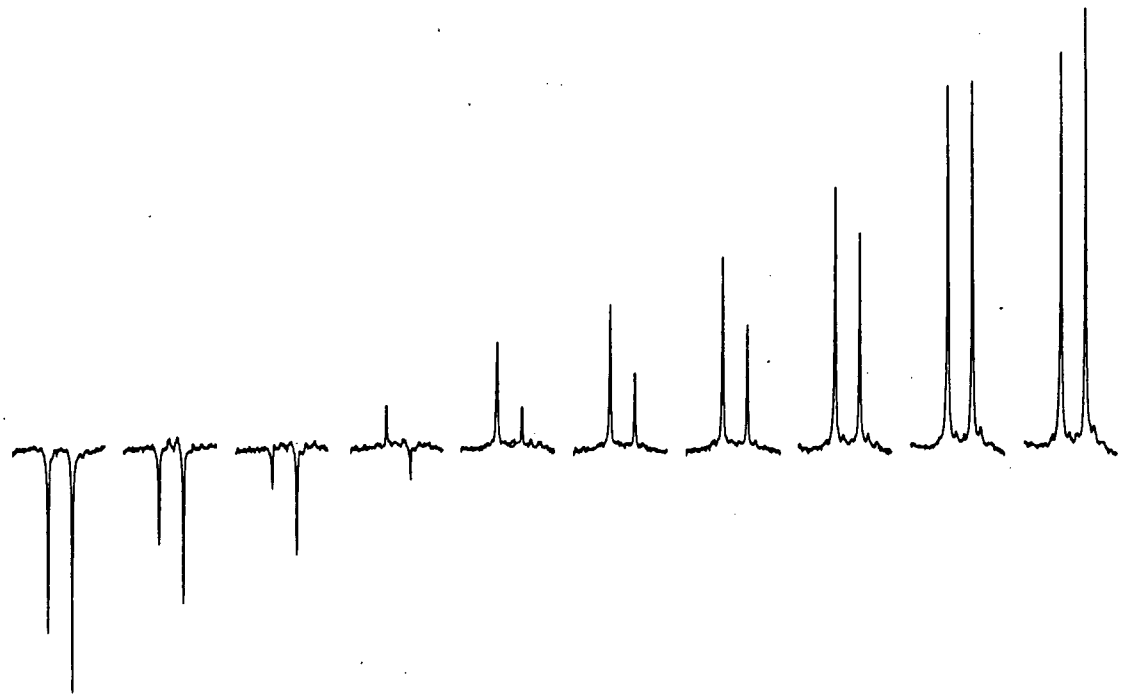

Figure 17.2. Typical IR data set. Delay times are 30, 50, 70, 100, 130, 150, 180, 250, 500 and 1000mS. 61.4MHz, T=310K.

^{13}C spectra were recorded at 100MHz using the WH400's software for the saturation recovery experiment and also at 50MHz (CXP200) using the following phase alternating sequence.

$$[20\{(+X)_{90}-\tau_s-(+X)_{90}\}-\tau-(+X)_{90}$$
$$-20\{(+X)_{90}-\tau_s-(+X)_{90}\}-\tau-(-X)_{90}]$$

where $\tau_s > T_2^* \simeq 50$mS. Typically 200 scans were used. Some data are shown below

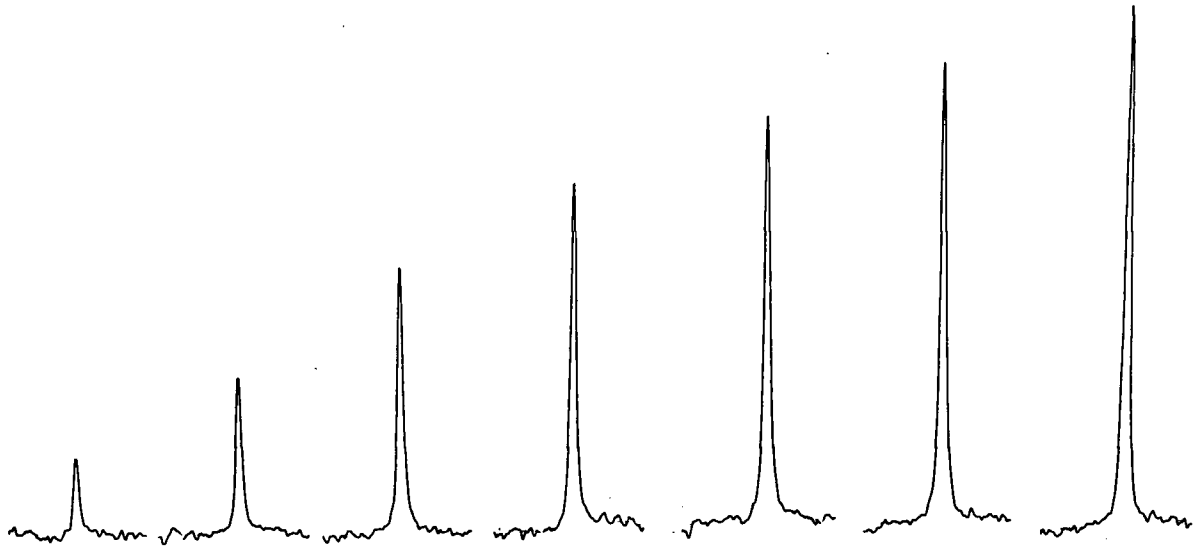

Figure 17.3. Typical SR data set. The delay times are 2, 5, 10, 15, 20, 30 and 100s. 100.6MHz, T=310K.

17.5 ANALYSIS OF NMR DATA

T_1 data were analysed by the standard method *(175)* of measuring peak heights and doing a least-squares-fit to a semi-log plot of magnetisation *vs.* delay using the following equations.

$$m_\tau = m_\infty(1 - ke^{-\tau/T_1})$$

hence $$\ln(m_\infty - m_\tau) = \ln(k) - \tau/T_1$$

where m_∞ is the equilibrium magnetisation ($\simeq m_\tau$ for $\tau > 5T_1$) and k=1 for a saturation recovery (SR) experiment or k=2 for an inversion recovery (IR) experiment.

18. NMR ERROR DISCUSSION

As with ESR there are a number of sources of error. The experimental errors are different from ESR, instrumental artefacts play a much larger role in NMR experiments than in ESR experiments.

18.1 ON APPROXIMATING THE SPECTRAL DENSITIES

The spectral densities are of the form

$$j(\omega) = \frac{\tau_c}{1+(\omega\tau_c)^2} \qquad (18.1)$$

where ω is the Larmor frequency of the nucleus being studied and τ_c is a linear combination of the rotational eigenvalues for an asymmetric rotor. τ_c is 10-200pS and ω is a maximum of 100MHz (for ^{13}C at 9.4T), giving $(\omega\tau_c)^2$ a maximum value of <0.02, *i.e.*, an error in assuming $j(0)=j(\omega)$ of <2%, well within experimental error. However, it is interesting to note that this approximation is inappropriate for 400MHz proton spectra.

18.2 RESIDUAL CONTRIBUTIONS TO RELAXATION

There are a number of contributions to relaxation, their magnitude varies greatly from system to system. For quadrupolar nuclei, quadrupolar relaxation is the only significant source of relaxation. For spin 1/2 nuclei, there are many sources of relaxation. The major one for *dtc's* have

been discussed in Sect.16., other minor contributions are discussed below.

18.2.1 INTERMOLECULAR DIPOLAR RELAXATION

This arises from the translational diffusion of the solvent past the solute. The relaxation time of a spin I (in the solute) by a nucleus S (in the solvent) is given by *(182)*

$$T_1^{-1} \simeq D^2 S(S+1) N\eta/kT \qquad (18.2)$$

where $D = \hbar^{-1}\gamma_I \gamma_S r_{IS}^{-3}$. This assumes Debye diffusion in the fast motional limit and that the relaxation of S is independent of that of I, which is reasonable if $\gamma_I >> \gamma_S$. For protons[47] in chloroform diffusing past a ^{13}C nucleus we have $S=\frac{1}{2}$, η the viscosity at T=300K is 0.57cP and the proton number density is 7.5×10^{21} spins/cm^3. This gives a T_1 of 30000s, an error of 0.1% for a 30s T_1 typical for the ^{13}C in our system. As deutero-chloroform was used as solvent the error will be negligible.

---

[47] In theory the chlorine atoms make a 10x larger contribution than the proton. However their relaxation times are very fast (they are quadrupolar nuclei) and they are unlikely to make any contribution to the relaxation of the solute.

18.2.2 INTRAMOLECULAR DIPOLAR RELAXATION

The ^{14}N nucleus bound to the ^{13}C may cause dipolar relaxation. The T_1 for this is given by *(182)*

$$T_1^{-1} = \frac{2}{15} I_N(I_N+1)D^2J(\omega) \qquad (18.3)$$

In the fast motional limit, for isotropic motion $J(\omega)=10\tau_c$ hence

$$1/T_1 = 3/8D^2\tau_c \qquad (18.4)$$

For our case $\tau_c \simeq 20$pS at 300K and r=1.33A *(183)*, giving a T_1 of $\simeq$ 500s. However, τ_c is estimated from ESR data assuming isotropic motion. The correlation time for the motion affecting the dipolar relaxation (end-over-end with respect to the C-N bond) is probably longer and T_1 may be sufficiently short to make a significant contribution to the relaxation.

18.2.3 FLUCTUATIONS IN THE SCALAR COUPLINGS

Relaxation of the ^{14}N nucleus contributes to the ^{13}C relaxation *via* the coupling, J_{CN}. The T_1 for this mechanism is given by

$$T_1^{-1} \simeq (2/3)J^2S(S+1)\tau'$$

where
$$\tau' = \frac{\tau_N}{1+(\omega_N-\omega_C)^2\tau_N^2} \qquad (18.5)$$

assuming fast isotropic motion. For our case we have S=1 and $\tau_N \simeq 0.1$mS (see Sect.16.2). $J_{CN} \simeq 15$Hz hence $T_1 \simeq 15000$s, a negligible contribution.

18.2.4 INTERNAL MOTION

Contributions from pyrollidine ring pucker are negligible (see appendix 22.8). The diethyl derivative is a similar size to the pyrollidine derivative and both give the same results for ESR data *(88)*. However, its stereochemistry is different, the ethyl groups are probably vertical with-respect-to the plane of the molecule. There is a large steric hindrance between them so one will stick up and one down. Fluctuations in this geometry are unlikely to affect the ^{13}C relaxation times, but this conformation will reduce the diffusion coefficients for rotation about the x and z axes. This may account for the incompatibility of the ^{13}C results and the D-NMR and ESR results.

18.3 ERRORS FROM DATA ANALYSIS

The semi-log data analysis method is very sensitive to the m_∞ value used. To minimise this effect the experimental data was interactively fitted to an exponential.

Multi-exponential fitting methods are available *(166)(168)(184)(185)(186)(187)(188)(189)(190)(191)* which in principle do not need an m_∞ value. These methods give reasonable results with poor m_∞ values (*i.e.*, at low SNR), but do not give reliable results unless an m_∞ value is included in the data set *(43)*. Also these methods can be used to correct for mis-set pulse lengths and r.f. inhomogeneity. However, their use with small noisy data sets (as is the case here) is questionable *(192)*.

18.4 ERRORS IN T_1 MEASUREMENTS

T_1 measurements of low sensitivity nuclei with long relaxation times are extremely demanding on the spectrometer. In our case the experiment may last three days, during which the transmitter must remain stable, the spinning rate must be constant, the magnetic field should not drift and the temperature should be constant. Other sources of error arise from r.f. inhomogeneity, paramagnetic impurities, temperature gradients and diffusion of the probe out of the coil *(157)*.

There is little that one can do about variable spinner, transmitter or temperature instability, other than to reject suspect data. Temperature instability was not a problem,

although temperature gradients of >1°C are present across the coil *(193)*. The field of the CXP 200 appears to be stable. Experiments with the WH400 were done with a deuterium lock. SR experiments are insensitive to r.f. inhomogeneity, but it can cause problems in IR experiments. This effect can be minimised by using short sample tubes. The effects of the probe diffusing out of the coil can also be minimised by using short samples. It is essential to remove paramagnetic impurities when measuring long T_1's as they greatly reduce the relaxation time *(e.g. (175)(182)(194)*. All samples were prepared from copper-free nickel salts and deoxygenated before use.

19. NMR RESULTS AND DISCUSSION

19.1 ^{13}C RESULTS

The ^{13}C relaxation results are shown in Table 19.1. The errors are estimates only and just serve as a guide to the relative reliability of the relaxation times. The results are averages of, or selected values from, several runs. (See appendix 22.12 for the complete data).

Temp K	50.3MHz	100.6MHz	T_1(CSA)
310	22±1	10±1	60±10
323	16±1	11.5±1	125±20
333	11.5±2	8±1	165±30

Table 19.1. ^{13}C T_1's for Et_2dtc. (secs).

The CSA tensor was determined from the powder spectrum, but there is some ambiguity in the assignment of the y and z components of that tensor. (The x component can be uniquely determined from the dipolar splitting of the powder pattern, see appendix 22.3). As we have an over-determined system (5 pieces of relaxation data and 3 unknowns) we should be able to resolve the ambiguity from the relaxation data. However, the fastest rotation axis is about the C-N bond (*i.e.*, the interchange of the y and z components is the most important contribution to the relaxation time). If we assume $R_x >> R_y, R_z$ in Eqn.16.4 then T_1 is independent of η. Hence within

experimental error we cannot distinguish between the y and z components of the CSA tensor. (The corollary, of course, is that we don't need to anyway!)

19.2 DEUTERIUM T_1 RESULTS

The deuterium relaxation results are shown in Table 19.2 (see appendix 22.11 for the complete data).

Temp K	30.7MHz		61.4MHz	
	N	R	N	R
310	0.167	0.207	0.162	0.200
323	0.185	0.265	0.185	0.270
333	NA		0.187	0.242

Table 19.2. Deuterium T_1's for d-9 Py_2dtc. Times are secs.

The 61.4MHz and 30.7MHz results are identical as expected. The spectra for the 333K results show extra peaks indicating that the sample is decomposing. These T_1 values are suspect.

The quadrupolar splitting constant for our compound in solution is not available, however these values are nearly constant for alkyl compounds *(195)*. A value of 175kHz was used.

19.3 DISCUSSION

The two deuterium T_1's can be combined with the ^{13}C data and, using Eqn.16.4 and Eqn.16.7 solved for the diffusion tensor using non-linear least-squares-fit procedures *(196)*. The results are shown in below.

Temp K	R_x	R_y	R_z
310	non-convergent		
323	60.2	8.9	-0.9
333	46.9	10.5	-1.7

Table 19.3. The diffusion tensor from ^{13}C and ^{2}H data

The unsatisfactory results are probably attributable to the low quality of the ^{13}C data.[48] Also simulations using known values for the diffusion tensor show that the ^{13}C relaxation time is essentially independent of R_x, this may lead to incorrect convergence of the fitting routine, especially coupled with the large errors in the ^{13}C T_1's.

The deuterium data can be combined with the ESR data and sucessfully inverted (Part.5).

---

[48] The ^{13}C data are also incompatible with the ESR data.

PART 5.

COMMENTS ON THE COMBINED NMR-ESR STUDIES

20. COMBINED ESR AND NMR RESULTS AND DISCUSSION

20.1 INTRODUCTION

The NMR and ESR results have been combined to obtain the rotational diffusion tensor for MPy_2dtc in chloroform. Although the results span a limited temperature range they demonstrate the utility of combined ESR-NMR studies to obtain diffusion tensors. Also they provide a starting point to explore some approximation methods for extracting diffusion tensors from ESR data alone. Furthermore the results can be used to check the validity of the hydrodynamic model for rotational diffusion.

20.2 COMMENTS ON DATA INVERSION

Inversion of non-linear equations can be problematic, especially if good starting values are not available, or there are large errors in the data. Some workers *(151)(180)* studying diffusion tensors with NMR have resorted to incrementally searching a range of possible values for R_x, R_y and R_z. This is a reasonable approach because the range of values for the R's are quite constrained. (They are all positive and one can use hydrodynamic models to get order of magnitude values for them). For our system good starting values for R_x and R_y+R_z are available by using the approximation methods outlined in Sect.15. However, one has to invert the data initially to ensure these approximations are valid so the generality of this approach is

questionable.

One serious problem arises when inverting the ESR data because Eqn.12.23 is symmetric with respect to the interchange of R_x and R_y, *i.e.*, $\lambda(\omega)$ and $\lambda(0)$ are not completely independent functions. However, an incremental search works reasonably well for this function as we know, on geometric grounds, that $R_x > R_y, R_z$ (and all are positive). This approach also gives a good physical feel for λ_{00}.

The data were finally inverted with an incremental search of the ESR and deuterium data to get good starting values, followed by inversion using a Newton-Raphson procedure *(196)* to get the final values.

Incremental searching is a very inefficient approach if one doesn't have a reasonable idea of the domain of $\underset{\sim}{R}$, especially if the data contains errors. The efficiency can be greatly improved by searching for ratios of the relaxation times and ratios of spectral densities. This reduces the systematic errors in the data and halves the amount of data to be searched. A failure to obtain a match for the ratios usually indicates a fundamental error in the program, *e.g.* assigning the axes incorrectly. This approach is very useful in the initial stages of data reduction.

20.3 THE DIFFUSION TENSOR

Five independent pieces of information were obtained. Two ESR spectral densities, two deuterium relaxation times and one ^{13}C relaxation time. As we only need three independent

pieces of information to get the diffusion tensor we have an overdetermined system and thus a choice of solutions. As the equations are non-linear it is best to try to invert the data in groups of three and then cross-check the results. Grouping the two pieces of ESR data with a third is not useful (unless an incremental search is done) because of the symmetry alluded to in Sect 20.2; the data will not converge. The ^{13}C data proved to be unreliable (see Sect.19.3) so the only route was to invert the two deuterium relaxation times and j(0) (the more reliable of the two ESR spectral densities) and cross-check to see if $j(\omega)$ is correct. The results are shown in Table 20.1. The 333K pyrollidine NMR data are not reliable because the sample decomposes. The values shown for this temperature are from an incremental search of the ESR data. The errors correspond to the range of R values that give spectral densities that are within 5% of the observed values. These errors are quite respectable for an underdetermined system.

Temp(K)	R_x	R_y	R_z
310	57.6	6.5	2.6
323	82.5	7.3	2.3
333	90±10	4±3	10±5

Table 20.1. The diffusion tensor.

20.4 THE HYDRODYNAMIC MODEL

One goal of measuring diffusion tensors is to establish the geometry of a molecule in solution. The solution geometry for our probe is well defined so we can use our results to test the validity of the hydrodynamic model, the usual model used to relate the diffusion tensor to the geometry.

The dimensions of the probe can be established by a combination of crystallographic data and molecular models. Also one has to account for dead-volume *(113)*. The solvent is of finite size and, for instance, cannot penetrate the gaps between the sulphurs. The volume of the probe thus appears larger to the solvent than the true volume. The probe thus approximates a rounded parallelepiped with dimensions x,y,z, of 1.6x0.5x0.25 nm. Hydrodynamic theories have only been developed for ellipsoids, but fortunately the probe is well approximated by an ellipsoid with dimensions 1.75x0.65x0.3 nm. (see Fig.20.1)

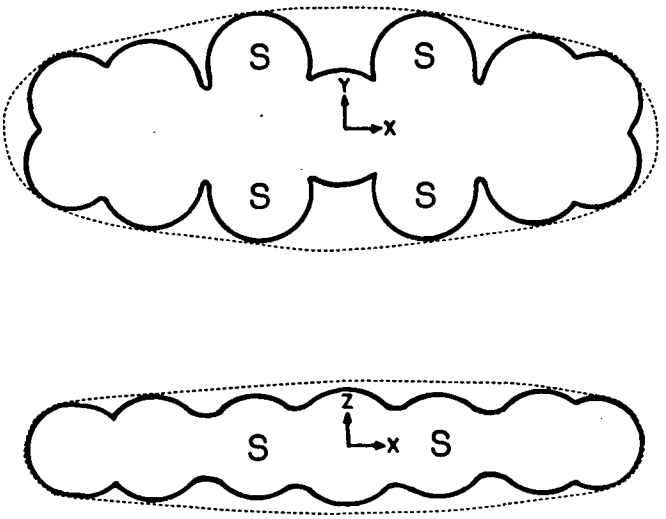

Figure 20.1. The probe as an ellipsoid.Scale is 1cm=0.5nm. Solid line is Van-der-Waals shape. Dotted line is ellipsoidal approximation.

The diffusion coefficients for an ellipsoid from the hydrodynamic models given by Perrin *(108)* and Youngren and Acrivos (YA) *(111)* are

$$R_i^{stick} = 3kT/4\pi a^3\eta(4C_i)$$

$$R_i^{slip} = 3kT/4\pi a^3\eta(\lambda_i \rho_1\rho_2) \qquad (20.1)$$

where 'a' (=x/2) is the length of the major semi-axis; C_i are calculated from Perrin's equations as outlined in *(88)*; λ_i are the coefficients given by YA and ρ_1, ρ_2 (a and b in YA's notation) are the semi-axis ratios, z/2a and y/2a. Note that Eqn.20.1 imply that, although the diffusion coefficients are different, the temperature dependence is

identical, both are viscosity dependent.

The appropriate friction coefficients for our probe are

	x	y	z
slip	0.22	1.46	0.635
stick	0.098	0.362	0.328

Table 20.2. Friction coefficients for the probe.

The predicted diffusion coefficients are thus

	R_x	R_y	R_z
T=310			
slip	230	34	79
stick	8.1	2.2	2.4
T=323			
slip	267	40	92
stick	9.4	2.6	2.8
T=333			
slip	300	45	103
stick	10.6	2.9	3.2

Table 20.3. Predicted diffusion coefficients for MPydtc.

Both boundary conditions give results that are an order of magnitude in error. This is not unexpected, but the failure to predict the observed order of the diffusion coefficients is disturbing. Also the relative magnitudes do not agree well. The observed value for R_x/R_p is $\simeq 7$ whilst the slip model gives $\simeq 4$ and the stick model $\simeq 3$. This implies that scaling the results to lie between the two boundary

conditions, as has been suggested *(197)*, is not satisfactory; the tensor elements behave differently. R_x has more slip character than the other two modes of motion. This is consistent with the cavity model for motion: A significant population of the molecules occupies cavities in the liquid that are large enough to permit the molecule to freely rotate, or at least undergo large angle jumps, about the x-axis (which sweeps out the smallest volume), but only a small number of the cavities are large enough to allow free rotation about the other two axes (which sweep out much larger volumes). The population of free rotors has the effect of increasing the diffusion rate and decreasing the activation energy for the rotation relative to that expected from hydrodynamic models. This is also consistent with the ESR observations discussed in (Sect.15) and other workers *(198)*.

The peculiar ordering of R_x and R_y is difficult to explain, but may reflect local anisotropy in the medium, possibly due to a weak coordination with the chloroform.

20.5 SUMMARY OF THE RESULTS

Three conclusions may be drawn from this work. a) It has been demonstrated that ESR and NMR studies can be combined to give the rotational diffusion tensor of the probe. b) The isotropic model for rotational diffusion is extremely misleading. c) The hydrodynamic model, while not misleading, fails to account for the behaviour of our probe. There is

still scope for developing this model, but a theory incorporating large angle jumps (or solvent cavities), anisotropic motion and discontinuous media may be needed.

20.6 A STRATEGY FOR MEASUREMENT OF DIFFUSION TENSORS

Firstly it should be commented that obtaining NMR relaxation measurements from dilute solutions of insensitive nuclei is extremely time consuming and very error prone. Recent developments in NMR technology have improved this situation, but instrument time is still at a premium. For this reason any strategy that reduces use of NMR spectrometers is of interest.

Secondly, the objective of the exercise is to obtain single particle correlation times for a solute in the fast-motional regime. Multi-particle correlation times are not a useful objective. Studies in neat liquids are interesting, but rather restrictive. Slow-motional studies in NMR have yet to be developed. Slow-motional studies in ESR are better developed, but it remains to be demonstrated that diffusion tensors can be reliably extracted from such spectra.

Given the above comments, how does one design a probe to obtain the best information? As discussed previously the probe should be stable with a well defined geometry and be sufficiently soluble to permit NMR studies. In addition the probe must be able to provide at least three independent pieces of data.

Consider the requirements for an NMR only study first. There should be only one relaxation mechanism contributing to the measured T_1, *i.e.*, only quadrupole nuclei should be used, although recent work using proton dipole-dipole couplings looks promising *(199)(200)*. There should be at least three magnetically distinct nuclei. Furthermore the orientation of the major axis of the quadrupole tensor for the these nuclei should be such that at least two different azimuthal angles and one polar angle $\neq 90°$ are needed to characterise their dispositions. Also the major axes must not be orthogonal. In our probe there are two magnetically inequivalent deuterons on the pyrollidine ring. The third nucleus is in the plane. We used ^{13}C, but ^{14}N or Pd could, in principle, have been used. Our third nucleus was an unsuccessful choice, but this seems to be a general problem with NMR. Two suitable nuclei can be found, but finding a third is difficult. Also the relaxation times are relatively insensitive to the azimuthal angle of the major axis of the quadrupole tensor. Ideally the azimuthal angles should be well separated, azimuthal angles of 20° and 25°, for example, may not provide enough discrimination to obtain reliable results. For these reasons it is common to resort to another spectroscopic technique to obtain the extra information. IR, LS and Raman studies have been combined with NMR to this end, but these techniques restrict one to neat liquids or strong (>10%) solutions. Here we have combined (for a first time) NMR and ESR measurements to get

the extra data. ESR allows the use of dilute solutions, but requires a paramagnetic species. In our case this is easily achieved by changing the central metal of our probe. This however, is the major restriction to this approach; there must be diamagnetic and paramagnetic analogs of the probe.

The design of paramagnetic probes is best considered in the light of Eqn.12.22. In our case this equation simplifies considerably because of axial symmetry. However, in general most of the reduced spectral densities have to be retained, but the basic form of Eqn.12.22 is unchanged by these extra terms so for the purpose of this discussion we can use the following expression for T_2.

$$T_2^{-1} = \sum_k J(0)_k [A(K+m^2) + A_g m + G] + X \qquad (20.2)$$

where the sum over k is used to denote that more than one eigenvalue for the asymmetric rotor is retained. The non-secular terms, $j(\omega)$, are not negligible, but do not affect the arguments so they are dropped for convenience.

Firstly we note that the spectrum will contain K (=2I+1) lines so the larger the nuclear spin coupled to the electron the better. For instance, vanadium, I=7/2, with eight lines gives better statistics than nitrogen, I=1, which gives three lines. If the magnetic tensors are orthorhombic and I>1 the complete diffusion tensor may be obtained from the ESR spectrum. However, if one wishes to do

this *via* the spectral densities the spectrum must contain at least 2k+1 lines, 2k for the k j(0) and j(ω) terms and one for the residual line-width, X. Also the eigenvalues are not linearly independent. Obtaining three spectral densities does not guarantee that the complete diffusion tensor can be found. However, if the data are to be combined with NMR results from two nuclei then a two line ESR spectrum will suffice if direct inversion methods are used.

It is desirable to have a large range of line-widths in the ESR spectrum to obtain reliable data. As the m_i dependence of line-width is carried almost entirely by the hyperfine anisotropy (A in Eqn.20.2) this should be quite large, but not so large that the fast-motional criterion fails for the temperature range of interest. Also the approximations discussed in Sect.14 will have to be examined. The hyperfine coupling, A_0, itself should also be large to prevent line overlap. Line overlap can also be minimised by keeping the residual line-width small. This can be achieved by using probes with no unresolved hyperfine coupling and keeping the g-anisotropy small. The latter is responsible for the spin-rotation term, the major contribution to the residual line-width.

It is interesting to note that for nitroxides the center line (m_i=0) carries very little motional information. In fact most of this information is carried by the m_i=1 line. This can be turned to advantage though, by subtracting the width of the center line from the outer two lines and

then subtracting the widths of these two lines, the relaxation Eqn.12.22 is thus considerably simplified.

To summarise, the ideal probe for ESR/NMR studies should have the following requirements.

Paramagnetic and diamagnetic structural analogs.

Magnetic tensors that are not isotropic.

At least two non-coincident axial tensors.

The geometry should be well defined, but easily tailored.

The g-tensor anisotropy should be small and the hyperfine tensor anisotropy large.

The isotropic hyperfine splitting should be such that line-width/line-splitting<0.2.

The nuclei for NMR studies should be quadrupolar.

The probe should possess enough symmetry that the orientation of the diffusion tensor is known.

The *dtc* class of probes certainly fit most of the above requirements. Their principal failings are the low solubility of the nickel complexes and the axial symmetry of the hyperfine coupling and g-tensors. However, as demonstrated here this is just an inconvenience, they can still be used to obtain the diffusion tensor. Also their geometry can, and has been, tailored for motional studies. It may be possible to tailor their chemistry for work in aqueous solvents and also improve the solubility of the nickel complexes.

20.7 FINAL REMARKS

The persistence of the hydrodynamic model for interpreting motional studies can be ascribed to three factors. For molecules that are much larger than the solvent this theory is quite accurate. However, how large the probe molecule/solvent molecule size ratio has to be before the hydrodynamic model fails is still unknown, although there have been some recent advances in this area *(201)(202)*. The isotropic model has been extensively used to interpret motional results. This approach has probably obscured the inadequacies of the hydrodynamic model and if its use persists it will seriously hamper progress in molecular dynamics studies. Also the friction coefficients scale with a^3, the largest molecular axis. A 10% variation in 'a' produces a 30% variation in the calculated correlation time. This will greatly influence the agreement or otherwise with the hydrodynamic theory. For instance, is the Van-der-Waals radius the appropriate measure of the dimensions of molecules rotating in solution? The apparent better agreement of the 'slip' rather than the 'stick' model may be a result of a systematic underestimation of the molecular dimensions.

The conceptual simplicity of the hydrodynamic model makes it very attractive. The model remains to be developed for non-spheroidal molecules. Youngren's and Acrivos's approach allows this, but the gap still remains. Obvious candidates for development are carbon-tetrachloride and

carbon disulphide, both of which have been thoroughly studied and have simple geometries. If the model fails for these two cases, then models accounting for discontinuities in the solvent and 'free-rotation' in solvent cavities *(203)(204)(136)(205)(206)* will need to be developed, or the inertial models *(50)* extended to anisotropic motion. Further studies of the 'probe in a solvent' type, as is discussed here, will be needed to point the way for theoretical developments of that kind.

PART 6.

NOTES ON THE DIGITAL ACQUISITION OF ESR SPECTRA

21. THE DIGITAL ACQUISITION OF ESR SPECTRA

21.1 INTRODUCTION

This section will address the digital acquistion of ESR spectra from two points of view, namely, the development of the software and hardware of the digital acquisition system; the development of the algorithms for the processing and analysis of the spectra.

Digital acquisition systems are not novel (for reviews see *(116)(207)* for examples see *(140)(208)(209)(198)(210)(211)(212)(213)*), but at the time of construction of our system, the micro-processer was at the leading-edge of technology (*e.g.* memory was expensive) and the personal computer had not been invented. Some of the aspects of design and methodology reflect this. Notably, the use of off-line data processing and the lack of real-time averaging facilities.

Early spectra were collected on paper-tape and processed on the Amdahl 470 at the UBC computing center *(140)*. Later, this link to the Amdahl was upgraded by the purchase of a magnetic tape unit. The use of a main frame computer places virtually no restrictions on memory or speed, so the primordial nature of our microprocesser (a Fairchild F8) was not a great disadvantage. The system was further improved by the acquisition of a DEC LSI-11 micro-computer. This computer permitted the use of interactive graphics (which were not available for the

main-frame at that time), but restrictions in memory size and speed now had to be considered.

Analysis of digital ESR spectra is more complicated than for most digital spectra because of the variability of the abscissa (field-sweep) data. Algorithms and numerical methods for manipulating digital spectra are scattered throughout the literature, but an overview of the techniques needed for processing ESR spectra is sadly lacking. Such an overview will not be attempted here, but the basic algorithms used will be briefly reviewed and this information should be of interest to anybody attaching a personal computer to an ESR spectrometer.[49]

A question that might be asked is, 'why bother to digitise ESR spectra ?', (especially considering the time needed to develop the hardware and software). The reasons are three-fold; the precision of spectrum measurement is improved by at least a factor of five; the analysis time for spectra is reduced by 2-3 orders of magnitude; digital spectra can be manipulated in a manner that is difficult or impossible using analog methods (*e.g.* DISPA). Thus both the quality and quantity of information available from a spectrum is substantially increased.

---

[49] The software was developed for motional studies only, *i.e.*, spectra consisting of a few broad lines that are measured accurately. This is reflected by the absence of software relating to spectral analysis (see *(214)(215)* for examples) or deconvolution programs *(216)(217)(218)*.

21.2 THE HARDWARE

A block diagram of the system is given in Fig.21.1. A simplified flow-chart for the software is shown in Fig.21.2

Briefly the system operates as follows. The operator enters the sample identification *etc. via* the terminal and starts the acquistion program. When the field scan is started the temperature is measured and the sample information written to the tape. Field/amplitude data are then taken simultaneously and 16 bit data point pairs written to the tape in blocks of 50 pairs. Between each block the Gaussmeter reading and the corresponding Fieldial voltage are collected. This is continued until the end of the scan when acquisition is stopped. The temperature is measured again, the microwave frequency is taken and the calibration data written to the tape. The data file can then be transferred to the DEC LSI-11 for analysis.

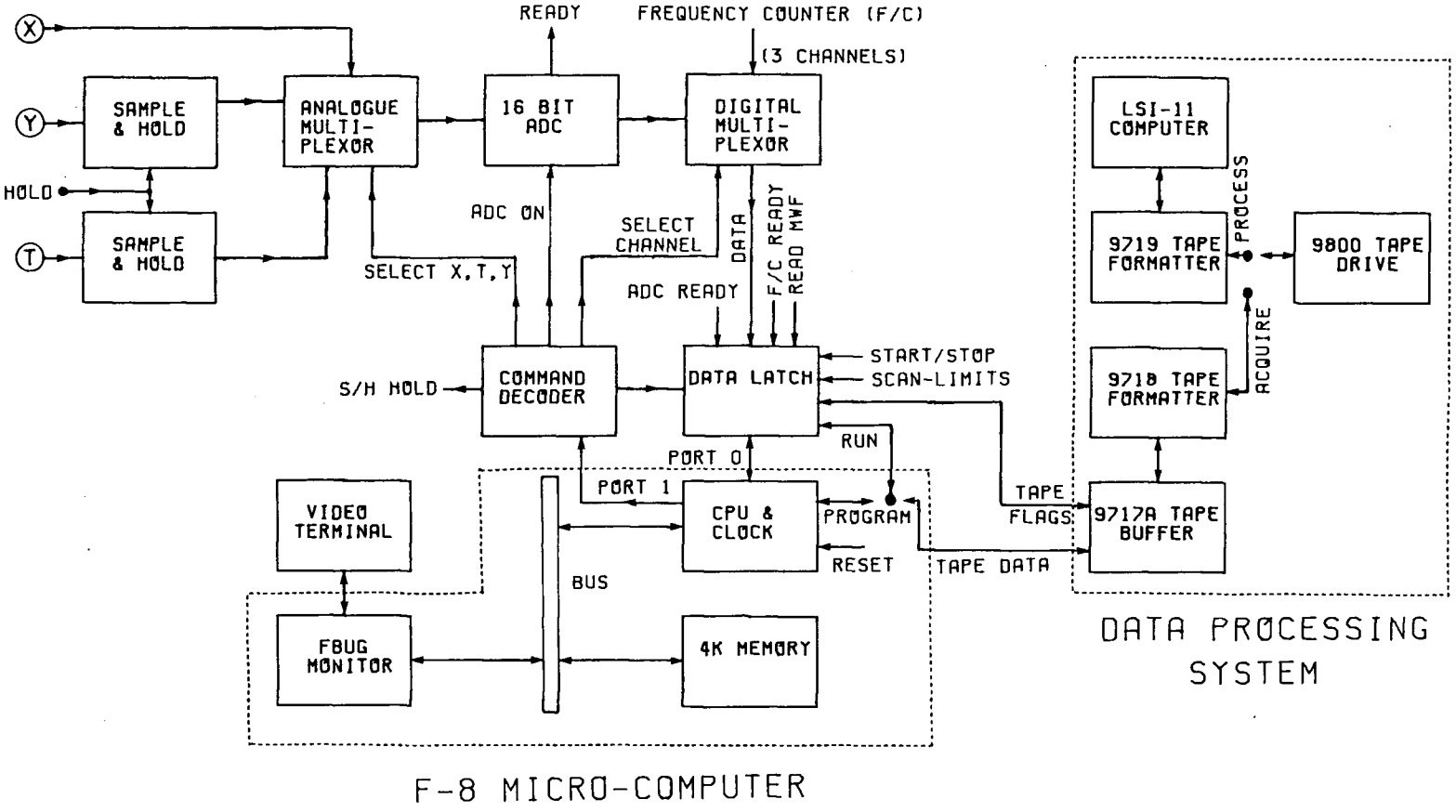

Figure 21.1. Block diagram of the acquisition system.

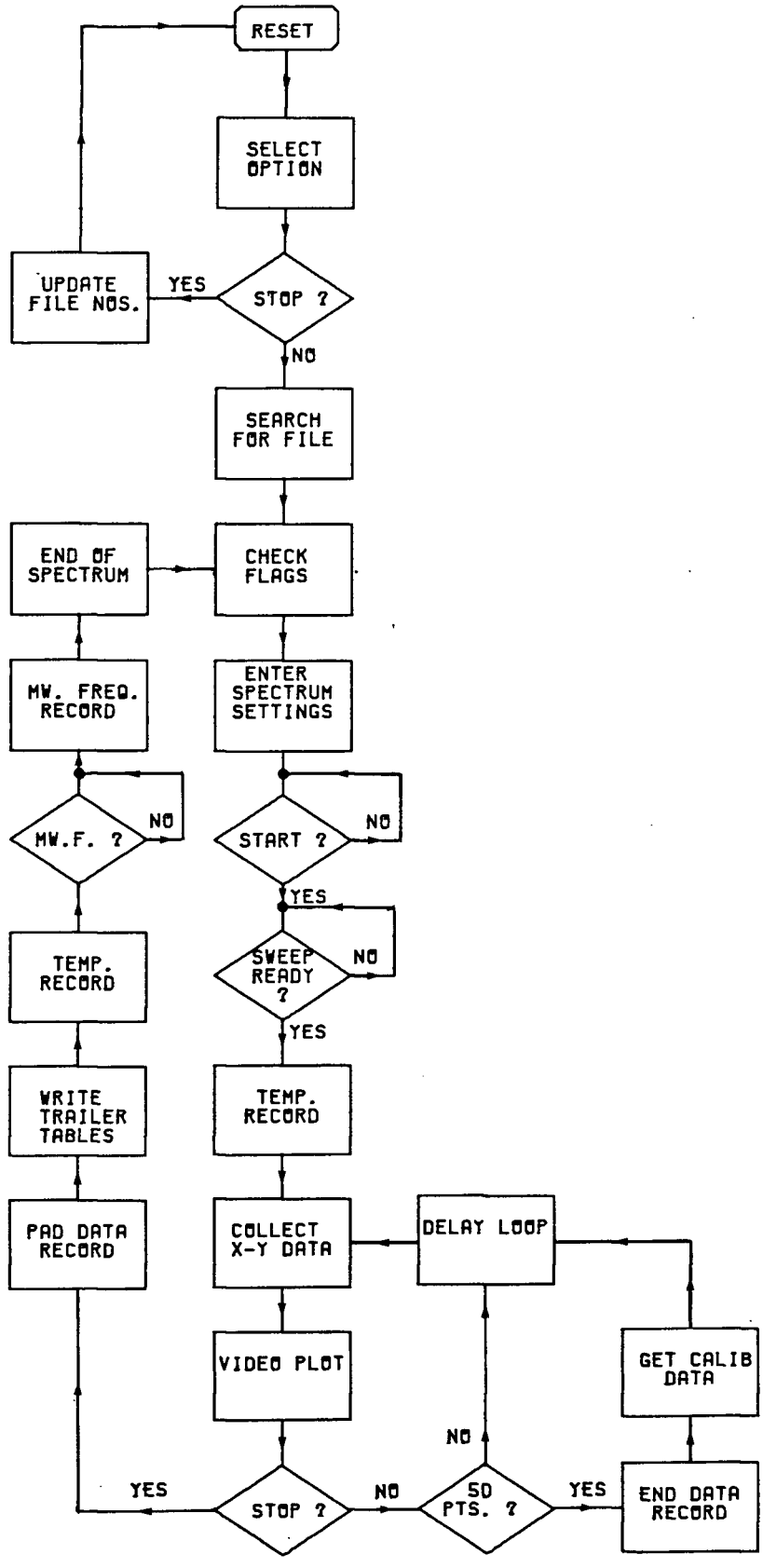

Figure 21.2. Flow-chart for the software of the acquisition system.

21.3 THE BASIC PROBLEMS IN ACQUIRING ESR SPECTRA

A number of noise sources in ESR, that are masked by the inherent time constant of the chart recorder, become apparent when one first records a digital spectrum. These noise sources depend on the spectrometer, but typical examples are; dispersion leakage, acoustic noise, magnet noise and miscellaneous cross-talk. The most severe of the latter is modulation of the spectrum by the modulation coils in the Gaussmeter probe. Careful placement of this probe is essential. (Also see Sect.14.8)

Magnet noise poses a number of serious problems. Both the width and the center of field sweep are variable[50] so some method of calibrating the sweep is essential. However, the real problem is the noise from the Fieldial sweep mechanism. The field is incremented in an inconsistent and non-linear fashion resulting in a data set that, although equally spaced with-respect-to time, is not equally spaced with-respect-to magnetic field. This has a great influence on the software design as it necessitates the collection of both field data and spectrum data; doubling computer-memory requirements. Also enough points must be collected to allow for reliable interpolation of the data. Most of the software discussed here relates to this problem. Once an equally spaced data set is created the software development is

---

[50]The front panel settings of the Fieldial are not very accurate and vary slowly with time. The field sweep can also be non-linear, although we have not detected this on our system. Algorithms to shift and expand/compress the data are thus an essential part of the software.

relatively straight-forward.

21.4 ADC RESOLUTION

There are four basic types of data collected by our system, the Fieldial voltage (X-data, the field), the signal from the phase-sensitive-detector, PSD, (Y-data, the amplitude), thermocouple data (the temperature) and Gaussmeter data. The Gaussmeter data are already available in digital form and need not concern us here.[51]

For display purposes a 10 bit[52] resolution of the Y-data are quite adequate. However if extensive numerical manipulation is to be done 12 or more bits are desirable to avoid problems with digitisation noise *(116)(219)*. Similarly for the X-data, 10 bits is fine, but if, for example, one wishes to maintain a 0.1G resolution over a 1000G sweep to avoid amplitude distortion *(220)*, then 13-14 bits are required. Moreover, the Fieldial voltage runs from 0-5V, as opposed to -10V to +10V for the Y data so if one uses the same ADC for both data sets and no amplifiers another 2 bits are required. In practice, the X resolution is limited by noise to ≃12 bits.

We wish to measure to temperature to ≃0.01° (*i.e.*, <1% at room temperature)[53] over a wide temperature range. The

---

[51] A resolution of at least 1:10^6 is required for Gaussmeter measurements, *i.e.*,20 bits.

[52] Analog to digital converters (ADC's) have a resolution of 2^n where n is the number of 'bits' of resolution. Hence a 10 bit resolution is ≃1:1000)

[53] This is a requirement for biological studies. An accuracy of 0.1° over a range of -70°C to +120°C is required for this work.

thermocouple voltage is amplified 1000x to ±3V (max.) so a 15 bit ADC, at least, is desirable.

21.5 NO. OF POINTS COLLECTED. THE NYQUIST CRITERION

The maximum number of useful data points that can be collected is limited by three factors; X noise, amplifier band-width and computer memory and speed.

The X signal-to-noise ratio (SNR) is ≃2000:1 so unless averaging is done there is little to be gained by collecting more than 2K points.[54] Averaging is not meaningful if data are collected at a rate above the Nyquist frequency. For a band limited amplifier the Nyquist rate[55] is ≃1/time-constant, typically <5Hz, or <2000 points for us. One can arrange to decrease the time constant and increase the scan time so that more points are gathered, but 16K points occupies 64 Kbytes, 1/4 of the available computer memory. This means that the data processing has to be done 'off-the-disc', which is slow, rather than 'in core'. Also, 'in core' processing of >16K data points is sufficiently slow to make interactive processing unuseful so the data has to be box-carred back to <4000 points before use. This of course improves the apparent SNR, but it is just as

---

[54] A K is 1024 or 2^{10} and is a convenient size unit to use with computers, especially if the data are to be used with Fourier transforms.

[55] Note that here the Nyquist rate is determined by the amplifier band-width, not the spectrum (as in NMR). The Nyquist rate for a Lorentzian is infinite so the system band-width is always the limiting factor. For further discussion of Nyquist rates and ESR spectra see *(219)(221)(27)*.

efficient to collect less data with a higher PSD time constant. The conclusion to be drawn is that, for our system, 2000 points is the maximum size for a spectrum. Though in general more would be desirable.

21.6 FILTERING METHODS

Filtering (smoothing) methods have been fairly extensively studied *(222)(223)(224)(225)(226)(227)*. Only two methods will be discussed here, box-car filtering (Sect.21.8) and analog (time-constant) filtering.

An important point to note is, that once a data set is acquired, filtering does not improve the precision of the data *(145)*, it is purely cosmetic (*i.e.*, it only improves the apparent SNR). Filtering is important as many algorithms are not very stable in the presence of noise. Also searching by eye is difficult.

The Nyquist rate, (N_r), for data acquired with a low pass amplifier is

$$N_r = (2\pi\tau)^{-1} \qquad (21.1)$$

where τ is the time constant (inverse band-width) of the amplifier. This means that we have the choice of acquiring large amount of data at a low time constant (*i.e.*, noisy-data) and numerically filtering it (with a box-car in

this case), or of collecting smaller amounts of filtered data (*i.e.*, at a higher time constant; analog filtering)

Box-car filtering *(228)* just consists of averaging adjacent points (Sect.21.8) so consider the case of collecting 'n' points with a SNR of S_0 and box-carring to 'm' points (n/m will be integral), the SNR, S, is then given by *(229)*

$$S = S_0\sqrt{(n/m)} \tag{21.2}$$

with a corresponding decrease in resolution of n/m. Now the maximum number of meaningful points acquired for a time constant τ_0 in a scan time, T, is from Eqn.21.1

$$n = N_k T \propto \tau/\tau_0 \tag{21.3}$$

If we increase the time constant to τ then we get m' meaningful points

$$m' \propto T/\tau \tag{21.4}$$

We could of course acquire at a rate faster than the Nyquist frequency, but no further information is obtained; the data

should be acquired at a rate consistent with the amplifier band-width. Hence we get from Eqn.21.2-Eqn.21.4

$$S = S_0\sqrt{(\tau/\tau_0)} = S_0\sqrt{(n/m')} \qquad (21.5)$$

i.e., box-carring confers no advantage over analog methods for a given scan time. However, this analysis ignores two factors, the distortion caused by filtering and the nature of the noise. Analog filters shift and broaden the peaks in an asymmetric manner *(30)*. Box-carring just broadens the peaks and thus is the more desirable of the two methods. The analysis also assumes that the noise is Gaussian. In practice ESR spectrometers produce a large amount of so called 1/f noise (baseline drift and offset), which increases with scan time. Thus, it is better to rapidly scan several (noisy) spectra and box-car average, than to do one long scan with a large time constant.

The penalty for box-car averaging is the acquisition and manipulation of a large number of points. This can be overcome by real-time averaging. Memory and speed restrictions of the LSI-11 limit the usefulness of this approach for us, but it would be worthwhile pursuing if a faster computer was available.

In practice a compromise is used, data are acquired at the Nyquist rate using the maximum time constant consistent

with a distortion free spectrum (*i.e.*, <1/50 of the time to sweep the narrowest feature of interest *(30)*). The data are then box-carred on the LSI-11 down to 2048, 1024 or 512 points depending on the end use.

21.7 INTERPOLATION

As mentioned previously the sweep is not quite linear, mainly due to noise. The data are thus not equally spaced in terms of the magnetic field. For most purposes this is of no consequence, providing both the X and Y data are used for analysis. However, most algorithms, notably integration, execute faster if the data are equally spaced. Some algorithms, *e.g.* the FFT *(25)(26)* and Savitsky-Golay smoothing *(227)* require the data to be equally spaced. For these reasons it is desirable to interpolate the data to obtain an equally spaced data set. Here, data were interpolated and/or box-carred (*vide supra*) to 512, 1024 or 2048 points, depending on the end use. Powers-of-two are used to maintain compatibilty with FFT routines and the graphics terminal.

A number of interpolation schemes are possible, Lagrangian interpolation, cubic splines, or a sliding piecewise polynomial.[56] Lagrange interpolation is extremely

---

[56] A n'th order polynomial is fitted to points 'i' to 'i+n' and the data interpolated for this range of points. The polynomial is then fitted to the 'i+n' to 'i+2n' points *etc.*. A cubic spline is a piecewise cubic polynomial fit with the extra constraint that the derivatives at the end-points must be continuous between adjacent 'pieces' *(230)*.

unstable *(231)* especially in the presence of noise. Cubic splines also show instability in the presence of noise. Sliding polynomials can seriously distort the spectrum at low-data densities *(232)*. We used a quadratic polynomial and avoided low data densities. (Cubics provided no improvement and increase the interpolation time).

21.8 BOX-CAR INTERPOLATION AND FILTERING

This is a convenient method of reducing the size of data sets. It can also be used to produce an equally spaced data set from an unequally spaced data set. Briefly, it works as follows, each (X,Y) data point is loaded into an element of an array (the box-car). The index of the array element is determined by the range of values that X lays in. For instance, all X values 0<X<9 are assigned to element 1. For 10<X<19 they are assigned to element 2 *etc.* The Y values are summed and loaded into the array element determined by the corresponding X values as described above. The number of pieces of data summed in a particular box-car are stored in another array; the index numbers being determined as for the Y-data. When this process is complete the data are averaged and empty box-cars filled by linear interpolation or extrapolation.[57] (Note that this is not the same as a running average, which is a convolution with a box-car *(233)*.)

---

[57] The first and last few points in a sweep were often not collected. These portions of the data were zero-filled, flagged and ignored in subsequent calculations.

Generally the data were interpolated to 2^n points then box-carred back to 2^{n-1} points. Box-carring improves the apparent SNR by $\sqrt{(n/m)}$ where 'n' is the initial number of points and 'm' the final number. The penalty is a resolution loss of (n/m).[58]

21.9 PEAK SEARCHING AND FITTING

Automatic peak fitting was achieved as follows. First the baseline was located (*vide infra*) and the noise level (standard deviation; δ) determined. The data were searched for peaks only using data further than 5δ's from the baseline to avoid spurious fits. The difficulties of distinguishing high-frequency noise mixed with the signal and the signal itself were avoided by stepping through the data at intervals of 5% of the sweep-width. Extrema were located by changes in the sign of the slope of the line joining adjacent step points. This of course produces problems in locating peaks with widths less than 5% of the sweep-width. If the SNR is low the step size can be reduced, but then difficulties in identifing broad peaks occur (the slope change must be greater than the noise level). This method cannot be generalised to all types of spectra, but it is extremely reliable when tailored for specific applications, notably spectra from nitroxides in membranes.

---

[58]Note that for a spectrum where the box-car is much smaller than the line-width, as in our case, the effect on resolution can be ignored. This is not true for the time constant, where the time-constant approaches the time taken to scan the line.

Once a peak is found it can be fitted (locally) to a cubic or quadratic. Quadratics are more reliable for broad peaks and cubics for narrow peaks.[59] The fitting window is set to half of the step size. If the noise level is high or the initial fit is ambiguous the size of the window is automatically increased. Further details of the algorithm and its performance can be found in *(88)*.

The problems outlined above are all eliminated by interactive fitting. The operator selects the peaks and window size *via* a graphics terminal. However, this approach is more time consuming and introduces a degree of subjectivity when very noisy spectra are fitted.

21.10 BASELINE FITTING AND FLATTENING

For linear baseline artefacts added to a peak f'(x) we have an observed signal

$$y' = f'(x) + b(x) + c \qquad (21.6)$$

where b is the baseline drift and c is the DC offset. If we use the subscripts *l* and *r* to denote the left and right sides of the spectrum then

---

[59] That is broad and narrow with-respect-to the fitting window. The fitting window being the number of points fitted to the peak, in the vicinity of the peak.

$$y'_l = f'(x_l) + b(x_l) + c$$

$$y'_r = f'(x_r) + b(x_r) + c \qquad (21.7)$$

If the spectrum goes to the baseline *i.e.*, $f'(x_l)=f'(x_r)=0$ then we can determine b and c from the data. However, to meet this criterion requires very large data sets, or low data densities, as the sweep-width must be at least 5x the width of the broadest line in the spectrum.[60] Most baseline flattening algorithms, *e.g.(234)*, rely on having large areas of signal-free spectrum available to define the baseline, but if one uses a small data set with high data densities this will generally not be the case.

If the signal has a center of symmetry then we can use this to establish the baseline. We have

$$\Delta y = y'_l + y'_r = f'(x_l) + f'(x_r) + b(x_l) + b(x_r) + 2c \qquad (21.8)$$

we can choose our left and right data points such that, for a derivative spectrum, $f'(x_l)=-f'(x_r)$, hence

---

[60] Ideally one could average the data in proportion to the slope of the line, but this is difficult to do in real-time.

$$\Delta y = b(x_l) + b(x_r) + 2c \qquad (21.9)$$

we can now use another set of symmetric points to solve for b and c. Strictly we should iterate as the spectrum center is a function of the baseline. However, for a single line, the center of the spectrum is steep so that the cross-over position is not very sensitive to small baseline changes.

For *dtc* studies, where a single line, scanned fairly rapidly, is collected, we can assume that the drift is negligible, hence we can determine the DC offset easily.

The above methods lend themselves well to interactive graphics methods of baseline correction. The operator corrects the data for b and c *via* the terminal cursor keys. However, it is impossible to uniquely determine b and c by these methods and spectra with large drifts should be rejected. The sensitivity of this approach can be improved considerably by observing the integral while correcting the derivative data for b and c. The sensitivity to changes in 'b' and 'c' is increased by n and n^2 respectively, where n is the resolution of the graphics terminal.[61] The algorithm for interactive baseline flattening is shown in Fig.21.3

---

[61]One could expand the baseline, but this is not useful with noisy spectra.

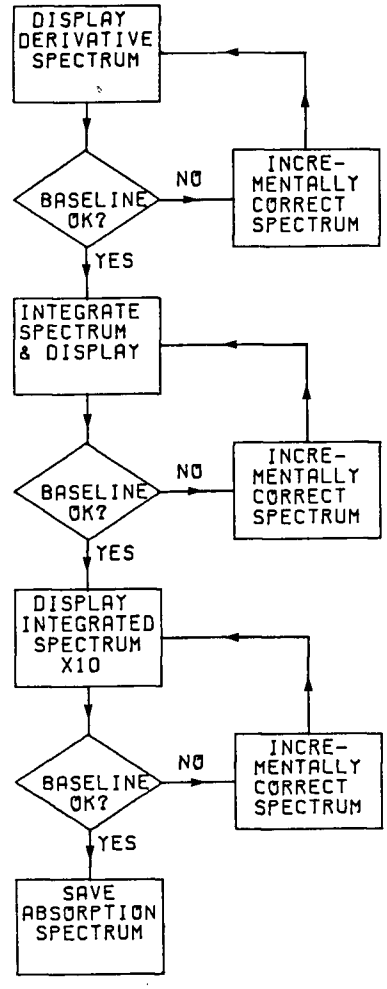

Figure 21.3. Flow chart for interactive baseline flattening.

21.11 INTEGRATION OF SPECTRA

The integration of ESR spectra and the associated errors has been discussed in a number of papers *(235)(236)(237)(238)(239)* and will not be reviewed here. All integrations were performed using Simpsons rule with an interpolated data set. Care has to be taken to remove baseline artefacts as

the integral is very sensitive to them (*vide supra*). No serious problems were encountered, except at low data densities where random steps are introduced into the spectrum (Fig.21.4).

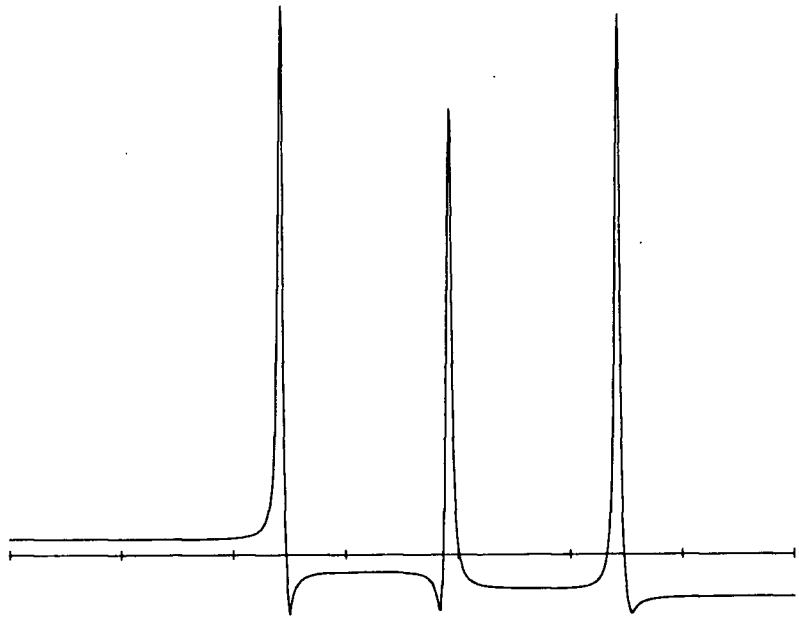

Figure 21.4. The effect of low data density on integration.

This effect is discussed in detail by Phillips and Herring *(27)*. The effect of data density on the average integration error for three algorithms is shown in Fig.21.5-Fig.21.7. (The 'averaged Simpsons' is just the average of two Simpsons rule integrations starting at different data points; see *(27)*). The data density is simply the number of points *per* peak-to-peak line-width.

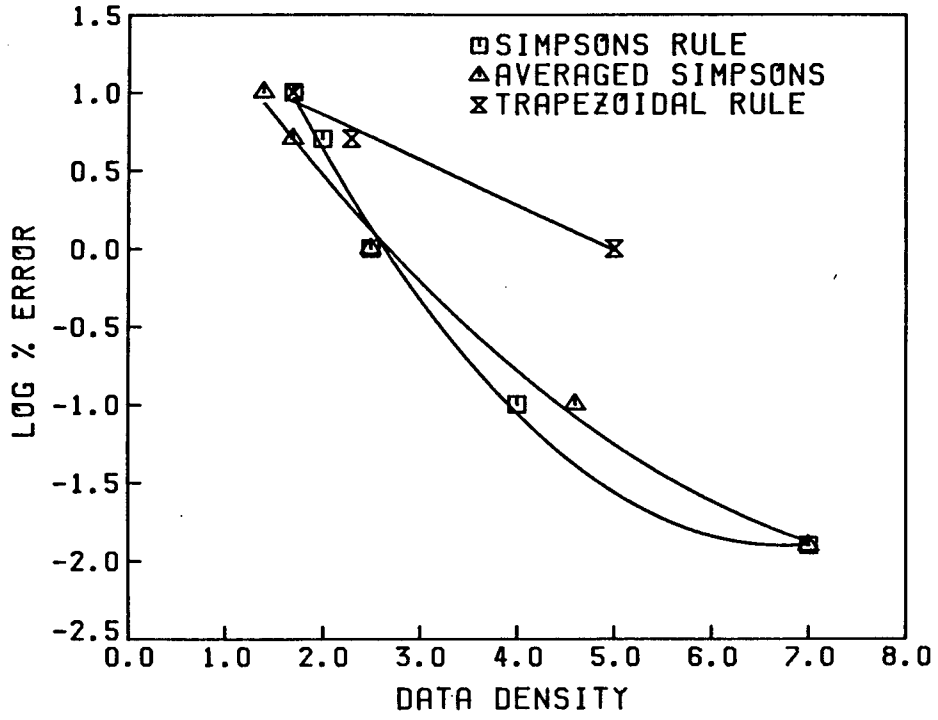

Figure 21.5. Integration errors *vs.* data density for the integration of a derivative to an absorption signal.

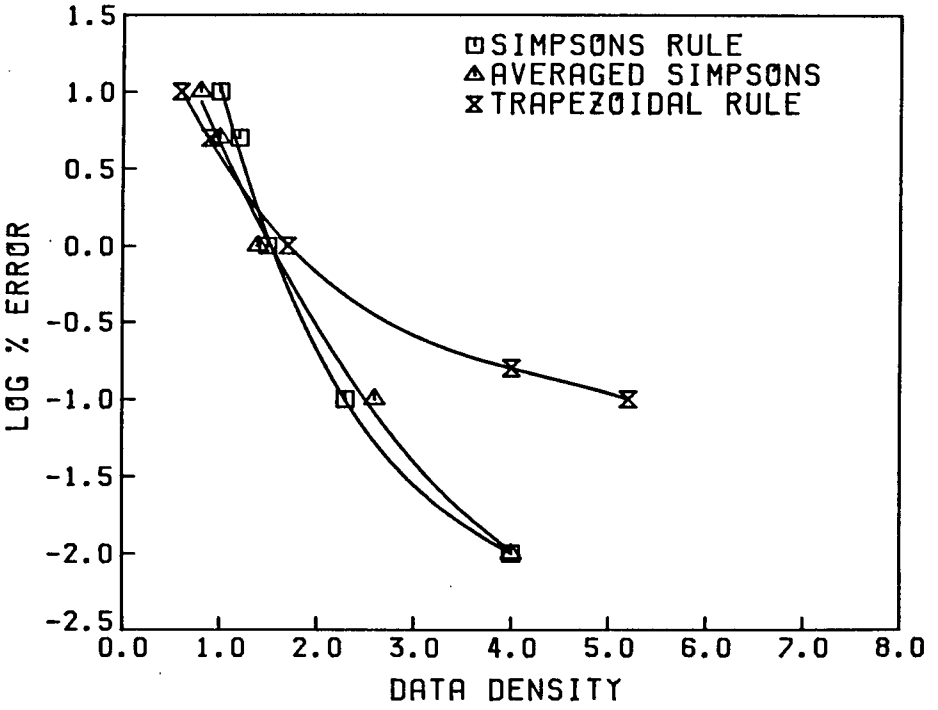

Figure 21.6. Integration errors *vs.* data density for the area of an absorption signal.

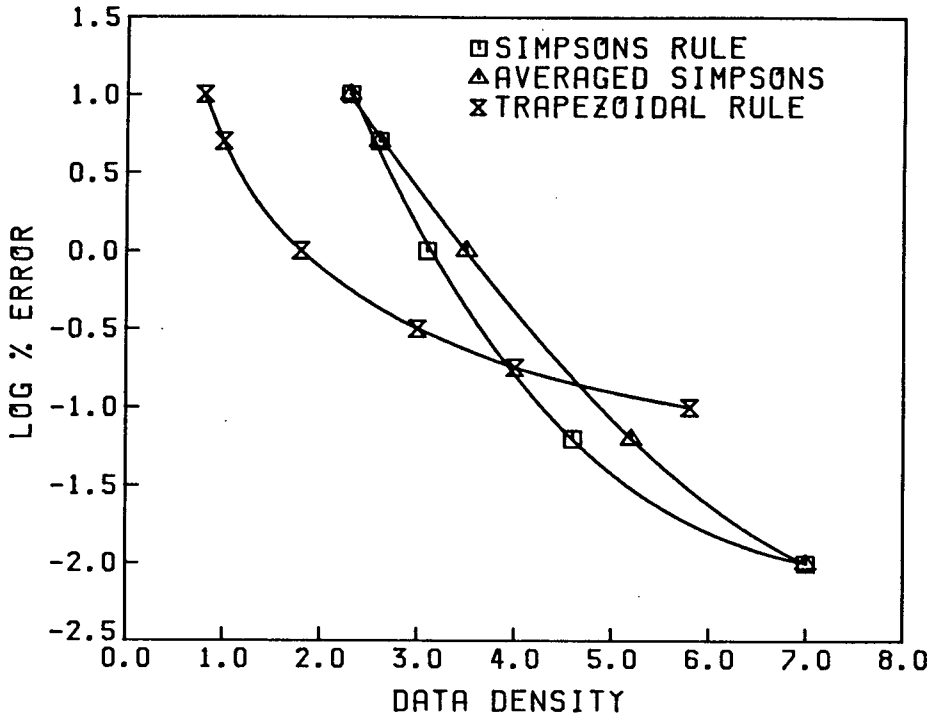

Figure 21.7. Integration errors *vs.* data density for the integration of a derivative to the area.

Note that this error is entirely due to low data density and not noise or truncation. Also note that such low densities are not unusual in NMR and for some commercial ESR data stations.

21.12 ADDITION AND SUBTRACTION OF SPECTRA

The addition and subtraction of ESR spectra is non-trivial. The position of the spectrum depends on the microwave frequency, the magnetic field and the radicals g-shift. Also the data are not equally spaced and the sweep-width and number of acquired points is not constant.[62] (Shifting

---

[62] The sweep-width is constant to within 1%, however this can cause large artefacts when subtracting spectra.

spectra is described in more detail below).

The unequal data spacing and number of data points is easily taken care of by interpolation, as previously described. If Gauss are used as the X-data then changes in sweep-width and field are readily dealt with, one simply changes the two calibration parameters before converting the data to Gauss. Generally the data is converted back to integers before use and care has to be taken to keep track of the desired portion of the spectrum.

Compensating for microwave shifts is more difficult as the g-values must be known. One can assume the g-factors are the same and correct accordingly, but the best approach is *via* interactive graphics. The spectra (after interpolation and matching the sweep-widths) are displayed and matched interactively. They can then be subtracted (interactively) at one's leisure. However, one has to be careful if the spectra have g-shift differences, the results can be misleading. An example of this method is shown in Fig.21.8-Fig.21.10

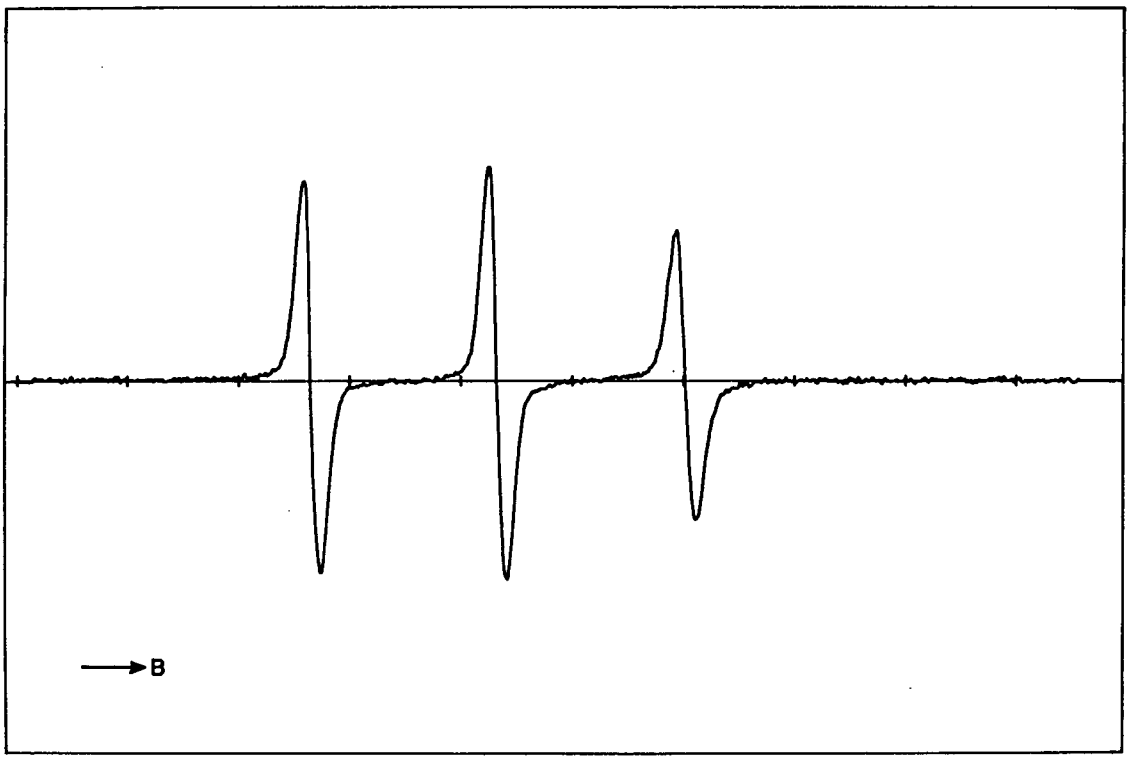

Figure 21.8. Spectrum of the free spin-probe.

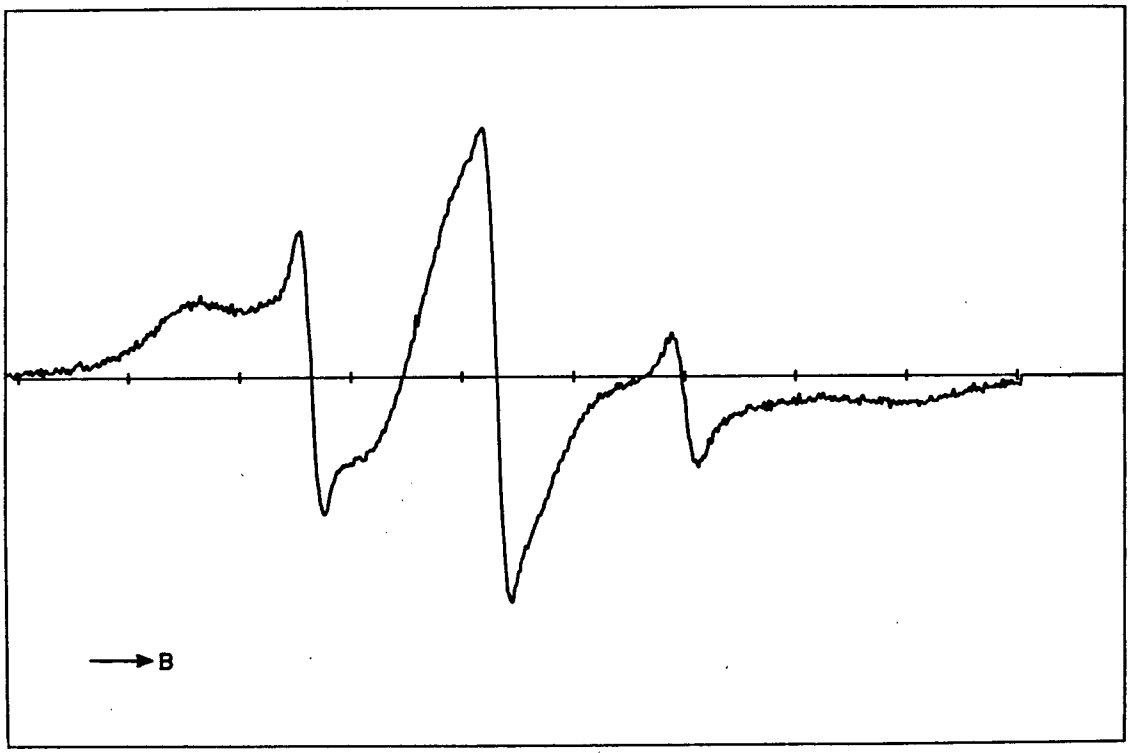

Figure 21.9. Spectrum of free and bound spin-probe in red blood cell ghosts.

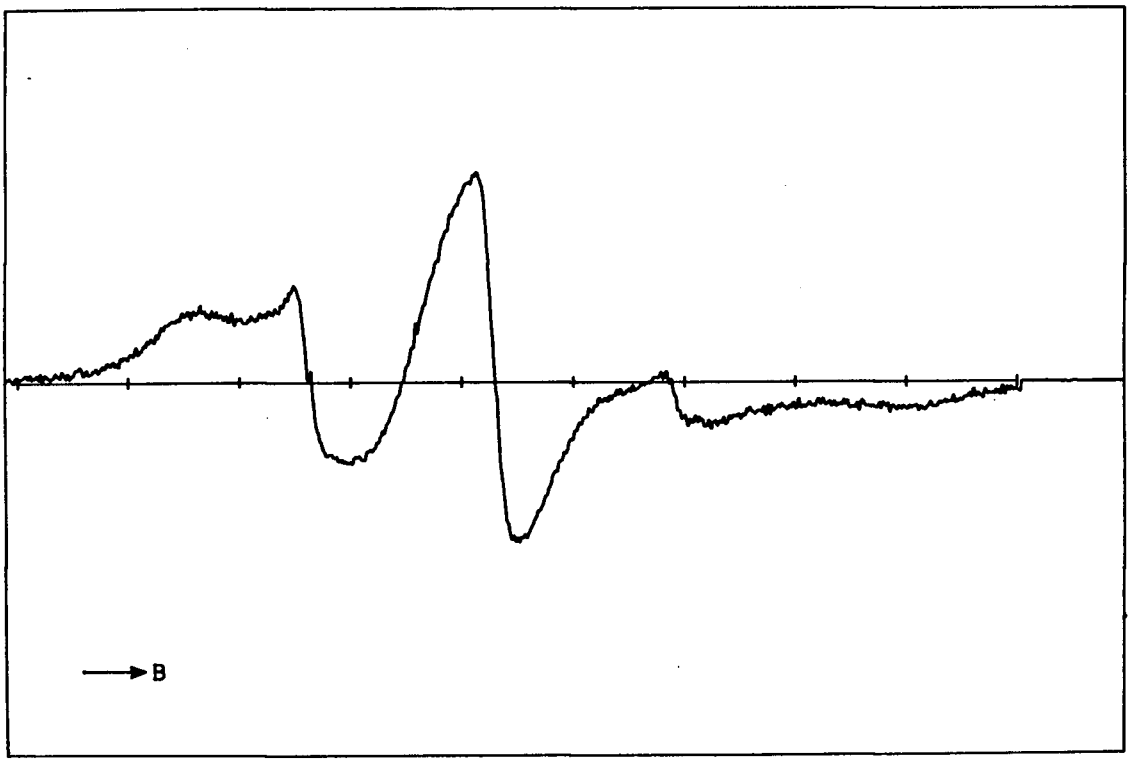

Figure 21.10. Spectrum of a bound spin-probe. Found by subtracting the free probe spectrum from the combination spectrum above.

21.13 SHIFTING SPECTRA

This is again non-trivial and as pointed out above can be misleading. It is thus pertinent to discuss some of the underlying theory.

To first order the transition frequency is given by (with A_0 in the appropriate units)

$$\hbar\omega = g_0\beta B_0 m_s + A_0 m_i m_s \qquad (21.10)$$

or in terms of the line-position, B_z,

$$B_z = \hbar\omega/g_o\beta \qquad (21.11)$$

where, because we do field swept experiments, ω is the microwave frequency.

If we wish to compensate a line-position for a new microwave frequency ω' then

$$B'_z = (g_o\omega'/g'_o\omega)B_z \qquad (21.12)$$

If we want to shift the whole spectrum, $\Delta=B'_z-B_z$, then

$$\Delta B = \frac{g_o\beta}{\omega}[\omega'/g'_o-\omega/g_o] \qquad (21.13)$$

If the g-values are not known they must be found by other means *e.g.* Hydes algorithm *(29)*. However, g-shifts are generally small and the ratio g_o/g'_o can be set to one. g-shifts may be compensated for by the same formulas (with $\omega'=\omega$), but this can be very misleading, unless it is known that the shift is due to solvent effects, for instance.

If both the microwave and g-values are shifted then the correction is most easily done interactively, but as this obscures the underlying assumptions one has to especially

careful when using this approach.

The center of the resonance, B_0, does not necessarily correspond to the center of the sweep or, more importantly, with the center of any other spectrum. In this case the data are corrected simply as follows.

$$B'_z = B_z + \Delta B$$

where $$\Delta = I' - I \qquad (21.14)$$

I' and I are the new and old values for the intercept of the calibration. See Sect.13.9. Changes in sweep-width are compensated for by interpolation. Assuming the change is linear across the spectrum, the data are interpolated at intervals of sweep/N, where N is the number of interpolated points and sweep is the new sweep-width.

The above correction procedures are superficially trivial, however, they implicitly assume that the data are continuous, whereas the data are discrete. This causes problems because the desired shifts are rarely integral multiples of the data resolution. Changing the sweep-width is even more problematic as that is equivalent to a shift that varies across the spectrum. The problem is solved by converting the spectrum x-data to Gauss and then interpolating the spectrum to get the points corresponding to the desired shifted/expanded spectrum. The original

spectrum should have a large data density as errors can accumulate rapidly if several or, large, shifts are done.

Also care must be taken to adopt a consistent sign convention for the direction of the shifts. Here the convention is $\Delta=X'-X$, where X' is the corrected value and X is the original value and Δ is the desired shift.

APPENDICES

22. APPENDICES

22.1 NOMENCLATURE

For the purposes of this thesis metal carbodithioate (dithiocarbamate) complexes are denoted as follows; MR_2dtc, where M is the central metal and R is an alkyl or ring substituent on one end of the complex, which are as follows.

Me	methyl
Et	ethyl
Py	pyrollidinyl
Oc	n-octyl
Mp	morpholinyl
Hxm	hexamethyleniminyl
Ocm	octamethyleniminyl
Od	octadecyl

Hence bis(diethyl-N-carbodithioate)^{63}Cu(II) is abbreviated to $^{63}CuEt_2dtc$ and bis(pyrolidinyl-N-carbodithioate)^{63}Cu(II) is abbreviated to ^{63}CuPydtc. The MR_2dtc are given the generic title of dithiocarbamates, denoted *dtc*'s, where M is a divalent metal, usually nickel(II) or copper(II). The 'imine' nomenclature is archaic and now only refers to an NH double bonded to a carbon. The correct nomenclature is 'azacycloalkane', but the older nomenclature will be

retained here.

22.2 THE ^2H NMR SPECTRUM OF PYROLLIDINE

The deuterium spectrum of neat d_9 pyrollidine was recorded at 30.7MHz and 61.4MHz. A spectrum consisting of three lines was obtained; one line due to the amine deuteron and two peaks, separated by 1.16ppm, due to the methylene deuterons. The low field peak was assigned to the pair of methylene groups attached to the nitrogen and the high field peak assigned to the other (ring) methylenes. Line-widths were resolution limited (1Hz for the WH400 and 5Hz for the CXP200). From the Karplus equation *(240)* we would expect the deuteron coupling around the ring to be <0.2Hz and will make no contribution to relaxation. The ^{14}N relaxes too fast to make any contribution to the spectrum. The two methylene peaks are sufficiently well separated (1.76ppm for the nickel salt) that overlap presents no problem *(241)*.

Relaxation time for the neat pyrollidine were recorded at 310K and 323K on the CXP200 at 30.7MHz and are shown in Table 22.1

Temp	Ring methylene	N methylene	Amine deuteron
310	2.43	2.40	1.36
323	1.89	1.75	0.67

Table 22.1. ^2H relaxation times for neat d_9 pyrollidine. Times are secs. The N methylene is adjacent to nitrogen.

The relaxation times will not be interpreted here other than to comment that the relaxation times for the methylene deuterons are consistent with axial diffusion of the pyrollidine, as might be expected. The primary use of these values is to set the cycle time ($5T_1$) for the inversion recovery experiments. These values provide an upper limit for the T_1 for the dithiocarbamate complex, which being a larger molecule will have a shorter T_1.

22.3 NMR SPECTRAL PARAMETERS

The assignments for the NMR parameters are shown in Fig.22.1 and Fig.22.2 The chemical shift anisotropy was measured from Fig.22.3. Line-positions were assigned from this spectrum and the crossovers of the dispersion spectrum (not shown). The x component was assigned from the dipolar splitting which is largest along the C-N bond.

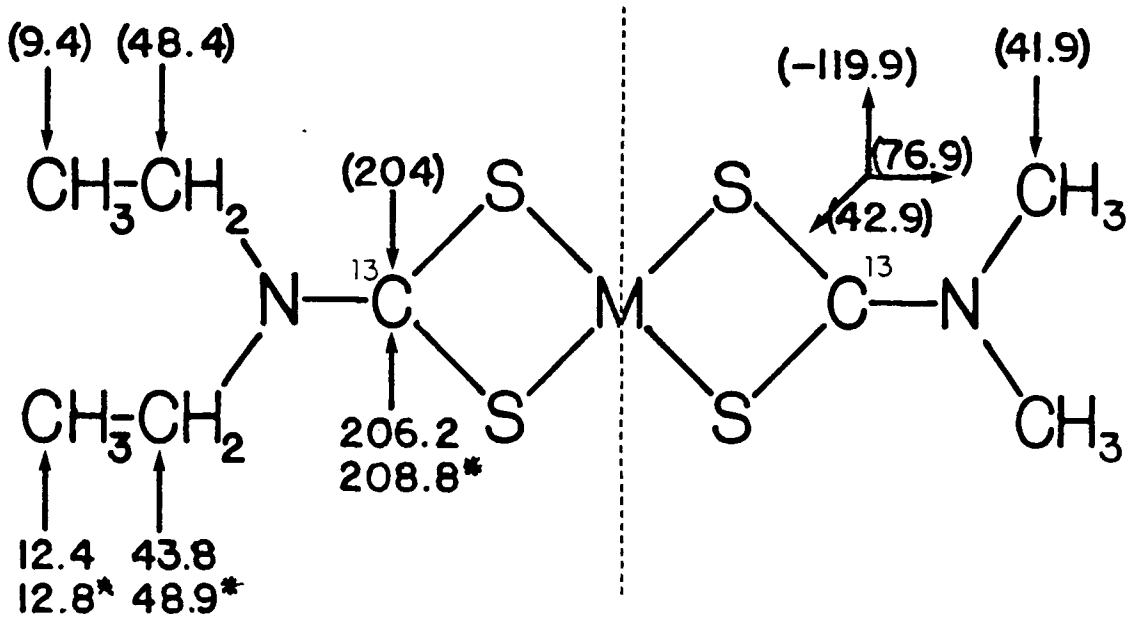

Figure 22.1. Chemical shift value for nickel *dtc*'s in ppm. 0.1M soln in $CDCl_3$. Ext. TMS ref. * denotes values for a 1M ^{13}C enriched K^+Et_2dtc in D_2O. ( ) denote solid state values, the CSA tensor is traceless.

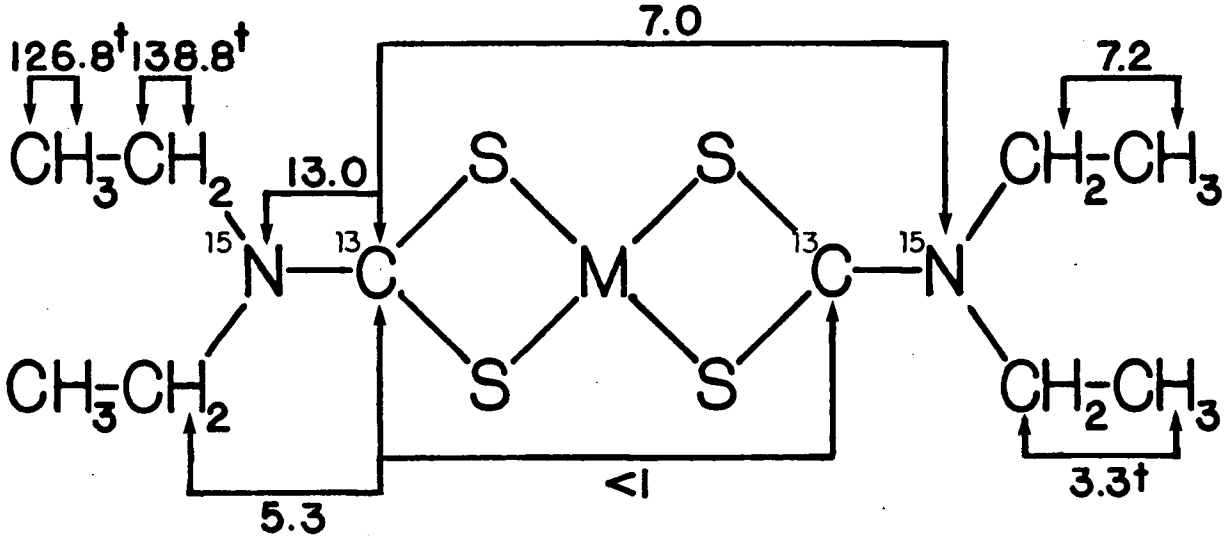

Figure 22.2. Coupling parameters (Hz) for nickel *dtc*'s. 0.1M soln. in $CDCl_3$. † denotes values for 1M soln. of potassium derivative. ^{15}N couplings are from 10^{-3}M soln. of $^{13}C, ^{15}N$ enriched methyl derivative.)

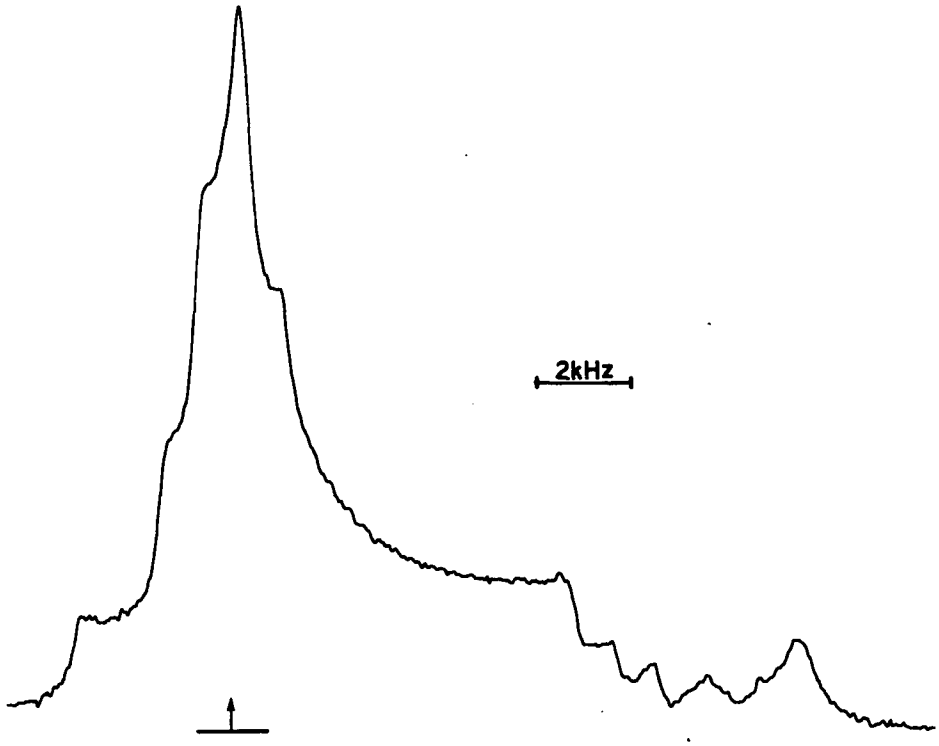

Figure 22.3. The powder spectrum for $NiEt_2dtc$ at 50.3MHz. The arrow denotes the external benzene reference.

22.4 ESR SPECTRAL PARAMETERS

The magnetic tensor parameters for CuPyDtc are *(44)*

A_{xx} = -119MHz	g_{xx} = 2.022
A_{yy} = -106MHz	g_{yy} = 2.018
A_{zz} = -474MHz	g_{zz} = 2.088
A_o = -233MHz	g_o = 2.043

22.5 COMPARISON OF REDFIELD AND OTHER THEORIES

An alternative approach to dealing with first order wave-functions is to do a van-Vleck transform *(242)* so that the perturbation terms are carried by the operators rather than the wave-functions. The transition frequencies are then simplified (ω_{res} -> ω_0). However, the spectral densities are modified, *i.e.*,

$$j(\omega_{res}) \rightarrow j(\omega_0)(1+f) \qquad (22.1)$$

where ω_{res} is the first order transition frequency, ω_0 is the zero order transition frequency and f is the van-Vleck correction term. Using a Taylor expansion of Eqn.22.1 with ω_{res} it is easy to show that $f \simeq \omega_0 \omega_a j(0) j(\omega)$ where ω_a is the hyperfine coupling frequency, *i.e.*, the first order corrections are products of the reduced spectral densities.

Comparison of our results with other workers to first order is complicated by the differing degrees of approximation used by the various workers. However, if we set ω_{res} -> ω_0 and ω_a -> 0 in all cases and drop all terms of order higher than ω_a/ω_0 (which are equivalent to C^2 terms in our work) then a comparison is feasible. Wherever a second order (C) term occurs in our equation there should be a corresponding f term in the other theories. This is more-or-less the case, but given the differences in approach (Redfield *vs.* linear-response *vs.* stochastic Liouville) the

agreement cannot be expected to be exact. For instance it is not clear which terms correspond to the correction for B_0 to B_z in our theory.

22.6 HAMILTONIAN IN A SPHERICAL BASIS

The relevant magnetic interaction tensors in a spherical basis are given by *(90)(99)*

$$F_a^{\pm 2} = \tfrac{1}{2}(A_{xx} - A_{yy}) \qquad F_g^{\pm 2} = \tfrac{1}{2}(g_{xx} - g_{yy})$$

$$F_a^0 = \sqrt{\tfrac{2}{3}}\left[A_{zz} - \tfrac{1}{2}(A_{xx}+A_{yy})\right] \qquad F_g^0 = \sqrt{\tfrac{2}{3}}\left[g_{zz} - \tfrac{1}{2}(g_{xx}+g_{yy})\right]$$

The ± 1 elements are zero because the tensors are symmetric. The relevant second rank tensor operators are

$$\begin{aligned}
A_a^{\pm 1} &= \mp\tfrac{1}{2}[\hat{I}_{\pm}\hat{S}_z + \hat{I}_z\hat{S}_{\pm}] \\
A_a^{\pm 2} &= \tfrac{1}{2}\hat{I}_{\pm}\hat{S}_{\pm} \\
A_a^0 &= \sqrt{\tfrac{2}{3}}\hat{I}_z\hat{S}_z - \tfrac{1}{2}\sqrt{\tfrac{1}{6}}[\hat{I}_+\hat{S}_- + \hat{I}_-\hat{S}_+] \\
A_g^0 &= \sqrt{\tfrac{2}{3}}\hat{B}_z\hat{S}_z \\
A_g^{\pm 1} &= \mp\tfrac{1}{2}\hat{B}_z\hat{S}_{\pm} \\
A_g^{\pm 2} &= 0
\end{aligned}$$

22.7 NOTES ON UNITS FOR ESR

Relaxation theories are usually derived in energy units; ESR spectra are measured in Gauss. This can lead to confusion (what are the units of T_1 ? *(243)*) and programming problems. For this reason a brief discussion of units used in this work is given below.

If H is the half-width at half height for Lorentzian line[63] the peak-to-peak width of the derivative is thus

$$H = \frac{\sqrt{3}}{2}\Delta H_{pp} \tag{22.2}$$

as $H=(\pi T_2)^{-1}$ we then get

$$T_2^{-1} = \pi\frac{\sqrt{3}}{2}\Delta H_{pp} \tag{22.3}$$

For T_2 to be in the usual units (sec rad^{-1}) ΔH_{pp} must be in Hz. To convert from Gauss we use[64]

---

[63]DISPA shows that the *dtc* lines are very close to Lorentzian.

[64]Our experiment is field swept so this conversion is not strictly valid. However, this causes no problems, even in the slow-motional regime *(39)(244)*.

$$h\nu = g\beta B$$

hence $$\nu(\text{Hz}) = h^{-1}g\beta B(\text{Gauss}) \qquad (22.4)$$

with the Bohr magneton, β and Plancks constant, h, defined in their usual units. Hence we get

$$\Delta H_{pp}(\text{Hz}) = h^{-1}g_0\beta\Delta H_{pp}(\text{Gauss})$$

and thus $$T_2^{-1} = \pi\frac{\sqrt{3}}{2}g_0\beta h^{-1}\Delta H_{pp}(\text{Gauss}) \qquad (22.5)$$

For the line-positions (ignoring the small first order correction) we have

$$\nu_z(\text{Hz}) = h^{-1}g\beta B_z(\text{Gauss}) \qquad (22.6)$$

and for the g anisotropy (Δg)

$$\Delta\nu_g(\text{Hz}) = h^{-1}g\beta B_z(\text{Gauss}) \qquad (22.7)$$

note that B_z is the position of the line of interest, which is not the same as B_0 so $\Delta\nu_g$ depends on line-position.

Finally the hyperfine splitting is given by

$$A_0(\text{MHz}) = 2.8047(g/g_e)a_0(\text{Gauss}) \qquad (22.8)$$

where g_e is the free-electron g-value. The hyperfine splitting constant may be obtained from the spectrum to allow for any temperature dependence, but it only appears in the second order terms so the literature value is adequate.

Dimensional analysis of Eqn.12.22 gives us that the units of $j(\omega)$ is rad s^{-1} and R is sec rad^{-1}. Substituting in typical values we find that j is $\simeq$1nS and R$\simeq$1Grads^{-1}. It is thus sensible to use nS and GHz as our base units. These may be used directly in the above equations with no modifications. In fact it is essential to use these units to avoid floating-point overflow in the program. The ω^4 term in Eqn.12.23 is especially troublesome.

22.8 ON PYROLLIDINE RING PUCKER

In the solid state NiPydtc is puckered by some 0.03nm out of the plane of the molecule *(183)*, the polar angle of the C-D bond in the ring methylenes is thus ±11° different from the value for the planar ring. This means that the ring may 'ripple' on the time scale of the NMR relaxation. If the ring 'ripples' much faster than the relaxation time then the polar angle averages out and the planar approximation is valid. (There is some evidence that the ripple is fast on

the ESR time scale *(245)* and hence also on the NMR time scale). If the the ring is essentially rigid (*i.e.*, the activation energy for the ring flip is high) on the NMR time scale the relaxation times are a superposition of the the times for each ring conformation. However, as sine and cosine functions are fairly linear in between 20° and 40° (the polar angles required) the results once again average out (within experimental error) to the planar case. If the 'ripple' is on the same time scale as the relaxation (≃1s) then the problem is complex and the fluctuation will contribute to the overall relaxation of the molecule. However, we can readily test for this effect as we have an over-determined system. We just have to check for consistency between the two deuterium relaxation results and the two corresponding ESR reduced spectral densities. The results at both 310 and 323K are entirely consistent with each other, the original (planar) approximation is thus valid.

22.9 THE FAST-MOTIONAL LIMIT

Redfield theory is only valid in the fast motional limit, *i.e.*, the molecular motion must be on a time scale much faster than the relaxation time, $R^{-1} >> T_2$, where R is the smallest element of the diffusion tensor. If $R^{-1} \simeq T_2$ then the motion is said to be in the slow-motional regime and Redfield theory breaks down. The above equation reduces to $R >> \Delta H_{pp}/200$, where R is in Grad s^{-1} and ΔH_{pp} is the

peak-to-peak line-width, in Gauss, of the broadest line in the spectrum. In this and previous work *(88)* the theory breaks down (*i.e.*, $j(\omega)$ or the SR term become negative) when ΔH_{pp}>20G. For an arbitrary limit of 10% this equation corresponds to an R of 1 Grad s^{-1} as found by the approximation methods in Sect.15. for the cases where $j(\omega)\simeq 0$.

22.10 ESR LINE-WIDTH DATA

Peak-to-peak line-width data for ^{63}CuPydtc in toluene. Mean microwave frequency was 9.06 GHz. Mean line-positions (high to low field) were 3270G, 3192G, 3115G and 3039G.

Temp °C	Width in Gauss			
-44.3	3.62	5.45	10.74	19.99
-39.0	3.35	4.99	10.06	19.12
-35.4	3.28	4.85	9.54	16.57
-34.7	3.30	4.76	9.01	16.11
-30.0	3.12	4.58	8.44	15.46
-25.0	3.09	4.35	7.76	13.58
-20.0	2.95	4.18	7.32	12.43
-15.1	2.99	4.10	6.89	11.53
-10.5	3.00	4.12	6.95	11.46
-5.1	3.04	4.01	6.07	10.47
0.0	2.97	3.90	6.11	10.21
4.0	3.06	3.96	5.99	9.43
9.8	3.00	3.91	5.90	9.18
19.9	3.14	3.84	5.69	8.48
30.4	3.23	3.96	4.04	7.70
35.9	3.32	4.15	6.25	7.59
40.9	3.40	4.15	5.37	7.57
46.5	3.23	4.16	5.29	7.49
50.1	3.50	4.23	5.49	7.33
55.6	3.71	4.30	5.56	7.13
61.0	3.83	4.45	5.41	7.13

Table 22.2. Line-width data for CuPydtc in chloroform. Widths in order of field-position. High-field first.

22.11 NMR RELAXATION DATA. DEUTERIUM

Deuterium T_1 relaxation data data for d_9NiPydtc in chloroform. Delays are in seconds unless otherwise noted. Amplitudes are in arbitrary units. N denotes the magnetisation amplitude of the two methylenes adjacent to the nitrogen. R denotes the magnetisation amplitude for the other two methylenes. T is the temperature.

Delay	N	R
0.02	-8.43	-10.42
0.03	-7.49	-9.88
0.05	-3.88	-6.21
0.07	-1.60	-4.20
0.10	1.60	-1.35
0.13	4.10	1.50
0.15	5.80	2.90
0.18	7.70	4.80
0.25	10.52	8.70
0.50	14.61	14.85
1.00	15.91	16.80
1.50	15.60	17.80

Table 22.3. T=310K. 61.4MHz.

Delay	N	R
0.02	-7.39	-9.00
0.03	-6.69	-8.70
0.05	-3.70	-5.80
0.07	-2.14	-4.51
0.10	0.50	-2.05
0.13	2.40	0.0
0.15	3.60	1.10
0.18	4.10	2.65
0.25	8.11	5.80
0.35	10.21	8.85
0.50	12.50	12.20
0.70	13.32	13.90
1.20	13.60	15.12
1.70	13.27	14.90

Table 22.4. T=323K. 61.4MHz.

Delay	N	R
0.03	-11.60	-13.40
0.05	-6.80	-8.80
0.10	-1.20	-3.60
0.15	3.10	0.0
0.20	7.60	3.50
0.25	11.00	7.00
0.30	13.20	9.10
0.40	16.40	12.80
0.50	18.50	15.60
0.70	20.10	18.30

Table 22.5. T=333K. 61.4MHz.

Delay	N	R
40.00	-4.00	-5.20
60.00	-2.80	-3.20
80.00	-1.10	-2.70
100.00	0.0	-1.55
120.00	0.70	-0.90
140.00	1.50	0.0
160.00	2.10	0.60
180.00	3.00	1.30
200.00	3.90	1.50
220.00	4.20	2.50
240.00	4.80	3.10
260.00	5.20	3.30
280.00	5.80	4.00
300.00	5.95	4.30

Table 22.6. T=310K. 30.7MHz. Times in mS.

Delay	N	R
20.00	-8.80	-9.20
30.00	-6.00	-9.20
70.00	-2.30	-5.40
90.00	-1.70	-3.20
110.00	0.50	-2.00
120.00	0.70	-1.60
150.00	2.50	0.0
200.00	4.90	2.50
300.00	7.80	5.80

Table 22.7. T=310K. 30.7MHz. Times in mS.

Delay	N	R
40.00	-6.40	-7.70
60.00	-4.75	-6.35
80.00	-2.75	-4.50
100.00	-1.80	-4.00
120.00	0.50	-2.40
140.00	1.10	-1.60
160.00	1.60	-0.70
180.00	2.50	0.40
200.00	3.50	0.60
220.00	4.10	1.30
240.00	4.80	1.90
260.00	5.50	2.90
280.00	6.10	3.35
300.00	6.60	4.20

Table 22.8. T=323K. 30.7MHz. Times in mS.

22.12 NMR RELAXATION DATA. ^{13}C

^{13}C T_1 relaxation data data for $NiEt_2dtc$ in chloroform. ^{13}C substitution on the CS_2 moiety. Delays are in seconds. Amplitudes are in arbitrary units. T is the temperature.

Time	Amp.
1.0	1.1
2.0	1.7
3.0	2.1
4.0	2.8
5.0	3.7
7.0	4.6
9.0	5.6
15.0	8.7
20.0	10.5
80.0	17.4

Table 22.9. T=310K. 50.3MHz.

Time	Amp.
2.0	3.40
5.0	4.90
10.0	11.75
15.0	15.15
100.0	20.20

Table 22.10. T=310K. 100.7MHz.

Time	Amp.
5.0	2.40
10.0	4.15
15.0	5.40
20.0	6.40
25.0	7.00
30.0	7.50
35.0	7.90
40.0	8.20
50.0	8.50
150.0	9.00

Table 22.11. T=323K. 50.3MHz.

Time	Amp.
2.0	4.55
5.0	8.65
10.0	13.95
15.0	17.40
20.0	19.30
30.0	21.40
100.0	24.72

Table 22.12. T=323K. 100.7MHz.

Time	Amp.
1.0	1.55
2.0	2.70
3.0	3.90
4.0	5.15
5.0	5.90
7.0	7.50
9.0	9.20
15.0	12.60
20.0	14.30
30.0	16.00
100.0	17.10

Table 22.13. T=333K. 50.3MHz.

Time	Amp.
5.0	8.55
10.0	11.90
15.0	13.90
20.0	15.00
25.0	16.00
30.0	16.40
35.0	16.85
40.0	16.90
50.0	17.05
150.0	17.40

Table 22.14. T=333K. 50.3MHz.

Time	Amp.
2.0	3.70
5.0	7.45
10.0	11.25
15.0	13.70
20.0	14.80
30.0	15.70
100.0	19.95

Table 22.15. T=333K. 100.7MHz.

REFERENCES

1. K.S.Cole and R.H.Cole, *J.Chem.Phys.* **9**, 341, (1941)

2. C.P.Poole, "*Electron Spin Resonance 2nd ed.*", Chap.12H, Wiley, 1983

3. M.A.Hemminga, J.H.Reinders and P.A.De Jager, *J.Magn.Reson.* **58**, 428, (1984)

4. A.Abragam, "*Principles of Nuclear Magnetism*", Chap.III, O.U.P., 1983

5. A.G.Marshall and D.C.Roe, *J.Magn.Reson.* **33**, 551, (1978)

6. A.G.Marshall, D.C.Roe and S.H.Smallcombe, *J.Anal.Chem.* **50**, 764, (1978)

7. A.G.Marshall, *J.Phys.Chem.* **83**, 521, (1979)

8. A.G.Marshall and D.C.Roe, *J.Anal.Chem.* **50**, 756, (1978)

9. A.Abragam, "*Principles of Nuclear Magnetism*", Chap.III pt.IIA, O.U.P., 1983

10. F.G.Herring, A.G.Marshall, P.S.Phillips and D.C.Roe, *J.Magn.Reson.* **37**, 293, (1980)

11. A.G.Marshall, R.E.Bruce, *J.Magn.Reson.* **39**, 47, (1980)

12. A.G.Marshall and Tao-Chin Lin Wang, *J.Anal.Chem.* **55**, 2348, (1983)

13. A.G.Marshall and R.E.Bruce, *J.Phys.Chem.* **84**, 1372, (1980)

14. F.G.Herring and P.S.Phillips, *J.Magn.Reson.* **57**, 43, (1984)

15. A.Carrington and A.McLachlan, "*Introduction to Magnetic Resonance*", Chap.11, Harper Row, 1969

16. C.P.Poole, "*Electron Spin Resonance 2nd ed.*", Chap. 12, Wiley, 1983

17. A.Abragam, "*Principles of Nuclear Magnetism*", pp93-96 Chap.III, O.U.P., 1983

18. R.H.Cole and D.W.Davidson, *J.Chem.Phys.* **19**, 1484, (1951)

19. C.P.Poole, "*Electron Spin Resonance 2nd ed.*", Chap.12G, Wiley, 1983

20. C.P.Poole, "*Electron Spin Resonance 2nd ed.*", Chap.6H, Wiley, 1983

21. J.W.Cooper, "*The Minicomputer in the Laboratory*", Chap.21, John Wiley & Sons, 1983

22. F.G.Herring and P.S.Phillips, *J.Magn.Reson.* **59**, 489, (1984)

23. C.P.Poole, "*Electron Spin Resonance 2nd ed.*", Chap.12I, Wiley, 1983

24. R.N.Bracewell, "*The Fourier Transform and its Applications. 2nd. ed.*", Chap.12, McGraw Hill, 1981

25. R.N.Bracewell, "*The Fourier Transform and its Applications. 2nd. ed.*", Chap.18, McGraw Hill, 1981

26. J.W.Cooper, "*The Minicomputer in the Laboratory*", Chap.20, John Wiley & Sons, 1983

27. F.G.Herring and P.S.Phillips, *J.Magn.Reson.* **62**, 19, (1985)

28. S.Makinen, *Rev.Sci.Instrum.* **53**, 627, (1982)

29. J.S.Hyde and J.R.Pilbrow, *J.Magn.Reson.* **41**, 447, (1980)

30. C.P.Poole, "*Electron Spin Resonance 2nd ed.*", Chap. 7H & 11F, Wiley, 1983

31. S.A.Zager and J.H.Freed, *J.Chem.Phys.* 77, 3360, (1982)

32. L.F.Yip. Unpublished work.

33. C.H.Sotak, C.L.Dumoulin and M.D.Newsham, *J.Magn.Reson.* **57**, 453, (1984)

34. E.Bartholdi and R.R.Ernst, *J.Magn.Reson.* **11**, 9, (1973)

35. R.R.Ernst, *J.Magn.Reson.* **1**, 7, (1969)

36. S.I.Parks and R.B.Johannesen, *J.Magn.Reson.* **22**, 265, (1984)

37. B.L.Neff, J.L.Acekerman and J.S.Waugh, *J.Magn.Reson.* **25**, 335, (1977)

38. J.M.Daubenfeld, J.C.Boubel, J.Delpuech, B.Neff and J.Escalier, *J.Magn.Reson.* **62**, 195, (1985)

39. J.H.Freed, G.V.Bruno and C.F.Polnaszek, *J.Phys.Chem.* 75, 3385, (1971)

40. G.Poggi and C.S.Johnson, *J.Magn.Reson.* 3, 436, (1970)

41. E.Lam. BSc.Thesis. UBC. 1985

42. J.M.Park. Unpublished work

43. P.S.Phillips. Unpublished work

44. F.G.Herring, J.M.Park, S.J.Rettig and J.Trotter, *Can.J.Chem.* 57, 2379, (1979)

45. D.Attanasio, *Inorg.Chem.* 16, 1824, (1977)

46. F.G.Herring and R.L.Tapping, *J.Phys.Chem.* 78, 316, (1974)

47. C.P.Poole, "*Electron Spin Resonance 2nd ed.*", Chap.11K, Wiley, 1983

48. F.Aubke. Personal communication

49. L.S.Singer and I.C.Lewis, *Appl.Spectrosc.* 36, 1, (1982)

50. R.D.McClung, *Adv.Mol.Relaxation Processes.* 1, 10, (1977)

51. D.R.Bauer, J.I.Brauman and R.Pecora, *J.Amer.Chem.Soc.* 96, 6840, (1974)

52. K.M.Larsson, J.Kowalowski and U.Henriksson, *J.Magn.Reson.* 62, 260, (1985)

53. W.G.Rothschild, "*Dynamics of Molecular Liquids*", , John Wiley, 1984

54. Newer Aspects of Molecular Relaxation Processes. Various authors., *Chem.Soc.Faraday Div.Symposium* 11, 1, (1976)

55. J.C.G.Griffiths, "*Vibrational Spectra and Structure. Vol.6. Ed J.R.During*", Chap.5, Elsevier NY, 1977

56. J.A.Barker and .D.Henderson, *Revs.Modern Physics* 48, 587, (1976)

57. J.T.Hynes, *Ann.Revs.Phys.Chem.* 28, 301, (1977)

58. M.W.Evans and J.Yarwood, *Int.J.Molec.Relax.* 21, 1, (1981)

59. B.J.Berne and R.Pecora, "*Dynamic Light Scattering*", Chap.15, John Wiley, 1976

60. D.Kivelson, *J.Chem.Phys.* **33**, 1094, (1960)

61. R.Wilson and D.Kivelson, *J.Chem.Phys.* **44**, 4440, (1966)

62. R.Wilson and D.Kivelson, *J.Chem.Phys.* **44**, 169, (1966)

63. J.Hwang, D.Kivelson and W.Plachy, *J.Chem.Phys.* **58**, 1753, (1973)

64. A.H.Maki and B.R.McGarvey, *J.Chem.Phys.* **29**, 31, (1958)

65. K.E.Falk, E.Ivanova, B.Roos, T.Vanngard, *Inorg.Chem.* **8**, 556, (1969)

66. J.J.Windle, A.K.Wiersena, *J.Phys.Chem.* **68**, 2316, (1964)

67. R.Kumari-Cowsik and R.Srinivarasan, *J.Chem.Phys.* **59**, 5517, (1973)

68. J.R.Pilbrow, T.D.Smith and A.D.Toy, *Aust.J.Chem.* **23**, 2287, (1970)

69. D.Coucouvanis in, "*Progress in Inorganic Chemistry VII ed Lippard*", J.Wiley, 1966,

70. R.Kirmse and B.V.Solovev, *J.Inorg.Nucl.Chem* **39**, 41, (1977)

71. C.P.Keijzers, G.F.M.Poulussen, E.DeBoer, *Mol.Phys.* **29**, 973, (1975)

72. E.Buluggia, A.Vera and A.A.G.Tomlison, *J.Chem.Phys.* **56**, 5602, (1972)

73. A.H.Maki and B.R.McGarvey, *J.Chem.Phys.* **29**, 35, (1958)

74. F.G.Herring. Personal communication

75. T.R.Reddy and R.Srinivarasan, *J.Chem.Phys.* **43**, 1405, (1965)

76. H.L.M.Van Gaal, J.W.Diesveld, F.W.Pijpers and J.G.V and J.G.M.Van der Linden, *Inorg.Chem.* **18**, 3215, (1979)

77. K.Nakamoto, J.Fujito, R.Condrate, Y.Morimoto, *J.Chem.Phys.* **39**, 423, (1963)

78. S.N.Choi, E.R.Menzel and J.R.Wasson, *J.Inorg.nucl.Chem* **39**, 417, *(1977)*

79. I.M.Kolthoff and E.J.Elving, "*Treatise on Analytical Chemistry. Vol.3 pt.II*", Chap.1, Wiley, 1961

80. A.J.Pilipenko and N.V.Melnikova, *Russ.J.Inorg.Chem.* **967**, 14, (1969)

81. D.C.Bradley, I.F.Rendall and K.D.Sales, *JCS.Dalton* **228**, 7, (1973)

82. F.G.Herring and J.M.Park, *J.Magn.Reson.* **36**, 311, (1979)

83. F.G.Herring and P.S.Phillips, *J.Mol.Struct.* **61**, 29, (1980)

84. F.G.Herring and P.S.Phillips, *J.Chem.Phys.* **73**, 2603, (1980)

85. J.F.Gibson, *Trans.Faraday.Soc.* **60**, 2105, (1964)

86. A.M.Swartz, W.Antholine, C.Mailer and B.Reichling, *Phys.Med.Biol.* **21**, 840, (1976)

87. R.D.Bereman and D.Nalewajek, *Inorg.Chem.* **16**, 2687, (1977)

88. P.S.Phillips. Masters Thesis UBC 1978

89. M.J.Weeks and J.P Fackler, *Inorg.Chem.* 7, 2548, (1968)

90. J.H.Freed and G.K.Fraenkel, *J.Chem.Phys.* **39**, 326, (1963)

91. C.P.Slichter, "*Principles of Magnetic Resonance 2nd ed.*", Chap.5, Springer Verlag, 1980

92. A.G.Redfield, "*Advances in Magnetic Resonance Vol.1*", p1, Academic Press, 1965

93. D.Kivelson, *J.Chem.Phys.* **33**, 1094, (1960)

94. N.M.Atherton, "*Electron Spin Resonance*", Chap.8 pt.11, Ellis Horwood, 1973

95. H.Sillescu and D.Kivelson, *J.Chem.Phys.* **45**, 3493, (1968)

96. W.A.Steele, "*Adv. in Chem .Physics Vol.XXXIV*", p1, John Wiley, 1976

97. N.M.Atherton, "*Electron Spin Resonance*", Chap.8 pt. 9 & 10, Ellis Horwood, 1973

98. J.H.Freed, *J.Chem.Phys.* **41**, 2077, (1964)

99. P.L.Nordio, "*Spin Labelling. ed. L. J. Berliner*", Chap.3, Academic Press, 1976

100. B.J.Berne and R.Pecora, "*Dynamic Light Scattering*", Appendix 7C, John Wiley, 1976

101. M.Mehring, "*Principles of High Resolution NMR in Solids*", Appendix 9A, Springer Verlag, 1983

102. W.T.Huntress, *J.Chem.Phys.* **48**, 3524, (1968)

103. M.Mehring, "*Principles of High Resolution NMR in Solids*", Appendix 9B, Springer Verlag, 1983

104. M.E.Rose, "*Elementary Theory of Angular Momentum*", Chap IV, Wiley NY, 1957

105. A.Abragam, "*Principles of Nuclear Magnetism*", Chap.VIII, O.U.P., 1983

106. R.T.Boere and R.G.Kidd, "*Ann. Reports in NMR Spectroscopy V13 ed G.A.Webb*", p319, Academic Press, 1982

107. Spiess, "*NMR. Basic Principles and Progress Vol. 15*", Chap.5, Springer Verlag, 1984

108. F.Perrin, *J.Phys.Radium* **5**, 33, (1934)

109. L.D.Favro, *Phys.Rev.* **119**, 53, (1960)

110. C.Hu and R.Zwanzig, *J.Chem.Phys.* **60**, 4354, (1974)

111. G.K.Youngren and A.Acrivos, *J.Chem.Phys.* **63**, 3846, (1975)

112. P.H.Elworthy, *JCS* **IV**, 3718, (1962)

113. J.T Edward, *J.Chem.Ed.* **47**, 261, (1970)

114. J.T.Hynes, R.Kapral and M.Weinberg, *Chem.Phys.Letters* **46**, 463, (1977)

115. G.D.Thorn and R.D.Ludwig, "*The Dithiocarbamates and Related Compounds*", Chap.2, Elsevier, 1962

116. J.C.Lindon and A.G.Ferrige, "*Progress in NMR. v14*", pp27-66, Pergamon 1980,

117. T.W.Phillips and K.P.Murphy, *J.Chem.Eng.Data* **15**, 304, (1970)

118. H.C.Brinkhoff, *Rec.Trav.Chim* **90**, 377, (1971)

119. G.Pegronal and A.Pignedoli, *Acta.Cryst.* **23**, 398, (1967)

120. A.Hudson and G.R.Luckhurst, *Chem.Rev.* **69**, 191, (1969)

121. N.M.Atherton, "*Electron Spin Resonance*", Chap.3, Ellis Horwood, 1973

122. J.E.Wertz and J.R.Bolton, "*Electron Spin Resonance*", Appendix, McGraw Hill, 1972

123. L.I.Schiff, "*Quantum Mechanics 3rd.ed.*", Chap.8, McGraw Hill, 1968

124. UBC REDUCE 1982

125. N.M.Atherton, "*Electron Spin Resonance*", Chap.8 pt.10, Ellis Horwood, 1973

126. G.K.Freankel, *J.Chem.Phys.* **42**, 4275, (1965)

127. L.K.White and L.Belford, *J.Amer.Chem.Soc.* **98**, 4428, (1976)

128. G.V.Bruno, J.K.Harrington and M.P.Eastman, *J.Phys.Chem.* **81**, 1111, (1977)

129. J.H.Freed and D.Campbell, *J.Phys.Chem.* **84**, 2668, (1980)

130. S.A.Goldman, G.V.Bruno, C.F.Polnaszek, J.H.Freed, *J.Chem.Phys.* **56**, 716, (1972)

131. R.Wilson and D.Kivelson, *J.Chem.Phys.* **44**, 154, (1966)

132. N.M.Atherton, "*Electron Spin Resonance*", Chap.9 pt.7, Ellis Horwood, 1973

133. G.Nyberg, *Mol.Phys* **12**, 69, (1967)

134. R.E.D.McClung, *J.Chem.Phys.* **51**, 3842, (1969)

135. P.S.Hubbard, *Phys.Rev.* **131**, 1155, (1963)

136. D.O'Reilly, *J.Chem.Phys.* **57**, 885, (1972)

137. J.Tait. Ph.D Thesis UBC 1974

138. E.R.Menzel and J.R.Wasson, *J.Amer.Chem.Soc.* **79**, 366, (1975)

139. J.C.M.Henning, *Rev.Sci.Instrum.* **32**, 35, (1961)

140. F.G.Herring, J.Mayo and P.S.Phillips, *J.Magn.Reson.* **34**, 413, (1979)

141. DLSQ in UBC CURVE 1984

142. H.C.Brinkhoff and A.A.Grotens, *Rec.Trav.Chim.* **111**, 253, (1974)

143. B.J.Bales, *J.Magn.Reson.* **38**, 193, (1980)

144. E.Heilbronner, *J.Chem.Ed.* **56**, 240, (1979)

145. D.W.Posener, *J.Magn.Reson.* **14**, 121, (1974)

146. M.Yu. BSc.Thesis. UBC 1981

147. D.R.Bauer, J.I.Brauman and R.Pecora, *J.Amer.Chem.Soc.* **96**, 6840, (1974)

148. F.I.Bartoli and T.A.Litovitz, *J.Chem.Phys.* **56**, 404, (1972)

149. E.J.Pederson, R.L.Vold and R.R.Vold, *Mol.Phys.* **41**, 811, (1980)

150. M.Fury and J.Jonas, *J.Chem.Phys.* **65**, 2206, (1976)

151. J.P.Kitzinger and J.M.Lehn, *Mol.Phys.* **22**, 273, (1971)

152. J.F.Harmon and E.J.Sutter, *J.Phys.Chem.* **82**, 1938, (1978)

153. C.W.R Mulder, J.Scriever and J.C.Leyte, *J.Phys.Chem.* 87, 2336, (1983)

154. W.H.Flygare, *J.Chem.Phys.* **41**, 793, (1964)

155. C.Deverall, *Mol.Phys* **18**, 319, (1970)

156. P.Vigny and J.Virlet, *J.Chem.Phys.* **47**, 4645, (1967)

157. G.C.Levy and I.K.Peat, *J.Magn.Reson.* **18**, 500, (1975)

158. E.D.Becker, J.A.Ferretti, R.K.Gupta and G.H.Weiss, *J.Magn.Reson.* 37, 381, (1980)

159. J.Kowalewski and G.A.Morris, *J.Magn.Reson.* **47**, 331, (1982)

160. R.R.Sharp, E.D.Becker and T.C.Ferrar, *J.Magn.Reson.* **8**, 298, (1972)

161. J.S.Waugh, *J.Mol.Spec.* **35**, 298, (1970)

162. J.L.Markley, W.J.Horsley and M.P.Klein, *J.Chem.Phys.* **55**, 3604, (1971)

163. R.Kaptein, K.Dijkstra and C.E.Tarr, *J.Magn.Reson.* **24**, 295, (1976)

164. I.M.Armitage, H.Huber, D.H.Live, H.Pearson and J.D.Roberts, *J.Magn.Reson.* **15**, 142, (1974)

165. R.L.Vold, R.R.Vold and H.E.Simon, *J.Magn.Reson.* **11**, 283, (1973)

166. T.P.Pitner and J.F.Whidby, *J.Anal.Chem.* **51**, 2203, (1979)

167. E.D.Becker, J.A.Ferretti, R.K.Gupta and G.H.Weiss, *J.Magn.Reson.* **37**, 369, (1980)

168. J.M.Berassau and F.Hyafil, *J.Magn.Reson.* **40**, 245, (1980)

169. L.M.Sweeting, *J.Magn.Reson.* **48**, 311, (1982)

170. R.K.Harris and R.H.Newman, *J.Magn.Reson.* **24**, 449, (1976)

171. H.Hanssum, *J.Magn.Reson.* **45**, 461, (1981)

172. M.Sass and D.Ziessow, *J.Magn.Reson.* **25**, 263, (1977)

173. G.H.Weiss and J.A.Ferretti, *J.Magn.Reson.* **61**, 490, (1985)

174. G.H.Weiss and J.A.Ferretti, *J.Magn.Reson.* **61**, 499, (1985)

175. E.Fukishima and S.B.W.Roeder, "*Experimental Pulse NMR*", Chap.3, Adisson Wesley, 1981

176. H.Hanssum, W,Maurer and H.Ruterjans, *J.Magn.Reson.* **31**, 231, (1978)

177. M.Levitt and R.R.Ernst, *J.Magn.Reson.* **55**, 247, (1983)

178. M.Levitt, *J.Magn.Reson.* **48**, 234, (1982)

179. K.Van Putte, *J.Magn.Reson.* **2**, 174, (1970)

180. R.L.Vold, R.R.Vold and D.Canet, *J.Chem.Phys.* **66**, 1202, (1977)

181. M.Mehring, "*Principles of High Resolution NMR in Solids*", Chap.4, Springer Verlag, 1983

182. A.Abragam, "*Principles of Nuclear Magnetism*", Chap.VIII pt.IIE, O.U.P., 1983

183. P.Newman, C.Raston and A.White, *J.C.S.Dalton* **13**, 32, (1973)

184. D.Canet, *Mol.Phys.* **36**, 1731, (1978)

185. G.Brauodakis, I.P.Gerothanassis, and J.Lauterwein, *J.Magn.Reson.* **52**, 288, (1983)

186. D.L.De Fontaine, D.K.Ross and B.Ternai, *J.Magn.Reson.* **18**, 276, (1975)

187. R.Gerhards and W.Dietrich, *J.Magn.Reson.* **23**, 21, (1976)

188. A.Brunetti, *J.Magn.Reson.* **28**, 289, (1977)

189. D.Grouch, S.Hurlbert and A.Ragouzeos, *J.Magn.Reson.* **49**, 371, (1982)

190. H.Hanssum and H.Ruterjans, *J.Magn.Reson.* **39**, 65, (1980)

191. J.Granot, *J.Magn.Reson.* **53**, 386, (1983)

192. A.Ejchart, P.Oleski and K.Wroblewski, *J.Magn.Reson.* **59**, 446, (1984)

193. J.Delikatny. Personal communication

194. P.H.Fries, N.R.Jagannathan, F.G.Herring and G.N.Patey, *J.Chem.Phys.* **80**, 6267, (1984)

195. J.P.Kitzinger and J.M.Lehn in, "*Nitrogen NMR. eds. G.A.Webb and W.Witanowski.*", Chap.3, Plenum, 1973

196. NDVINT in UBC NLE 1979

197. D.Hoel and D.Kivelson, *J.Chem.Phys.* **62**, 1323, (1975)

198. T.O.Seim, T.B.Melo and S.Prydz, *J.Magn.Reson.* **9**, 175, (1973)

199. D.Hoel and D.Kivelson, *J.Chem.Phys.* **62**, 1323, (1975)

200. M.T.Chenon, J.M.Bernassau, C.L.Mayne and D.M.Grant, *J.Phys.Chem.* **85**, 2733, (1982)

201. D.Chandler, *J.Chem.Phys.* **60**, 3508, (1974)

202. D.Chandler, *J.Chem.Phys.* **62**, 1358, (1975)

203. P.W.Atkins, *Mol.Phys.* **17**, 321, (1969)

204. P.W.Atkins, A.Lowestein and Y.Margalit, *Mol.Phys.* **17**, 329, (1969)

205. R.I.Cukier and K.Latakos-Lindenberg, *J.Chem.Phys.* **57**, 3427, (1972)

206. J.L.Dote, D.Kivelson and R.N.Schwartz, *J.Phys.Chem.* **85**, 2169, (1981)

207. W.E.Blass, *App.Spec.Rev.* **11**, 57, (1976)

208. T.E.Gough and F.W.Grossman, *J.Magn.Reson.* 7, 24, (1972)

209. I.Goldberg, H.R.Crowe and R.S.Carpenter II, *J.Magn.Reson.* **18**, 84, (1975)

210. C.H.Warren and L.Ramaley, *Applied Optics* **12**, 1976, (1973)

211. J.S.Hwang, R.P.Mason, L.Hwang and J.H.Freed, *J.Phys.Chem.* **79**, 489, (1975)

212. R.Trousson and M.Rinne, *Rev.Sci.Instrum.* **55**, 1989, (1984)

213. P.N.T.Lindsay and B.M.Peake, *J.Magn.Reson.* **47**, 365, (1982)

214. G.Brouwer and J.A.Jansen, *J.Anal.Chem.* **45**, 2239, (1973)

215. B.E.Barker and M.F.Fox, *Chem.Soc.Rev.* **9**, 143, (1980)

216. T.E.Gough and R.G.Hacker, *J.Magn.Reson.* **6**, 129, (1972)

217. T.E.Gough and K.O.Beiber, *J.Magn.Reson.* **21**, 285, (1976)

218. D.W.Kirmse, *J.Magn.Reson.* **11**, 1, (1973)

219. P.C.Kelly and G.Horlick, *J.Anal.Chem.* **45**, 518, (1973)

220. A.Forman and D.C.Borg, *J.Magn.Reson.* **31**, 311, (1978)

221. D.W.Posener, *J.Magn.Reson.* **13**, 102, (1974)

222. H.A.Buckmaster, S.Cohn-Sfetcu and D.J.I.Fry, *J.Magn.Reson.* **14**, 296, (1974)

223. M.U.A.Bromba and H.Zeigler, *J.Anal.Chem.* **51**, 1760, (1979)

224. M.U.A.Bromba and H.Zeigler, *J.Anal.Chem.* **55**, 1299, (1983)

225. M.U.A.Bromba and H.Zeigler, *J.Anal.Chem.* **55**, 648, (1983)

226. J.F.Kaiser and W.A.Reed, *Rev.Sci.Instrum.* **48**, 1447, (1977)

227. A.Savitzky and M.J.Golay, *J.Anal.Chem.* **36**, 1627, (1964)

228. D.Binkley and R.Dessy, *J.Chem.Ed.* **56**, 148, (1979)

229. R.Kaiser and W.R.Knight, *J.Magn.Reson.* **36**, 215, (1979)

230. R.E.Moore, "*Mathematical Elements of Scientific Computing*", Chap.3, Holt-Reinhart-Winston, 1974

231. A.D.Booth, "*Numerical Methods 3rd ed.*", Chap.3, Butterworths London 1966,

232. C.Giancaspro and M.B.Comisarow, *Applied Spectroscopy* **37**, 153, (1983)

233. R.N.Bracewell, "*The Fourier Transform and its Applications. 2nd. ed.*", Chap.3,, McGraw Hill, 1981

234. G.E.Pearson, *J.Magn.Reson.* **272**, 65, (1977)

235. R.T.Vollmer and W.J.Caspary, *J.Magn.Reson.* **27**, 181, (1971)

236. P.L.Hall, *J.Phys.D* **5**, 673, (1972)

237. I.B.Goldberg, *J.Magn.Reson.* **32**, 233, (1978)

238. D.B.Loveland and T.N.Tozer, *J.Phys.E* **5**, 535, (1972)

239. D.W.Posener, *J.Magn.Reson.* **14**, 129, (1974)

240. J.W.Elmsey, J.Feeney and L.H.Suttcliffe, "*High Resolution NMR Spectroscopy. Vol.1* ", Chap.5, Pergamon Press, 1965

241. J.Granot, *J.Magn.Reson.* **49**, 197, (1982)

242. E.C.Kemble, "*The Fundamenatal Principles of Quantum mechanics*", Chap XI, Dover, 1958

243. E.Fukishima and S.B.W.Roeder, "*Experimental Pulse NMR*", Chap.6 pt.E.1, Adisson Wesley, 1981

244. J.R.Pilbrow, *J.Magn.Reson.* **58**, 186, (1984)

245. A.Hudson and H.A.Hussain, *J.Chem.Soc.B* **11**, 1346, (1968)